Biodetection using fluorescence energy transfer from Quantum dot excited whispering gallery modes to fluorescent acceptors

Subha Jana

PSL UNIVERSITÉ PARIS

THÈSE DE DOCTORAT
DE L'UNIVERSITÉ PSL

Préparée à **l'École supérieure de physique et de chimie industrielles de la Ville de Paris**

BIODETECTION USING FLUORESCENCE ENERGY TRANSFER FROM QUANTUM DOT EXCITED WHISPERING GALLERY MODES TO FLUORESCENT ACCEPTORS

BIODÉTECTION PAR TRANSFERT D'ÉNERGIE DE FLUORESCENCE DE QUANTUM DOTS COUPLÉS À DES MODES DE GALERIE VERS DES ACCEPTEURS FLUORESCENTS

Soutenue par

Subha Jana

Le 10 Décembre 2021

Ecole doctorale n° 397

Physique et Chimie des Matériaux

Spécialité

Chimie des Matériaux

ESPCI PARIS | PSL

Composition du jury :

Rodolphe, JAFFIOL Professeur, Université de Technologie deTroyes	*Rapporteur et Président du jury*
Ngoc Diep, LAI Professeur associé, ENS Paris-Saclay	*Rapporteur*
Niko, HILDEBRANDT Professeur, Université de Rouen	*Examinateur*
Jérôme, WENGER Directeur de recherche, Institut Fresnel	*Examinateur*
Valentina, KRACHMALNICOFF Chargée de recherche, ESPCI Paris	*Examinateur*
Thomas, PONS Chargé de recherche, ESPCI Paris	*Directeur de thèse*

” Where the mind is without fear and the head is held high, where knowledge is free.”

Rabindranath Tagore

dedicated to dadu

Acknowledgement

Chapters of life begin and end, creating new memories, and leading us to the next chapter. This three years-journey of PhD has been a great chapter in my life, with many new memories, with both new and old friends, and this thesis would never be complete without thanking them.

Out of all the people, who comes to my mind first is my supervisor, Thomas. I arrived in France, a bit afraid and a bit nervous. His reassurances and support did not only make me comfortable in this new environment but also helped me to integrate into the lab. A supervisor probably plays the most important role in the PhD life of a student, teaching and guiding the fellow in the right direction. Thomas is not only a smart, and attentive advisor, he is much more. He is humane, he is supportive and capable of genuinely motivating students to think, learn and stay focused in research. I cannot thank him enough for being such an excellent teacher, and a generous guide to me. Just to follow in the footsteps of Indian students, “Thank you, SIR Thomas Pons!”

For every PhD student, fellow lab mates are an important support system. I am grateful to mine for being so welcoming, warm, and letting me be a part of this family even though I did not speak much French. I thank Alexandra, Nicolas, and Sandrine for being always nice and kind to me, also for those delicious chestnut cream cakes. Thank you, Marion, for helping me deal with many administrative offices. Thank you, Manon, for all those Angèle songs, and Eva, for helping me in the beginning. Thank you, Antoine, for your frequent help with the optics and the software. Mogha and Sheila! It was a pleasure being there with both of you during this whole journey. Thank you, Sophia, for keeping the lab energetic. Many thanks to Po and Fanny, my two excellent co-bureau. Yuzhou! You have been an excellent lunch buddy. Charlie K. (“K” for Kev or Kersuzan?), thank you for agreeing to uphold the legacy of cavity boys. Corentin and Mathias, thanks for those fun Friday evenings. Lina, thank you for all those Dolipranes and come on, I don’t eat that much. And Ningyuan, enjoy the coming three years in the lab. Thank you, our beloved coffee machine for keeping me alive and awake throughout the whole PhD. In the end, I thank all of you for putting up with my poor jokes, hopefully, you will miss it, at least for the coming few months.

Family! It has not been an easy journey to come all the way since the beginning. I simply cannot thank you enough for all your support, love, and your faith in me. Maa and Baba, you have undoubtedly done a great part by supporting and motivating me. Dadu and Dida, thank you for being there always for me. The love and support from Kaka, Kakima, Pisi, and all my cousins meant a lot. Geneviève and her family, thank you for all your love and support. It helped me keep going.

Each person who travels has friends, and a journey is never complete without them. I thank Trinu without whom I would probably not be writing this. Thank you Sayandip, Debanuj, Shouvik, and Pascal for all the adventures and the discussions. I also thank my friends from Maison de l'Inde and UptoParis for their support, activities, and discovering beautiful Paris together. Thanks to all of you, it did not get lonely here.

ESPCI and UPtoParis administration, especially Rositsa, Virginie, and Alexandra, thank you for all the support, smooth and efficient work processes. Because of you, even with the pandemic, everything worked out well.

Sincere love and support from many others who I could not mention here also led me to complete this PhD. If not with words, I acknowledge them with warm embraces from the heart. And I wish this life to continue in the same way with all your support to the horizon of a new chapter.

INTRODUCTION

In the last hundred years, tremendous effort in terms of research initiatives and allocation of economic resources have been made to develop schemes and technologies for more accurate and easy diagnosis of diseases. The importance of medical diagnosis also has been well-emphasized by Gandhi who asserted "*A correct diagnosis is three-fourths the remedy*." With the advancements in our scientific understanding and abilities to design complex systems, the field of medical diagnostics have progressed to a new era. The available diagnostic technologies are truly numerous in the current scenario; ranging from highly sophisticated MRI, PET-CT scan to simple paper based antigenic tests, all have been developed depending on the targeted applications. Detection of bio-chemical analytes is a crucial step in medical diagnosis. Each of these diagnostic technologies has their own advantages and drawbacks. The detection techniques are often recommended depending on the type of target analyte, required information and desired level of sensitivity. Another major outlook that often plays a big role in choosing a detection scheme is the ease of usage, cost and the portability. ELISA or enzyme-linked immunosorbent assay is one of the most widely used biochemical assays used in varieties of applications, ranging from the laboratory based biological analysis to the easy detection of pathogens. But being a heterogeneous assay, ELISA is not always easy to perform owing to the long incubation periods, and multiple washing steps. So recently Förster resonance energy transfer or FRET based homogenous bio-sensing assays have attracted a lot of attention for being rapid, easy to use and highly specific. Additionally, the development of highly fluorescent and photostable semiconductor QD based functional bioconjugates have led to many FRET based bio-sensing schemes, potentially helping the field to flourish. However, FRET based schemes suffer from some major disadvantages due to some inherited characteristics of the process. FRET only occurs in a significant rate when the donor and acceptor are placed in a distance range less than 10 nm, which makes this technique inefficient for the detection of larger biological molecules (e.g., large proteins, virus DNA/RNA). This results into lack of sensitivity and poor signal to noise ratio, often leading to false/ inconclusive test results. On the other hand, many recent studies showed that sensing schemes based on high quality-resonance modes or so called, whispering gallery modes (WGMs) of optical microcavities can lead to very high sensitivity in bio-detection platforms. But these schemes usually require expensive tunable lasers, tedious and precise alignment of the instrument and the microcavity, and also often suffer from background noises arising from the thermal fluctuations and non-specific interactions. However, another important characteristic of microcavity that is worth mentioning is the characteristic of their resonances that spread out as evanescent fields up to a few tens to hundreds of nm outside the cavity

surface. Thus these resonances can engage in energy transfer in ranges that is not achievable with a traditional energy transfer technique, such as FRET.

In this thesis, I propose a scheme to design a hybrid bio-sensing platform by interfacing the FRET based sandwich assay with optical microcavities to exploit the advantages of both the schemes, for example, high specificity of FRET and high sensitivity, longer range of energy transfer from WGM cavities. To be precise, the main motivation of this project is to design microcavity structures where fluorescent QDs are placed inside dielectric microspheres to enable strong coupling of their fluorescence to the cavity modes. In the next step, the goal would be to demonstrate energy transfer from these QDs to some optical acceptors present in the vicinity of the microcavity through the evanescent field of these modes. And in the final step, biofunctionality would be imparted to the microcavities, and also to the acceptors located in the external medium. That would enable a sandwich-like complex formation when the specific analyte is present in the solution, leading to cavity mode mediated enhanced energy transfer from the QDs to the acceptors. This configuration would allow the sensitive and specific detection of very large biomolecules that are not easy to sense using FRET based detection schemes.

To clearly and elaborately present the work done in this project, this thesis includes an introductory chapter to present the context of the work and basis of optical microcavities, Förster resonance energy transfer in the context of bioassays and semiconductor quantum dots. Then the manuscript will be divided into three different chapters, each focused on a particular step of our journey towards building a microcavity based biosensor.

- The **Chapter-2** will be focused on the fabrication of the optical microcavities. This part will involve synthesizing a few batches of QDs that would fulfil the spectral requirement to engage in the energy transfer process, and also possess other advantages such as high quantum efficiency and photo/chemical stability. The next step will be focused on incorporating this QDs into the dielectric microspheres for the fabrication of our optical microcavities. After the fabrication, the next goal will be to characterize the optical properties of these cavities using spectroscopic and imaging techniques. This will allow us to understand the fundamental characteristics of these cavities, and later utilize them for our targeted applications. A theoretical model should also be constructed to verify whether the WGM characteristics of these cavities match the regular analytical behavior of spherical resonators.

- The **Chapter-3** will be dedicated towards understanding the optical behavior of these microcavities when they are engaged in an energy transfer experiment. To this goal, a simple donor-acceptor conjugate will be designed using the QD loaded microspheres as optical donors and some dye-based nanoparticles as optical acceptors. The quantitative characterization of the energy transfer process, such as the analysis of the transfer rate and

efficiency, is also very important to have a better understanding of the process. Additionally, a side-by-side comparison of the cavity-based energy transfer with the traditional FRET would help us understand where we stand in terms of commercial and practical applications.

- The last part of the work, thus **Chapter-4** will be focused on designing a real biosensing assay on the basis of the donor microcavity-acceptor nanoparticle conjugated system in the previous chapter. To this aim, the first part of this chapter will involve imparting bio-specificity to the microcavities by some functionalization techniques. After successful bioconjugation, the next step will be to perform a simple model bio-sensing experiment. In our case, I will perform an assay to sense hybridization between two model DNA strands. This will help us to confirm the ability of these technique to successfully translate specific biological interactions. The final step will be to modify this model assay in order to perform a real biosensing, to be precise, the detection of a cancer biomarker called survivin in solution phase.

- In the final section of the thesis, the conclusion of the work and the future perspectives of the project are discussed elaborately.

TABLE OF CONTENTS

LIST OF ABBREVIATIONS

WGM	Whispering gallery mode
Env	Envelope
QD	Quantum dots
NP	Nanoparticle
SPR	Surface plasmon resonance
AB	Antibody
ELISA	Enzyme linked immunosorbent assay
FRET	Förster resonance energy transfer
RET	Resonance energy transfer
ET	Energy transfer
TR-FRET	Time resolved - Förster resonance energy transfer
DNA	Deoxyribonucleic acid
RNA	Ribonucleic acid
mRNA	messenger Ribonucleic acid
D-A	Donor-Acceptor
MDR	Morphology-dependent resonances
Q	Quality factor
TIR	Total internal reflection
PS	Polystyrene
dyeNP	dye nanoparticle
LDOS	Local density of states
FWHM	Full width at half maxima
LOD	Limit of detection
LCORR	Liquid-core optical ring resonator

CdSe/CdZnS	Cadmium selenide/cadmium zinc sulfide
TEM	Transmission electron microscope
TM	Transverse Magnetic
TE	Transverse Electric
CCD	Charge-coupled device
WGET	Whispering gallery-mediated energy transfer
PMD	Photonic mode density
RDDI	Resonant dipole-dipole interaction
R18	Rhodamine B octadecyl ester
TPB	Tetrakis (pentafluorophenyl) borate
PMMAMA	poly (methylmethacrylate-co-methacrylic acid)
DLS	Dynamic light scattering
PEI	polyethyleneimine
LP	Long pass
RT-PCR	Real time-polymerase chain reaction
ssDNA	Single stranded DNA
EDC	1-Ethyl-3-(3dimethylaminopropyl)carbodiimide.HCl
MES	4-morpholinoethanesulfonic acid
NHS	N-Hydroxysuccinimide
BSA	Bovine serum albumin
Cy5	Cyanine 5

CHAPTER 1: INTRODUCTION TO MICROCAVITY BASED BIOSENSING

CONTENTS

1.1 BIO-DETECTION:

1.1.1 Definition and introduction:

Bio-detection or bio-sensing is a general terminology referring to the processes to detect biological substances in vitro or in vivo. Simplifying the IUPAC definition, a bio-detection device uses specific biochemical interactions mediated by isolated enzymes, proteins produced by immunosystems, cells or tissues to detect biological analytes usually by electrochemical, thermal, and optical signals.[1]

A bio-detection device generally consists of two important components: a bio-recognition unit and a transducer. The bio-recognition unit helps the biosensor to bind to a target analyte with unique specificity. Transducers are responsible for translating the bioreceptor-analyte interactions into electrochemical, thermal, magnetic or optical signal. The analytes can belong to a broad range of biological entities, e.g.; genetic materials of viruses or bacteria, antibodies produced by immunosystems of infected living organisms, peptides or other biological elements[2]. These analytes can also be simple molecules like sugars[3] (e.g.; glucose, fructose, etc.), pollutants[4] (such as heavy ions like lead[5], mercury[6] and arsenic[7]) in water or toxic elements in food[8] and crops[9]. Owing to the vast and practical use of bio-detection platforms in clinical diagnosis for the identification of pathogens[10–13], food[14–16] and water quality[17–19] analysis and even for monitoring blood glucose level, tremendous research effort has been put into the development of this field in the last 50 years. One of the standard biochemical detection techniques that is often preferred for clinical and industrial purposes is called the enzyme linked Immunosorbant assay or ELISA[20] which uses specific enzymatic reactions that leads to some physical, such as colorimetric, change in the traditional format of the assay when the specific analyte is present in the sample. But in the recent times, many exotic properties of materials such as fluorescence[21–23], surface plasmon resonances (SPR)[24–26] and dielectric cavity resonances[2,27–29] are exploited to transduce and amplify detection signals. Label-free detection techniques[27] are progressively gaining attention for being simple, user friendly and often with improved sensitivity. In this section, I will discuss the mainstream detection techniques, and their principles in addition to their advantages and disadvantages. Finally I will propose a fluorophore loaded microcavity based bio-detection scheme that might be useful for building bio-sensing schemes with improved sensitivity and specificity.

1.1.2 Classification of bio-detection assays:

In the history of recent developments of biosensors, immunoassay is one of the most useful advancements. This analytical bio-chemistry tool, first developed by Rosalyn Sussman Yalow and Solomon Berson in 1950s is widely used in medical sciences as well as for research purposes in last few decades[30]. Immunoassays generally use antibodies (ABs) which are carefully designed for detection of specific biomolecules. Antibodies are usually advantageous as bio-recognition units because they can strongly and stably bind to the analytes with very high specificity. There are various kinds of transducer that are widely used in immunoassays. For example, radio-immunoassays utilize antibodies labeled with radio-active isotopes to indicate the formation of the analyte-antibody complex[31]. Other interesting labeling strategies involve the use of chemiluminescent[32], bioluminescent[33] or fluorescent[8] tags on the antibodies. In these formats, one antibody is labeled with at most a few reporter molecules. In contrast, ELISA, one of the most regularly used assays, utilizes enzyme-based catalytic activities to indicate the binding of the analyte to the antibody[34], by modifying either the color or absorbance or the fluorescence properties of substrate molecules. Each enzyme therefore acts as a multiplier, leading to an increase in sensitivity. Depending on the functioning mechanism, immunoassays can be of several different kinds, the major formats of operation are direct, indirect, sandwich and competitive.

1.1.2.1 Direct immunoassays:

In this kind of assays, the analytes directly bind to the bio-recognition units or antibodies. This complex formation can be quantitatively measured by observing the signal from the transducer which is attached to the antibody[35]. In general, the signal is measured as the optical, electrical or magnetic property of the system. This technique spares the users from the complexity of using catalytic ligands but the detection limit is comparatively higher than the label based detection.

In Figure 1.1 (A), a direct ELISA scheme is shown, where antigens/analytes are mobilized on the surface, then the primary antibody conjugates are added to it, followed by a washing step to remove the unbound antibodies. After that, when enzymatic substrate is added, depending on the presence of analyte-antibody complex on the surface, enzymatic activity signal would change.

1.1.2.2 Indirect immunoassays:

Unlike direct assays, indirect ones use a labeled secondary antibody as the transducer. After the formation of the sensor-analyte complex, the transducer antibody is introduced which selectively binds to the primary bio-recognizing antibody[36].

A scheme of indirect ELISA assay is given in the Figure 1.1 (B). Unlike the direct assay, in this case, the primary antibody does not possess the transducer enzyme conjugation, thus a secondary antibody-enzyme conjugate is required that binds to the primary antibody and provide transducing signals by reacting to the enzymatic substrates.

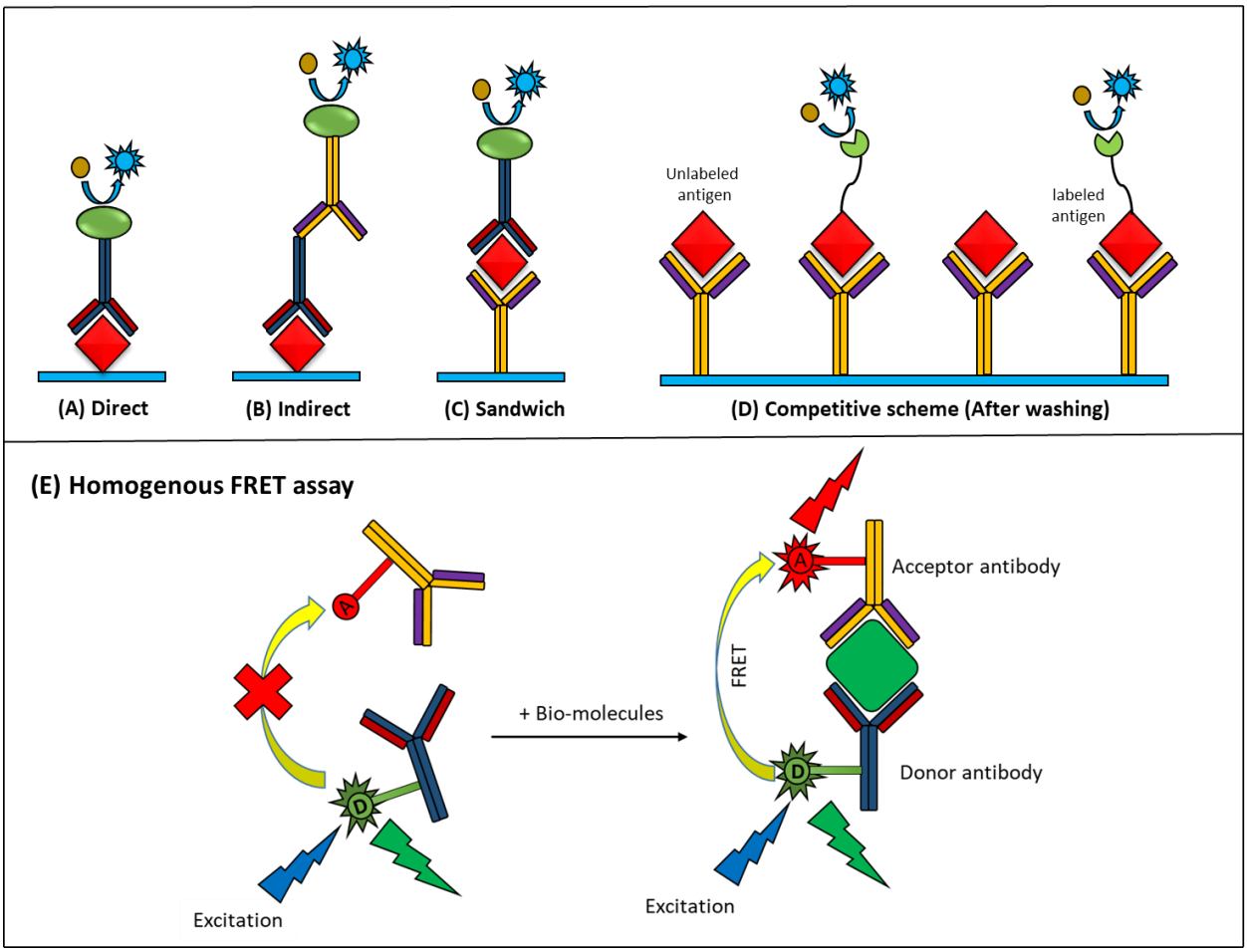

Figure 1.1: *(A-E) Different formats of ELISA assays: (A) direct, (B) indirect, (C) sandwich, and (D) competitive, (analyte in red, conjugated enzyme in green, substrate in yellow and product in blue). (E) Homogenous FRET sandwich assay (target analyte in green, D and A respectively are the optical donor and the acceptor).*

1.1.2.3 Sandwich immunoassay:

In this format of immunoassays, two specific antibodies are used to bind to the analyte from two opposite sites and form a 'sandwich complex'. At first, a capture antibody binds to the biomolecule of interest and blocks one face of binding, later the probe antibody binds to the other face of the analyte. The signal from the transducer provides quantitative information about the analyte. This technique is highly specific because it requires two different antibodies to bind to the analyte on the specific sites. This format is the most common one for Enzyme-linked assays (ELISA). During the past few decades, Förster resonance energy transfer (FRET)[37,38], chemiluminescence[39] and bioluminescence-based[40] immunoassays have been the topics of huge research interest to the scientific community. These assays too utilize the format of sandwich complex formation. A sandwich ELISA scheme is demonstrated in the Figure 1.1 (C).

1.1.2.4 Competitive immunoassays:

This format of assays is generally used when the size of the analyte is too small to be captured between two antibodies to form a sandwich complex. Instead of using a transducer antibody, this format utilizes the competition between labeled and unlabeled analytes to bind to the primary capture antibodies[41]. Depending on the functional mechanism and ease of using, competitive immunoassays can be of two kinds.

(A) Homogeneous competitive immunoassay: In this mechanism, an assay is prepared where labeled analytes are bound to the antibodies. When unlabeled sample is added, they compete with the labeled analytes and consequently replace a portion of the bound, labeled analytes. The signal from these free labeled analytes is used to know the amount of the sample analyte[42]. This kind of assays are called homogenous as they do not require any washing steps, making the process much simpler and user-friendly.

(B) Heterogeneous competitive immunoassay: The concept of this assay is very similar to the homogenous one, except in this case, the labeled, unbound analytes are washed away and the signal from the bound labeled analytes is measured to gain the information about the analyte concentration in the sample[43]. This assay is called heterogeneous as it requires an intermediate washing step. Figure 1.1 (D) shows a scheme where both labeled and unlabeled antigens are bound on the capture antibody coated surface.

ELISA is one of the most commonly used heterogeneous immunoassay that has extensive applications in bioanalysis, diagnosis, research labs as well as quality testing of products in industries. In spite of being widely used, ELISA or any other heterogeneous immunoassay involves multiple, long incubation periods and tidy washing steps which create difficulties for the users. In the recent times, a lot of efforts and progress have been made to develop user-friendly homogeneous assays based on Förster resonance energy transfer (FRET) which enables one-step, fast and direct detection of analytes both in competitive and other formats of immunoassays. A FRET sandwich assay scheme is shown in the Figure 1.1 (E), where two sets of antibodies labeled with respectively donor and acceptor fluorophores bind to the specific analyte forming a sandwich complex which enables the energy transfer process from the donor to the acceptor and the signal can be read by observing the enhancement of acceptor emission intensity or the quenching of donor fluorescence.

1.2 FRET BASED HOMOGENOUS IMMUNOASSAY

1.2.1 Förster Resonance Energy Transfer (FRET):

Energy transfer between a donor and an acceptor can occur through several different processes. The major ones are resonance energy transfer[44], electron transfer[45], reabsorption, collisional quenching[46] and excited state complex formation[47]. All of these processes are fundamentally and mechanistically different from each other. Dexter electron transfer is a non-radiative mechanism to transfer energy via the exchange of electrons between an excited donor and a relaxed acceptor. The range of transfer is very small, typically less than 1 nm. Reabsorption occurs when a photon is emitted by an excited donor molecule and subsequently absorbed by an acceptor. Intuitively, the complex formation and collisional quenching occur in a similar way[48]. The donor can form an excited-state complex with the acceptor to transfer its energy whereas the collisional quenching occurs just due to the collision between an excited donor and an acceptor.

In contrast to the mechanisms mentioned above, resonance energy transfer is a radiationless process where the donor and the acceptor are described as two oscillating dipoles with non-perpendicular relative orientation. The energy transfer occurs when they are in close proximity. The transferred energy is dissipated from the acceptor by either radiative (for fluorophores) or non-radiative (for quenchers) relaxation. FRET (Förster or Fluorescence Resonance Energy Transfer) is radiationless that means the

energy transfer occurs without the emission of a photon, instead it occurs due to the dipole-dipole interaction between the donor and the acceptor. The story of FRET begins when in an experiment performed in gaseous phase, Cario and Frank observed energy transfer from mercury to thallium atoms. Also in 1920s, French physicist Jean Perrin first coined the term 'transfert d'activation' to denote the transfer of energy between two molecules through interactions of two oscillating dipoles[49]. FRET is named after the German scientist Theodor Förster who developed the theoretical and mathematical understanding of the resonance energy transfer (RET). By 1948, he published his idea of RET and its significance in photosynthesis for plants[50]. Since the formulation, FRET has been widely applied in many fields, e.g., medical diagnosis, research experiments in biology and chemistry, bio-sensing assays and imaging. FRET is defined as a mechanism of non-radiative and through-space energy transfer from a donor to an acceptor moiety present within close proximity, usually less than 10 nm[51].

1.2.2 The theory of FRET:

The theory of resonance energy transfer has been developed by using both classical and quantum mechanical assumptions on the system which makes the theory reasonably complex. But the idea of the energy transfer and the parameters that control this process can be easily interpreted from these following final equations[51].

The rate of energy transfer between a donor and an acceptor separated by the distance 'r' can be given by equation 1.1.

$$\mathrm{K}_{ET}(\mathrm{r}) = \frac{\mathrm{Q_D}\kappa^2}{\tau_D r^6}\left(\frac{9000(\ln 10)}{128\pi^5 N\eta^4}\right)\int_0^\infty F_D(\lambda)\varepsilon_A(\lambda)\lambda^4\, d\lambda\,, \qquad (Eq.\,1.1)$$

where $\mathrm{Q_D}$ and τ_D are respectively the quantum yield and radiative lifetime of the donor in the absence of the acceptor, η is the refractive index of the medium, N is Avogadro's number. $F_D(\lambda)$ is the fluorescence intensity of the donor in the wavelength range λ to $\lambda + \Delta\lambda$ provided that the total fluorescence intensity (calculated as the area under the emission curve) is normalized to 1 and $\varepsilon_A(\lambda)$ is the extinction coefficient of the acceptor at λ. The term κ^2 stands for the relative orientation of the dipoles of the donor and the acceptor in space. The value of κ^2 is usually taken as 2/3 which is consistent for dynamic averaging of the donor and acceptor dipoles with random orientations. This equation provides the insight about the sharp dependence of the energy transfer rate on 'r'.

$$J(\lambda) = \int_0^\infty F_D(\lambda)\varepsilon_A(\lambda)\lambda^4\, d\lambda \;=\; \frac{\int_0^\infty F_D(\lambda)\varepsilon_A(\lambda)\lambda^4\, d\lambda}{\int_0^\infty F_D(\lambda) d\lambda}\,. \qquad (Eq.\,1.2)$$

Another important factor that determines the rate of the energy transfer is the spectral overlap between the donor emission and acceptor absorption (see Figure 1.2 (A)) which is given by the equation 1.2. Characteristically $F_D(\lambda)$ is unitless, so the unit of overlap integral $J(\lambda)$ depends on $\varepsilon_A(\lambda)$ and λ. Usually λ has the unit of nm and $\varepsilon_A(\lambda)$ is expressed in $M^{-1}cm^{-1}$, so the $J(\lambda)$ is generally given in the unit $M^{-1}cm^{-1}\,nm^4$. The Jablonski diagram for FRET between a donor-acceptor pair has been given in the Figure 1.2 (B).

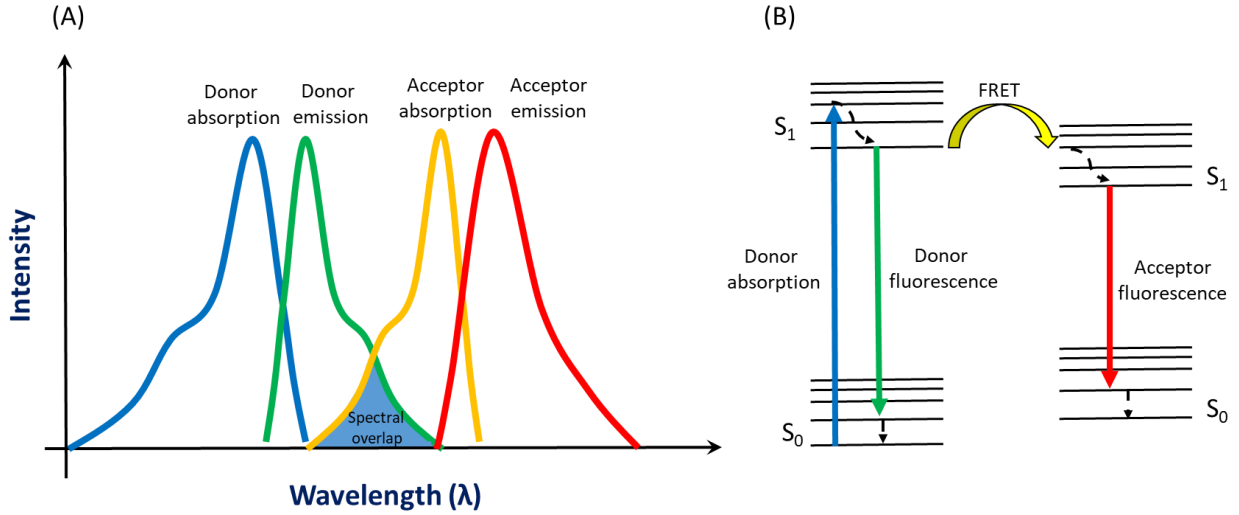

Figure 1.2: *(A) spectral overlap (blue shaded region) between the donor emission (in green) and acceptor fluorescence (in yellow), (B) Jablonski diagram for FRET (the dotted lines represent vibrational relaxation).*

In most of the real-lab bio-chemical experiments, the notion of energy transfer rate is not always practical to use, instead the idea of the Förster distance (R_0) is more useful and convenient for quick interpretation. R_0 is defined as the distance between the donor and the acceptor when the energy transfer rate is 50%. The Förster distance can also be expressed as equation 1.3 which can be used to easily calculate R_0 from the quantum yield of the donor and the spectral properties of the donor and the acceptor.

$$R_0^6 = \left(\frac{9000(\ln 10)Q_D\kappa^2}{128\pi^5 N\eta^4}\right)\int_0^\infty F_D(\lambda)\varepsilon_A(\lambda)\lambda^4\, d\lambda\,. \qquad (Eq.\,1.3)$$

Equation 1.3 can be made more simple and ready to use by just plugging in the constants so that the equation become more convenient to use for calculating R_0. The simplified version can be given by equation 1.4.

$$R_0 = 0.211\left(Q_D \kappa^2 \eta^{-4} J(\lambda)\right)^{1/6} \text{ Å}, \qquad (Eq. 1.4)$$

R_0 generally lies within the 4-8 nm range for traditional donor-acceptor chromophore pairs. Once the value of R_0 is derived, the rate of energy transfer can be calculated using a simple equation 1.5.

$$K_{ET} = \left(\frac{R_0}{r}\right)^6 \frac{1}{\tau_D}. \qquad (Eq. 1.5)$$

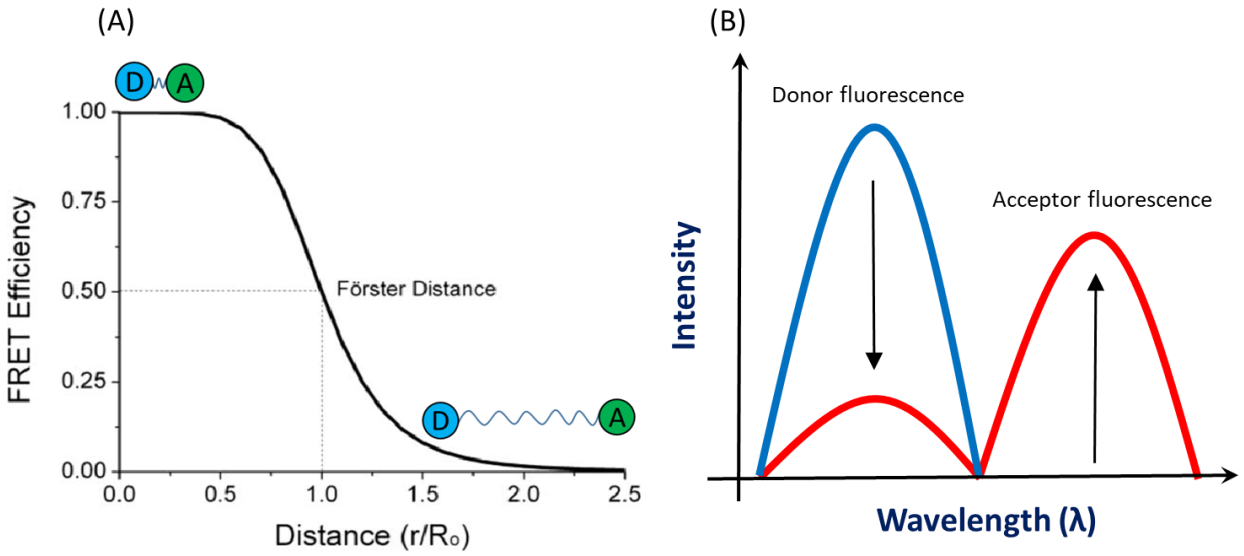

Figure 1.3: *(A) Dependence of FRET efficiency on the donor-acceptor distance, (B) Donor-only fluorescence (blue) and donor-acceptor conjugate fluorescence (red).*

Energy transfer is a competitive mechanism with electronic relaxation. Transfer only happens with a significant efficiency when its rate is comparable to the decay rate of the donor excited state, otherwise electronic relaxation dominates and very little RET occurs during the excited state lifetime of the donor. The efficiency of energy transfer (E) can be expressed using the equation 1.6.

$$E = \frac{K_{ET}(r)}{K_{ET}(r) + (K_{rad} + K_{non-rad})}, \qquad (Eq. 1.6)$$

where K_{rad} and $K_{non\text{-}rad}$ are respectively the rate of relaxation through radiative and non-radiative processes. Together these radiative and non-radiative processes only are responsible for the relaxation of the donor in the absence of any acceptor.

Equation 1.6 can be re-written in terms of the Förster distance (R_0) using the relation of eq.1.5, as:

$$E = \frac{R_0^6}{R_0^6 + r^6} . \qquad (Eq. 1.7)$$

Equation 1.7 suggests that the efficiency of energy transfer strongly depends on the donor-acceptor distance. In the Figure 1.3 (A), it can be seen that when the distance goes below R_0, the efficiency of energy transfer quickly approaches to 1, contrarily the efficiency drops quickly when the distance increases above R_0. For example, when the donor-acceptor distance is twice of the R_0, the efficiency is only 1.54%.

The efficiency of transfer is typically calculated from the relative donor fluorescence intensity of the donor-acceptor conjugate (F_{DA}) and donor-only (F_D) using the equation 1.8. F_D and F_{DA} respectively can be calculated by integrating the donor fluorescence before and after adding the acceptor, as shown in the Figure 1.3 (B)

$$E = 1 - \frac{F_{DA}}{F_D} \qquad (Eq. 1.8)$$

A similar equation 1.9 can also be derived to calculate the efficiency that involves the lifetime of the donor in the presence of the acceptor (τ_{DA}) and without the acceptor (τ_D).

$$E = 1 - \frac{\tau_{DA}}{\tau_D} \qquad (Eq. 1.9)$$

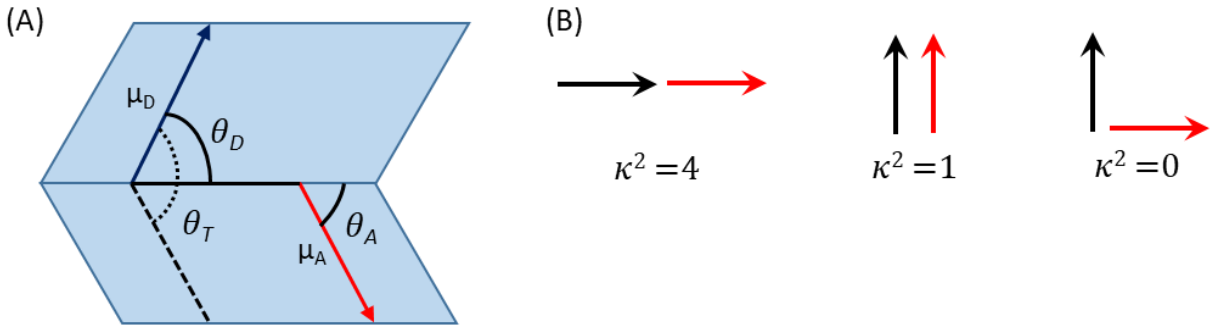

Figure 1.4: *(A) orientation between the donor (μ_D) and acceptor (μ_A) dipoles, (B) donor-acceptor relative dipole orientations and their corresponding κ^2 values.*

One of the key parameters in the dynamics of Förster resonance energy transfer is the orientation factor (κ^2) which have been previously used in the equations but has not been widely elaborated. κ^2 is related to the relative alignment of the donor and the acceptor dipoles (given as in Eq. 1.10). The rate of energy transfer is linearly dependent on the orientation factor making it a key parameter.[51]

$$\kappa^2 = (cos\theta_T - 3cos\theta_D\ cos\theta_A)^2\ , \qquad (Eq. 1.10)$$

where, θ_D and θ_A respectively are the angles that the donor dipole (μ_D) and acceptor dipole (μ_A) make with the line adjoining them, and θ_T is the angle between the donor and acceptor planes (see Figure 1.4 (B)). In solutions where the donors and the acceptors usually do not align themselves in a fixed orientation, the value of κ^2 is taken to be 2/3 which is derived as an average value with the assumption that the fluorophores randomly orient themselves via rotational diffusion at the moment of energy transfer. But in various circumstances, the donors and acceptors orient themselves in a particular fashion which allows to utilize the equation 1.10 to calculate a case-dependent orientation factor. The value of κ^2 can vary from 0 to 4. The value of κ^2 is 0 when the donor and the acceptor dipoles are perpendicular to each other, in that case, theoretically no energy transfer should happen. For parallel dipoles the value is 1 and for head-to-tail parallel orientation κ^2 takes the maximum value of 4 (see all the orientations in Figure 1.4 (B)). Fluorescence anisotropy experiments on the FRET pairs limits the value of κ^2 which in turns minimizes the error for experiments to measure distance using FRET[51].

To summarize the key points, the efficiency of FRET is governed by several parameters, but the major ones are:

1. The distance between the donor and the acceptor (r) that should be typically less than 10 nm for a significant efficiency of FRET.
2. The spectral overlap (J(λ)) between the emission spectra of the donor and the absorption spectra of the acceptor.
3. The relative orientation (associated by κ^2) between the dipole moments of the donor and the acceptor.

1.2.3 The applications of FRET:

FRET based experimental techniques are extensively used in various fields of sciences including medical and molecular biology, biochemistry, materials and polymer chemistry[52]. In the field of biology, structural and conformational changes of proteins and DNA can be accurately studied up to sub-nanoscale precision that is the reason why FRET is called 'Spectroscopic nano-ruler'[52]. Some examples of FRET being applied for scientific studies are discussed below.

1.2.3.1 Study of Conformational and structural dynamics:

Most of the bio-chemical reactions involve structural changes of bio-moieties in their pathways. For example, Protein and RNA folding[53], DNA bending in small and large angles[54,55,56], DNA-protein[57], RNA-protein[58], protein-protein[59] interactions are widely studied using FRET-based techniques. The most general scheme extracts the distance distribution of FRET pairs from the fluorescence intensity of the donor and the acceptor which can be interpreted to predict the dynamics of biochemical reactions including the formation of the intermediate states. For example, there was an ambiguity regarding the structure of apolipoproteins (ApoA-I) which are responsible for regulating the metabolism of cholesterol. Because of the formation of discoidal structure, techniques like x-ray crystallography was not sufficient to predict the conformation of apolipoproteins. There were two possible suggestions of arrangement, one is the formation of belt like structure around the lipid and the other one is by folding antiparallel α-helices in a picket-fence conformation. The issue to predict the conformation was resolved using RET where two amino acids were tagged with FRET pairs allowing the energy transfer to occur from the donor to the acceptor that can only occur in one of the proposed possible arrangements. This experiment revealed the actual conformation to be belt-like rather than the formation of fence[51,60].

FRET based techniques are exploited to determine the distance between the active sites of a macromolecules (e.g., proteins, DNA, RNA and peptides) by covalently labeling one site with a donor and the other one with an acceptor[52]. The efficiency of FRET provides very accurate information about the structure and the size of a protein, but the only condition that is applied is that the distance between the donor and the acceptor does not change during the excited state lifetime of the donor.

1.2.3.2 Material and polymer sciences:

FRET based techniques are widely used to study cell-material interfaces quantitatively. These experiments reveal information which are valuable to comprehend cellular responses and the chemical changes in matrix proteins due to various substrates interacting with the cell surface[52].

Numerous studies have been performed where amino acids[61], carbohydrates[62] and biomolecules[63] are used as spacers between the donor and acceptor to understand how parameters like chain length influences the rigidity of the polymer. Some other studies have also been done to show how energy transfer rate varies when the number of amino acid units are manipulated in the spacer peptides[64]. These studies help to understand the flexibility of different regions in the three-dimensional protein structures.

1.2.3.3 RET based sensors:

FRET has been applied extensively to develop sensors for detecting both small molecules and biological macromolecules like proteins, peptides and DNA[65]. FRET based sensors have a lot of advantages over the conventional biochemical techniques because resonance energy transfer allows to investigate the conformational states of bio-moieties in real time with high spatio-temporal resolution[51].

A lot of research has been done on FRET based pH sensors[66], assays to detect ions[67] and small molecules[68] and measure intracellular pH[69] to study the complex biochemical reactions occurring in the cellular level. In a recent study to understand a variety of cellular functions, a RET based pH sensor have been developed where a napthalimide fluorophore is used as a FRET donor and a rhodamine B dye is utilized as an FRET acceptor[70]. Morpholine was appended as a potential lysosome targeting group to the FRET donor which can induce chemical reactions responsible for changing the pH of the intracellular matrix[71]. The FRET sensor is capable of switching the fluorescence from green to red within the neutral to acidic pH range. In another study[72], a FRET based chemosensor has been developed by using fluorescein as energy donor and ring-opened rhodamine B as acceptor to selectively detect Hg^{2+}.

1.2.4 Perspectives of FRET Based Immunoassays:

1.2.4.1 Advantages:

Based on the principle of bio-chemical interaction between antibody and antigen, immunoassays are designed for highly specific detection of analytes. ELISA, which is one kind of heterogeneous immunoassays, is widely used for bioanalysis and diagnostics but the multiple incubation and washing steps make it complicated and requiring some expertise from the end-user to perform. On the other hand,

homogenous RET based immunoassays have proven to be simple, user friendly and reliable[8,44]. Recently these are designed to have wide range of applications from biomarking of proteins to the detection of environmental and food toxins**.** This kind of immunoassay utilizes the spectral dynamics of the donor-acceptor complex to detect biomolecules and excludes the complex washing steps used in heterogeneous assays which makes it a rapid and one-step detection technique. For a long time, organic fluorophores were predominantly used as donor-acceptor FRET pairs but in the recent times there have been a lot of research on quantum dots for labeling in FRET based immunoassays[73], which will be further discussed in section 1.3 of this chapter.

The most common FRET based immunoassay operates in non-competitive design which is widely known as "sandwich immunoassay". In this format, two different kinds of capture probes such as, antibodies, one attached to an optical donor and the other one connected to an optical acceptor, are mixed together and then the sample of interest is added to the mixture. If the specific analyte is present in the sample, then the two different kinds of antibodies will bind to their corresponding binding sites and form the sandwich complex (Figure 1.1 (E)). An optimal range of wavelength is selected to specifically excite donor and minimize the contribution of direct excitation of the acceptor. Due to the close proximity (~ 10 nm) and spectral overlap, FRET occurs from the sensitized donor to the acceptor which can be qualitatively and quantitatively followed by looking at the quenching of donor fluorescence or the emission from the acceptor. Time resolved spectroscopy is also used to observe the binding kinetics. The efficiency of FRET can be accurately determined from the change in the fluorescence lifetime of the donor. Due to the presence of acceptor's decay channel, the lifetime of the donor will decrease. Time resolved fluorescence energy transfer (TR-FRET) which is a practical combination of time-resolved fluorescence spectroscopy and FRET, is often preferred over the steady-state fluorescence techniques due to lower background related problems and improved sensitivity and fewer false positive/negative results[74].

Various simple coupling chemistry techniques are widely used to react the functional groups of antibodies to donor/acceptor fluorophores that enables us to detect a vast range of analytes. The simplicity of this test and reduced complexities regarding washing steps, makes it a very useful detection platform even suitable for non-professional end users.

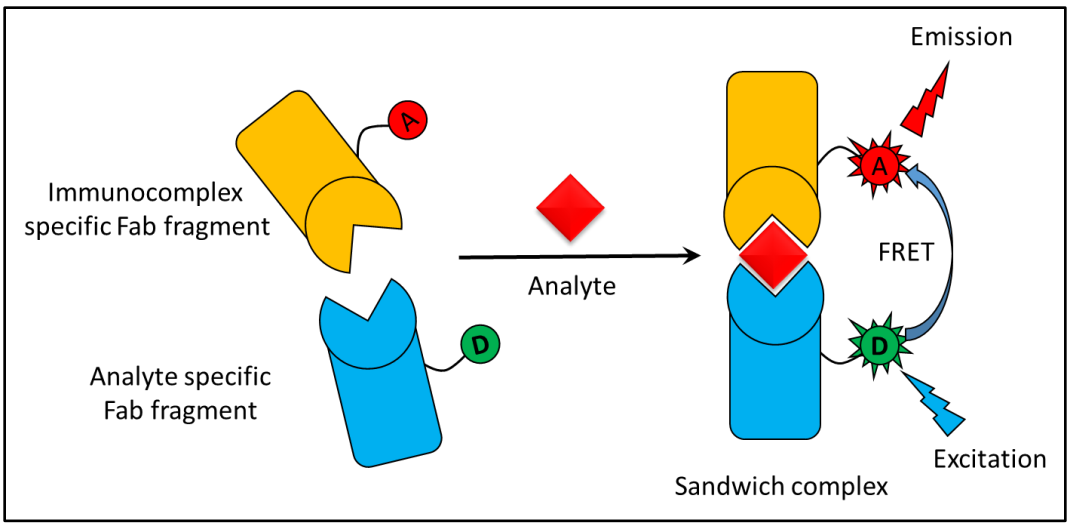

Figure 1.5: *A time-resolved FRET scheme for specific detection of morphine[42]. (Image source: doi.org/10.1021/ac048379l)*

As an example, a TR-FRET based assay has been demonstrated by Pulli et al. for the sensitive detection of morphine[42] (see in Figure 1.5). An analyte (morphine) specific antibody fragment is labeled with donor organic fluorophores which yields an immune complex upon binding with morphine. On the other hand an antibody-fragment with very high binding-specificity to the immune complex has been tagged with acceptor fluorophore. This one step homogenous FRET assay could detect the presence of morphine already at a concentration as low as 5 ng/mL without any cross-reactivity to other opiates like codeine or heroin. Later the same principle was applied for the efficient detection of (-)- Δ9-tetrahydrocannabinol (THC)[75] and mycotoxin from wheat extracts[9].

1.2.4.2 Disadvantages:

Even though FRET based immunoassay has been adopted as a useful, simple and cost-effective bio-detection technique, but there are some disadvantages such as the limitation of the maximum size of the analyte that can be detected which results into lack of sensitivity and low accuracy of the outcome. The major issue that FRET based detection platforms face, appears due to its strong inverse dependence on the donor-acceptor distance.

As mentioned in the equation 1.5, the efficiency of FRET (E) varies inversely with the 6th power of r, donor-acceptor distance. The optimum D-A distance where the FRET pairs have significant efficiency is between 1-10 nm. Beyond 10 nm distance, the rate of resonance energy transfer become significantly low[64]. In case

of majority of the homogenous fluorescence assays, the FRET efficiency significantly depends on the size of the sandwich complex produced due to the coupling of the donor and the acceptor labelled antibodies to the target analytes. The large dimensions of many antibodies (e.g.; Immunoglobulin G or IgG antibody has the dimension of 14.5 nm × 8.5 nm × 4.0 nm, with antigen binding sites separated by 13.7 nm)[76] and target analytes (e.g.; antigen proteins, long stranded DNA and mRNA sequences) frequently yields complexes where donor and acceptor are placed above the suitable FRET range. Not only does it decrease the signal-to-noise ratio but also it leads to false read-out of signals. Also the relative dipole orientation of the donor and acceptor is a critical factor in FRET assays, the FRET efficiency theoretically drops down to zero if the dipoles are perpendicular to each other.

In the recent time, many alternative methods have been proposed to augment the distance range of energy transfer using, for example, energy migration in nanoassemblies[77], energy transfer to metallic nanoparticles[78–80], or energy transfer between lanthanides and semiconductor quantum dots (QDs)[81–83], and using the resonances of optical microcavities which we will present in the following section.

1.3 Quantum dots (QDs): In the light of bio-sensing application

1.3.1 Introduction:

Colloidal semiconductor nanocrystals which are most commonly known as quantum dots (QDs), are one of the most promising and widely acclaimed nanomaterials with potential applications in various fields, ranging from biological imaging, bio-/chemo-sensing to the fabrication of optoelectronic devices (e.g., light emitting diodes, photodetectors, solar cells, etc.). In the context of biological applications, the major advantage of QDs arises due to the facile conjugation of biomolecules to the surface of the QDs that allows us to exploit the inherited opto-electronic properties of the QDs in parallel to the desired biological selectivity and functionality. Another interesting property of QDs that makes them quite interesting in terms of applications is their ability to function as optical donors or acceptors or both in energy transfer systems. Since the beginning of the development of this field, traditional quantum dot materials often have core-shell or core-multishell configurations forming interfaces between two or more semiconductor

materials. Most widely sought QDs are often found to be derived from binary semiconductor materials such as II-VI (e.g., CdSe and CdTe), III-V (e.g., InP and GaAs) in colloidal nanocrystalline forms[65].

1.3.2 Brief history of QDs: Development and application in biosensing:

Alexei Ekimov, a Russian physicist at Vavilov State Optical Institute, was studying the color formation in glasses due to semiconductor doping when he discovered nanometer sized crystals of CdS, CdSe, CuCl and CuBr with interesting optical properties. This was the very first observations of nanocrystals. The theoretical understanding came from another Russian physicist, Alexander Efros in 1982 who explained the behavior of nanocrystals by the confinement of their charge carriers and the formation of discrete energy levels. Later the theory was supported by the experiments done by Louis Brus at Bell Labs who performed a controlled synthesis of CdS colloidal nanocrystals with average size of 4.5 nm. He observed that these nanocrystals exhibited a substantial blueshift of their absorption compared to bulk CdS, which supported the theory of quantum confinement of electrons and holes[84,85].

During the initial stage of developments, more efforts were focused on the controlled and uniform synthesis and understanding the fundamental properties of QDs. Later, resonance energy transfer (RET) was thoroughly demonstrated by Bawendi Lab in 1996, who introduced the idea to use smaller QDs as optical donor and larger ones as acceptors (see Figure 1.6 (B)). This long range RET was well-explained by assuming QD-QD dipole coupling which is a classic hallmark of Förster resonance energy transfer (FRET)[86,87]. The development of QDs as potential FRET based biosensor passed the landmark when the first demonstration of QD- bioconjugates came around in 1998 which was both stable in aqueous environment and functional as cellular probes[88,89]. Later many reports of QD based bio-sensors were designed to probe biological interactions, such as biotin-avidin[90], antibody-antigen[91] and even to precisely quantify the amount of proteins[92] present in a solution. Most of these studies performed steady state emission as well as time-resolved lifetime measurements to provide insight into the underlying energy transfer processes which indeed fits the theory of FRET. During the last two decades, myriad of research groups have studied and published many demonstrations involving QD-bioconjugates for sensing applications[93–97] which have made this platform more available, advantageous and user-friendly for being used in practical purposes. Many examples can be found where QD-bioconjugates have been used to detect DNA[98,99] , RNA[100,101], proteins[102–104], antigens[105,106] and even small molecules[107,107].

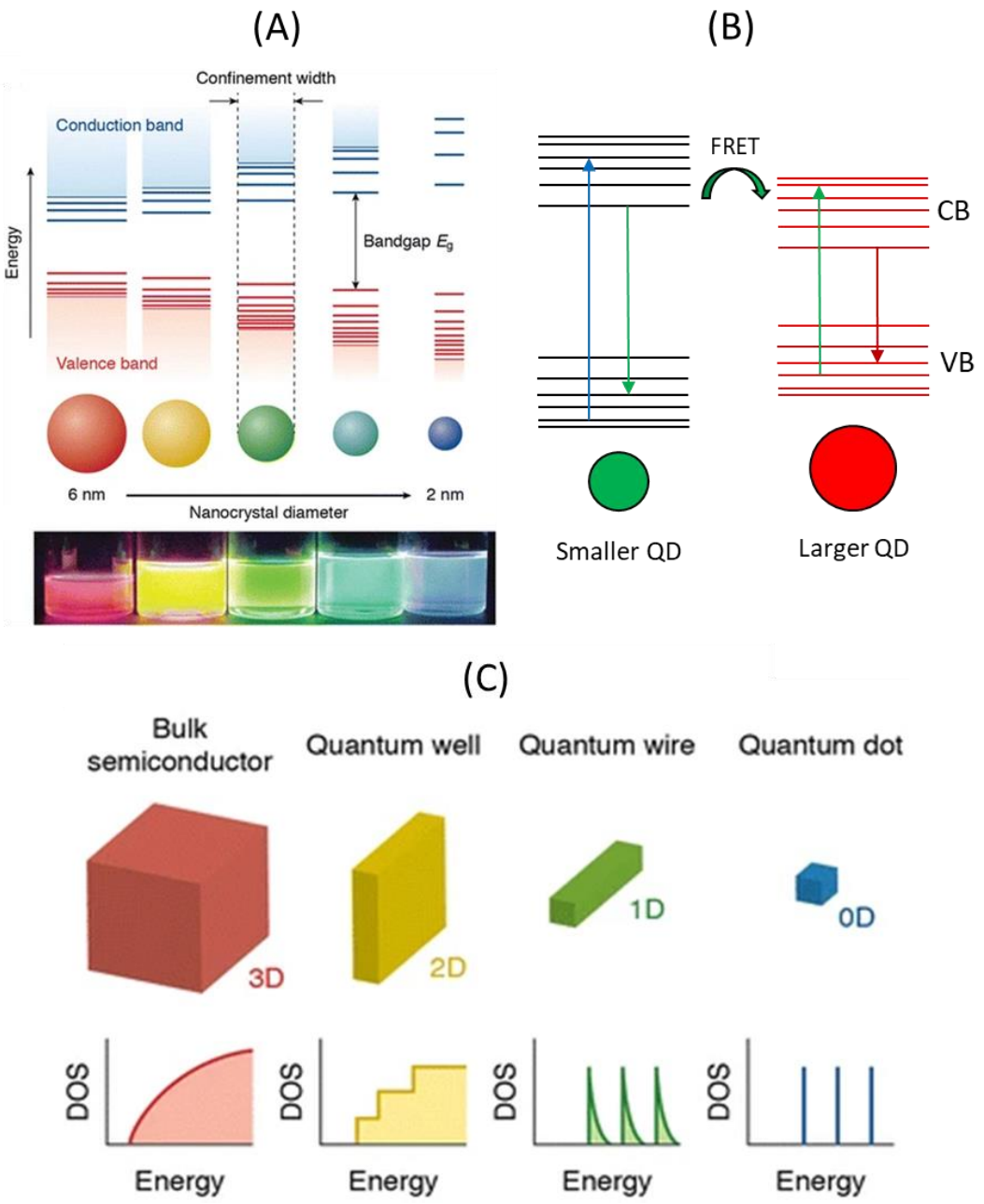

Figure 1.6: *(A) Size-dependent opto-electronic properties of QDs, (B) FRET from a smaller QD to a larger one, (C) different kinds of quantum confinements in nanocrystals. (Image source: doi.org/10.1007/s41061-016-0060-0)* [108]

1.3.3 Opto-electronic properties of QDs:

Since the beginning of their discovery, QDs have appeared as a topic of interest for their unique optical and electronic properties which has a great dependence on their dimensions. Similar to the original semiconductor material, QDs also have an intrinsic bandgap. Incident light must have equal or higher energy than the bandgap for an electronic transition to occur from the valence to the conduction band. This electronic transition consequently creates an excited state electron in the conduction band and a positively charged hole in the valence band, which are bound to each other by Coulombic attraction force. Such kind of electron-hole pair is often referred as a "quasiparticle" called "exciton". The exciton has a certain lifetime which greatly depends on the material and the size of the particle, but in general when the electron and the hole recombine radiatively, it emits the energy of the exciton as a photon. The major difference in between QDs and their bulk counterparts lies in their electronic structure[109]. Bulk semiconductors generally form a continuous valence and conduction bands whereas QDs have electronic structure formed by discrete states that is similar to individual atoms which gives them the name "artificial atoms".

Probably the most interesting and widely exploited fact about QDs is their size-dependent optoelectronic properties which allow us to precisely tune their bandgap, thus the color of their emission[108] as shown in Figure 1.6 (A). These properties are exhibited by QDs due to an effect called "quantum confinement" which can be precisely interpreted with the "particle in a box" theory. When the radius of a particle is smaller than the Bohr excitonic radius for that particular material, the particle enters the quantum confinement regime and start to exhibit stronger correlation between its opto-electronic properties and dimension, and discretization of its electronic states due to the charge wavefunction going to zero at the border of the nanocrystals. In that case, the exciton is squeezed to fit into the low dimensional structure, and the energy of the exciton drastically varies with the size. Not only QDs, depending on the degree of quantum confinement which can vary in different directions in a nanostructure can lead to different kinds of electronic properties in materials. If the exciton is spatially confined in all directions, a QD is formed, whereas if the exciton is trapped in 2-axes, it results into a quantum wire. If the exciton is confined only in one direction, a quantum well is formed[108]. Thus, the electronic structure for nanomaterials also varies with the shape. How the density of electronic states for these materials vary is given in Figure 1.6 (C).

The quantum confinement effect on the opto-electronic properties of a particle is determined by how the size of it is compared to the bulk Bohr excitonic radius (a_B)[110,111]. The Bohr excitonic radius can be calculated using the following equation 1.11.

$$a_B = a_H \varepsilon_r \left(\frac{m}{\mu}\right), \qquad (Eq.\ 1.11)$$

where a_B is the Bohr exciton radius, a_H is the hydrogen atom Bohr radius (~ 0.53 Å), ε_r is the dielectric constant of a semiconductor, m is the mass of a free electron, and μ is the reduced mass of the exciton defined as;

$$\frac{1}{\mu} = \frac{1}{m_e^*} + \frac{1}{m_h^*}, \qquad (Eq.\ 1.12)$$

where m_e^* and m_h^* are, respectively, the effective masses of the electron and the hole in the semiconductor materials.

For ***weak confinement regime,*** the radius (R) of the particle should be smaller than a_B and R > a_e, a_h, where a_h and a_e are the Bohr radius respectively for the positive hole, and the negative electron. In this case the dominant energy is the Coulomb term that takes effect by shifting the excitonic energy states to a higher energy[110]. This energy shift (ΔE) for the excitonic ground state can be calculated by equation 1.13[112].

$$\Delta E = \frac{\hbar^2 \pi^2}{2R^2}\left(\frac{1}{m_e^*} + \frac{1}{m_h^*}\right) = \frac{\hbar^2 \pi^2}{2\mu R^2}. \qquad (Eq.\ 1.13)$$

For ***moderate confinement regime*,** the radius of the particle is in the same range as a_B. And the other condition which should also be satisfied is a_h < R < a_e, a_B. This kind of confinement is evident in small QDs, where the motion of a photo-excited hole is well-restricted[110,112].

The ***strong confinement regime***[110,111] is achieved when the following conditions such as, R << a_B and R << a_e, a_h all are satisfied. The most important two factors in case of strong confinement regime are,

(1) The Coulomb interaction of electron-hole is small, and it's acting as a perturbation,
(2) The electron and the hole behave independently within the exciton.

The confinement energy ($E_{Confinement}$) which causes the excitonic states to shift, can be calculated using the equation 1.13.

There is also an additional energy associated to the Coulombic attraction between the positive hole and negative electron of the exciton, which can be given by $E_{coulomb}$ in equation 1.14[112].

$$E_{Coulomb} = -\frac{1.8\, e^2}{\varepsilon_r R}, \qquad (Eq.\ 1.14)$$

where ε_r the size dependent dielectric constant of the semiconductor, and e is the charge of an electron.

So the total energy corresponding to the radiative recombination of an excited QD can be given as the sum of the bandgap energy, the quantum confinement energy and, the bound excitonic energy related to the Coulombic attraction between the electron and the hole (equation 1.15)[112].

$$\begin{aligned} E_{Total} &= E_{Bandgap} + E_{Confinement} + E_{Coulomb} \\ &= E_{Bandgap} + \frac{\hbar^2 \pi^2}{2\mu R^2} - \frac{1.8\, e^2}{\varepsilon_r R} \end{aligned} \qquad (Eq.\ 1.15)$$

1.3.4 Various types of core-shell QDs:

Growing shells on the cores of QDs increases the quantum efficiency of particles as well as protect them against external conditions which can lead to their oxidation. It also allows the surface dangling bonds to be passivated. The growth of a shell can also modulate the optical properties of the nanocrystal, it can widen their spectral emission window beyond that of the core. Forming shells allows to manipulate the delocalization of the wave function of each charge carrier (the electron and the hole), thus control the bandgap of the material. The shell is necessarily made of a semiconductor material different from the core. There are several types of core/shell QDs depending on the alignment of the valence and conduction bands of the shell relative to the core, Figure 1.7[109].

For **type I QDs,** the shell possesses a larger bandgap than the core. In particular, the valence band for the core is located in a higher energy than that of the shell, potentially trapping the hole at the core. On the other hand, the conduction band of the core has lower energy than that of the shell which confines the electronic wavefunction at the core. As both the charge carriers are trapped inside the core, the excitonic recombination takes place there. The bandgap of the shell material has minimal effect on the emission wavelength of the QDs in this scenario, but in many cases, the quantum efficiency have been improved[108], thanks to the passivation of the core surface. The examples of type I QDs are CdSe/ZnS and InAs/CdSe.

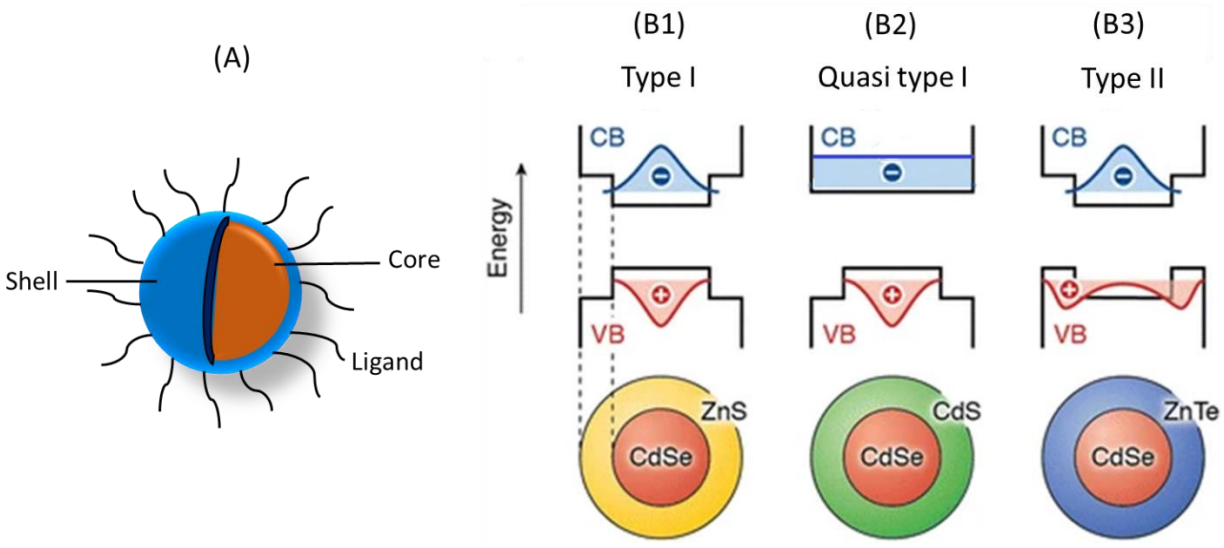

Figure 1.7 *(A) schematic of core/shell QDs. Delocalization of electronic and hole wavefunction in core/shell (B1) type I, (B2) quasi type I, and (B3) type II QD (Image source: doi.org/10.1007/s41061-016-0060-0)*[108]

In case of **type II QDs**, one of the charge carriers is confined at the core whereas the other carrier is localized in the shell of the QDs. Here the exciton recombines at the interface of the two materials, which results into a redshift of the photoluminescence. The lifetime of the exciton is also relatively longer due to the smaller overlap of the electronic and hole wavefunctions. The examples of type II QDs are ZnTe/CdSe, CdTe/CdSe and CdS/ZnSe[113].

For **quasi-type I** QDs, either of the bands (valence or conduction) for both the core and shell have similar energy so that the wavefunction for one of the charge carriers is delocalized all over the volume of the QD. In contrast, the other charge carrier is strictly confined in either of the materials. One of the examples is CdSe/CdS QDs[108,113].

A crucial factor that has to be considered while choosing the shell material is the crystallinity of it with respect to the core. If the lattice parameters of the core and the shell are very different from each other, then defect or trap states are formed at the interface which reduces the photoluminescence efficiency by introducing more non-radiative recombination pathways[114,115].

For in vivo biological applications of QDs such as live cell imaging, it is very important to choose a biocompatible or low-toxic material to grow shells on core QDs to minimize leaching of toxic core

elements such as cadmium. ZnS in that regard, is a great option due to its low toxicity for short-term usage and relatively wide band gap (~ 3.54 eV) which allows us to obtain a type I bright and stable QDs[94].

1.3.5 Insights into the synthesis of QDs:

Many synthesis schemes to achieve bright, photo- and chemically stable nanoparticles and QDs have been reported in the literature. These schemes can be sorted out in two different methods for understanding, which are respectively "top-down" and "bottom-up". "Top-down" method generally induces strong force to break down larger particles into smaller ones. This kind of techniques suffer from some disadvantages like the lack of precise control over the size and shape of the particles and also very strong force can induce damages to the properties of the materials. "Bottom-up" synthesis on the other hand, provides much more precise control over the size and the shape of the particles. Individual atoms or molecules work as the building blocks for constructing nano/microstructures, which allows to promptly manipulate the dimensions of the resulting structures.

Traditionally, inorganic materials have mostly been synthesized by high-temperature ceramic methods that typically goes beyond 1000 ^{0}C. This kind of techniques do not allow much flexibility in terms of size and shape control or choosing the precursors or reaction conditions (e.g., pH). During the exploration of new synthesis routes, solution phase methods have gained much popularity due to much greater chemical flexibility and potential for size and shape control. Hydrothermal or solvothermal synthesis techniques have been proven advantageous from many aspects. In this kind of techniques, precursor solutions are heated in a sealed vessel, which allows to control many parameters regarding the reactions such as, the choice of solvent, pH, reagents, precursors, dopants, etc. As the reactions occur in moderate temperatures, it is also possible to isolate metastable intermediates which is not possible in case of high temperature synthesis schemes. Also the resultant products are in general, highly (nano)-crystalline and with low polydispersity[116].

1.3.5.1 Understanding the reaction kinetics: LaMer model for NP synthesis:

To obtain nanoparticles with controlled size and shape, and narrow size distribution, many parameters concerning the reaction can be carefully controlled. The LaMer model, proposed in the 1950s, provides conceptual insight regarding the reaction process for the formation of nanoparticles in solution based processes[117]. Upon mixing and solubilization of the precursors into the reaction media, the concentration of the reactants increases creating a degree of supersaturation. When the level of supersaturation

surpasses the critical nucleation threshold, nucleation starts to take place, reducing the degree of supersaturation as shown in Figure 1.8. If the rate of nucleation surpasses the rate of solubilization of the precursors, then eventually the rate of nucleation surpasses the rate of solubilization of the precursors, then eventually the new nuclei. At that point, there are a few major pathways that the nanoparticle growth process may follow: (1) monomer addition, whereby additional precursor units or monomers deposit onto the already formed nuclei, (2) Ostwald ripening, through which energetically disfavored small nuclei or particles dissolve and deposit onto more thermodynamically favored larger particles, (3) coalescence, whereby multiple nanoparticles come together and fuse to form larger ones.

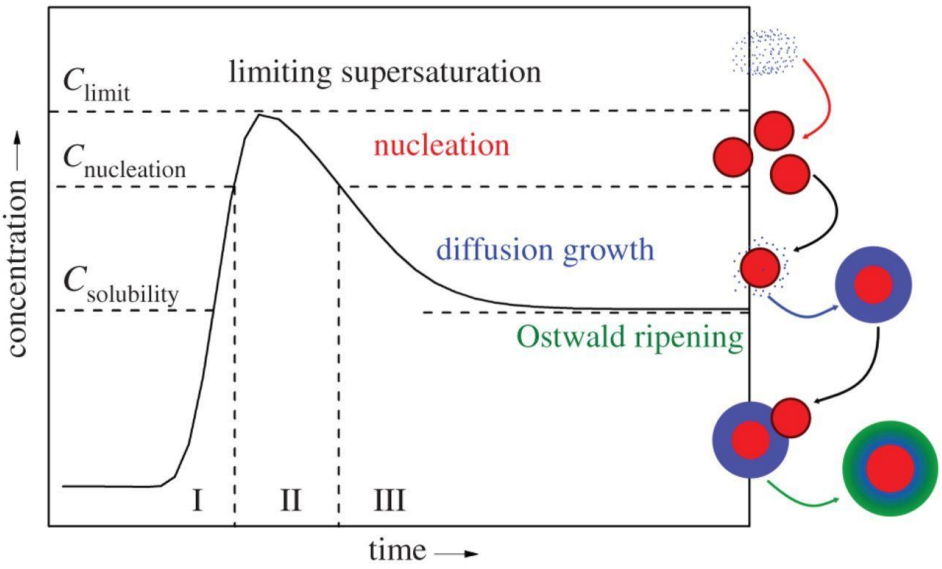

Figure 1.8: *LaMer model of nanocrystal growth*[118].

In conventional solution-based synthesis schemes, such as sol-gel or hydro/solvothermal reactions, precursor solubilization continuously happens due to the factors like slow heating and sufficient initial precursor amount, most of the time that is enough to maintain the precursor concentration above the critical nucleation threshold. It results into continuous nuclei formation, parallel to the growth of the nanoparticle. If the reaction is carried out for sufficiently long enough time, then the particle average size will 'focus' onto a narrow size distribution. As suggested by Sugimoto in 1987, the rate of diffusion limited growth will vary with particle size in such a way that small particles will grow faster than the large ones[119].

Focusing of the particle size distribution takes place, which minimizes the dispersity but increases the average size of the particles.

Another approach to minimize the reaction time and obtain a narrow size distribution is being often used by separating the nucleation and the growth periods. In this scenario, precursor solubilization happens very fast surpassing the critical nucleation concentration and a rapid nucleation burst happens which brings down the precursor concentration below the critical point which ceases the formation of new nuclei. This can be achieved by limiting the precursor amount, so that the rapid nucleation consumes the whole precursors, or quenching the reaction or by removing the driving force (e.g., heat source) so that further nucleation does not happen. This leads to the formation of nuclei of similar size, which then grow homogenously. This allows us to both control the average size and obtain narrow distribution. This approach has been used extensively in hot-injection methods for the growth of metal, metal oxides, and particularly in the production of QDs[118].

1.3.5.2 Role of ligands:

Surface ligands play very important roles in terms of controlling shape and size during synthesis, providing a template for assembly, and improving the photoluminescent quantum yield, which are not quite intuitive from the LaMer model. Peng *et al.* reported that the concentration of ligands in a non-coordinating solvent can be a deciding factor to tune the balance between nucleation and growth, thus allowing the fine control on the size and dispersity[120]. The growth nature of different inorganic crystal facets are often anisotropic, that results into high energy facets growing faster than the low energy ones. Ligands in other hand, are often used to kinetically control the shape of nanoparticles via selective adhesion.

In case of biological applications of nanoparticles (or QDs), ligands play many major roles such as making them dispersible in water/buffer, protecting the surface from oxidation in aqueous medium, providing surface functionality to attach biomolecules (e.g., proteins, amino acids, DNA, RNA and small molecules). The main approach to render nanoparticles stable in aqueous media is to replace the hydrophobic capping ligands with hydrophilic ones (e.g., with carboxylic acid, thiols, phosphines and amines anchoring groups attached to hydrophilic functions).

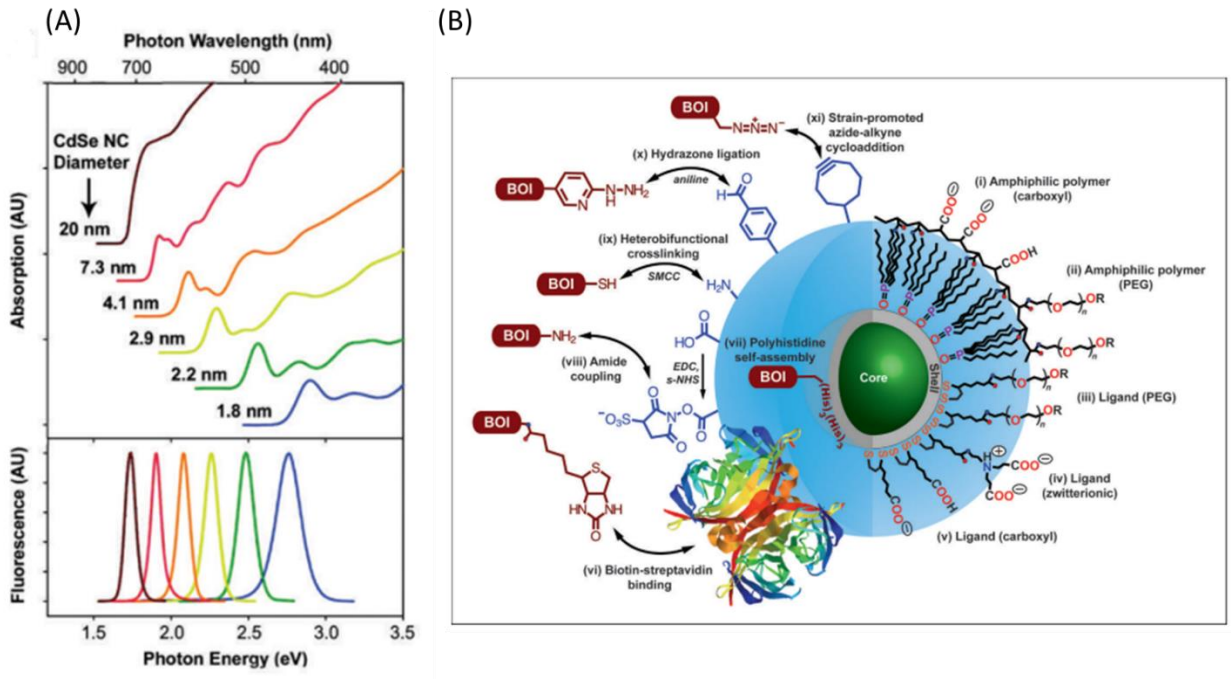

Figure 1.9: *(A) size-dependent absorption and emission spectra of CdSe QDs. (Image source: doi.org/10.1021/ar9001069)*[121]*, (B) Various surface functionalization methods of QDs. (Image source: doi.org/10.1366/12-06948)*[122]

Another approach is to use an amphiphilic polymer to encapsulate the nanoparticles into a micelle like structure via hydrophobic interaction, providing a spacer between the solvent and the nanoparticle's surface. For nano-biomaterials, ligands affect their toxicity, cell permeability and even in vivo fate. Biocompatible ligands can improve the circulation time of nanoparticles in blood by reducing non-specific interactions with other proteins, and attached receptor molecules can guide them to reach target by specific interactions[65].

1.3.6 Advantages of QDs in energy transfer experiments:

QDs have many desirable opto-electronic and chemical properties that makes them convenient to be used for biological applications. Vast variety of QD based bio-conjugates have been designed in the last two decades with diverse functionalities and superior performance. Numerous literatures can be found where QDs have shown unprecedented advantages in FRET based experiments.

One of the properties that makes QDs advantageous from the perspective of FRET experiment and fluorescent labelling is their **narrow and symmetrical photoluminescence** spectrum which allows us to finely tune the spectral overlap for energy transfer while using them as optical donors[122,123] (see in Figure 1.9 (A)-QD photoluminescence spectra). In contrast to organic dye donors which present a red tail in their emission spectrum, their narrow photoluminescence spectrum is easy to separate from the acceptor signal.

QDs also have **broad absorption cross section** that increase steadily toward UV from their first absorption band. This makes it possible to excite the donor QDs far deep in the blue/UV without directly exciting the organic dye acceptors which most often absorbs in the visible range. The absorption cross section can approach values 10-100 times than that of dyes[65,124].

Core-shell QDs have been proven to be very valuable for FRET applications for their extraordinary **photoluminescence quantum yield**[125,126], and unparalleled **photo- and chemical-stability**[65,127] compared to regular organic fluorophores. Another property that makes QDs a precious option is their **spectral tunability**[128–130]. QDs also have two perpendicular dipole emission, compared to just one in case of molecular fluorophores[131]. It is possible to cover the whole visible spectrum (green to red) just by changing the size of the QDs even with the same material composition (see in Figure 1.9 (A)).

Many opportunities are also available to exploit the versatile **surface chemistry** of QDs to design innovative materials. Due to their non-trivial size and surface area, QDs can typically be conjugated to multiple copies of proteins, nucleic acid sequences, drugs and bio-receptor molecules[132]. Many QD-bioconjugates have been demonstrated that are stable in aqueous medium and with particular bio-functionality[65]. A scheme with commonly used bio-conjugation strategies is given in the Figure 1.9 (B).

One of the early studies demonstrating the use of bioconjugated QDs as optical donors in FRET based sensing was reported by Goldman *et al.* in 2005[133]. This study reports the detection of 2,4,6-trinitrotoluene (TNT) explosive in aqueous environment using a competitive FRET scheme. Here an analyte specific antibody fragment conjugated to CdSe/ZnS QD acts as the donor and a quencher dye-labeled TNT analogue acts as the acceptor. Prior to the addition of sample, the donor and the acceptor are bound together, resulting in the quenching of the donor fluorescence. Later when the sample is added, if TNT molecules are present in the solution, they replace some fraction of the bound TNT analogue-quenchers from the QDs, effectively recovering QD fluorescence. (See the scheme in Figure 1.10)

Figure 1.10: *QD-bioconjugate (donor) based FRET scheme for the detection of TNT.*

A study in 2014 by Wegner *et al.* reported a FRET based sensing scheme for the detection of epidermal growth factor receptor (EGFR). In this scheme a time gated detection mechanism was used to study the FRET from a Tb-complex donor to a QD acceptor[134].

Even though QD labeled bioconjugates have shown to possess several advantages in FRET based bio-sensing platforms, still there are a few drawbacks in these schemes leading to problems, such as lack of sensitivity, and even false/inconclusive experimental output. One of the major problems of QD-bioconjugates is due to the large size of QDs compared to single dyes. Additionally, large surface area of QDs makes it difficult to precisely control the number of acceptors or biomolecules attached to the surface.

Now, as the principles of FRET assays and the properties of semiconductor QDs have been presented, I will briefly discuss the last building block of the sensing modality developed in my thesis, mainly whispering gallery mode microcavities and their use as biosensors.

1.4 WHISPERING GALLERY MODE MICROCAVITIES:

1.4.1 Dielectric micro-sensors:

In the modern era, dielectric micro-sensor systems have emerged as the foundation of many advanced applications, the ubiquity of which can be attributed to their low-cost fabrication methods, speed and flexibility of using and the vast applications in optical technology such as photodiodes, optical fibers and light sources. One of the basic properties that makes dielectric microstructures distinctive is their ability to confine an electromagnetic wave and bringing it to interfere with itself so that only a few resonant specific frequencies can reside within the cavity without suffering much loss of energy[135–137]. These specific optical frequencies inherently depend on the geometry and the material properties of the micro-structures, any change in these parameters such as heating and deformation of the geometry or changes in the relative refractive index can be detected by monitoring the change in the intensity or the shifts in the resonant frequencies. Thus microcavity based sensors can act as an optical signal transducer which opens up a crucial path to realizing the next generation of high-performance optical sensors[138].

With the recent advances in the field of sensor technologies, the need of mankind has come to the realization of sensors with ultra-sensitivity in the areas such as bio-medical and environmental sciences. One special kind of optical sensors that has attracted significant research interest is whispering gallery mode (WGM) enabled microcavities which have been shown to have sensitivity to detect even single molecules and their dynamics.

1.4.2 Whispering gallery mode cavities: Brief history and introduction

An optical cavity or a resonator is defined as a structure consisting of a set of two or more number of mirrors or mirror like structures that can restrict a propagating light wave in a closed path. Because of their ability to confine large optical powers into a small volume, cavities can enhance the possibility of light-matter interaction inside or in the surrounding vicinity which makes them ideal for applications like in the fabrication of nonlinear optical elements, optical signal processing and sensing[139]. Resonances inside cavities are widely studied phenomena in the field of wave-physics in various different scenarios such as for acoustic, optical and mechanical wave patterns. But in most of the cases, these resonances have great dependence on material properties such as chemical composition or refractive indices and

geometric parameters like size and shape, that is the reason why these kind of resonances are called morphology-dependent resonances (MDRs) [138].

Whispering gallery mode (WGM) is one of the well-recognized MDRs that has been first explained by Lord Rayleigh in case of acoustic waves. The term "whispering gallery" emerged from the gallery of whispers in St. Paul's Cathedral in the UK where the particular dimension of the structure supports the constructive interferences of the propagating pressure waves guided around the concave wall[139]. In theory, the key for acoustic WGMs lies in the geometry of the structure, the acoustic resonant modes are formed due to the repeated reflections and in-phase interferences that, considering negligible absorption, scattering, and material dispersion should continue forever. In real scenarios, without any external excitations, losses through the surface via tunneling damps the intensity of the WGMs providing it a finite lifetime. Lower losses arising due to the structural or material improvements increases the lifetime of the modes, which leads to the physical understanding of the quality-factor (Q) that quantitatively signifies the ability of the structure to retain the reflecting wave. In general, WGMs are a subcategory of MDRs with the special properties such as high Q surface mode natures. Around the world, many other architectures supports the favorable geometry for acoustic WGMs such as the Victoria Memorial in Kolkata, India that had been greatly studied by the Nobel laureate C V Raman following the footprints of Lord Rayleigh[140].

Not only in the acoustic domain, WGMs have been widely studied in the optical domain and many applications based on WGMs are available in the field of optical technologies and sensing. For WGMs to occur in electro-magnetic (EM) domain, a similar enclosed concave interface is required to retain the reflecting propagating light. In general, WGM optical resonators have higher refractive index than the environment which enables the trapping of light inside the resonator via total internal reflections (TIRs). Consequently, when the propagating light makes a full turn and comes back with the same phase, constructive interferences take place forming these very sharp WGM resonances[134].

1.4.3 Useful topics regarding WGM resonators:

Even though considerable progress has been made in transferring optical microcavity based technology to real life applications, still significant amount of exploration is required towards further applications, to improve the quality and cost-efficiency of fabrication, to design proper system integration and also to have even better theoretical understanding. With the motivation towards having a compatible resonator

for a particular application, here, I will discuss some general ideas regarding the commonly used micro resonators.

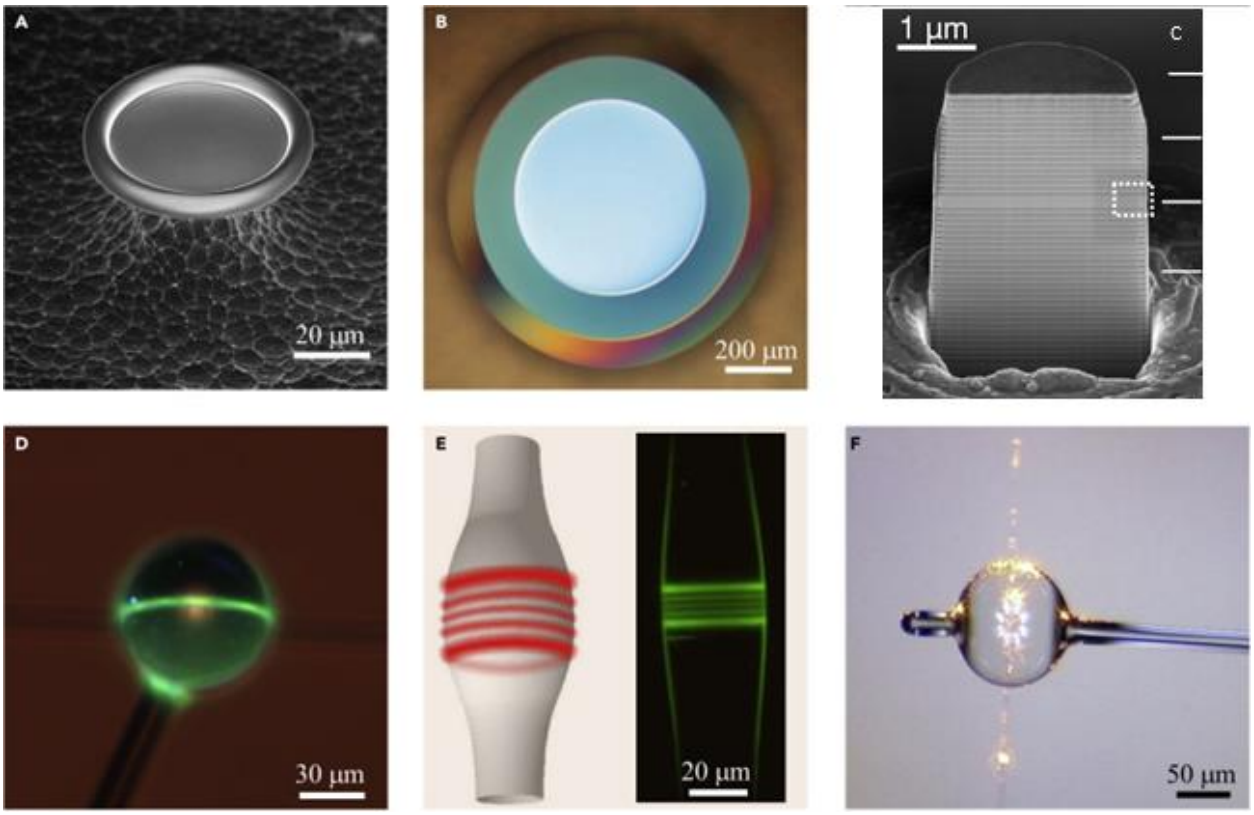

Figure 1.11: *Images of some of the common shaped resonators: (A) microtoroid[141], (B) microdisk[142], (C) micro cylinder[143], (D) microsphere[144], (E) microbottle[145], and (F) microbubble[146].*

1.4.3.1 Insights into the shapes:

WGMs have been studied in various kinds of geometric structures, the simpler ones such as spherical[144], disc[142] and ring resonators[147] and also more complex ones like toroidal[141], tubular[145], and microbubble resonator[146]. Cylindrical cavities are easy to fabricate but a major disadvantage of them is that the coupled light generally migrates along the long axis and eventually disappears, even if there is negligible material absorption, additionally they are difficult to couple to the excitation source[139,148]. Spherical resonators, in the other hand, possess a great advantage as they can effectively trap light and be easily prepared from a wide variety of materials with very high monodispersity. Many geometric resonators (e.g., toroid and bottleneck structures) suffer from greater scattering loss of confined light due to line-edge roughness and defects resulting from etching which leads to a low Q resonator. Wedge geometries with shallow angles

enable to push the mode away from scattering surfaces resulting in a high Q resonator. Conical resonators made of polymers known as micro-Goblets have attracted research interest due to the lithography-based mass fabrication and multiplexed functionalization. Polygonal resonators have also been appealing since crystalline cavity structures can be easily fabricated via laser-heated pedestal growth (LHPG) using a powerful CO_2 or YAG laser[138]. Some of the common circular mode-supporting geometries that are often used are shown the Figure 1.11.

1.4.3.2 Composing materials of WGM resonators:

One of the most crucial factors that leads to the occurring of WGMs inside optical cavities is the confinement of EM waves via total internal reflection at the external cavity interface which is dominated by the relative refractive index of the cavity. Larger refractive index contrast between the cavity and the external medium minimizes the radiative loss via strongly confining the modes, resulting into a very high Q factor of the cavity. On the contrary, resonant modes extends further into the external media in case of low Q resonator. The other factors that determine the quality of the cavity are related to the losses introduced by the material, such as material's absorption and the scattering from the surface of the cavity which is governed by both the material and fabrication techniques. So, the choice of material is also a crucial factor for the fabrication of cavities aimed towards specific applications. Since the research on cavity based systems have gained well reputation for various potential applications, different kinds of materials have been explored to fabricate resonators, such as, zinc oxide (ZnO)[149], silica (SiO_2)[150], titanium dioxide (TiO_2)[151], silicon carbide (SiC)[152], silicon nitride (Si_3N_2)[153], magnesium fluoride (MgF_2)[154], sapphire[155], and polymeric materials like poly (methyl methacrylate) (PMMA)[156], polystyrene[157], polydimethylsiloxane (PDMS)[158]. Hybrid structures like metallo-dielectric resonators[159] and coated spheres were also investigated to improve the robustness and signal intensities[138].

1.4.3.3 Common fabrication techniques:

Numerous techniques are available that are often exploited to fabricate optical micro resonators depending on their targeted applications. Three major parameters that are taken into account for the fabrication of a microcavity, are (A) the targeted Q-factor, (B) ease of fabrication, and (C) the suitability for the integration into devices.

Cylindrical microcavities can be easily constructed from a jacket removed optical fiber. The cladding thickness of the cavity which is quite important for controlling the optical path length of the WGMs, can be manipulated by careful etching using hydrofluoric acid[160]. Many of the toroid or disc shaped cavity

fabrication relies on sophisticated mechanical polishing techniques[161]. A conventional method is, at first a small cylinder of a high refractive index material (such as CaF_2) is loaded onto a rotor, and then a diamond abrasive separates a WGM supporting region on the cylinder[139]. Spherical micro resonators are comparatively the easiest to prepare. Silica micro resonators are often prepared by melting the tip of a glass fiber[135,162]. This technique is cost-effective and allows fine control of the size, but only one microsphere can be prepared at a time which makes the process slow. Commercial fiber splicer technique is also used to cut fiber edges and heat them up to form spherical microspheres[163]. Polymer microspheres (made of materials such as poly (methylmethacrylate) or PMMA, polystyrene (PS) etc.) have also gained popularity due to their ease of fabrication and the flexibility to finely control their size dispersity by colloidal synthetic methods[164]. Polymeric spherical cavities can be prepared by physical methods, such as emulsification[165], coacervation[166] and spray drying[167], or by chemical methods such as heterogeneous polymerization[138]. Another convenient technique to prepare polymer microsphere is to prepare a long fiber (made of PMMA or other polymers) with a controlled thickness, then melt the tip of the fiber for making microspheres, similar to the process of making glass microspheres[168]. Microfluidic techniques are also used to prepare highly monodispersed spherical cavities already loaded with fluorescent dyes. Sol-gel chemistry technique that uses molecular precursors as building blocks to obtain high performing optical materials are also gaining a growing interest for being cost effective and flexible[169]. For example, silica microspheres can be prepared via base catalyzed hydrolysis of tetraethylorthosilicate (TEOS)[170,171]. Fabrication technique like reflow smoothing greatly improves the quality of these spheres by minimizing the surface roughness[138]. Lithographic techniques are also often used to fabricate on-chip resonator arrays with precise control over size parameters.

1.4.4 Understanding TIRs in spherical WGM cavity:

The total internal reflections and the consequential WGMs can be easily understood in a spherical resonator[135]. WGMs are generally represented as closed-trajectory rays confined within the cavity by total internal reflections from the surface of the cavity, as seen in the Figure 1.12.

Let us consider a dielectric microsphere with radius a, refractive index N and a ray of EM wave with wavelength (λ) << a, is propagating inside the sphere. If the ray is hitting the surface of the sphere with an angle i that is greater than the critical angle (i_c), then the ray would be trapped inside by total internal reflection. The relation can be expressed as:

$$i > i_c = \sin^{-1}\left(\frac{1}{N}\right) \qquad (Eq.\ 1.16)$$

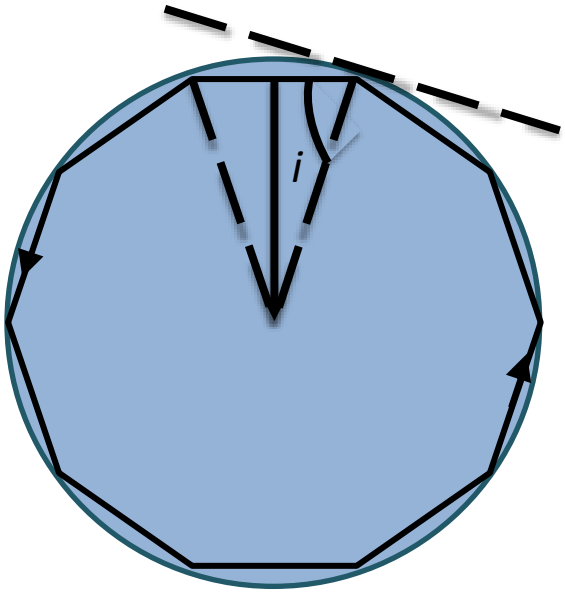

Figure 1.12: *Total internal reflection of a ray inside a spherical microsphere (i and j respectively are the incident and reflection angle of the ray).*

All of the subsequent incident angles should be equal due to the spherical symmetry of the microsphere. As the trapped ray propagates just below but very close to the surface, the distance covered by the ray should be ≈ $2\pi a$. If the total traveled distance is an integer-multiple of the wavelength in the medium, then the wave should return to its starting point with the same phase, leading to constructive interferences[139]. It can be simply expressed as:

$$2\pi a \approx l \times \frac{\lambda}{N}, \qquad (Eq.\ 1.17)$$

where λ/N is the wavelength of the light in the medium and l is an integer. The resonance condition written in terms of size parameter (x) would be:

$$x = \frac{2\pi a}{\lambda} \approx \frac{l}{N}. \qquad (Eq.\ 1.18)$$

The number of wavelengths l which covers the total one trip around the equator of the microsphere can be considered as the angular momentum in usual sense. If we consider the ray to be the trajectory of a photon, its momentum can be written as:

$$p = \hbar k = \hbar \times \frac{2\pi N}{\lambda}, \qquad (Eq.\ 1.19)$$

when the incident ray hits the interface at a near-glancing angle, such as $i \approx \frac{\pi}{2}$, then the angular momentum (L) can be expressed as:

$$L \approx ap = a \times \frac{2\pi\hbar N}{\lambda} = \hbar l\,. \qquad (Eq.\ 1.20)$$

As an example, if we consider a polystyrene microsphere of 5 µm radius and the trapped light inside has λ = 625 nm, then we can calculate $l \approx 80$, thus whispering gallery modes can be simply understood as high angular momentum electromagnetic modes resulting from in-phase interference of light, propagating inside a resonator via total internal reflections.

1.4.5 Coupling light into a resonator:

Power stored in a WGM follows a Lorentzian line shape which can be expressed as:

$$P(\omega) = P_0 \frac{\left(\frac{\gamma_0}{2}\right)^2}{(\omega-\omega_0)^2+\left(\frac{\gamma_0}{2}\right)^2}, \qquad (Eq.\ 1.21)$$

where $P(\omega)$ signifies the power stored in the mode, ω_0 = the resonant frequency, γ_0 = full width at half maxima (FWHM) and P_0 = the amplitude of the WGM.

There are many ways to couple light into WGM cavities. A widely used and quite effective technique is to adiabatically couple a tapered optical fiber close to the surface of the resonator and use it at as excitation channel (see the Figure 1.13 (A)). The transmitted power from the cavity can be monitored as a function of scanning frequency which should theoretically exhibit a dip that can be fitted with a Lorentzian function[27]. The central frequency should be the same as the WGM frequency and the width should give the value of FWHM of the WGM, and the corresponding quality factor of the cavity can be calculated. But there is an experimental parameter that controls the intensity of the dip which is called the coupling efficiency, β. That can be written as;

$$P_t(\omega) = P_0 - \beta P(\omega)\,, \qquad (Eq.\ 1.22)$$

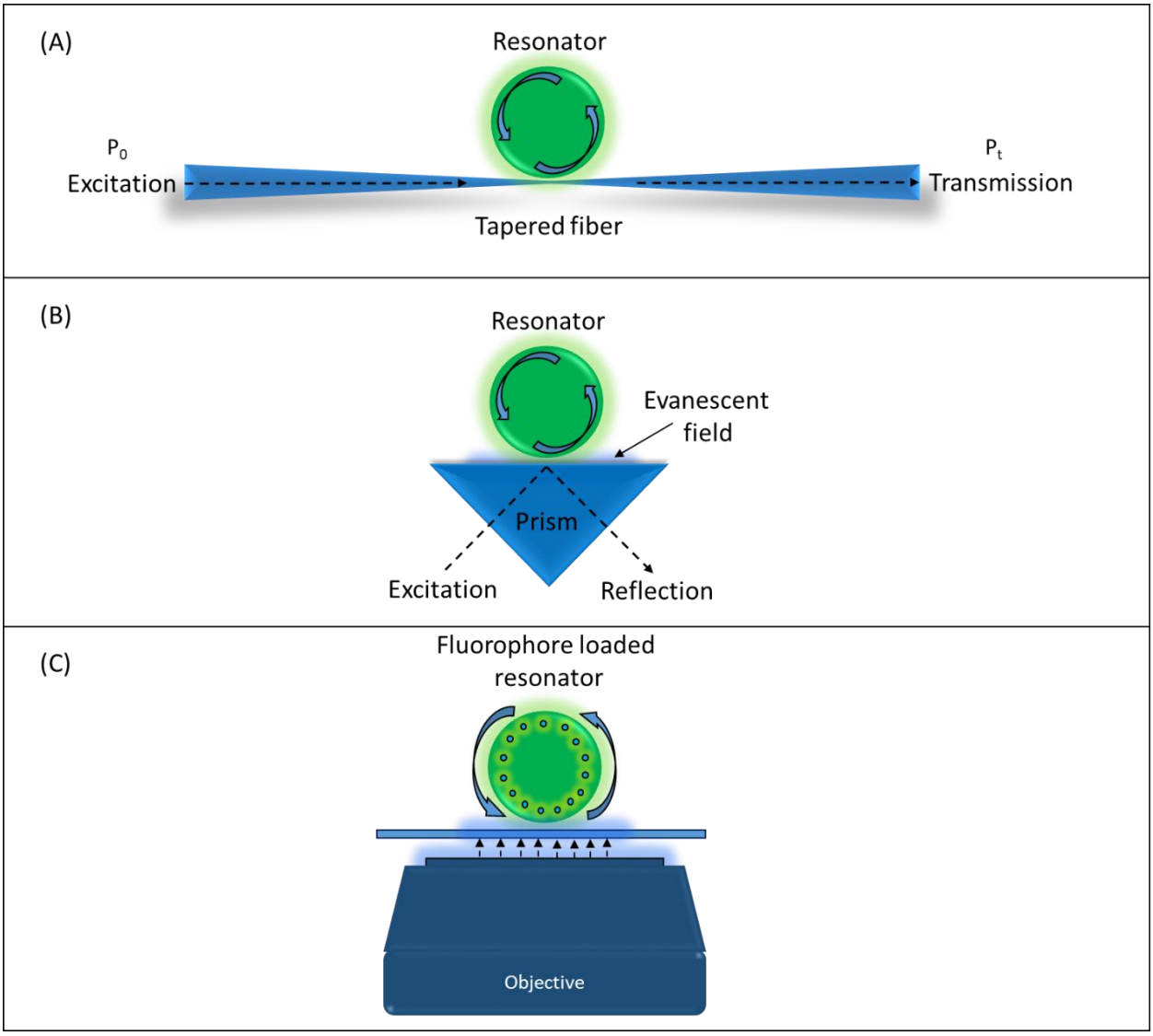

Figure 1.13: *Some common strategies to couple light into the resonators, (A) via tapered fiber, (B) via prism, and (C) direct excitation of a fluorophore filled cavity with a laser via a microscope objective.*

where P_0 stands for the total input power throughout the range of scanning frequency. Among the other coupling techniques, through-prism coupling is among the earliest ones, where a laser beam is directed into a prism, and then performs TIR on its surface[172,173]. The resulted evanescent field at the prism surface is utilized to couple into the WGM resonator (see Figure 1.13 (B)). Both the reflected and transmitted intensities well-explored is spherical resonator that is either coated or embedded with fluorophore entities. As seen in Figure 1.13 (C), a direct laser beam from a microscope objective can directly excite the emitters located inside the microspheres. The fluorescence then would excite the WGMs of the

resonator[174,175]. It has been observed that if the emission wavelength overlaps with the position of the WGMs then the spontaneous emission is highly enhanced due to the densification of local density of states (LDOS). This phenomenon is widely known as Purcell effect[176].

1.4.6 Purcell effect:

Optical microcavities have long been known to enhance the spontaneous emission of a fluorophore as well as altering the energy transfer rates between donor-acceptor pairs. This phenomenon can be directly comprehended from the expression of transition probability of spontaneous emission given by Fermi's golden rule as:

$$\Gamma_{ij} \propto |M_{ij}|^2 \rho(\nu_{ij}) \ , \qquad (Eq.\ 1.23)$$

where Γ_{ij} is the rate of the transition between the excited state i and ground state j; M_{ij} is the transition matrix element determined by the wavefunctions associated with the electronic levels; $\rho(\nu_{ij})$ is the density of states of the photons at the transition frequency often called the photonic mode density or PMD[177]. PMD is altered when the fluorophore is present close to an interface of different refractive indices or inside a polymer microcavity which consequently influences the rate of spontaneous emission of a fluorophore, also the energy transfer between molecules.[176] In the vicinity of a resonant cavity, the PMD is increased which enhances the radiative decay rate of the fluorophores. This phenomena was first described by Edward Mills Purcell during 1940s[178]. The enhancement factor of the emission rate is called Purcell factor (F_P) which is given by the following;

$$F_P = \frac{3}{4\pi^2} \times \frac{\lambda}{N} \times \frac{Q}{V}, \qquad (Eq.\ 1.24)$$

where, λ is the wavelength of the light in air (or vacuum), N, Q and V respectively are the refractive index, quality factor and the mode volume of the cavity.

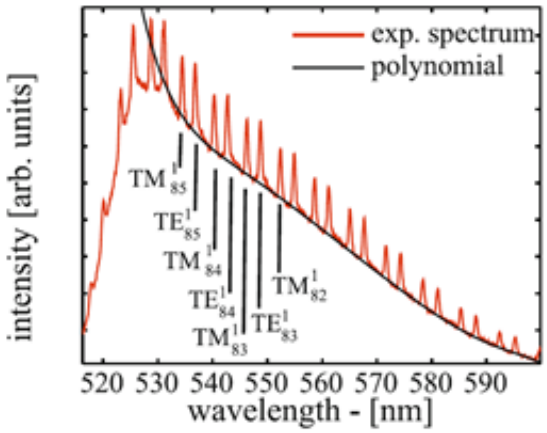

Figure 1.14: *A typical emission spectrum of a polystyrene microcavity (radius = 4.95 µm) coated with CdSe/ZnS QDs, showing sharp resonance modes, and broad free space emission*[179].

Since the cavity is resonant only for specific wavelengths, the Purcell effect manifests itself as the appearance of narrow peaks on top of the broad envelope emission spectrum: at these specific wavelengths, the radiative decay rate of the emission is increased thanks to the Purcell effect, and hence the proportion of light emitted at these resonance positions is enhanced compared to the free space emission spectrum (see in Figure 1.14)[179]. This is an easy and useful trick one can use to characterize the position of the resonances.

1.4.7 Applications of WGM resonators:

Optical resonators composed of two or more mirrors are of great interest in the branches of linear and non-linear optics but their system integratibility and mode stability are quite inadequate for building compact devices which promotes dielectric WGM resonators as great alternatives due to their high Q-factor, ease of fabrication and usages. These resonators have found their ways for practical applications in the field of linear, non-linear, quantum optics and optical communications[180,138,181]. Another field in which WGM cavities have now been widely desired is in sensing of biological and chemical analytes[27,182,183]. The applications of these resonators make up a long list depending on their structures, optical properties, and targeted applications, here I will just discuss them in brief, considering two major perspectives: one for applications in opto-photonic elements, second one for sensing applications.

1.4.7.1 Opto-photonic applications of WGM resonators:

WGM resonator based Photonic filters have been a useful development in the field of advanced communications and radar technologies to overcome the shortcomings of microwave filters by

simultaneously providing narrow bandwidth and wide-tunability[181]. WGM cavities are also used as optical and photonic single-resonator filters for the generation of monochromatic EM waves[184]. Wavelength tunable filters have also been demonstrated by using micro-ring resonators with a photosensitive coating but they have disadvantages of having small speeds and low accuracy[185]. Coupled optical fiber resonators are widely used as high-order optical filters[186]. WGM resonators with high Q-factors have also found usages as stabilization filters in optoelectronic oscillators and feedback elements for external lasers[181,187].

Another important and widely recognized application of WGM resonators is continuous wave micro-lasers. The high Q-factor significantly reduces the lasing threshold. Lasing have been widely demonstrated in liquid aerosols and microdroplets[188]. WGM lasers based on cylindrical capillary resonators have been a huge interest of study in the last few decades due to their simplicity. Generally a dye-doped high ($\eta_{solvent} > \eta_{glass}$) refractive index solvent (acts as active gain medium) flows inside the glass capillary that is normally illuminated. The propagating light penetrates into the active medium, and couples to the WGM resonances corresponding to the internal capillary circle. It is also possible to generate lasing from the active media with lower refractive index than the capillary; for that the capillary wall must have to thin enough so that the evanescent field can couple to the gain medium[189]. Low threshold lasing has also been demonstrated in rare earth metal ion (e.g.; neodymium (Nd^{3+})[190], erbium (Er^{3+})[191] etc.) doped silica microspheres. WGM based lasing has also been shown in semiconductor QDs (such as CdSe[192], CdTe[193], InAs, GaAs[194] etc.) coupled microcavities. Significant developments have been made recently in the fabrication of single QD based microlaser which is a topic of interest in quantum electrodynamics (QED) study.

Other applications of WGM resonators involve the fabrication of efficient and compact optical switches and modulators, in oscillators and hyper-parametric wave mixing process[181].

1.4.7.2 Sensing applications:

Many sensing platforms have been demonstrated that uses WGM enable optical resonators. Probably the most research has been focused on bio-chemical sensing to attain assays with improved sensitivity. The high-quality factor of the resonance modes makes it possible to detect the binding activity of a very small analyte that changes the effective refractive index when it binds to the surface of the resonator. As the main motivation of this thesis is to finally fabricate a bio-detection platform, the available sensing strategies based on micro-cavities, their advantages and perspectives should be discussed in detail (see the next section).

Refractive index sensing has been demonstrated in many studies using simple spherical micro-cavities. The WGM resonances of a cavity shift when the external refractive index changes due to events, such as alteration of the outside medium/solvent, absorption or adsorption of analytes onto the cavity surface. This change can be correlated to precisely measure the refractive index of an unknown medium[195]. This principle is also adopted to build humidity, and gas sensors[196]. For example, a humidity sensor[197] based on hydrophilic coating of silica nanoparticles on a glass microsphere is reported. A group has performed the detection of ethanol vapor using a porous ZnO coating onto a silicon-on-insulator micro-ring resonator[198]. Even though the detection principle is almost same for these applications, but careful surface modification is required for the detection of specific analytes.

One of the other common sensing applications is temperature-variation sensing. WGM resonator-based temperature sensors generally rely on the temperature dependent change of material's refractive index ($\mathrm{d}\eta/\mathrm{d}T$) or thermo-optical properties. Additionally thermal expansion/contraction properties characterized by expansion coefficient ($R^{-1}\,\mathrm{d}R/\mathrm{d}T$), also play a key role for the fabrication of temperature sensor[135]. Polymers such as, polydimethylsiloxane (PDMS) are good choices as they have high thermo-optic changes. Even through crystalline materials have less sensitive refractive index in comparison to the polymers but the anisotropy in their structure allows differential tracking of two modes (transverse electric and transverse magnetic) with different polarizations[138].

Compressive forces and mechanical strains applied to an optical resonator may cause the shifting of WGM resonances by inducing changes in the shape and the relative refractive index of the material. The wavelength of the WGM resonances are finely tuned by the application of mechanical strains on the resonator. An experiment performed with a 960 µm hollow PMMA spherical resonator showed that the cavity resonances have a force sensitivity measured as, $\mathrm{d}\lambda/\mathrm{d}F = 7.664\ \mathrm{nm/N}$, which suggests the potential use of WGM cavities in building micro-optical force sensors[199,200].

Another study was attempted towards building a miniature optical gyroscope by sequentially coupling several WGM resonators to a waveguide. Even though attaining a perfect configuration where all the resonators are perfectly coupled in a single waveguide and all of them possess the same resonant frequency is very challenging, this conformation brings in the potential of improving the sensitivity by several order of magnitude compared to conventional ones[201].

1.4.8 WGM cavity-based biosensors: Principles and progress

As the main motivation of this thesis is oriented towards developing a bio-detection scheme using WGM active micro resonators, so the current state of the art for WGM based bio-sensing techniques, general principles and their perspectives should be discussed into details.

The quality of a good bio-sensor is characterized by factors like, selectivity, sensitivity, stability and reversibility, most of which is controlled by the bio-chemical receptor[139]. The sensitivity, however, is also often influenced by the transducing mechanism. In a high performing bio-sensing scheme, the receptor and the transducer together work to enhance the signal-to-noise (SNR) ratio, shorten the response time and lower the detection limit. The primary goal of a sensor is to bring out the maximum amount of information, both qualitative and quantitative, regarding the analyte present in the smallest amount of sample with high sensitivity and specificity.

1.4.8.1 General schemes of bio-sensing with WGM cavities:

WGM resonators are progressively finding applications as transducers for specific detection of biomolecules. One of the major advantages of WGM based sensor is the capability of label-free bio detection which means, no chemical modification of the analyte is required. This makes the detection process non-invasive as well as probing light usually do not influence the biophysical interactions of the bio-analytes[27].

Most of the WGM based schemes involve the functionalization of the resonator surface with molecular receptor probes specific to the analytes. When present, the target analytes bind to the specific receptors located on the resonator's surface, providing a detectable change of opto-electronic signal suggesting the binding activity. A typical setup generally involves a tunable laser coupled to a fixed micro-resonator (via techniques such as, using tapered fiber etc.) and the transmitted intensity is being recorded with a photodetector (see in Figure 1.15)[27]. The laser, at first is tuned to match a WGM frequency of the micro-cavity which is characterized by a Lorentzian dip in the transmission spectra. The minimum of the dip represents the WGM wavelength, and the corresponding Q-factor of the mode can be calculated by using the simple relation: $Q=\lambda_{WGM}/\Delta\lambda$, where λ_{WGM} and $\Delta\lambda$ are respectively the wavelength and the FWHM of the mode. The binding of an analyte would change the effective refractive index and alter the WGM propagation path length, which would consequently cause the resonant wavelength to shift, the magnitude of which is denoted as $\Delta\lambda_{Shift}$. This shift can be correlated to a particular analyte, and even allow

to measure the number of analytes bound to the surface[202]. As these analytes act as scattering (or other loss mechanism) sources, the rate of cavity relaxation also increases, thus effectively degrading the Q-factor of the cavity which can be characterized by the broadening of the resonance mode.

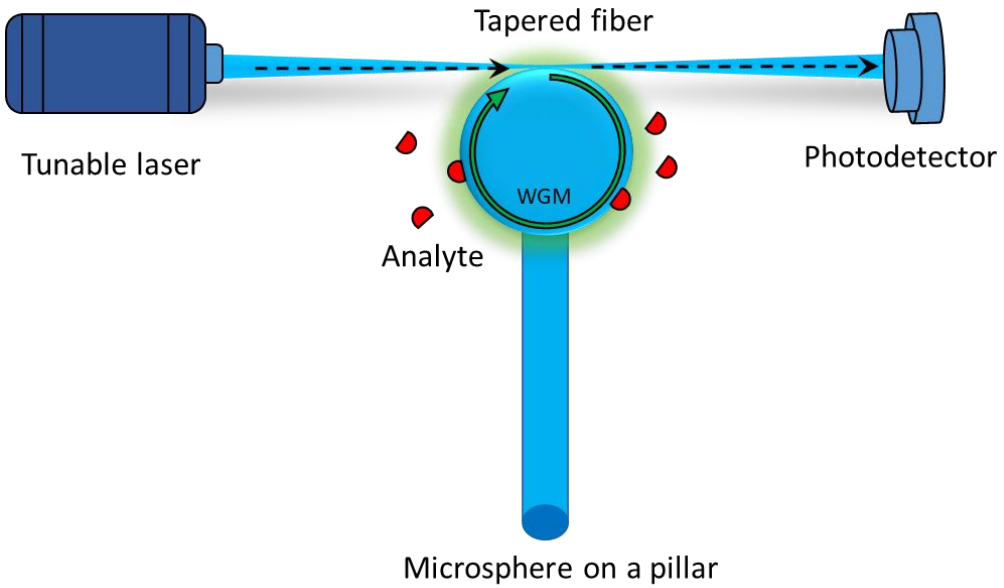

Figure 1.15: *The WGM microsphere coupled to a tunable laser (excitation source) and a photodetector (to record transmitted intensity) through a tapered fiber. Analytes (in red) are interacting with the evanescent field of the microsphere.*

In the Figure 1.16 (A), the WGM resonance wavelength before and after the binding are respectively λ_1 and λ_2, and their corresponding FWHMs are $\Delta\lambda_1$ and $\Delta\lambda_2$. The resonant shift is thus represented as $\Delta\lambda_{Shift}$, and the peak broadening is characterized as $\delta\lambda$. This resonance wavelength shift in case of a spherical resonator can be derived from the first order perturbation theory[203,204], and given as the following;

$$\frac{\Delta\lambda}{\lambda_{WGM}} = \frac{\alpha_{ex}\sigma}{\varepsilon_0(\eta_s^2 - \eta_e^2)a}, \qquad (Eq.\ 1.25)$$

Where α_{ex} is the excess polarizability of a single bio-analyte, σ is the analyte density on the resonator surface, ε_0 is the free-space permittivity, η_s and η_e are respectively the refractive index of the resonator and the environment, and a is the radius of the spherical resonator. The limit of detection (LOD) of a specific bio-analyte can also be expressed by equation 1.26 assuming that the analyte is not influenced by its neighbors[27,202];

$$\sigma_{LOD} = \frac{\varepsilon_0 a(\eta_s^2 - \eta_e^2)F}{\alpha_{ex} Q}, \qquad (Eq.\ 1.26)$$

Where, σ_{LOD} represents the minimum analyte surface density, Q is the quality factor of the cavity and F represents what fraction the wavelength shift ($\Delta\lambda_{\mathrm{Shift}}$) is compared to the linewidth (FWHM of the mode) of the resonance.

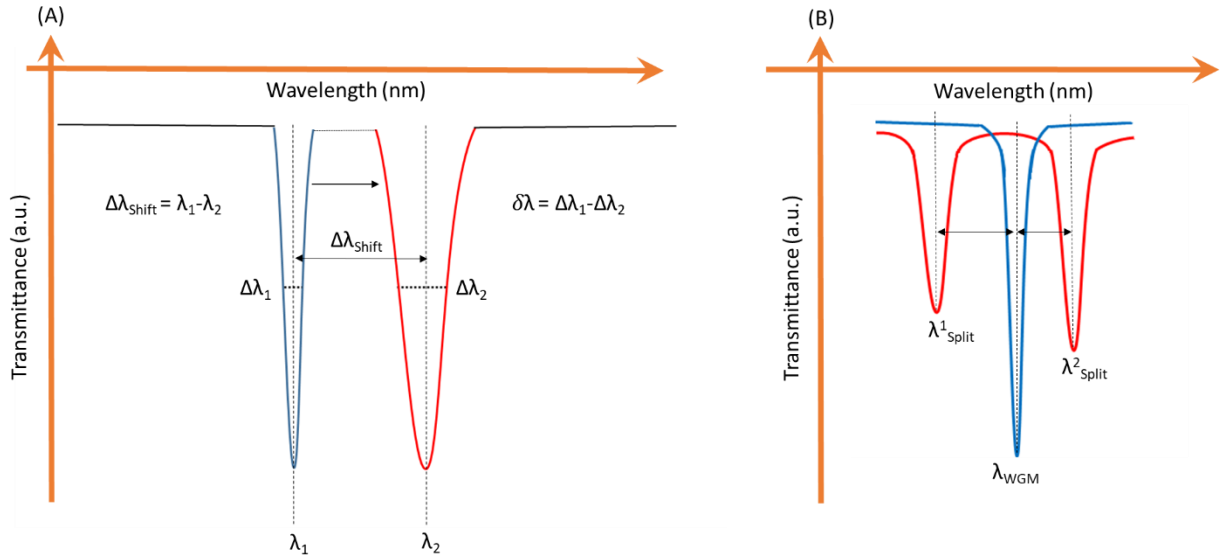

Figure 1.16: *(A) Redshift ($\Delta\lambda_{\mathrm{Shift}}$) and broadening ($\delta\lambda$) of a WGM transmission dip, where* λ1 *and* λ2 *respectively are WGM wavelengths before and after shifting, (B) mode-splitting spectra (Blue and red line respectively before and after the splitting).*

When the analyte is a nanoparticle (NP) that interacts with the evanescent WGM field, the degeneracy of the clockwise and counterclockwise mode can be lifted resulting the splitting of the mode (see Figure 1.16 (B)). However, the maximum reactive resonant shift can be obtained when the NP binds to the equator of a spherical resonator. This shift then can be expressed as the following[138];

$$\frac{\Delta\lambda}{\lambda_{WGM}} \cong D \frac{R_{NP}^3}{R^{\frac{5}{2}} \lambda_{WGM}^{\frac{1}{2}}} \exp\left(-\frac{R_{NP}}{L}\right), \qquad (Eq.\ 1.27)$$

where, D is a factor related to the refractive indices of the resonator, its environment, and the NP, R_{NP} is the radius of the NP, and L is the characteristic evanescent field length. The exponential factor is

introduced to take into account the decay of the evanescent field of the WGM across the NP radius. Even if the NP is not directly attached on the surface of the cavity but within the evanescent field, it can still introduce absorption and scattering losses, and the shift associated can be given using the following relation;

$$\frac{\Delta\lambda\,(z+a)}{\Delta\lambda\,(a)} = \frac{\exp\,(-(Z+a)L)}{\exp(-a/L)} = \exp(-Z/L) \qquad (Eq.\ 1.28)$$

This equation (1.28) relates the resonance shift for the NP located at distance Z from the cavity surface[138,205]. It also allows to determine the potential that the NP faces due to the evanescent field.

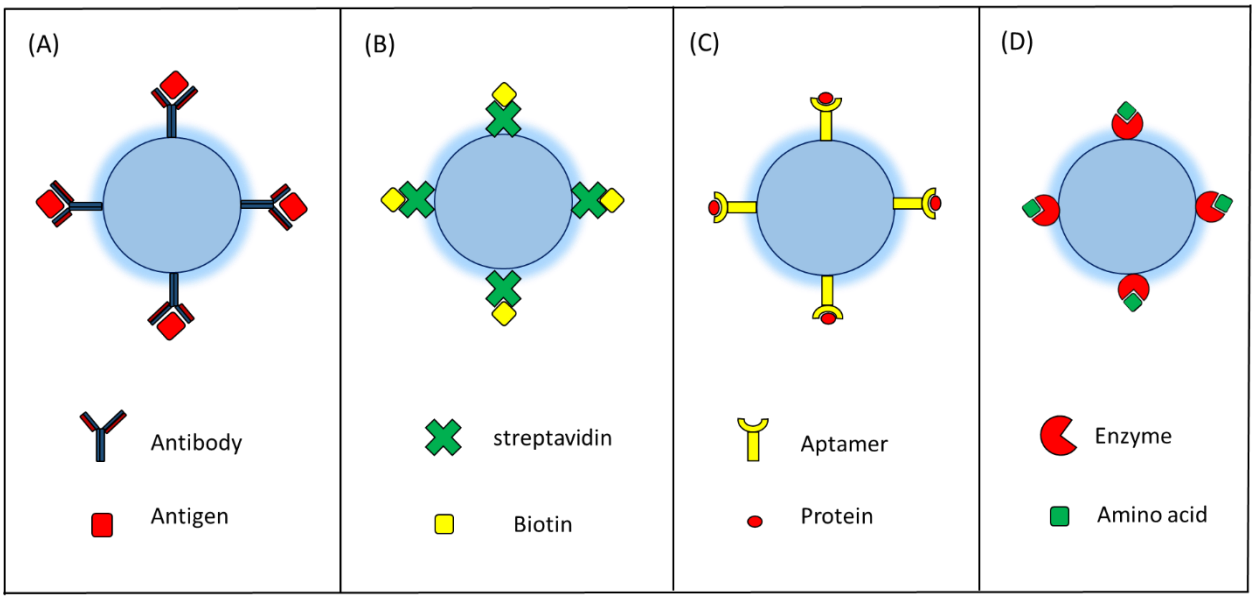

Figure 1.17: *Some of the interaction probing schemes with bio-functionalized glass microspheres: (A) antibody-antigen, (B) streptavidin-biotin, (C) aptamer-protein, and (D) enzyme-amino acid.*

Another important step for building a WGM based biosensor is to introduce surface functionality for facilitating specific interactions with the analytes as well as to reduce non-specific interactions. Nonspecific binding can be a governing factor when working with the plasma or blood serum where interference can be caused by secondary biomolecules. For example, proteins can be easily adsorbed onto the glass cavity surface. Thus processes like silanization of glass microcavities are required that would minimize nonspecific binding, as well as allow further attachment of receptor biomolecules such as, biotin/streptavidin[206], proteins[150,207], DNA[208] or antibodies[209,210]. Usage of bio-conjugation pairs such as streptavidin-biotin complexes that has strong interaction affinity enhances the chances of specific

interactions, moreover, opens up vast possibilities of further conjugation of other biomolecules. Some of the sensing platforms with bio-functionalized glass microsphere is given in the Figure 1.17. However, these functionalization layer must be less than a few 10s of nm thick so that the evanescent field can effectively reach the analyte[135].

1.4.8.2 Some recent progresses in the WGM based sensing:

In the last two decades, a number of exciting applications of WGM resonators have been reported ranging from label free and labeled in vitro detection to in vivo sensing of biomolecules. All these experiments together attempt towards a common goal of translating WGM based biosensing platform to real life applications. Here, I will discuss some of the state-of-the-art schemes that have been developed in the recent time.

One of the earliest works on label-free bio-detection with micro-resonator was reported in 2003 by Vollmer et al., where they used a silica microsphere functionalized with receptor DNA strands to quantify the DNA hybridization on the microsphere surface with the LOD ~ 6 pg/mm^2, moreover a multiplexed DNA detection scheme was also shown to discriminate a single nucleotide mismatch in an 11-mer oligonucleotide[211]. The same group later also reported the detection of cylindrical *E.Coli* bacteria with the sensitivity of ~ 10^2 bacteria/mm^2, introducing a factor to correct for the shape of the bacteria[212]. Later in 2008, they demonstrated the detection of a single influenza virus from the reactive mode-shifting, and the size and mass of the bound virion (below the mass of a HIV virus) was also directly inferred from the resonance shift. They managed to achieve the LOD for an icosahedral shaped virus called MS2 down to 0.2 pg/mm^2 [213]. With the advancement of the instrumentations and analysis techniques, a WGM sensor was reported to exhibit single molecule sensitivity and possess selectivity to specific single binding events[182]. The platform allowed the monitoring of specific molecular interactions transiently, hence mitigating the need for high binding affinity and avoiding permanent binding of targets to the receptors, thus sensor lifetime had to be increased, allowing long timespan kinetics to be observed[138].

Myriad of studies with different kinds of resonator platforms targeted towards diverse applications found their ways following the footprints of some of the earlier studies. In recent time, liquid-core optical ring resonator (LCORR) fabricated from fused silica capillary has been employed for bio-sensing[183,214]. The circular cross-section of the LCORR supports high quality WGMs that have been exploited to build a label-free digital platform for target DNA detection as reported by Lee et al. In this scheme, they coated the interior surface of the LCORR with a layer of capture DNA probes that acted as the gain media and

intercalating dyes were used to ensure WGM lasing only when complementary target DNA was present[215]. Another report demonstrated protein sensing in blood sample where indocyanine green (ICG) fluorophore was dissolved in blood plasma and then injected into a LCORR. ICG molecules bound to the plasma proteins and lipoproteins, resulting in enhanced fluorescence and WGM intensity[189].

Biosensor made of liquid crystal has also been reported for real-time sensitive tracking of the adsorption and desorption kinetics of acetylcholinesterase enzyme and its inhibitors, which leads to the potential ability of the platform for studying enzymatic reactions[216]. Ouyang et al. has fabricated an on-chip opto-fluidic platform based on polymeric micro toroids which functions as highly sensitive ELISA assay. They demonstrated the detection of a disease biomarker (vascular endothelial growth factor or VEGF) with the sensitivity that is 2 orders of magnitude higher than the commercially available ELISA[217]. Another similar study reported the fabrication of an on-chip opto-fluidic resonator-based ELISA assay that is faster, more sensitive and requires much less sample amount than the standard ELISA assay. This technique was then used to detect the interleukin-6 or IL-6 protein with a LOD of 1 fg/mL (38 aM)[218].

Polymer microspheres loaded with fluorophores such as QDs has also attracted much attention due to their simplicity of fabrication and photo-stability of QDs that provides ability to study the dynamics for long time. As an example, Beier et al. reported the fabrication of CdSe/ZnS QD loaded polystyrene microcavities that can selectively adsorb and detect thrombin, but not BSA[219]. Similar studies with QD doped WGM sensors have also been reported to sense alcohol in water and bacterial spores in water[179].

One of the most fascinating aspects that has gained a lot of popularity in the recent time is the application of WGM cavities for in vivo (in live cells and organisms) study and sensing. The major challenges that any in vivo sensing platform face are due to the biocompatibility of the probe, especially it should not interfere with the regular cellular pathways. Another important challenge is the ability of the probe to be well up taken by the cell/organism and the signal-to-noise ratio should be good enough to be differentiated from the interference of the non-specific interactions[183]. The first report of the internalization of active nanocavities (made of GaAs doped with InAs QDs) in living cells (PC3 cancer cells) was given by Shambat et al. in 2013 which has opened the possibility of remote optical in vivo sensing down to the limit of a single cell[220]. Later intracellular biocompatible WGM cavity probes have been designed targeted towards many interesting new applications. For example, Himmelhaus et al. reported real time sensing of biomechanical forces of endothelial living cells using intracellular coumarin-6 dye doped PS resonators[221]. Another useful application where bar code type cellular tagging of individual cells for their real time

tracking, intracellular sensing and adaptive imaging was demonstrated by incorporating fluorescent resonator beads into the cellular cytoplasm via endocytosis[222,223]. Martino et al. have demonstrated multiplexed tagging and 3D tracking of cancer cells in a spheroid by incorporating multiple silica microdisk resonators into each cell[224]. Using a similar platform, Lv et al. performed real time tracking of 106 macrophages which can potentially be applied for the study of cellular dynamics during the development of cardiovascular diseases[225]. Another recent study reported a WGM resonator based intracellular sensing technique to monitor the contractility of individual cardiac cell in living organisms. In this study fluorescent PS microspheres were internalized into cardiac cells and the brightest WGM mode intensity was monitored over time. The contraction of the cardiomyocyte would consequently augment the density of the myofibrils which would increase the environmental refractive index in the vicinity of the resonators causing the resonance/lasing mode to red shift. This quantitative reactive shift signal can be further utilized to study the mechano-biological effect of a drug on the cardiac cells[226].

1.4.9 A broad perspective of WGM based sensing: Advantages and drawbacks

To summarize, numerous studies have demonstrated significant advantages and flexibilities to use WGM resonators for bio-sensing applications such as strong signal-to-noise ratio, cheap and easy fabrication methods with various options of shapes and materials, facile surface functionalization, possible integration to on-chip platforms and excellent sensitivity. Even with these great advantages, WGM resonators have not yet managed to enter the world of mainstream real-life sensing applications. There are a number of important challenges that need to be carefully addressed for the WGM cavity-based sensors to become a reality. Due to large size, the cavities are often difficult to incorporate in living organisms without perturbing the regular cellular functions. Complex cellular media give rise to unwanted non-specific background signal which often makes reactive shift-based detection challenging. The optical detection of WGM signal at near-infrared is most desired, yet really difficult in highly scattering and absorbing biological media such as body tissue[183]. As majority of the WGM sensing utilizes the basis of reactive shifts of the WGM resonances, the background noise due to the change in temperature or bulk refractive index fluctuations becomes unavoidable. Furthermore, even though WGM cavity-based sensors have proven to have unprecedented sensitivity down to single virus and molecular level, but often this sensitivity comes with a cost of expensive fabrication techniques and complex electronics for signal measurement or amplification. Thus, in terms of ease of usage or simplicity and cost-effectiveness

commercial enzymatic assays, such as ELISA still hold major advantages. To be desired in mainstream diagnostic or industrial product-quality checking assays, the WGM based techniques would have to be more accessible and economical, at the same time preserving the advantages such as great sensitivity.

1.5 Whispering Gallery mode mediated Energy Transfer (WGET) sensors: A proposed scheme of biodetection:

As discussed in the previous section, most of the WGM based bio-sensing techniques are based upon the reactive shift of the WGM resonances which makes this technique highly sensitive to the external environment. However, this shift is subjected to thermal instability caused by undesired fluctuations in cavity size and relative refractive index. This might result in large nonspecific background fluctuations. In addition, most of these techniques require expensive tunable lasers and high-resolution spectrometers very precisely aligned with the WGM resonators.

On the other hand, FRET based homogenous (sandwich) assay is one of the most common immunoassays. It is highly specific due to the usage of capture probes (antibodies, DNA strand etc.) and easy to perform: the excitation and detection occur in the far field of the fluorophores and only necessitate broad band fluorescence detection with two spectrally distinct spectral filters, one for the donor and the other for the acceptor. On the other hand, the strong inverse dependence (see equation 1.29) of the rate of this non-radiative energy transfer (K_{FRET}) to the donor-acceptor distance (r) limits the size of the analyte that can be efficiently detected to 1-10 nm.

$$K_{FRET} \propto \frac{1}{r^6}. \qquad (Eq.\ 1.29)$$

Biomolecules of large sizes lead to the formation of sandwich complexes which are not usually detectable using FRET based assays. Therefore, the sensitivity of these FRET based schemes are limited.

Interestingly, the evanescent field of microcavity resonators decays exponentially outwards from the cavity surface as seen in equation 1.30, effectively extending up to tens to hundreds of nanometers above the surface.

$$I_z \propto I_S \exp\left(-\frac{z}{L}\right), \qquad (Eq.\ 1.30)$$

where I_s and I_z respectively represent the WGM field intensity at the cavity surface at distance z from the surface, and L is the characteristic decay length of the WGM. Any particle present within this evanescent field experiences the electromagnetic potential of the resonator, introducing losses to the cavity modes through scattering and absorption. From the EM theory of resonators, if the particle acts as fluorescent acceptor, an energy transfer might take place from the microcavity to the acceptors through the coupled modes. We name this energy transfer mechanism whispering gallery mode mediated energy transfer or WGET. This however introduces another additional loss mechanism to the resonator which reflects as the quenching of mode intensity and degradation of the Q-factor, in addition to the enhancement in acceptor's fluorescence.

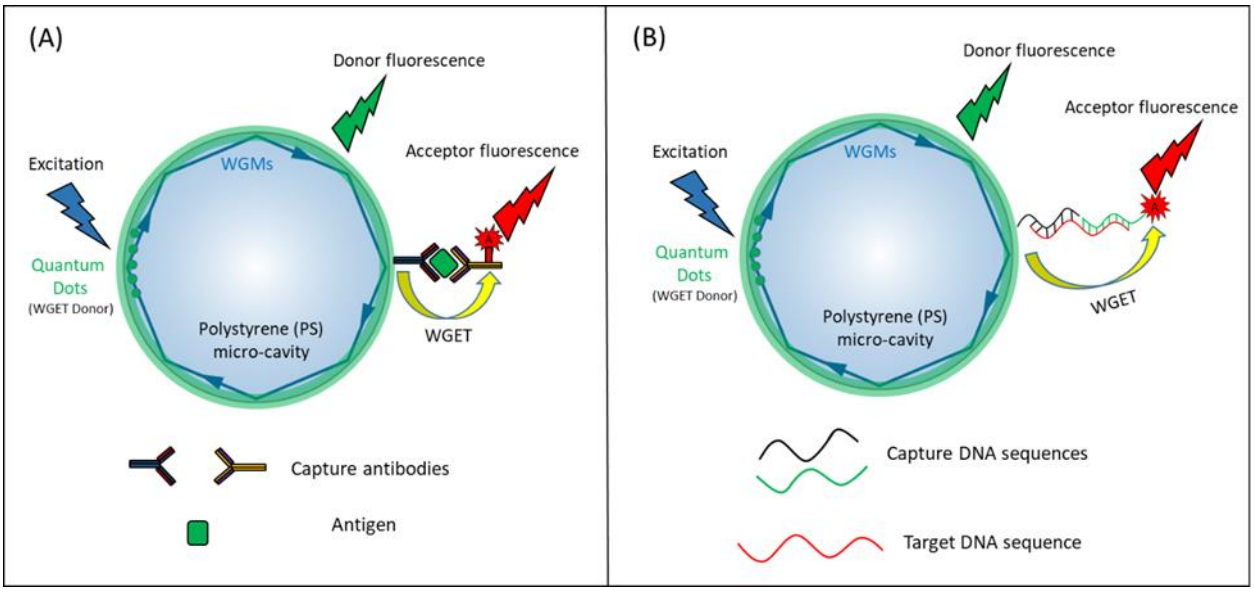

Figure 1.18: *WGET sensing schemes: (A) antibody-based antigen detection, (B) capture probe-based DNA detection.*

Here, I propose a detection scheme interfacing the FRET based sandwich assay and WGM cavities where the advantages of both schemes, for example the specificity of FRET assay, and sensitivity and long-range sensing ability of WGM cavities can be realized. To this aim, I propose to design microcavity structures in which fluorescent QDs are located inside dielectric polymer (PS) microspheres to enable strong coupling of their fluorescence with the cavity WGM modes. This cavity modes then can be utilized as optical donors

for long range energy transfer to fluorescent acceptors via the evanescent field. In contrast to traditional FRET donors which are generally single dyes or QDs, these cavities possess significant brightness arising from the accumulation of emission from thousands of QDs. In addition, the QDs would provide great photostability to these cavities which would enable them for sensing under continuous illumination for prolonged period. The bio-specificity can be introduced to these microcavities by surface conjugation of capture probes such as antibodies or capture DNA strands. On the other hand, a fluorescent entity, such as a nanoparticle with high brightness and absorption cross section, conjugated to capture probes can be utilized as the acceptor probe. As seen in the Figure 1.18, in the presence of the specific bio-analyte, a 'WGET enabled' sandwich complex would form allowing energy transfer from the QD fluorescence to the acceptors via the cavity modes. The figure shows two schemes corresponding to the detection of antigens and target DNA biomarkers.

There are several major advantages of this scheme such as, large biological assemblies that are difficult to detect using FRET schemes can be easily and efficiently sensed owing to the long evanescent tail of the cavity modes. Moreover, unlike in FRET, a photon trapped inside a high Q-resonator circulates around the microsphere and comes into contact hundreds to thousands of times with the acceptor, which potentially increases the chances of interaction, making the detection mechanism even more sensitive. Consequently, this should significantly lower the limit of detection of an analyte.

1.6 MOTIVATION AND OUTLINE OF THE THESIS:

In the previous section, I have discussed the advantages of using WGM cavities in bio-sensing and proposed a bio-detection scheme to avail these advantages in an energy transfer-based sandwich assay.

In this thesis, I will discuss a step-by-step attempt towards building this WGET cavity-sensor and demonstrate the sensing of a target analyte. It is important to mention here that I will mainly focus on the donor microcavities and assembling them with the acceptor counterpart to build the WGET biosensor, whereas the acceptor moieties which are dye-loaded polymeric nanoparticles (dyeNPs) will be provided to us by the group of Dr. Andreas Reisch and Dr. Andrey Klymchenko (LBP, University of Strasbourg).

In the second chapter I will concentrate on the fabrication of these donor microcavities. The first step of building these fluorescent micro-resonators is to synthesize an appropriate batch of QDs that is bright, photo-stable, and also fulfills the spectral requirements to be able to engage in energy transfer to the

acceptors. The next challenge will be to find a strategy to incorporate these QDs into the polymeric microcavities and examine the coupling of the QD emission to the cavity resonance modes. The scheme then should be optimized to attain the best conditions for obtaining high Q-resonators. Detailed optical characterization should also be performed to attain better understanding regarding these cavities.

The third chapter will be dedicated to the in-depth study of the energy transfer process through whispering gallery modes in a simple donor-acceptor conjugate (donor microcavity+ acceptor dyeNPs) before going into building a more complicated assay. This would clarify our understanding regarding WGET and allow us to characterize the rate and efficiency of this process. A detailed comparison between FRET and WGET process might also help us to realize which one of these two processes is more advantageous so that we can evaluate the potentials of WGET sensors towards commercial and practical applications. Later this intensive study would assist us towards designing a real bio-sensing assay.

In the final chapter of the thesis, I would focus on designing a WGET assay for the specific detection of a target biomarker DNA strand. The first step towards this goal should be imparting biospecificity onto the microcavities. An easy and effective bio-conjugation strategy should be explored in detail to coat the microspheres with capture DNA probes. The final goal would be then to execute the 'WGET based DNA assay' by mixing the probe attached donors (microcavities) and acceptors (dyeNPs) with the target DNA strands and evaluate the performance of the detection. The measurement of limit of detection (LOD) would then give us the idea of achievable sensitivity with this assay.

CHAPTER 2: QUANTUM DOT LOADED OPTICAL MICROCAVITIES

CONTENTS

2.1 INTRODUCTION:

Whispering gallery resonators have been a topic of extensive research in the past few decades due to their peculiar optical properties and potentials to be used in practical applications, such as, bio- and chemo-sensing[27,174,227], low-threshold lasing[228], and to fabricate optical and photonic elements[229]. Numerous studies can be found that report diverse fabrication strategies of WGM microcavities depending on the targeted applications. One of these techniques to make WGM enabled microspheres is to incorporate fluorophores (e.g., dyes, QDs etc.) into polymer and silica microstructures with higher refractive index than the environment. In this chapter, we will elaborately discuss the fabrication and opto-electronic characteristics of a novel spherical WGM resonator, to be more precise, fluorescent quantum dot (QD) loaded optical microcavities. I will start the discussion with the brief procedure to synthesize the quantum dots (QDs) followed by their structural and optical characterizations. I will also analyze the advantages that QDs bring when used as optical donors. Then I will set out on the process of incorporating the QDs into polymer microbeads to form the optical microcavities. The distinct optical properties of these resonators will be discussed in detail. Other important aspects, such as, stability and spectral tunability of these microcavities, will be also examined to show the advantages for using them as potential participant in energy transfer experiments. The analytical and physical expressions of resonances in WGM enabled microcavities will also be explored in detail as it will help us to comprehend its properties and engage them in suitable applications.

2.2 QDs FOR THE FABRICATION OF THE FLUORESCENT MICROCAVITIES:

QDs are widely used as nano-emitters in case of many applications, such as, light emitting diodes[230], displays[231], sensing[232] and cell imaging[233], due to their interesting optoelectronic properties, ease of synthesis and stability in various solvents. QDs have also previously been reported to be used as emitters in optical microcavities[234]. Here, in this chapter, I will talk about the fabrication and characteristics of polystyrene microcavities loaded/doped with semiconductor QDs.

2.2.1 Specifications of the QDs:

For the experiments performed in this thesis, type I CdSe/CdZnS and CdSe/ZnS QDs have been used. The CdSe/ZnS QDs are comparatively smaller in size with fluorescence emission centered at 505 nm. From now-on, these QDs will be referred as QD505. The other type I CdSe/CdZnS QDs are slightly larger in size with emission wavelength around 525 nm, which will be referred as QD525.

There are several advantages of using these QDs to construct the optical microcavities, such as their high brightness, photostability and ease of loading into the microspheres. Additionally, the emission range of these QDs are of great importance too. The main motivation of this thesis is to finally construct an energy transfer-based biosensor where QDs placed inside microcavities will act as optical donors and fluorescent entities present in the vicinity of the cavities will act as optical acceptors. Thus, a significant spectral overlap between the donor and acceptor is very important to achieve a high efficiency of energy transfer, thus these two batches of the QDs are chosen in the way to ensure that – the optical properties of the acceptors will be discussed in the next chapter.

2.2.2 Synthesis procedures of QDs:

For our experiments, core multi-shell quantum dots were used that have been synthesized and dispersed in organic medium. The cores are composed of cadmium selenide (CdSe) and the shells are made from cadmium zinc sulfide ($Cd_xZn_{1-x}S$). For simplicity, the scheme can be broken into two steps: (A) Synthesis of core, (B) the growth of shells. Detailed protocols, adapted from the literature and lab expertise, are presented in the annex.

2.2.2.1 Synthesis of core:

The synthesis of the core has been carried out under inert argon atmosphere using a Schlenk line system (see Figure 2.1). A three neck round bottom flask has been used as the pot of reaction, where one inlet of the flask is attached to a condenser and the Schlenk line, and the other two have respectively been used to put a thermometer and add reactants, and a heating mantle is used as heat source. Two different methods have been used. The first method used for the QD505 batch is called 'hot injection method' where one or more precursors are quickly injected into the reaction mixture once the reaction reaches a certain temperature. This method has been developed by Alivisatos and Bawendi et al. for synthesizing

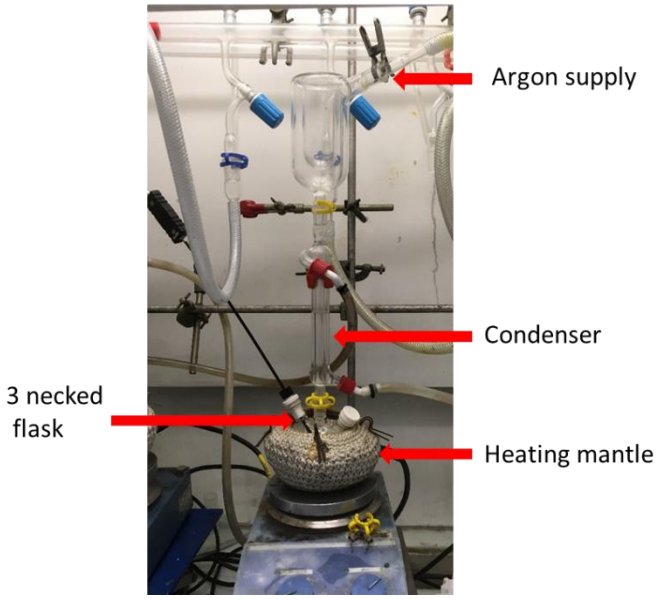

Figure 2.1: *Schlenk line setup for colloidal synthesis of QDs.*

monodisperse CdS, CdSe and CdTe QDs[235,236]. The second method, used for the QD525 batch, involves mixing both cadmium and selenium precursors at room temperature and slowly heating the solution. Both reactions involve the production of homogenous nuclei. After the nucleation has occurred, a homogenous diffusion-controlled growth is observed, that leads to the 'size focusing' of the QDs, resulting into a narrow and homogenous distribution of QDs[237]. The ligands present in the reaction mixture are responsible for providing colloidal stability to the formed nanocrystals.

To prevent oxidation of the cores, complete removal of water and oxygen is necessary by degassing using a vacuum pump through the Schlenk line. The dynamics of core formation during the reaction can be easily followed by recording the emission spectra of the reaction solution. The fluorescence intensity of

the solution enhances and red shifts as the reaction proceeds by growing the cores larger. Once cores are formed, the reaction can be quenched by cooling the solution down to room temperature. To obtain a stable colloidal suspension of cores, organic ligands like oleic acid or oleylamine are added to the solution. Ethanol, a polar solvent, is suitable to wash and purify the cores by precipitation. The cores are finally redispersed in non-polar hexane.

2.2.2.2 Synthesis of shells:

Shell growth on colloidal QDs serves very important purposes such as to provide protection from oxidation, enhance the fluorescence, modulate dispersibility in solvents and introduce surface functionalities. Here the shell of the QD505 batch was composed of ZnS, to ensure an optimal confinement of the exciton in the CdSe core and prevent red shifting of the emission wavelength. The shell of the QD525 was composed of CdZnS, which enables growing thicker shells, thanks to a lattice parameter that is closer to CdSe, at the expense of a slightly larger emission redshift. The shell was deposited using either a single precursor as metal and sulfur source (cadmium and zinc diethyldithiocarbamate) in a layer-by-layer injection sequence, or by dropwise injection of a mixture of zinc diethyldithiocarbamate and zinc stearate.

2.2.3 Structural characterization of QDs:

There are many different techniques available that are usually employed to get structural information of nano- and micro-structures such as transmission electron microscopy (TEM)[238–241], scanning electron microscopy (SEM)[242–245], atomic force microscopy (AFM)[245–248] and scanning tunneling microscopy (STM)[249–252]. Each of the techniques have their own advantages and drawbacks but the most commonly used technique that is often exploited to characterize QDs is TEM which ideally gives information such as shape, size, morphology, dispersity, crystallinity and even, compositions of QDs[253].

The high-resolution mode of TEM can typically reach the resolution as low as 0.1 nm which makes this technique ideal for imaging even very small QDs[254]. This technique also makes it possible to differentiate between the core and the shell of a QD due to their different compositions and crystallinity[255]. TEMs use high energy electrons as probes, have much better resolution compared to optical microscopes due to

the significant difference of diffraction limits between electrons and photons. TEM can be operated in two very different modes that are named respectively, bright-field and dark field.

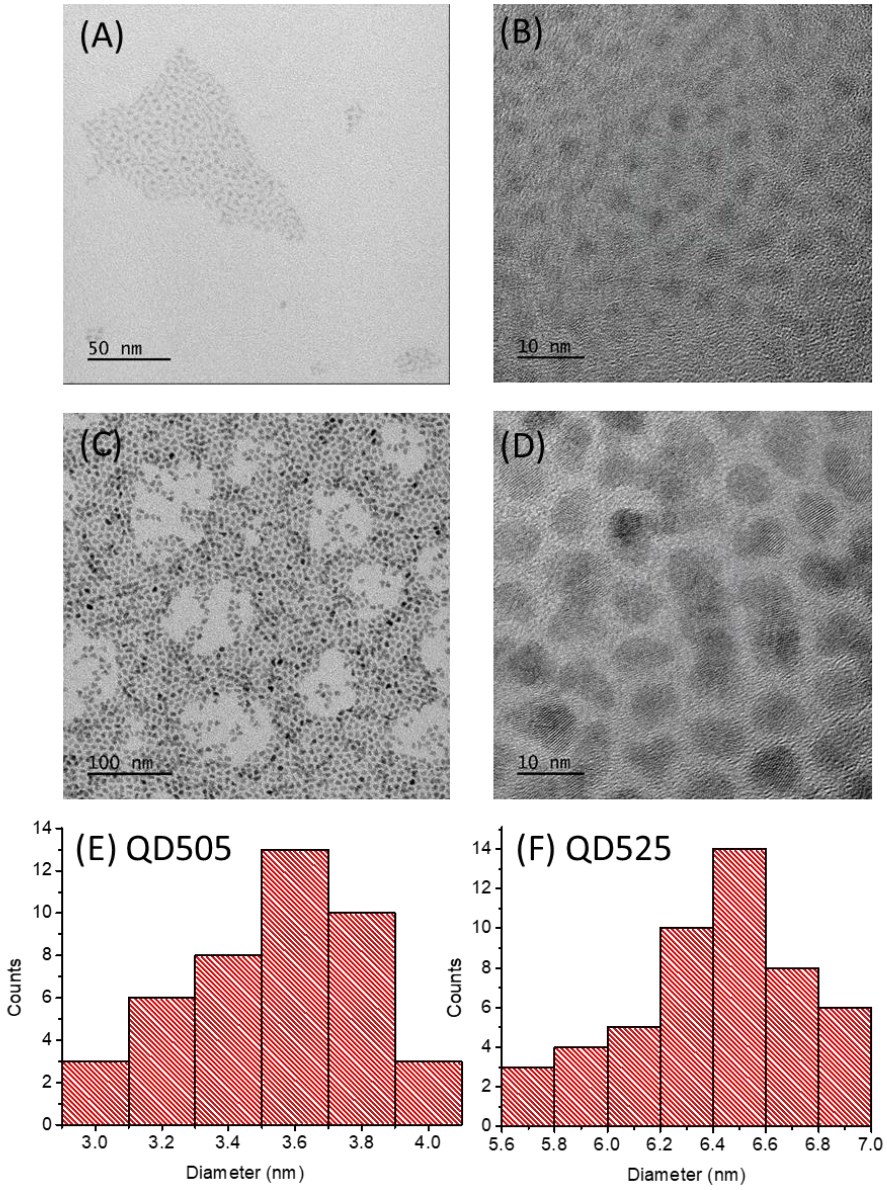

Figure 2.2: *TEM images of (A, B) QD505 (core-shell) and, (C, D) QD525 (core-shell), and size distribution histogram of (E) QD505, and (F) QD525.*

Here we have employed bright-field TEM to investigate the shape and average size of respectively QD505 and QD525, with the help of Xiangzhen Xu at LPEM. Figure 2.2 (A, B) and (C, D) respectively represent the

TEM images of QD505 and QD525, recorded with a JEOL 2010F microscope on copper-based grids. QD505 is typically very small with an average diameter of 3.5±0.2 nm and QD525 has an average size of 6.4±0.3 nm. The size distributions of these QDs can be found in Figure 2.2 (E) and (F). Both QDs are not perfectly spherical.

2.2.4 Absorption and emission properties of the QDs:

The absorption and fluorescence properties of the QDs (QD505 and QD525) in hexane were investigated using an absorption spectrophotometer and a fluorimeter (see in Figure 2.3). Broad absorption feature with increasing values in the shorter wavelengths and narrow emission spectral feature can be observed in the spectra. There is a significant Stoke's shift between the excitonic absorption peak and the emission maxima.

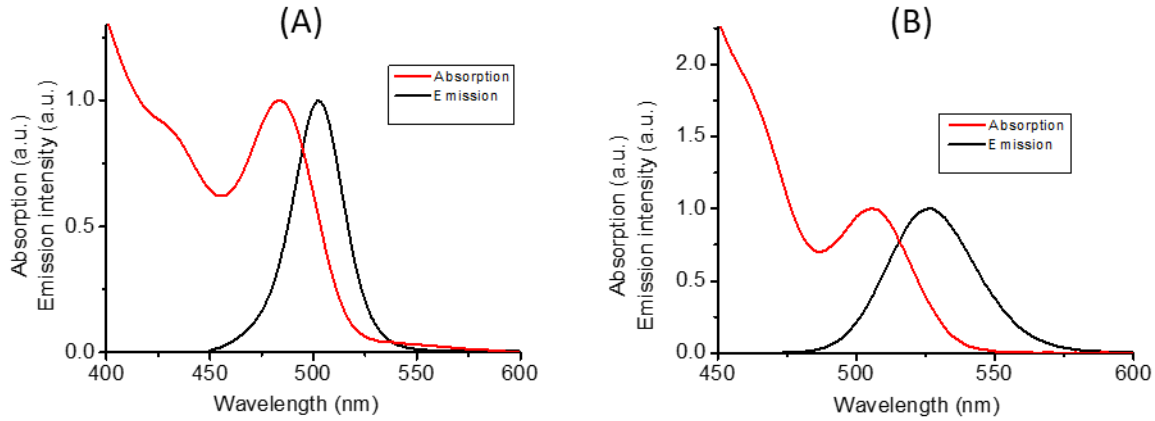

Figure 2.3: *Absorption and emission spectra of (A) QD 505, (B) QD 525*

2.3 PREPARATION OF QDS-POLYSTYRENE MICROCAVITIES:

2.3.1 Process for loading QDs into microspheres:

A one step infusion technique is used to load the QDs into the polystyrene microspheres (average diameter 10 µm) to prepare the QD based microcavities. The microspheres are bought from Sigma-Aldrich) as an aqueous suspension (concentration = 10% solid, density = 1.05 g/cm^3, whereas the QDs are dispersed in organic medium (hexane). As the first step of the loading process, it is important to separate the microspheres from the aqueous medium and resuspend in a mixture of chloroform and butanol. On the other hand, a QD-chloroform solution is prepared and injected into the suspension of microspheres. The chloroform causes swelling of the polystyrene matrix and opens up nanopores into which QDs may diffuse from the outer solution phase (see the scheme in Figure 2.4). The microspheres are then separated from the excess QDs and resuspended into water.

In a typical experiment, QDs are precipitated from hexane using ethanol and resuspended in chloroform at a concentration of 15 µM. 5 µL (~10^6 microspheres) aqueous solution of polystyrene microspheres are added to 2 mL of ethanol and centrifuged at 2000 g for 5 seconds. The supernatant is then removed leaving the solid microspheres at the bottom. The microspheres are resuspended using 1 mL of butanol:chloroform mixture (3:7, 2:1 in volume, respectively) and 25 µL of the QD solution (QD505, QD525, respectively) were added, for a 0.375 µM final concentration (Table 2.1). The solutions were mixed on a rotary agitator for 4h at room temperature. The microspheres are then centrifuged at 2000 g for 10 seconds and washed with ethanol 3 times to remove the solvent and excess QDs. The microspheres are finally resuspended in 500 µL of water.

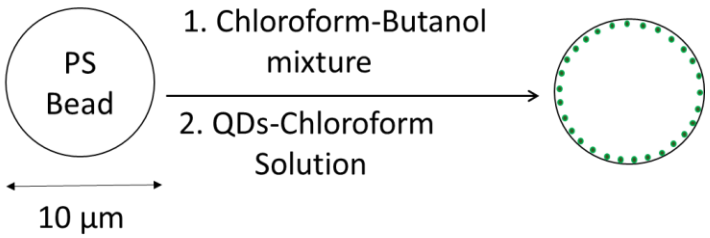

Figure 2.4: *Process to load QDs into microspheres*

QD sample	Butanol: Chloroform (Total volume = 1 mL)	Concentration of QDs
QD505	3:7	0.375 µM
QD525	2:1	0.375 µM

Table 2.1: *The ratio of solvents and QD concentration used for loading the microspheres.*

2.3.2 Critical discussions regarding the loading process of the microspheres:

A few critical points here are to be noted; first, the ratio of the chloroform and butanol has to be optimized depending on the QD batch (see solvent ratio in table 2.1). Lower amount of chloroform than the optimal volume causes the QDs to aggregate, due to the higher polarity. They form clusters, increasing the inhomogeneity and degrading the quality of the cavity resonances. Higher amount of chloroform in the mixture makes the QDs more soluble in the loading infusion which limits their diffusion into the microspheres. At the optimal chloroform: butanol ratio, QDs are still individually soluble in the solution, but migrate efficiently inside the low polarity, chloroform-swelled, polystyrene microspheres. Figure 2.5 (A) and (B) respectively show the confocal images of microspheres obtained from loading infusions with butanol to chloroform ratio 9:1 and 1:9.

Secondly, the concentration of QDs in the infusion solution also play a crucial role in terms of brightness and the QD-homogeneity of the microcavities. Very low concentration of QDs results into less bright microcavities and more concentrated than the optimal one causes the QDs to form clusters. Figure 2.5 (C) and (D) respectively represent the confocal images of microspheres with lower and higher QD concentration than the optimal range in loading infusion. A series of experiments suggested that the optimum amount of QD525 that can be loaded into total 10^6 microspheres is ~ 0.5 nmol (see section 2.3.3).

In third, the longer infusion time helps to confirm that the QD diffusion process has reached an equilibrium resulting into bright QD-microcavity systems. Figure 2.5 (E) shows the confocal image of a microsphere with less than 5 minutes loading time. The significantly bright and homogenous distribution of QDs in a

microsphere loaded in optimum condition can be seen in the Figure 2.5 (F). The confocal microscope setup and the imaging process will be discussed in detail in the following section 2.4.

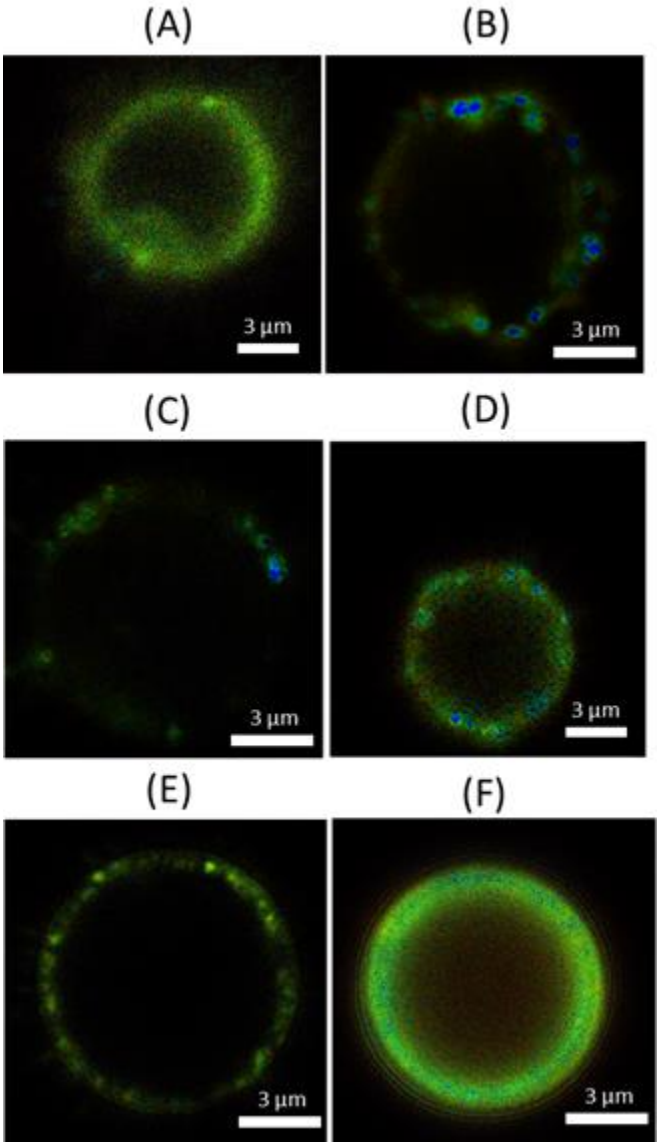

Figure 2.5: *Confocal image of a microsphere prepared in the following conditions; (A) at 9:1 BuOH:$CHCl_3$, (B) at 1:9 BuOH:$CHCl_3$ (C) at lower than optimum QD concentration, (D) at higher than optimum QD concentration, (E) low loading time, (F) at optimum condition.*

2.3.3 How much QDs are loaded into the microspheres?

A series of experiments were performed to find out the approximate amount of QDs that is loaded into each microsphere. Due to slight inhomogeneity in the distribution of QDs from one microsphere to another, each of them might not contain the exact same amount of QDs, thus an average loading for each of the microcavity can be calculated.

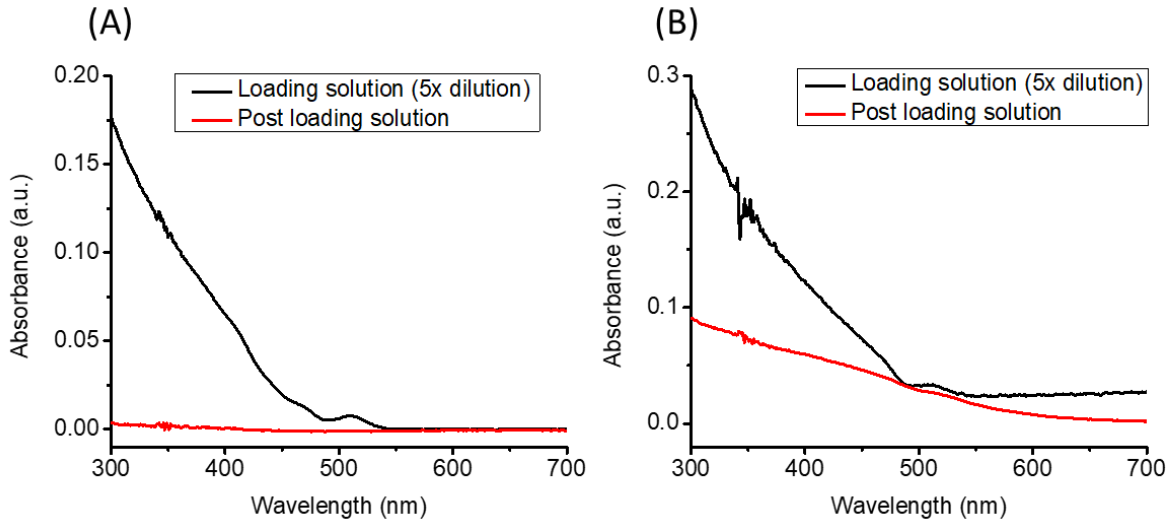

Figure 2.6: *The absorption spectra of the loading infusion before (corresponds to 5 times dilution) and after the loading for (A) experiment 1, (B) experiment 2.*

In the previous section describing the loading process of microspheres, it has been mentioned that 0.375 nmol (= 25 µL at 15 µM concentration) of QDs in the infusion results in bright and homogenous microcavities. Here, two experiments of QD (QD525) loading have been performed and, in each case, the amount of QDs used in the infusion is higher than 0.375 nmol to ensure maximum possible loading.

In experiment 1, a solution of QDs in hexane is prepared from the stock. The concentration of the solution is deduced from the absorption spectra using Beer-Lambert's law (Absorbance (A(λ)) = molar extinction coefficient (ε(λ)) × concentration × optical path length) assuming that the molar extinction coefficient of the QDs is approximately 1 $\mu M^{-1}.cm^{-1}$ at 350 nm (measured at the end of the synthesis) and the optical path length = 1 cm. Then 500 µL of the QD solution (containing 0.545 nmol QDs) is centrifuged, then redispersed in 20 µL $CHCl_3$ and added to the infusion of butanol and chloroform for the loading of the ($\sim 10^6$) microspheres (as explained in the section 2.3.1). In Figure 2.6 (A), the absorption spectrum of the QD solution (corresponding to 5 times dilution of the loading solution) is given in the black curve. After

the completion of the loading process, the microcavities are separated from the infusion and the absorption of the supernatant is measured (red curve, Figure 2.6 (A)). And the calculated concentration of QDs in the supernatant is negligible, ~ 0.001 nmol. Thus, the amount of QDs loaded into the microspheres is ~0.544 nmol.

To confirm this observed limit of QDs amount in loading, another similar experiment (experiment 2) has been performed where the loading was performed with even more QDs (~0.711 nmol). After the loading, the absorption spectrum of the supernatant solution (Figure 2.6B) shows contribution from QD absorption and from diffusion, suggesting that small QD clusters started to form at this higher QD concentration. These clusters remain in the supernatant and thus not incorporated into the microspheres.

Thus, under optimal conditions, the total amount of QDs loaded into 10^6 microspheres can be approximated to be ~ 0.5 nmol. Each of the microspheres in average contain ~ 3×10^8 QDs. This corresponds to a surface density of QDs in the microspheres ca. 1 QD/nm^2. This density is higher than that of a compact monolayer, suggesting that the QDs are not simply deposited on the microsphere surface, but instead penetrate the outer polystyrene polymer layer.

2.4 Optical studies of the QD based microcavities:

After the preparation of the QD based microcavities, the next step is to thoroughly understand and characterize their structural and optical properties.

2.4.1 Instruments used to study the microcavities:

2.4.1.1 Confocal set up:

A confocal microscope was used to capture the images of the QD-microcavities. The setup schematics is given in the Figure 2.7. The microscope was equipped with a 100x, NA = 1.45 oil objective. A laser (wavelength = 405 nm, power = 0.5 mW-0.8 mW, and switchable between both pulsed and continuous mode) was coupled to the microscope as excitation source and used to obtain the images of the microspheres as well as to record the fluorescence spectra from the confocal volume located on the equator of the microcavities.

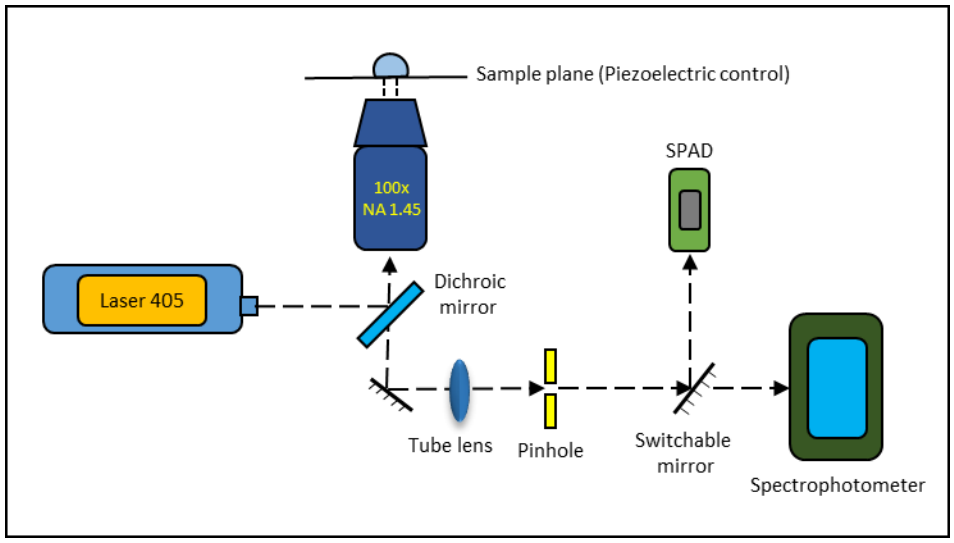

Figure 2.7: *The schematic diagram of the confocal microscope setup.*

A white lamp with appropriate filter sets (exc: 425-60, dichroic: LP485, em: 505-40) helps to focus on the microsphere using the binoculars (not shown in Figure 2.7). A LP485 (long pass 485 nm) dichroic was used to eliminate the laser excitation from the fluorescence path. The fluorescence is focused with a tube lens onto a pinhole to collect emission only from the confocal volume and block the emission coming from

out-of-focus planes. The focal plane of the microscope objective lens was placed at the equator of a microsphere so that the cross-sectional area can be observed. The fluorescence signal is detected by a pair of single photon avalanche diodes (SPAD). Then the sample scanning enabled by the piezoelectrics forms the image of the whole microsphere. The resolution limit of the image is ca. 0.5 µm. A mirror is placed on the detection path to guide the fluorescence to the SPAD. When the mirror is removed, the fluorescence goes to the spectrophotometer that records the emission spectra of the microsphere.

2.4.1.2 Wide field set up:

Another wide-field microscope set-up (see Figure 2.8) equipped with a 100x NA 1.45 oil objective was also used to record the fluorescence from the whole microsphere instead of just the focal volume. In this microscope, a white lamp acts as the excitation source, and a filter cube (exc: 425-60, dichroic: LP485, em: 505-40) was used to excite the QDs and record the fluorescence from the whole microcavities. The fluorescence was first focused by a tube lens then by another lens onto an objective (10x air, NA 0.3) and sent to the spectrophotometer via a single mode optical fiber. A mirror is placed in the detection path to divert the fluorescence to a charge-coupled device or CCD camera to get the image of the whole microsphere.

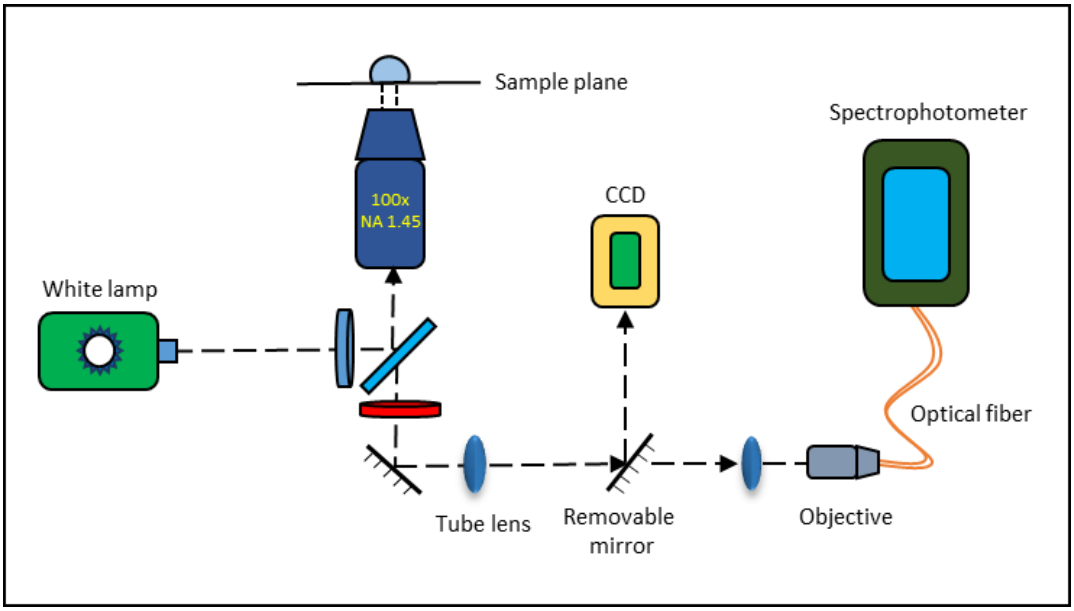

Figure 2.8: *The schematic diagram of the wide-field microscope setup (dark blue filter represents excitation, light blue one represents the dichroic and red one represents the emission filter.*

2.4.2 Images and the emission spectra from the microscopes:

In Figure 2.9 (A) shows a typical image of a microcavity obtained with the confocal microscope. The QDs are concentrated around the edge of the microsphere forming a bright ring. The fluorescence intensity profiles across a microsphere (image showed in Figure 2.9 (E)) along the red straight lines (horizontal and vertical) are shown in the Figure 2.9 (F), where the X-axis represents the spatial distance of scanning. The two peaks in each of the intensity profile represent the two edges of the bright ring along the scanning line. The average profile width is ca. 1.3 µm, slightly larger than the spatial resolution of the instrument (ca 0.5 µm). This suggests that the penetration depth of the QDs can be in between a few hundreds of nm to a couple of microns. The organic solvent opens up the nanopores that allow the diffusion of the QDs into the microspheres a few hundreds of nm below the surface. As the QDs travel inside, the porosity of the microspheres decreases which causes the QDs to stop and stay just below the surface of the microspheres.

A typical emission spectrum of the collected fluorescence is shown in Figure 2.9 (B), where the confocal volume has been placed at the equator of the microsphere loaded with QD525. The spectrum shows a broad envelope emission, corresponding to the spectrum of QD emission in free space.

In addition, the spectrum shows a series of regularly spaced pairs of peaks, corresponding to coupling of the QD emission to the transverse magnetic (TM) and electric (TE) whispering gallery modes of the QD-microcavity. QD intensity is brighter at these particular wavelengths due to the Purcell effect, as will be discussed later. The whispering gallery mode intensity at a peak is denoted here as I_{WGM}, and the envelope intensity, on the other hand, is denoted as I_{Env}. Emission spectra collected from the whole microsphere in a wide-field microscopy setup (Figure 2.9 (D)) also show similar feature as in Figure 2.9 (B). The image of a microsphere obtained with the CCD (10 s exposure time) is given in the Figure 2.9 (C).

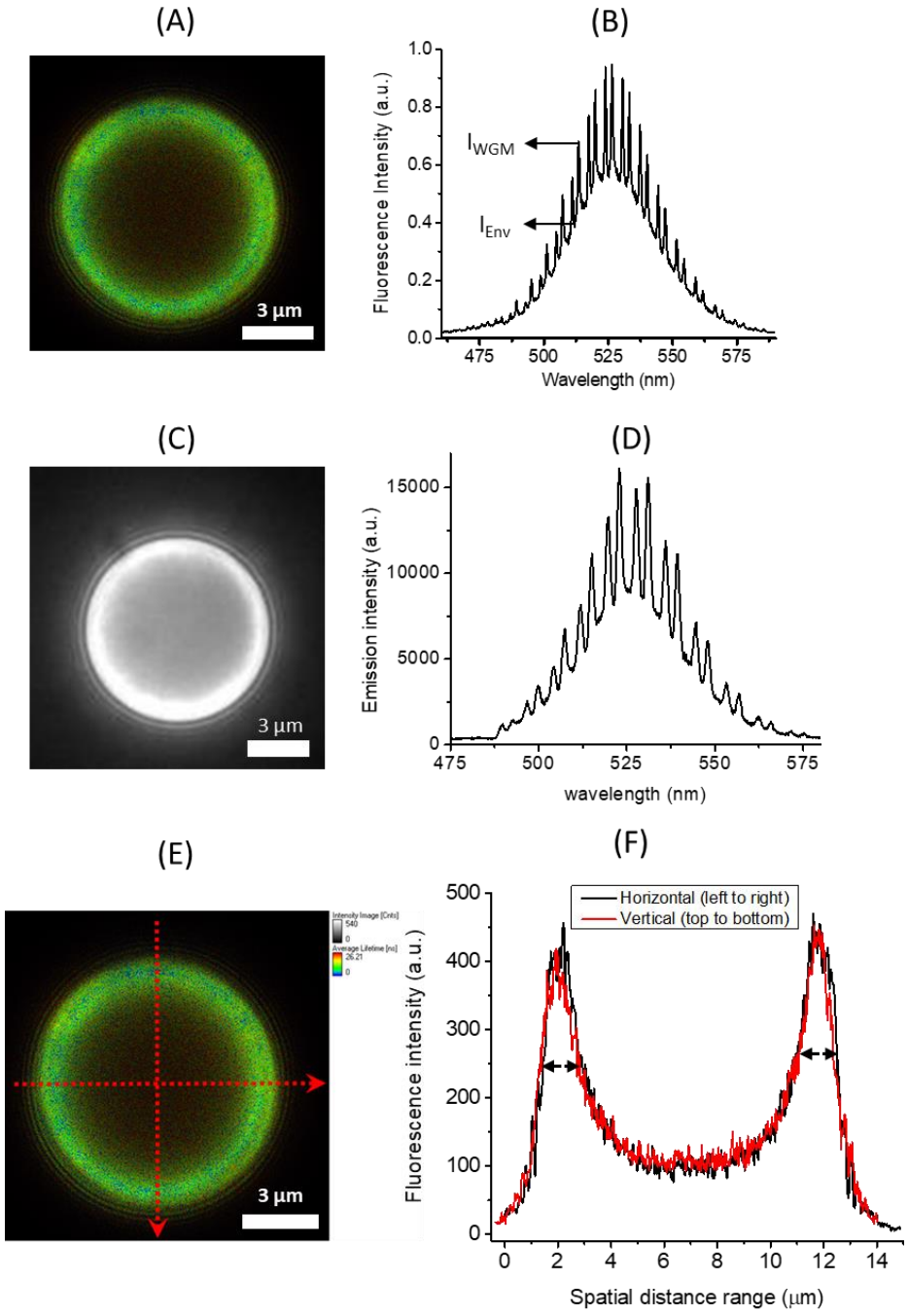

Figure 2.9: *(A) The confocal image of a microsphere loaded with QD525, (B) the fluorescence spectra from a confocal volume on the surface of QD525-microcavity, (C) The CCD image of a microsphere loaded with QD525 and (D) fluorescence spectra from the whole QD525-microcavity using a wide-field microscope. (E) Confocal image of QD525-microcavity superimposed with the scanning lines, and corresponding (F) fluorescence intensity profiles.*

2.4.3 Does the spectrum change with the excitation and detection volume?

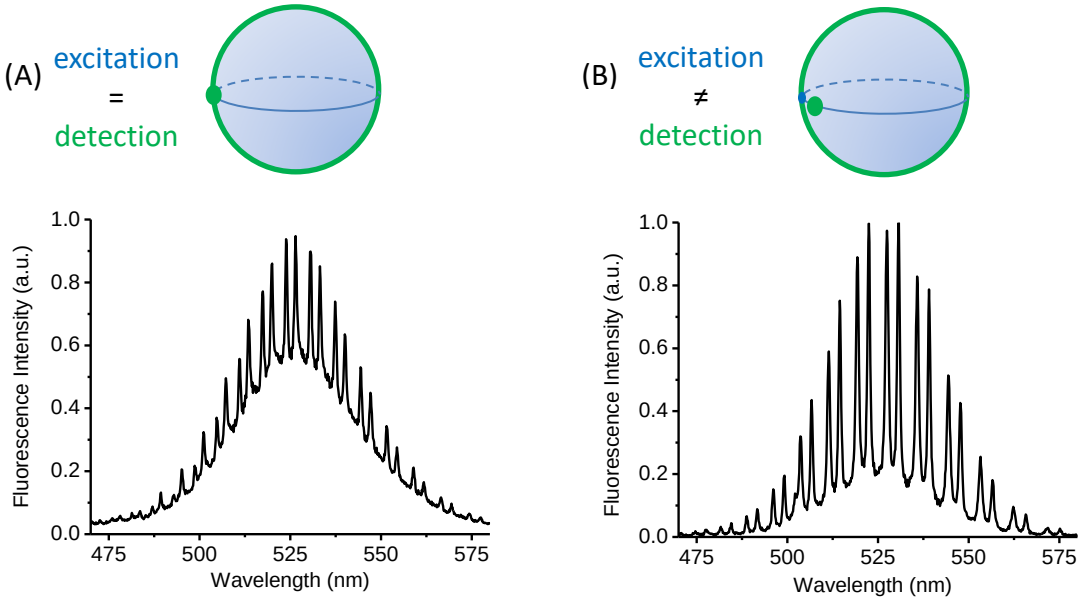

Figure 2.10: *Fluorescence emission spectra when the detection pinhole is (A) at the same spot as the excitation spot, (B) located away from the excitation spot.*

A photon emitted by a QD and traveling in a whispering gallery mode eventually exits the microsphere, at a point which may be distinct from the QD location. An experiment was performed to see if the relative location of excitation and detection volumes on the surface of the microcavity have any effect on the spectra. Figure 2.10 (A) represents the emission spectra from the microcavity when the excitation and detection volume are the same. Then, the pinhole of the confocal microscope was slowly moved to a different location to decouple the excitation and detection volumes. An interesting observation regarding the fluorescence emission of the microcavity is when the detection pinhole is located away from the excitation spot, the emission spectrum consists mainly in the WGM peaks with a smaller contribution from the free space emission as shown in Figure 2.10 (B). This observation can be well explained as, when the fluorescence is collected from the excitation volume, most of the free space emission of QDs is also collected in addition to the propagating WGMs. Whereas, when the detection volume is located away from the excitation volume, the free space emission is not much collected, only the fraction of light traveling within the microsphere by total internal reflection effectively reach the detector.

2.4.4 Does the fluorescence lifetime of QDs change inside the microcavity?

An experiment was performed to investigate if the fluorescence lifetime of the QDs changes as an effect of being placed inside a dielectric microsphere. A time-correlated single photon counting (TCSPC) instrument was utilized to compare the lifetime of QDs in hexane (~0.05 µM) and inside microspheres (20 µL of QD-microsphere solution + 200 µL water).

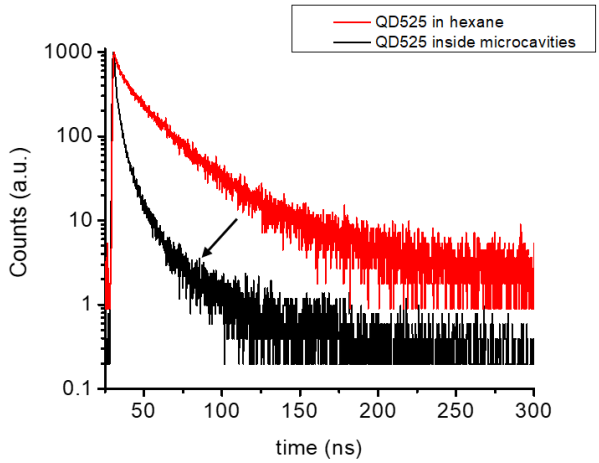

Figure 2.11: *Lifetime of QD525 in solution vs inside polystyrene microcavities.*

The lifetime of QD525 decreased substantially when loaded into the microcavities compared to the solution phase (in hexane) as seen in Figure 2.11. This can be a consequence of Purcell effect (due to the presence of dielectric environment) and/or increase in the non-radiative decay channels. It is difficult to draw any concrete conclusion from this as the microenvironment of the QDs in these two cases are not comparable.

2.5 THEORETICAL UNDERSTANDING OF WHISPERING GALLERY MODE CAVITIES:

A thorough theoretical understanding of WGM is very important for further realization of various applications based on optical microcavities such as a highly sensitive biological sensor or opto-photonic elements. Here, in this section, I will discuss the fundamentals of the WGM resonances occurring in spherical micro resonators to gain better analytical perspectives. This will help us to exploit the

advantages of these resonators and utilize them for practical applications. Moreover, it will allow us to confirm that the behavior observed in case of QD loaded microcavities is consistent with the principles of spherical resonators. As our main interest lies in building an energy transfer-based bio-detection scheme using the QD loaded microcavities as optical donors, it is of foremost interest to estimate the electromagnetic (EM) field distribution both below and above of the cavity interface which will be elaborately discussed in this section.

The radiation mechanism of a whispering gallery resonator can be represented as an interesting electromagnetic problem. The scattering of light by a spherical structure of arbitrary size (a) and relative refractive index (N) can be derived from the Lorentz-Mie theory. This theory can also be modified to understand the whispering gallery resonances arising from light trapped inside microcavities. The schematics of the sphere in polar coordinates (r, θ, φ) is given the Figure 2.12.

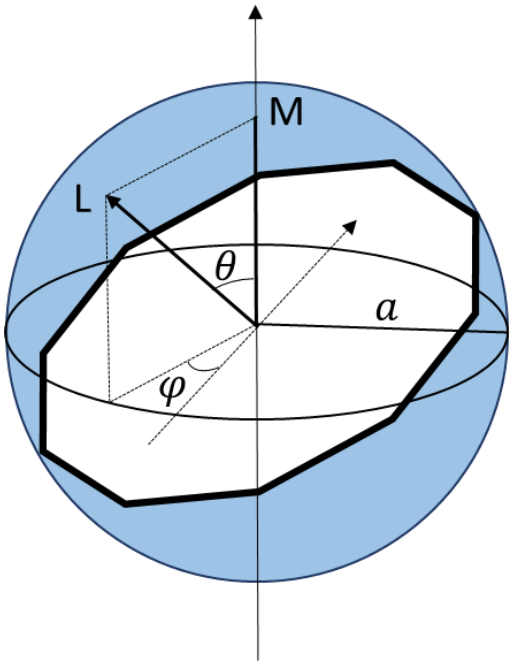

Figure 2.12: *Angular momentum (L) associated with WGM and its projection (M) on the polar axis.*

A classical electrodynamic approach called Hansen's method[256] can be appointed to solve the vectorial Helmoltz equation[135]. The angular dependence of the solutions can be described by vectorial spherical harmonics[257] defined as in equation set 2.1.

$$\left.\begin{aligned} \vec{X}_l^m &= \vec{\nabla} Y_l^m \times \frac{\vec{r}}{\sqrt{l(l+1)}} \\ \vec{Y}_l^m &= \frac{r\vec{\nabla} Y_l^m}{\sqrt{l(l+1)}} \\ \vec{Z}_l^m &= Y_l^m \hat{r} \end{aligned}\right\} \quad (Eq.\ set\ 2.1)$$

To elaborately represent each WGM field, we use a set of three parameters which are respectively the polarization, and the mode numbers (l and m). The polarization of the oscillation can be either transverse electric (TE) or transverse magnetic (TM). The direction of the electric field $\vec{E}$ (magnetic field $\vec{B}$, respectively) polarization for TE (TM, respectively) modes is given in the Figure 2.13 (A) and (B). θ_i and θ_r respectively represent the angles of incident and reflection of a EM ray with wave vector $\vec{K}$ on the interface of two media with refractive indices η_1 and η_2. The parameter l signifies the angular mode number that indicates the order of the spherical harmonic Y_l^m to describe the angular field distribution. Y_l^m is the eigenfunction of the square of orbital momentum operator, simply represented as

$$L^2 Y_l^m = \hbar^2 l(l+1) Y_l^m \quad (Eq.\ 2.2)$$

The index m represents the azimuthal mode number. The value of m is related to the eigenvalue of the orbital angular momentum operator along Z axis operating on the spherical harmonic Y_l^m, which can be written as;

$$L_z Y_l^m = \hbar m Y_l^m \quad (Eq.\ 2.3)$$

For a definite value of l, m can have $2l$+1 values, ranging from +l to –l.

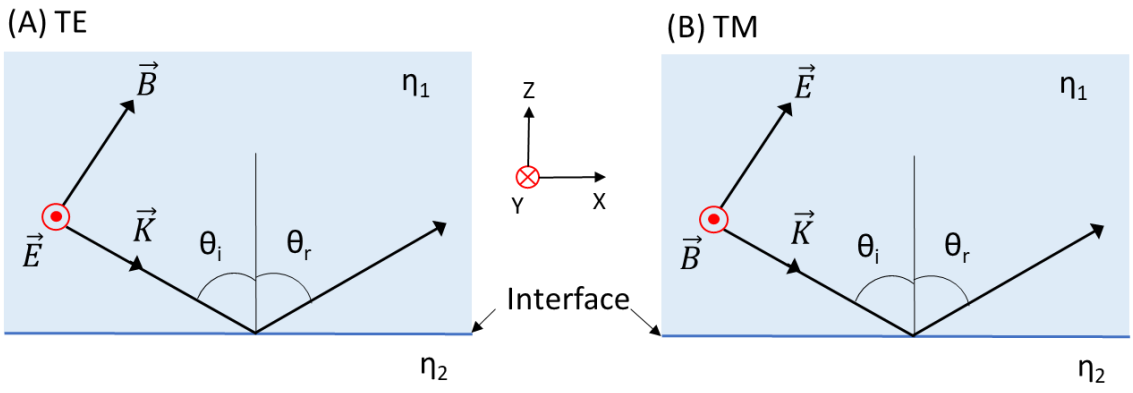

Figure 2.13: *The directions of electric ($\vec{E}$) and magnetic ($\vec{B}$) field vectors for (A) TE and (TM) mode at a dielectric interface.*

With the help of the mode numbers and the angles in polar co-ordinates, we can express the electric and magnetic field for both the polarizations, as in equation set 2.4 and 2.5.

$$E_{lm}^{TE}(r) = E_0 \frac{f_l(r)}{k_0 r} X_l^m(\theta,\varphi)$$
$$B_{lm}^{TE} = \frac{E_0}{ic}\left(\frac{f_l'(r)}{k_0^2 r} Y_l^m(\theta,\varphi) + \sqrt{l(l+1)}\frac{f_l(r)}{k_0^2 r^2} Z_l^m(\theta,\varphi)\right)$$

(Eq. set 2.4)

$$E_{lm}^{TM}(r) = \frac{E_0}{N^2}\left(\frac{f_l'(r)}{k_0^2 r} Y_l^m(\theta,\varphi) + \sqrt{l(l+1)}\frac{f_l(r)}{k_0^2 r^2} Z_l^m(\theta,\varphi)\right)$$
$$B_{lm}^{TE} = \frac{iE_0}{c}\frac{f_l(r)}{k_0 r} X_l^m(\theta,\varphi)$$

(*Eq. set* 2.5)

Where, E_0 and k_0 respectively represent the electric field and the wave vector at the interface. Moreover,

$$f_l(r) = \psi_l(Nk_0 r) \text{ for } r < a \qquad (Eq.\ 2.6)$$

$$f_l(r) = \alpha\psi_l(k_0 r) + \beta\psi_l(k_0 r) \text{ for } r > a \qquad (Eq.\ 2.7)$$

are solutions of Riccati-Bessel radial equation. $\psi_l(\rho) = \rho\, j_l(\rho)$ and, $\chi_l(\rho) = \rho\, n_l(\rho)$, where j_l and n_l are spherical Bessel and Neumann functions, respectively[135,258].

2.5.1 Positions of resonances:

One of the primary motivations of building this analytical model is to find the positions (in terms of wavelength or frequency) of these WGM resonances. If the tangential components of the electric and magnetic field of the WGMs are assumed to follow the continuity principle, then the positions of the resonances can be calculated as follows,

$$\psi_l(Nk_0 a) = \alpha\psi_l(k_0 a) + \beta\chi_l(k_0 a) \qquad (Eq.\ 2.8)$$
$$P\psi_l'(Nk_0 a) = \alpha\psi_l'(k_0 a) + \beta\chi_l'(k_0 a) \qquad (Eq.\ 2.9)$$

Where $P = N$ for TE polarization and $P = N^{-1}$ for TM polarization[135,258]. To find the exact solutions to this pair of equations, we need to find the values of the constants α and β, which eventually lead to complex frequencies. A method developed by Lam et al.[259] can be used to numerically evaluate the positions of the whispering gallery mode resonances analytically. This method leads to several solutions for the positions of resonances, associated with the radial mode numbers or n.

2.5.2 Mode numbers of WGM:

The WGM resonance peaks can be represented using a set of three integers n, l and m. To summarize, n is associated with the radial function, l and m signify the classical quantization of the angular momentum. In case of a perfect spherical resonator, the resonances have degenerate m values, leading to no particular dependence on m.

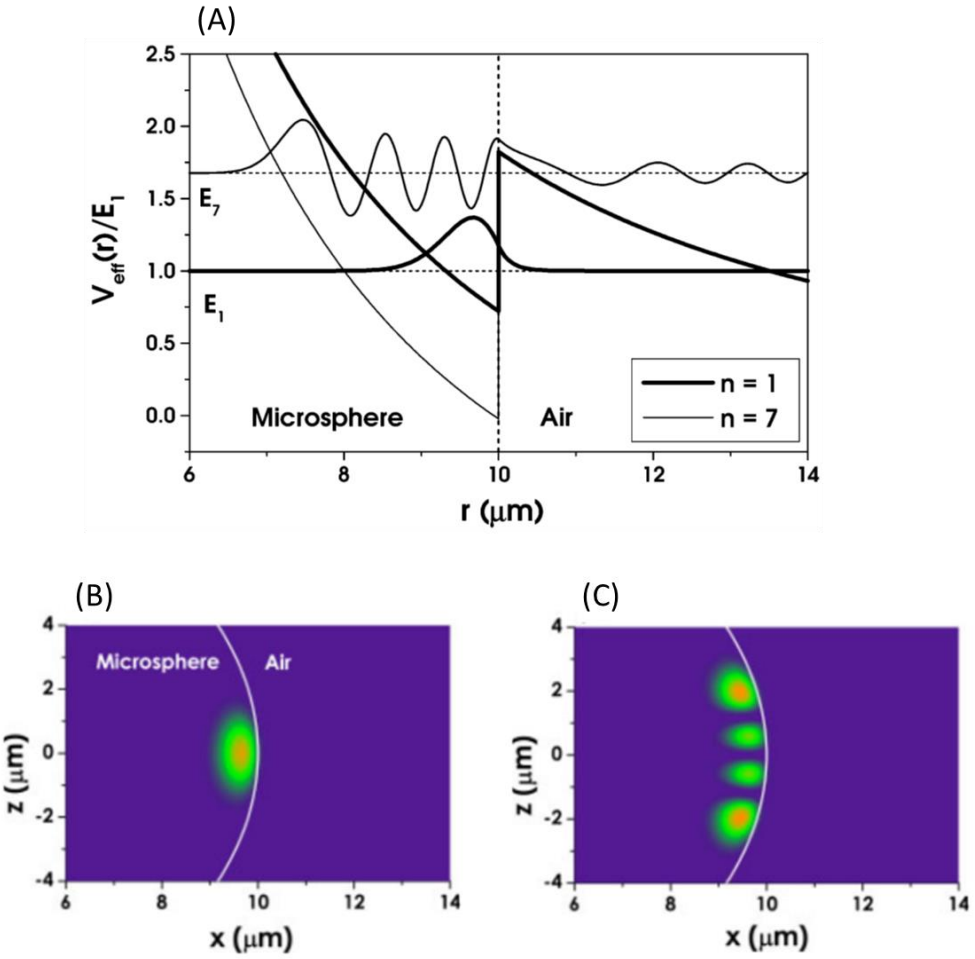

Figure 2.14: *(A) Effective potential energy diagrams and electric field intensity for respectively n = 1 (bold line) and n = 7 (light line) modes with l = 100, (B) Poynting's vectors for TE mode (n = 1, l = 100) with (B) $|l\text{-}m|$=0, (C) $|l\text{-}m|$=3 [Calculation performed on a silica microsphere (radius = 5 μm, N =1.45)] (Image source: https://doi.org/10.1002/lpor.200910016)*[135]

The physical interpretation of these mode numbers can be easily explained from the Figure 2.14. In Figure 2.14 (A) the effective potential energy has been plotted as a function of radial distance for a TE mode (l = 100) with radial mode numbers respectively n = 1 and n = 7 for a silica microsphere with size, a = 10 µm and refractive index (*N*) = 1.45. The number of nodes in the potential curve in radial direction for a given radial mode number, n, can be calculated as (n-1). Thus there is no node in the effective potential function in radial direction for n = 1, whereas, for n = 7, the potential energy curve contains 6 nodes[135].

On the other hand, the number of nodes in the energy flux on the microsphere surface for a mode can be calculated from the angular and azimuthal mode numbers (l and m). Figure 2.14 (B) and (C) show the Poynting's vectors of a TE mode (n = 1, l = 100) occurring on the surface a silica microsphere with size (a) = 10 µm and refractive index (*N*) = 1.45. For the Poynting's vector in Figure 2.14 (B), $|l\text{-}m|$ = 0, thus there is no node in it. On the other hand, the Poynting's vector in the Figure 2.14 (C) has $|l\text{-}m|$value = 3, therefore 3 nodes are present in it[135].

The lowest lying state which has the radial mode number n = 1 resides as close as possible to the surface of the sphere and has the maximum angular momentum possible, so that the condition $l \approx Nka \approx Nx$ can be fulfilled. Light trapped into this strongly confined state can only escape via tunneling through the potential energy barrier which extends to Na for this particular state. This far-extended tail of this state suggests a very weak coupling of this mode to the outside medium and very high quality factors[135]. Modes that have higher radial mode number (n>1) are not as well confined as the n = 1 modes, thus they have lower Q-factor and easily leak through the surface. They are not generally identifiable in the WGM spectra of the resonator.

2.5.3 Free spectral range of the WGMs:

Free spectral range (FSR) that represents the spacing between two adjacent modes with same polarization and n value, but with a difference of one unit in their l value can be calculated for a spherical microcavity using the equation 2.10[135,258]. To a first approximation:

$$\Delta\nu_{n,l}^{\Delta l=1} \approx \frac{c}{2\pi Na} \qquad (Eq.\ 2.10)$$

The spacing between two adjacent TE and TM modes with same n and l value:

$$\Delta\nu_{n,l}^{TE,TM} \approx \frac{c}{2\pi Na}\frac{\sqrt{N^2-1}}{N} \qquad (Eq.\ 2.11)$$

2.5.4 Quality factor:

The electromagnetic field of a WGM decays in the form of radiation from the resonator. The quality factor is the physical parameter to determine the damping process in a resonator, in other words it characterizes the ability of a microcavity to store energy inside for a time, τ. The general way of representing quality factor is as the ratio of the central frequency to the bandwidth of the resonant mode as seen in equation 2.12.

$$Q = \frac{\lambda}{\Delta\lambda} = \frac{\omega}{\Delta\omega} = \omega\tau \qquad (Eq.\ 2.12)$$

Where ω stands for the central frequency, Δω signifies the linewidth of the resonant mode, λ is the central wavelength and Δλ denotes the full width at half maximum of the resonance mode. For simple understanding, the rate of relaxation of a cavity is inversely proportional to its quality factor[135,260]. High quality resonators are better at storing energy inside which makes them more desirable for practical applications in the field of opto-electronics. Not only spherical resonators, but also other structures like cylindrical, micro disks, toroidal structures have been demonstrated to have very high-quality factors.

To characterize various loss mechanisms from a resonator, we can simply represent the quality factor as,

$$\frac{1}{Q} = \frac{1}{Q_{Rad}} + \frac{1}{Q_{mat}} + \frac{1}{Q_{Scatt}} + \frac{1}{Q_{Cont}}. \qquad (Eq.\ 2.13)$$

And the total cavity relaxation rate ($\Gamma_{\text{Resonator}}$) can be expressed as the following:

$$\Gamma_{Resonator} = \Gamma_{Rad} + \Gamma_{mat} + \Gamma_{Scatt} + \Gamma_{Cont}. \qquad (Eq.\ 2.14)$$

The first term Q_{Rad} is associated with the radiative losses which can be calculated using a semi-classical WKB approximation. Q_{Rad} is inversely proportional to the rate of radiative losses (Γ_{Rad}). The solution reveals that the quality factor associated with the TM mode is slightly lower than the TE mode. Also, the radiative loss is inversely proportional to the size of the cavity. When the ratio of the diameter of the cavity to the wavelength of the trapped light or $a/\lambda \geq 15$, then $Q_{Rad} > 10^{11}$, thus the radiative loss is negligible[135].

The absorption of light by the composing material of the cavity and bulk Rayleigh scattering contribute to the term Q_{mat}[135]. The rate of relaxation associated with it is denoted by Γ_{mat}. The value of Q_{mat} can be approximated as equation 2.15 where α is the attenuation coefficient,

$$Q_{mat} \cong \frac{4.3\times10^3}{\alpha}\frac{2\pi N}{\lambda}, \qquad (Eq.\ 2.15)$$

Q_{Scatt} is associated to the losses due to the scattering by surface roughness caused by small clusters. The rate of losses through scattering is denoted as Γ_{Scatt}. Q_{Scatt} can be calculated by using a model derived as the corollary of Rayleigh scattering by small particles[261]. Then the Q_{Scatt} can be expressed as:

$$Q_{scatt} = \frac{\lambda^2 a}{2\pi^2 \sigma^2 b}, \qquad (Eq.\ 2.16)$$

where the σ and b respectively are the RMS size and the correlation length of the inhomogeneities[262].

Q_{Cont} is related to the losses (with rate = Γ_{Cont}) by surface contaminants either introduced during the fabrication process or via adsorption from the environment (e.g., atmospheric water or other contaminants).[135]

Q-factor of microspheres made of fused silica (size = 500-1000 µm) have been reported to reach as high as 10^8-10^9 at 633 nm[262]. Spherical water micro-droplets (size = 15.3 µm) loaded with Rhodamine 6G[263] has been also reported to have Q-factor ~ 10^8. Polystyrene microspheres in water has also been shown to possess Q-factor 10^4-10^6 at 770 nm[264,265].

2.6 Q-FACTOR OF THE QD LOADED MICROCAVITY:

The Q-factor of the microcavity provides much information regarding the decay process of the propagating electromagnetic resonances of the microcavity. Presence of an analyte within the evanescent field of the microcavity affects the Q-factor by altering the effective refractive index of the cavity; this phenomena has been widely exploited to construct many microcavity based bio-sensors[27,266]. Also, if the whispering gallery modes of a microcavity engage in energy transfer to an optical acceptor present near the surface, the quality factor value will be affected. With the help of a high-resolution spectrophotometer, it is possible to evaluate the Q-factor of a microcavity.

The spectrophotometer attached to the confocal microscope (at LPEM, ESPCI Paris) that has been utilized to record the fluorescence spectra of the microcavities, does not possess resolution high enough to resolve the width of the WGMs which is important for the direct estimation of the Q- factor of the modes. Therefore, another spectrophotometer facility with higher resolution (ca. 0.1 nm) at the Laboratoire Interdisciplinaire Carnot de Bourgogne (ICB) in the University of Bourgogne was utilized. I thank Dr. Jean-Claude Weeber for his help with the measurements. Even though this high-resolution spectrophotometer

does not have enough resolution to completely resolve the width of the WGMs, still it makes it possible to have a better estimation of the lower limit of the Q- factor of the QD loaded microcavities.

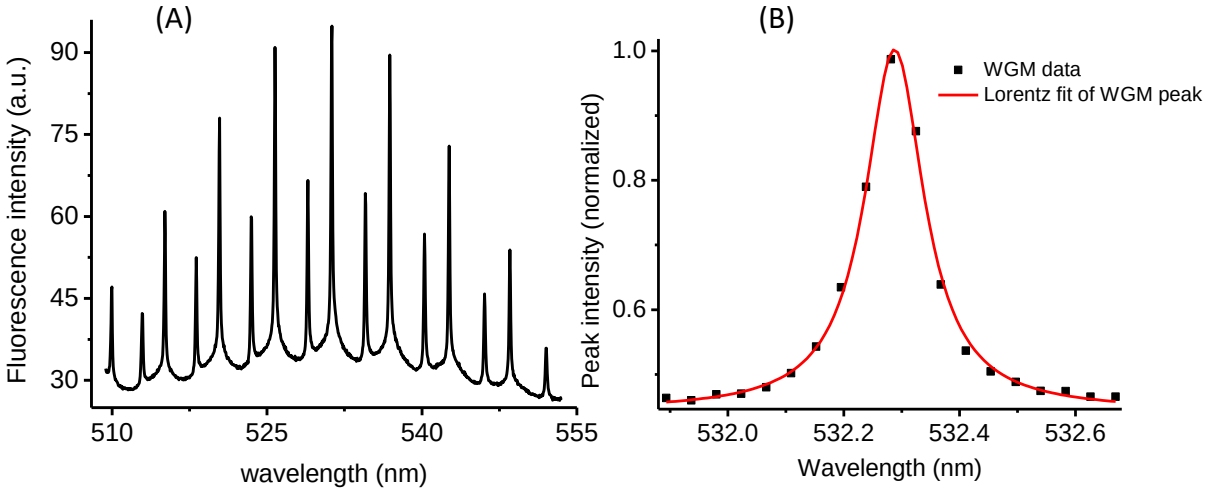

Figure 2.15: *(A) High resolution fluorescence spectra from QD525 loaded microcavity, (B) Lorentzian fit of a high resolution WGM peak.*

2.6.1 Measurement of Q for the QD-microcavity:

A spectrum recorded with a high-resolution spectrophotometer is shown in Figure 2.15 (A). As the detection volume is placed away from the excitation volume, the spectrum mainly consists of propagating WGMs with minimal contribution from the free space emission. The modes have been fitted with Lorentzian function (Figure 2.15 (B)) and the linewidth is typically 0.125 nm. This corresponds to the spectrometer resolution limit. This shows that we are not able to resolve the mode spectral width with this technique, and that the quality factor of the modes, $Q = \lambda/\Delta\lambda$, is greater than 4200. This value is only a lower bound, and previous studies showed that WGM quality factors in similar polymer microspheres can exceed 10^6 in water[264].

Another relation that can be derived from the expression of Purcell effect, might be useful for qualitative comparisons. Purcell factor (F_P) is defined by the factor of enhancement of a fluorophore's spontaneous emission rate due to the change in its environment, for example, by incorporating the fluorophore inside a resonant cavity[267]. Thus, this enhancement of relaxation rate can be expressed as the following:

$$\Gamma_{Cavity} = \Gamma_{Free} + \Gamma_{Free}.F_P$$

$$\Rightarrow \frac{\Gamma_{Cavity}}{\Gamma_{Free}} - 1 = F_P \propto Q\,, \qquad (Eq.\ 2.17)$$

where, Q, Γ_{Cavity} and Γ_{Free} are respectively the quality factor of the cavity, rates of spontaneous emission of the fluorophore inside the cavity and in free space. Now, the equation 2.17 can be related to the spectra, as $\frac{\Gamma_{Cavity}}{\Gamma_{Free}}(\lambda) \propto \frac{I_{WGM}}{I_{Env}}(\lambda)$. Thus, a practical and useful relation can be written as:

$$Q(\lambda) \propto \frac{I_{WGM}}{I_{Env}}(\lambda) - 1 \propto \frac{1}{\Gamma}\,, \qquad (Eq.\ 2.18)$$

where Q(λ) is the quality factor of the microcavity at wavelength λ, I_{WGM} and I_{Env} are respectively the intensity of the WGM and the envelope at wavelength λ. Γ is the total relaxation rate of the microcavity which can be expressed as, $\Gamma = \Gamma_r + \Gamma_{nr}$, where Γ_r and Γ_{nr} are respectively the radiative and non-radiative decay rate of the cavity[174]. This relation can be useful to understand how the Q-factor of the QD-microcavities depend on the loading QD concentration.

2.6.2 Dependence of Q on the QD loading concentration:

A series of experiments were performed to determine how the Q-factor of these microcavities change with the amount of QDs in the loading solution. The concentration of QDs during incubation with the microspheres was varied in between 0.0003 µM to 2.22 µM and the corresponding ratio (averaged on a set of 8-10 beads) of WGM peak intensity, I_{WGM}, to envelope emission intensity, I_{Env}, were plotted as a function of the wavelength. It is observed that the I_{WGM}/I_{Env} stayed within a close range (~5-6) when the concentration was varied between 0.0003 µM to 0.3 µM which suggests that the Q factor of the microspheres (using Eq. 2.18) does not change much with the loading concentration of QDs within this range. Two confocal images of microspheres within the loading concentration range of 0.15 µM and 0.3 µM are given in the Figure 2.17 (A) and (B). Above the concentration of 0.3 µM (for the concentrations; 1.15 µM and 2.22 µM), the QDs tend to form large clusters on the surface of the microspheres which leads to very high scattering and lower quality of the WGMs, as evident from Figure 2.17(C). This translates as broader peaks and lower I_{WGM}/I_{Env}. Below the concentration of 0.0003 µM, the microspheres are loaded inhomogeneously with QDs and the signal from the microspheres becomes quite low under our experimental conditions.

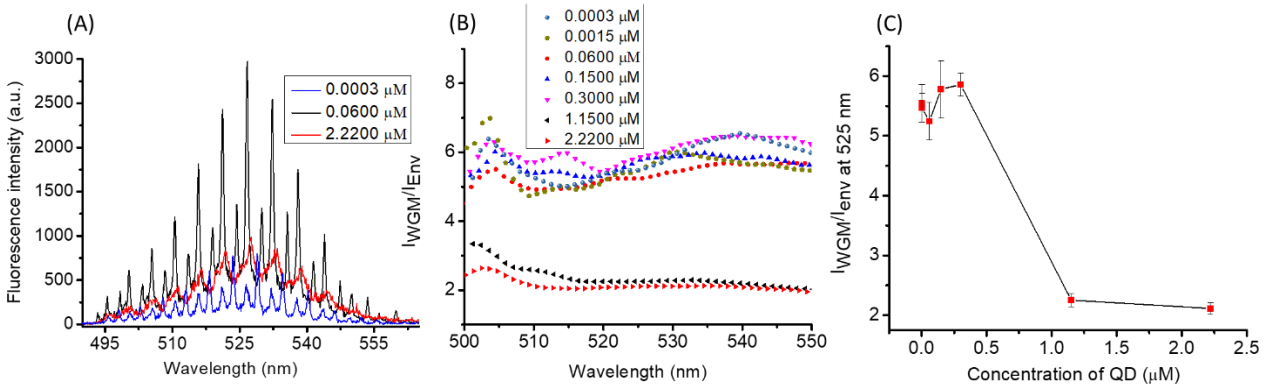

Figure 2.16: *The dependence of Q-factor on the QD loading concentration, (A) emission spectra from microspheres (confocal volume on the equator) obtained with three different QD-loading concentrations, (B) WGM to envelope emission intensity from emission spectra of microspheres obtained with various loading concentrations, and (C) WGM to envelope emission intensity ratio at 525 nm vs. the corresponding loading concentration.*

Moreover, the I_{WGM}/I_{Env} ratio does not change much with the emission wavelength (λ) for a particular loading concentration which suggests that the Q-factor of the microcavity stays almost constant throughout the range of emission wavelength. For the measurements presented in this work, I have always remained in a concentration range where the I_{WGM}/I_{Env} was optimal. For an optimum range of QD concentrations in the loading infusion, the values of I_{WGM}/I_{Env} stayed within a close range which implies that the QD concentration within this range has very little influence on the Q-factor of the microcavities.

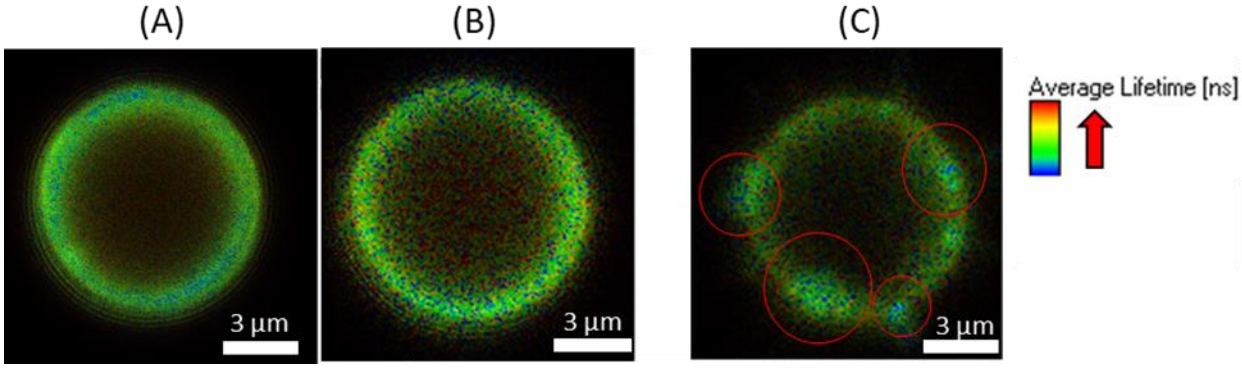

Figure 2.17: *Confocal images (A, B) of microspheres within the loading concentration range of 0.15 μM and 0.3 μM. (B) Confocal image of a microsphere at higher range of concentration (1.15 μM); the red circles indicate some of the QD clusters.*

2.7 WGM POSITIONS: A COMPARISON BETWEEN THE EXPERIMENT AND THEORY

The experimental fluorescence spectra of the QD-microcavities as seen in Figure 2.18 (A), consists of sharp peaks as discussed before. To confirm that these peaks originate due to the resonances occurring inside the microcavity, the positions of the resonances can be numerically calculated considering a system with same size, shape and refractive index as the QD-loaded microcavities. As mentioned in section 2.5.1 for solving equations 2.8 and 2.9 to get the positions of resonances, the method described by Lam et al.[259] can be used where the wavelengths of WGMs of a microsphere of radius *R* can be expressed asymptotically as a function of the angular mode number (l) , radial mode number (n), using the dimensionless parameter $x = 2\pi a/\lambda$:

$$x_{l,n} \sim \nu + a_i \left(\frac{\nu}{2}\right)^{1/3} - \frac{Np}{\sqrt{N^2-1}} + 0.3a_i{}^2(4\nu)^{-1/3} + \frac{N^3 p(2p^2/3-1)a_i}{(2\nu^2)^{1/3}(N^2-1)^{3/2}}, \qquad (Eq.\ 2.19)$$

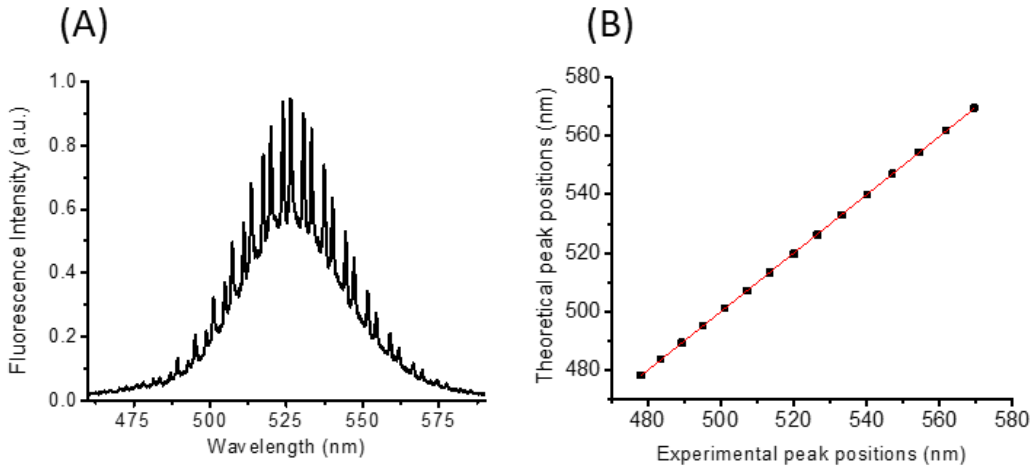

Figure 2.18: *(A) A typical fluorescence spectrum from a QD525 loaded microcavity, (B) theoretical WGM peak positions vs. peak positions from spectrum (A).*

where $\nu = l + \frac{1}{2}$, $N = n_s/n_e$, where *N* is the relative refractive index, n_s and n_e are the refractive indices of the microsphere and the environment solution. $p = 1$ for TE and $p = 1/N^2$ for TM modes, and a_i is the i^{th} zero of the Airy function. Here we only consider $n = 1$ modes, since the widths of higher order modes are much higher and are not distinguishable in our spectra. Assuming a refractive index of 1.33 for the water solution, the series of peaks can be fitted with a unique set of *a* and *N* parameters. For the spectrum

shown in Figure 2.18 (A), for angular mode numbers ranging from 475 nm to 575 nm, this corresponds to a radius of 3.82 µm and a refractive index of 1.798 (see the corresponding theoretical vs experimental peak position in Figure 2.18 (B)). In general, all the fitted radii lie within the 3.5-6 µm range of the distribution of the microspheres. The fitted microsphere refractive indices are all above the refractive index of polystyrene (η_{PS} = 1.59-1.6)[268], which can be attributed to the contribution of the QDs to the effective refractive index of the microsphere outer layer.

2.8 SOME INTERESTING ADVANTAGES OF THE QD-MICROCAVITY:

There are some distinguished advantages of these QD-based microcavities which arise mainly due to the interesting properties and stability of the QDs. Some of the advantages are the following:

2.8.1 Tunable fluorescence of QD-microcavity:

It is possible to load the microspheres with QDs of various emission wavelength and cover a broad range (500-700 nm) of the visible spectrum (Figure 2.19 (A)). The important advantage here is that even though the shape of the envelope or free space emission varies with the original emission profile of the QDs, the quality of the WGMs are equivalent for all of the different populations.

2.8.2 Photostability of the QD-microcavity:

The photostability of the QD-microcavities depend on the stability of the QDs itself. In the wide-field microscope setup, fluorescence intensity of microspheres loaded with QD505 and QD525 under continuous illumination of a white lamp at 450 nm excitation wavelength and 5 W/cm^2 excitation power at the sample plane for 200 seconds, at 10 acquisitions per sec were recorded. The intensity remains at ca. 95% of the initial value, for a period of time enabling 2,000 measurements (Figure 2.19 (B)).

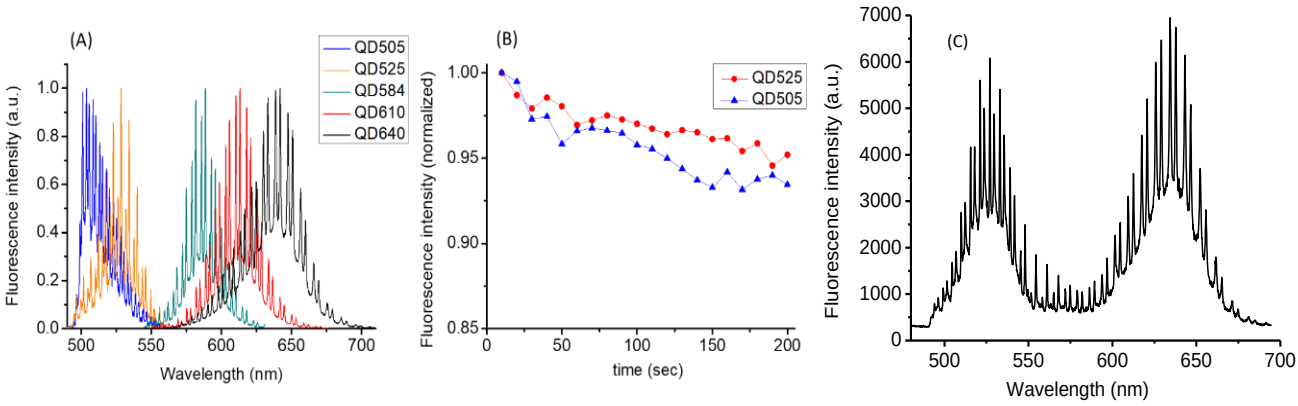

Figure 2.19 *(A) Emission spectra of a microsphere from an equatorial point that is loaded with QDs having emission maxima at (from left to right respectively) 505 nm, 525 nm, 584 nm, 610 nm ad 640 nm. The last three batches of QDs have been synthesized following protocols similar to those described in Yu et al.*[269]*, and Li et al.*[270] *(B) Fluorescence intensity of microspheres loaded with QD505 and QD525 under continuous illumination at 450 nm, 5 W/cm*^{2} *at the sample plane for 200 sec, at 10 acquisitions per second. (C) Emission spectra from the confocal volume on the surface of a microsphere loaded with two batches of QDs (with emission maxima respectively 525 nm and 640 nm).*

2.8.3 Broad emission range from the same microcavity:

Broad range of emission from the same microcavity can be achieved by loading more than one population of QDs into the same microspheres. In Figure 2.19 (C), two different populations of QDs, with emission maxima respectively centered at 525 nm and 640 nm, have been loaded into the same microcavities to obtain a very broad range of WGM emission (500-690 nm).

2.9 Discussion: Controlling the WGM mode intensity:

2.9.1 Leaking of WGMs:

The observation from the emission spectroscopy performed on the confocal microscope suggested possible WGM energy loss due to the direct contact of the microcavity and the glass coverslip as shown Fig 2.20 (A). The high intensity modes may leak through the contact point of glass and polystyrene due to their matching refractive indices, resulting into low I_{WGM}/I_{Env}. To minimize the mode leaking, a layer of agarose gel (thickness 100-300 µm) was applied on the coverslip that would act as a buffer zone between the polystyrene microsphere and the glass, eliminating any possible direct contact (Figure 2.20 (B)). The agarose gel has the same refractive index (η = 1.33) as the surrounding water for the QD-microcavities. This conformation resulted into ~3 times enhancement (averaged over ~ 10 beads for each of the conformations) of the I_{WGM}/I_{Env} ratio as seen in Figure 2.20. The spectra 2.20 (C) and (D) are representatives of the fluorescence emission in the two conformations.

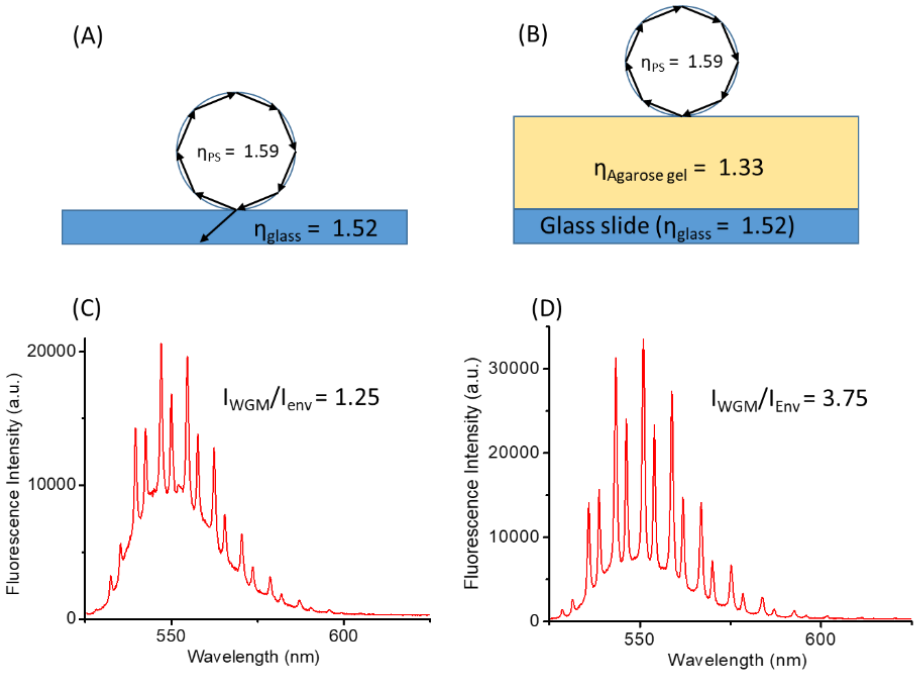

Figure 2.20 *Improving WGM/envelope intensity ratio by using agarose gel: (A) QD loaded microsphere directly on a glass coverslip, (B) when a layer of agarose gel was used as spacer, and (C, D) their corresponding emission spectra from the confocal volume located on the equator of the cavity, respectively.*

2.9.2 Elimination of the WGMs by changing solvent:

As whispering gallery resonances are results of total internal reflections of light at the cavity interface of two different refractive indices, it might be possible to completely eliminate them by matching the cavity refractive index to its surrounding. For this experiment, the surrounding solvent of the QD-microcavity has been changed from water (η = 1.33) to dimethyl sulfoxide (DMSO) (η = 1.48) to get closer to the refractive index of the polystyrene microspheres (η = 1.59). This resulted into the disappearance of almost all the WGMs and only persistent presence of the envelope emission as seen in Figure 2.21 (B).

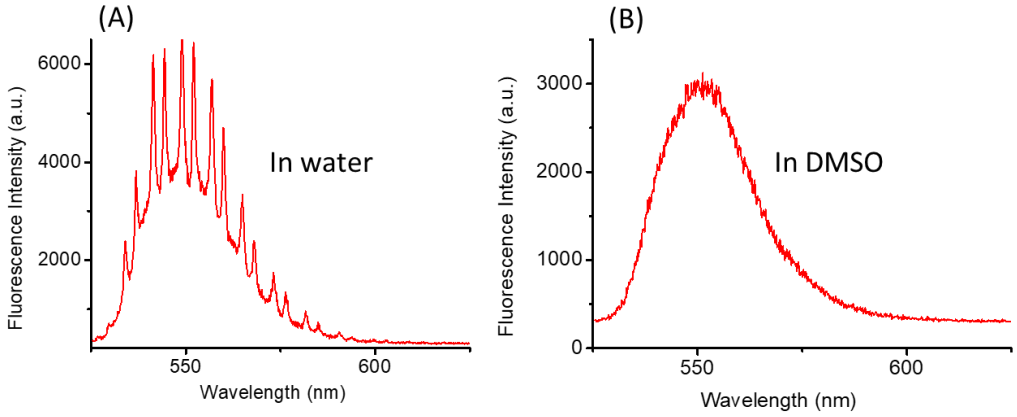

Figure 2.21: *Fluorescence spectra of a QD-microcavity in (A) water and, (B) DMSO*

2.10 CONCLUSION:

In this chapter, we have thoroughly discussed the fabrication process and important opto-electronic properties of the QD loaded optical microcavities. Our final goal is to utilize these microcavities as optical donors (in a system similar to FRET) for energy transfer to perform highly efficient and sensitive biosensing. To do that, it is very important to understand their basic optical and chemical properties at first.

In the beginning of the chapter, we have discussed the synthesis processes of the QDs, followed by their structural and optical characterizations. We then focused on constructing the optical microcavities by placing these QDs as nanoemitters inside PS microspheres. A series of experiments and optical measurements were performed to understand and control the characteristics of WGMs. Spectroscopic characterization revealed the efficient coupling of the quantum dot emission to the modes of the microcavity with high (> 4000) quality factors. We also discussed the fundamental physics behind the cavity resonances to have a clear understanding of the system. These QD-loaded microcavities have shown great photo- and chemical stability, and brightness.

This study will help us to proceed to our next challenge of engaging this QD-microcavities as optical donors in energy transfer experiments and further towards building a bio-sensing scheme.

CHAPTER 3: ENERGY TRANSFER

CONTENTS

3.1 INTRODUCTION:

In the past few years, whispering gallery mode (WGM) microcavities have emerged as a potential candidate for many applications, such as, bio-sensing[27], low threshold lasing[271], sensing of thermal and mechanical changes[272,273], and elements for optics and photonics[274]. The physics behind the characteristics of WGM microcavities have long been studied and well understood, but their development in the field of practical applications is quite recent and still a subject of extensive research. In this chapter, we will discuss the advantages and properties of QD loaded WGM microcavities for long range energy transfer, and how these properties can be exploited for highly sensitive bio-sensing applications. Förster resonance energy transfer or FRET is widely celebrated as one of the cornerstones for fluorescence-based bio-sensing, but these methods come with their own disadvantages inherited to FRET itself. Here, we will side-by-side compare FRET and whispering gallery-mediated energy transfer (WGET) to discover which one is more advantageous in terms of constructing sensitive biosensors. In particular, the success of microsphere WGM sensors relies on the extension of the mode as an evanescent field within a few tens to hundreds of nanometers above the microsphere surface. Many studies have revealed that the efficiency of energy transfer can be enhanced by several orders of magnitude when the donor and acceptor moieties are present inside the same cavity at both small ($<\lambda/10$) or large ($>\lambda/10$) separation[275,177]. In these configurations, energy transfer is not much influenced by the environmental conditions since both the fluorescent species are located inside the microsphere. Here in our configuration, only donors are embedded within the microcavity, and acceptors come from the outside within its evanescent field. This configuration makes it possible, for example, to design assays in which the acceptors bind to the surface of the cavity when a biomolecular target is present, similarly to FRET sandwich assays.

3.2 EFFECT OF A MICROCAVITY ON ENERGY TRANSFER:

The physical nature of the excitation energy transfer mechanism depends on the separation distance (d) of the donor and the acceptor. For long separation distances $(\mathrm{d} \gtrsim \lambda/10)$, the transfer is radiative, coupling being mediated by a real photon. For example, when a donor-acceptor pair resides inside a dielectric microcavity with a high separation distance, a photon emitted by the donor may travel inside the cavity medium to finally reach the acceptor and get absorbed. The high Q-factor of the cavity might increase the probability of reabsorption, often leading to the enhancement of radiative energy transfer process[177]. Whereas, for short separations (typically $\mathrm{d} \lesssim 10\ \mathrm{nm}$), the transfer may occur through FRET, which is a non-radiative process, being mediated by a virtual photon. However, both processes occur through the interactions between the dipole moments of the donor and the acceptor; the radiative transfer takes place through far field dipole interactions; in contrast, the non-radiative FRET proceeds through near field coupling. In many articles, microcavities have been shown to have an effect in energy transfer for both short and long ranges.[176]

In the last 20 years, many experiments have been performed to characterize the effect of photonic environment on energy transfer processes. The outcome of all these experiments, however, do not always point to the same conclusion. Some reports suggest the enhancement of non-radiative FRET whereas other studies found null effect and even suppression of FRET when the donor-acceptor pair is placed in a photonic environment. In an attempt to unify the diverse experimental descriptions, Cortes et al. proposed a general model in 2018 to case-wise understand the effect of photonic, such as dielectric and plasmonic environment on resonance energy transfer[276]. The enhancement of the spontaneous emission of a fluorophore in a photonic environment, characterized by Purcell factor (F_P) have been well understood since its first observation by Edward Purcell in 1940s. However, the effect of dielectric or plasmonic environment on non-radiative energy transfer processes was a matter of debate until recently, which can now be carefully analyzed using macroscopic QED and semi-classical approximations[276,277].

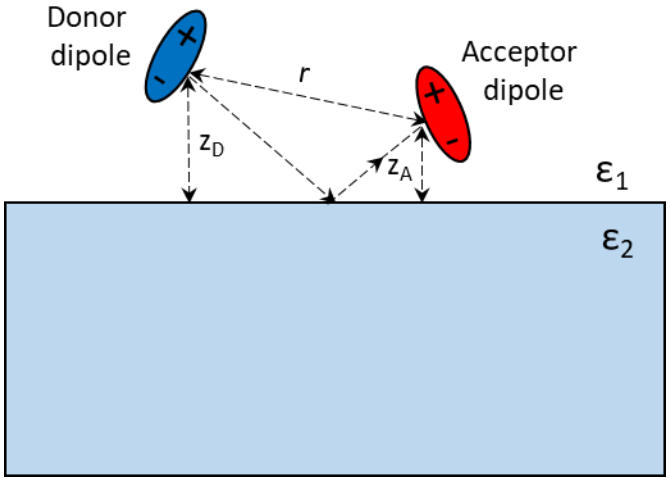

Figure 3.1: *A donor-acceptor (D-A) pair near a dielectric interface with two media having permittivity of ε_1 and ε_2 ($\varepsilon_1 \neq \varepsilon_2$). r, z_D and z_A respectively are the donor-acceptor separation, and their corresponding distances from the interface.*

Let us assume, a donor-acceptor pair is located near a photonic interface of two medium having different permittivity (as seen in Figure 3.1). The rate of spontaneous emission of the donor in that case can be expressed as the following using Fermi's Golden rule and the first order approximation.

$$\Gamma_{D,Rad} = \frac{2\omega_D^2 |p_D|^2}{\hbar \varepsilon_0 c^2} \left[\mathbf{n}_D . \mathrm{Im}\{\bar{\bar{G}}(\mathbf{r}_D, \mathbf{r}_D; \omega_D)\} . \mathbf{n}_D\right], \qquad (Eq. 3.1)$$

where ω_D is the radial frequency, ε_0 is the permittivity of free space, c is the speed of light, $\hbar$ is the reduced Planck's constant, $\{\bar{\bar{G}}(\mathbf{r}, \mathbf{r}; \boldsymbol{\omega})\}$ is the classical dyadic Green function related to the electric field dipole, and $\boldsymbol{\mu}_D = p_D \mathbf{n}_D$ represents the donor dipole moment. The subscript D stands for the parameters of the donor. However, the spontaneous emission rate depends on the PMDs of the photonic environment quantized by partial local density of states (LDOS). The Purcell factor is used to quantify the enhancement of spontaneous emission, thus can be given as;

$$F_P = \frac{\Gamma_{D,Rad}}{\Gamma^0_{D,Rad}}, \qquad (Eq. 3.2)$$

where, $\Gamma^0_{D,Rad}$ represents the donor radiative emission rate in free space. Quantum yield (Q_D) of the donor, that is defined as the ratio of radiative decay rate to the total decay rate (radiative + non radiative) of the donor, can also be related to the F_P. Thus, the overall enhancement of the spontaneous emission enhancement can be given as;

$$\frac{\Gamma_D}{\Gamma_D^0} = (1 - Q_D) + Q_D F_P \, . \qquad (Eq.\ 3.3)$$

On the other hand, assuming a semi-classical picture for non-radiative FRET that occurs through near-field dipole-dipole coupling between a donor and an acceptor, the rate of FRET can be given as the following;

$$\Gamma_{ET} = \frac{2\pi}{\hbar} \int d\omega \, |V_{EE}(\omega)|^2 \sigma_D(\omega) \sigma_A(\omega) \, , \qquad (Eq. 3.4)$$

where $\sigma_D(\omega)$ and $\sigma_A(\omega)$ represent the single-photon emission and absorption spectra of the donor and acceptor, V_{EE} is the term signifying resonant dipole-dipole interaction (RDDI) which is an analogous expression to LDOS but represents the magnitude of FRET dipole-dipole coupling, here the subscript EE stands for electric field components of the two dipoles. V_{EE} can also be written as the following;

$$V_{EE}(\mathbf{r}_A, \mathbf{r}_D; \omega) = -\frac{\omega^2}{\epsilon_0 c^2} \boldsymbol{\mu}_A . \bar{\bar{G}}(\mathbf{r}_A, \mathbf{r}_D; \omega_D) . \boldsymbol{\mu}_D \, . \qquad (Eq. 3.5)$$

It can be understood simply by considering that the electromagnetic field emitted by the donor can reach the location of the acceptor through free-space or via an intermediate interaction with the surrounding photonic environment (e.g., reflection on a dielectric interface, see Figure 3.1). The final electromagnetic field at the acceptor locations may either be enhanced or suppressed by the interaction with the photonic environment, leading to acceleration or deceleration of the energy transfer rate. Analogous to the Purcell factor, the enhancement in case of FRET can also be characterized as F_{ET}.

$$F_{ET} = \frac{\Gamma_{ET}}{\Gamma_{ET}^0} \qquad (Eq. 3.6)$$

So the total decay rate of the donor in the presence of the acceptor and in a photonic environment can be given as the expression 3.7.

$$\Gamma_{DA} = F_P \Gamma_{D,Rad}^0 + F_{ET} \Gamma_{ET}^0 + \Gamma_{D,Non-rad} \, , \qquad (Eq. 3.7)$$

where the first term is associated to the modified spontaneous emission and the second one denotes modified FRET rate, and the last term signifies non-radiative decay of the donor which is independent of the environment. Apart from the modification of the donor radiative decay rate, the non-radiative FRET rate and the acceptor's radiative decay rate are also modified due to the presence of the interface[278]. Whether the rate of FRET will be enhanced or suppressed or remain unchanged in the presence of a

photonic surrounding depends on various factors such as the permittivity (both the real and imaginary parts) of the two medium, and location of the donor-acceptor pair with respect to the interface. Additionally, the efficiency of FRET is given by the ratio of energy transfer rate to the total relaxation rate of the donor excited state. The enhancement factor (F_{Eff}) for FRET efficiency in photonic environment can be given as;

$$F_{Eff} = \frac{E}{E_0} = \frac{F_{ET}}{F_{ET}E_0 + [(1 - Q_D) + Q_D F_P](1 - E_0)} \qquad (Eq. 3.8)$$

Where E and E_0 respectively are the FRET efficiency with and without a photonic environment. With other parameters known, it is possible to deduce whether the FRET efficiency will increase or not in a photonic environment. However, the FRET efficiency can be enhanced even if $F_{ET} < F_P$ if the initial donor quantum yield is particularly low.

How does this translate in situations when the donors and acceptors are located within a microcavity, and, in particular, interaction with WGMs? Druger et al. first provided experimental evidence of enhanced long range radiative energy transfer between Coumarin-1 donors and Rhodamine 6G acceptors placed inside a single glycerol aerosol particle of ca. 10 µm in diameter[275]. They observed more than 5 times enhancement in the acceptor emission compared to the bulk system. According to their model, this enhancement of the acceptor luminescence is a consequence of the long-range energy transfer that occurs when the donor emits a photon into a cavity resonance mode which is damped through the absorption by the acceptor.

The influence of microcavities on FRET was first experimentally demonstrated by Barnes et al. In this report, they fabricated optical cavities where the donors (Eu^{3+} complex) and acceptors (tetramethylindocarbocyanine based dye) were deposited in separate layers of particular thickness, and monolayers of 22-tricosenic acids were used as spacers in between so that the donor-acceptor separation distance can be precisely fixed within the FRET range.[177] When this donor-acceptor layers were encapsulated inside a full silver mirror cavity configuration, the enhancement of acceptor emission accompanied by faster decay of the donor excited state were observed. In addition, these changes also depend on the separation distance of donor-acceptor layers, which is a classic signature of non-radiative FRET process. This enhancement of short-range energy transfer processes was attributed to the alteration of PMDs at the cavity interface.

In a recent study, Kushida et al. fabricated π-conjugated polymeric microspheres of energy-donating and energy-accepting polymers and their blends. First, they reported energy transfer from donor to acceptor species within the same microsphere doped with both donor and acceptor chromophores. Then they prepared microspheres doped with only donor, blend of donor and acceptor, and only acceptor and coupled them respectively side-by-side; long range propagation of WGMs (> 10 µm) occurs through the contact points of the microspheres converting the color of photoluminescence while maintaining WGM characteristics as shown in Figure 3.2.[279]

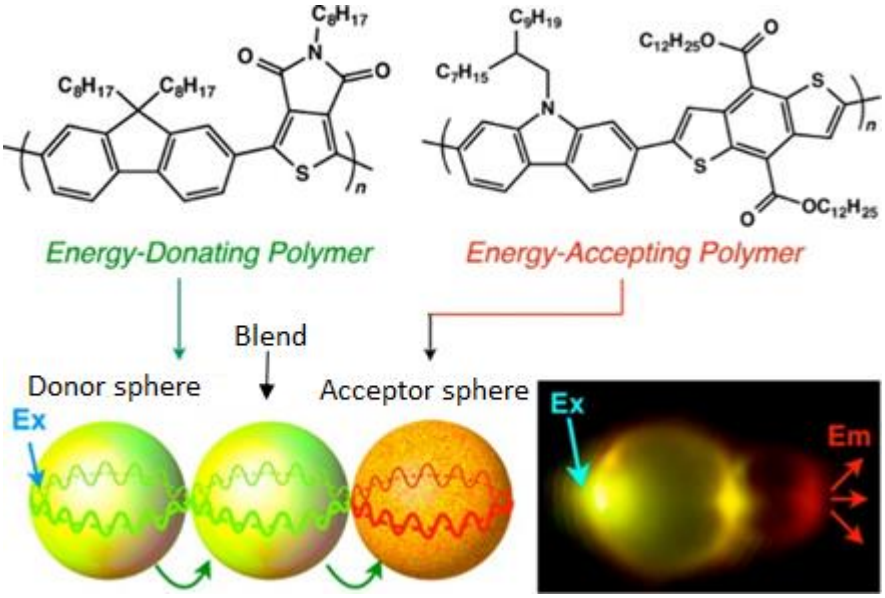

Figure 3.2: *Whispering gallery mode mediated energy transfer between microspheres made of π-conjugated energy donor and acceptor polymers*[279].

In all the above-mentioned studies, energy transfer occurs between donor and acceptor species located within the same microsphere at high concentration. In these configurations, energy transfer is not very sensitive to environmental conditions since the concentration and location of both fluorescent species are fixed. In order to enable sensing, either of the donor or the acceptor chromophore should have the flexibility to couple or decouple itself to/from the cavity upon an external stimulus, thus conditionally take part in the cavity enhanced energy transfer. This kind of configuration would allow us to provide biological selectivity to one of the chromophores so that this phenomenon can be harnessed for designing a sensitive and selective bio-sensing tool.

3.3 Rationale behind the whispering gallery mediated-energy transfer (WGET):

In a common FRET system, the rate of energy transfer is proportional to the sixth power of the separation distance between the donor and the acceptor that only allows efficient energy transfer to occur within the typical range of 10 nm. Optical microcavities with high quality factors are exceptional in confining light via total internal reflections[280]. The trapped electromagnetic radiation is distributed among many whispering gallery modes of the cavity. In the context of the final motivation of biosensing, our interest lies in the system where the QD donors are placed inside the microcavity (within a few hundreds of nanometers from the surface) where part of the QD emission couples to the WGMs as shown in the previous chapter, and fluorescent acceptors are present within close proximity outside of the cavity surface. The whispering gallery modes, which extend as an evanescent field outside the surface of the microsphere, can also engage in energy transfer to or from fluorescent analytes present in the vicinity of the microspheres. In general, the field decays exponentially, typically extending up to a few tens to hundreds of nm normal to the surface of the resonator.[135] Thus we expect that the distance range upon which energy transfer may occur with WGM microcavities will be much larger than that of FRET.

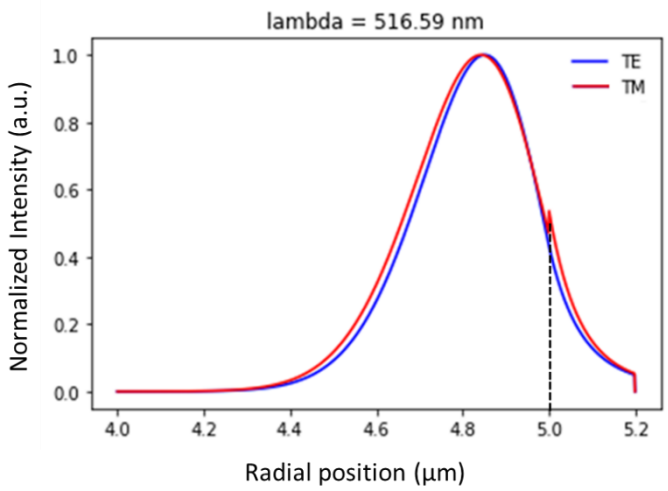

Figure 3.3: *Intensity distribution of a TE and TM whispering gallery mode along the radial axis of a 10 µm sized microcavity. The vertical dashed line represents the cavity interface.*

3.4 THE VARIATION OF THE WGM DECAY LENGTH:

How far the WGM extends outside the surface of the microcavity plays a major role in the sensitivity of it if to be used as sensor. The characteristic decay length of the WGM evanescent field depends on many parameters of the microcavity such as the size, refractive index, and the wavelength of the mode. The evanescent field extension length can be extracted from the intensity profiles outside of the microspheres.

The electric field ($\vec{E}$) for both the TE and TM modes can be calculated using the equations in chapter 2 (Section 2.5, Equation set 2.4 and 2.5). The WGM intensity profiles as a function of the distance from the center of microcavity (r), and mode numbers (l and m) can be calculated using the relation 3.9. Figure 3.3 depicts, in a situation similar to our experimental conditions, how the electric and magnetic field of a polystyrene microcavity of 10 µm size (mode numbers n=1, l=88) decay as a function of the radial position. Following the model presented in the previous chapter (Section 2.5, Equation set 2.4 and 2.5) both the electric and magnetic field reach the highest intensities at the position slightly below the cavity interface and extend further out from the surface but up to only a few hundreds of nanometers. How far the modes can travel is limited by several factors, such as the size, and relative refractive index of the microcavity and also the wavelength of the radiation[258]. The intensity profile outside the microsphere then can be fitted with a monoexponential decay (e^{-r/r^*} where r^* is the characteristic decay length) to extract the penetration depth of the mode.

$$I_{lm}^{TE,TM}(r) \propto \left|\vec{E}_{lm}^{TE,TM}(r)\right|^2 \qquad (Eq.3.9)$$

Figure 3.4 (A) shows how the penetration depth varies with the size of the microsphere. Here, the radius of the microcavity was varied from 4 µm to 8 µm, while considering modes with a wavelength within the 510-515 nm range. The mode number changed between l=70 to l=145 depending on the radius of the microcavity.

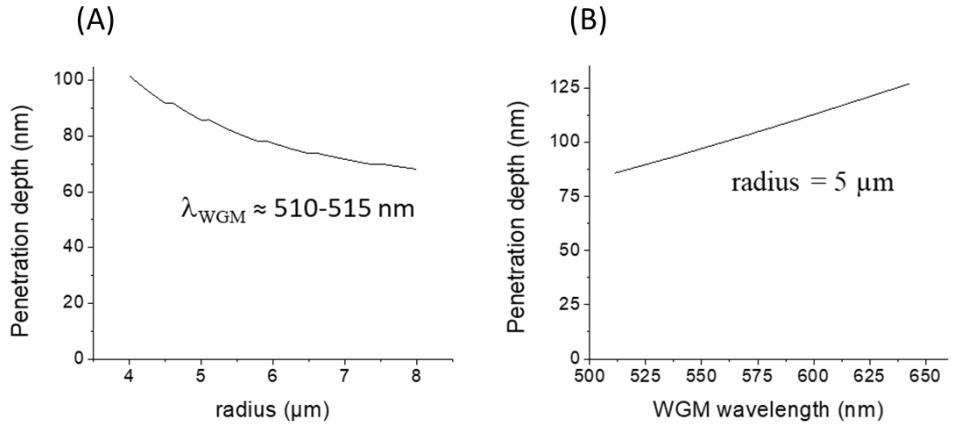

Figure 3.4: (A) *Penetration depth of a WGM vs. the radius of the microsphere,* ***(B)*** *Penetration depth vs. the WGM wavelength for a 10 μm sized microsphere.*

In Figure 3.4 (B), it can be seen how the penetration length of the evanescent field varies with the wavelength of the WGM. In this case, the microsphere radius is fixed at 5 μm and the mode number is varied from l = 70 to l = 89.

In both scenarios, even though the WGM decay length changes slightly with various characteristic parameters of the microcavity, still it stays within a close range (70 nm - 125 nm for the microspheres used in our experiments) which is many times higher than the typical FRET range.

To conclude, the extended evanescent tail of WGMs can engage in energy transfer in a much larger range (up to a few hundreds of nanometers) which is compatible for sensing very large biological assemblies. Thus it is of greater interest to build biosensors based on WGM microcavities. In later sections, we will thoroughly compare these two processes side by side to find their advantages and disadvantages.

3.5 INSIGHTS INTO THE WGET DONOR-ACCEPTOR PAIR:

An important step towards building a WGET based bioassay is to choose a suitable pair of donor and acceptor. In the previous chapter, we have introduced fluorescent QDs as optical donors and also thoroughly discussed the fabrication process of the QD loaded microcavities, where the emission of the QDs is efficiently coupled into the modes of the cavity. The desired properties that should be possessed by an ideal WGET acceptor are the follows,

(A) Similar to donor-acceptor pairs in FRET, there must be a **significant spectral overlap** between the donor emission and the absorption of acceptor moieties for WGET to occur.

(B) Acceptors with **high absorption cross section** or **molar extinction coefficient** are better at absorbing light, facilitating the energy transfer process.

(C) Fluorescent acceptors that have **high quantum efficiency** allow sharp and more efficient signal transduction. Additionally, **photostable** acceptors are advantageous for performing long experiments.

Organic dyes, fluorescent nanoparticles are suitable candidates to be used as WGET acceptors. In a recent work by Yuan et al., interfacial WGET has been demonstrated in liquid crystal micro-droplets where green emitting organic dye, Coumarin 6 was loaded inside the droplets to act as optical donor and various other organic dyes, such as, Texas Red,Rhodamine 6G, Rhodamine B isothiocyante, and R-phycoerythrin were used as acceptor moieties (see Figure 3.5)[188]. In the following section, the acceptor moieties that have been used for the experiments performed in this thesis will be introduced.

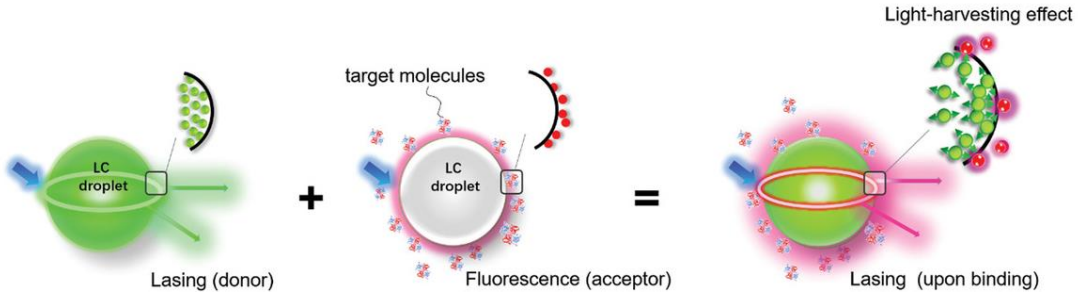

Figure 3.5: *Interfacial cavity energy transfer (WGET) in a liquid crystal micro-droplet*[188].

3.6 Optical Acceptors: Polymeric Dye Nanoparticles

Before the significant development in the field of QDs and nanoparticles, organic dyes have dominated as both FRET donors and acceptors. For sensitive bio-detection or single molecule sensing, the brightness of organic dyes is limited by molar extinction coefficients below 3×10^5 $M^{-1}cm^{-1}$ and quantum yield below unity. Therefore, the use of very high excitation power and smaller detection volume is unavoidable to achieve a good signal-to-noise ratio. Higher excitation power can also cause the organic dyes to photobleach quickly, resulting into short experiment spans. To improve the performance and stability of organic dyes, another approach has been explored by the "Nanochemistry and bioimaging" group at the University of Strasbourg.

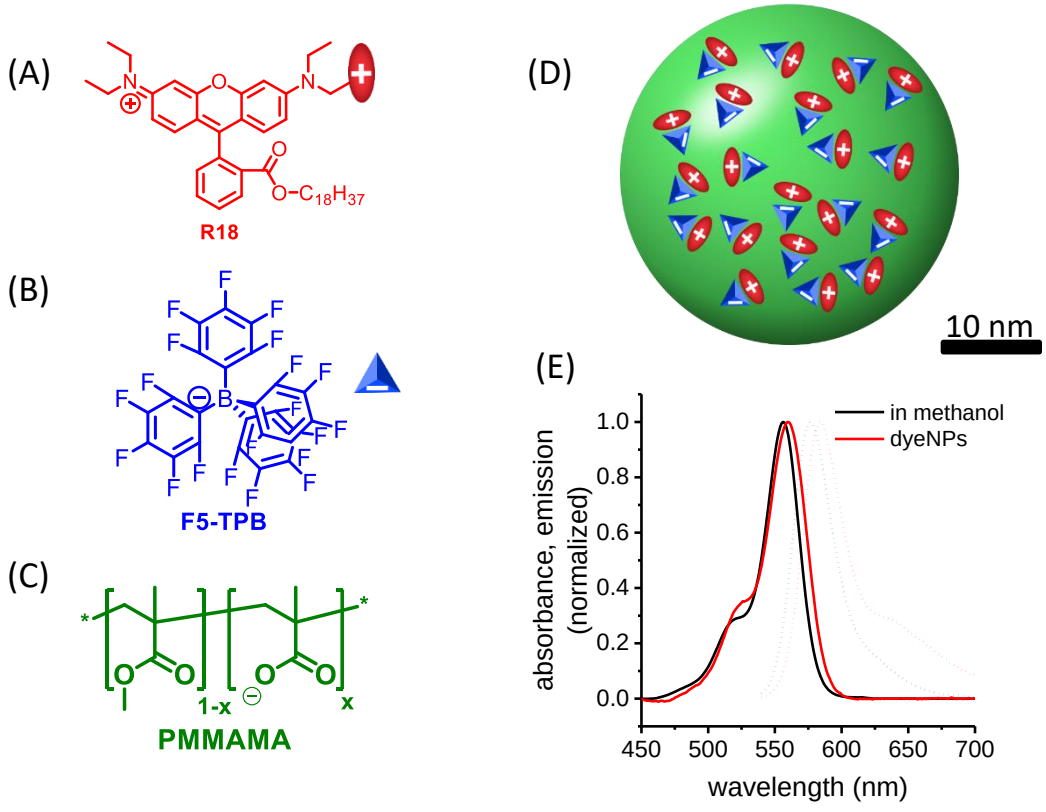

Figure 3.6: *The chemical structures of (A) rhodamine B octadecyl ester (R18) dye, (B) tetrakis (pentafluorophenyl) borate counter ion, and (C) poly (methyl methacrylate-co-methacrylic acid). (D) The schematic structure of the dye NP showing the dye-counterion complexes encapsulated inside. (E) Normalized absorption and emission spectra of R18/F5-TPB in methanol and R18/F5-TPB loaded dyeNPs. Emission spectra were recorded using an excitation at 530 nm.*

❖ The structure and optical properties of polymeric dye nanoparticles (dyeNPs):

The dyeNPs were synthesized through nanoprecipitation of poly (methylmethacrylate-co-methacrylic acid) (PMMAMA) together with the salt of a rhodamine B octadecyl ester (R18) with a bulky hydrophobic counterion, tetrakis(pentafluorophenyl)borate (30 wt% loading relative to the polymer) (see Figure 3.6). The use of bulky counterions as spacers and high loading concentration of the Rhodamine dyes ensure that short inter-dye molecular distance (ca. 1 nm) be achieved.

These dyeNPs have a hydrodynamic diameter of 60 ± 4 nm with polydispersity index of 0.11, as measured by dynamic light scattering (DLS). The dyeNPs incorporate about 3000 dye molecules per particle (based on their core size of about 35 nm, as determined previously by TEM, and their loading).[281] This results in a per particle absorbance of about 3.7×10^{8} $M^{-1}\cdot cm^{-1}$. The use of the hydrophobic, bulky counterion prevents aggregation of the dyes, as indicated by the absorption spectrum approaching that of the dye in organic solution, though a red shift of the emission spectrum was observed (see in Figure 3.6 (E)). The insulation of the dyes through bulky counterions allows maintaining a high quantum yield (QY) even at very high loadings,[281,282,283] which was determined here to be 36 ± 5%, resulting in a per particle brightness of 1.3×10^{8} $M^{-1}\cdot cm^{-1}$.

3.7 Assembling the donor (microcavity) - acceptor (dye Nanoparticles) system:

Before setting out on the journey to explore the possibilities of using WGET for biosensing, it is of great importance to thoroughly understand various aspects of this energy transfer process. Previously, the QD-microcavities have already been introduced as optical donor, and highly absorbing and bright dyeNPs are chosen to be used as optical acceptors. To construct and study a simple whispering gallery mode-mediated energy transfer system, the dyeNPs were conjugated to the surface of the QD-microcavity *via* electrostatic assembly.

As shown in Figure 3.7 (A), the QD525 and QD505 loaded microcavities were first coated with polyethyleneimine (PEI, MW = 1800 g/mol) to provide a positively charged surface. To do that, the QD-loaded beads (10^{6}) were incubated for 2 h in 500 µL aqueous solution of PEI (10 µg/mL) at room temperature. The sulfonate (SO^{3-}) groups on the surface of the microspheres help the positively charged PEI to be adsorbed.

The positively charged microspheres can be separated from the free PEI molecules by first adding 1.5 mL ethanol to the solution and then centrifuging at 3000 g for 5 mins. The solid sediment of microspheres then can be resuspended in water (volume 500 µL).

The PMMA-MA surface of the dyeNPs provides residual negative charges to them. Mixing the positively charged microspheres with the negative charged dyeNPs enables adsorption of the smaller dyeNPs on the surface of the microcavities. For the experiments in this chapter, the typical volumes of dyeNPs that were used range from 5 µL to 100 µL at 0.04 g/L for each 100 µL suspension (containing ca. 2×10^5 microspheres) of positively charged microcavities. The microspheres then were separated from the unbound dyeNPs by centrifuging at 2000g for 5 s and redispersed into water.

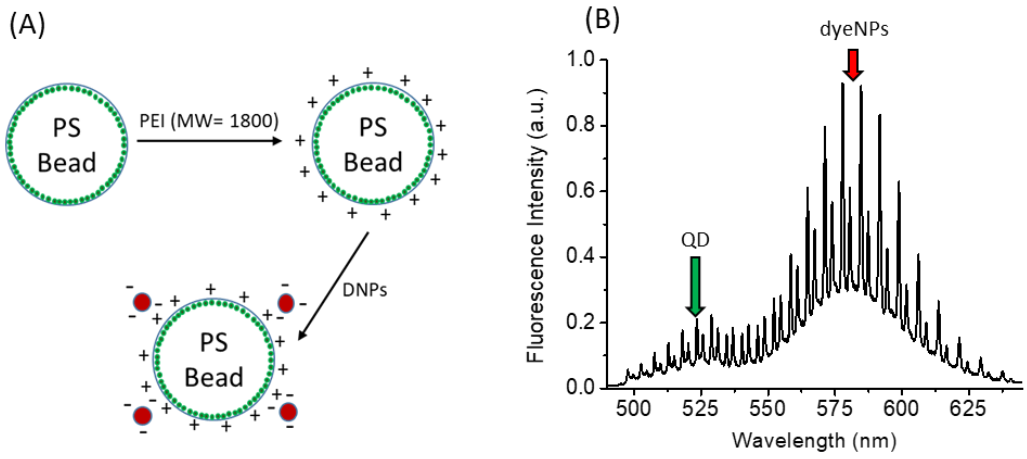

Figure 3.7: (A) *Electrostatic assembly of dyeNPs on QD-microcavities,* ***(B)*** *Typical fluorescence spectra from the confocal volume at the equator of a dyeNP + QD-microcavity donor-acceptor system.*

3.8 FLUORESCENCE EMISSION OF MICROCAVITY-DYENPS CONJUGATES:

After the electrostatic conjugation of acceptor dyeNPs on the surface of QD-microcavities, their optical properties were studied using a combination of confocal microscope and spectrophotometer (set up details in chapter 2, section 2.4.1.1). Fluorescence emission spectra were recorded using a laser (wavelength = 405 nm) to excite the confocal volumes on the equator of the microcavities. The spectrum

in Figure 3.7 (B) has been acquired from a QD525-microcavity conjugated to acceptors, consists of regularly spaced pairs of sharp WGM peaks on the top of a broad free space emission envelope. But the spectrum has now two different emission regions; the one around ca. 525 nm arises from the emission of the QDs, and the other one around ca. 580 nm comes from the dyeNPs.

On the wide-field microscope setup (section 2.4.1.2), a white lamp and a set of appropriate filters (see the filter descriptions later in Table 3.1) were used to excite and observe the emission of the QDs inside the microspheres which appeared green with bare eyes, but weaker than the microspheres without any acceptor. When the microcavities were observed through the emission channel for dyeNPs fluorescence, they showed strong red emission.

3.9 WHAT EXCITES THE DYE NANOPARTICLES? DIRECT EXCITATION OR ENERGY TRANSFER:

The emission spectra (see Figure 3.7 (B)) acquired from QD-microcavity + dyeNPs systems showed a strong red emission from the dyeNPs. There are two major possibilities regarding how the acceptor dyeNPs were excited which are the following,

- Direct excitation by the lamp or laser.
- Energy transfer from the QDs to the acceptors.

I performed three different experiments with the motivation to understand and evaluate this question.

3.9.1 Experiment 1: Comparing the total dyeNP emission in the absence or presence of QDs, at the single microsphere level, by spectrometry

To find out which one causes the excitation of the dyeNPs, we compared the fluorescence intensity of individual microspheres with and without QDs, coated with the same amount of dyeNPs and illuminated by the same laser intensity.

For the experiment, 100 µL (containing ~ 2×10^5 microspheres) of PEI coated QD505-microsphere suspension were incubated with 50 µL of 0.04 g/L dyeNP solution for 2h. After the assembly, the microspheres were purified and redispersed in 150 µL water as described in the section 3.7. The same procedure was followed to prepare microcavities coated with same amount of dyeNPs but without QDs.

Then, using a confocal microscope, fluorescence emission from the confocal volumes located at the equator of microspheres were recorded for both the samples, with and without QDs. The emission spectra from ~20 microspheres for each sample were averaged and plotted in Figure 3.8. Despite some variation in the dyeNP adsorption from one microsphere to another, Figure 3.8 clearly shows that the dyeNP fluorescence intensity is much higher in the presence of QD donors (red curve) than in absence of QDs (black curve), suggesting that dyeNP emission originate from energy transfer.

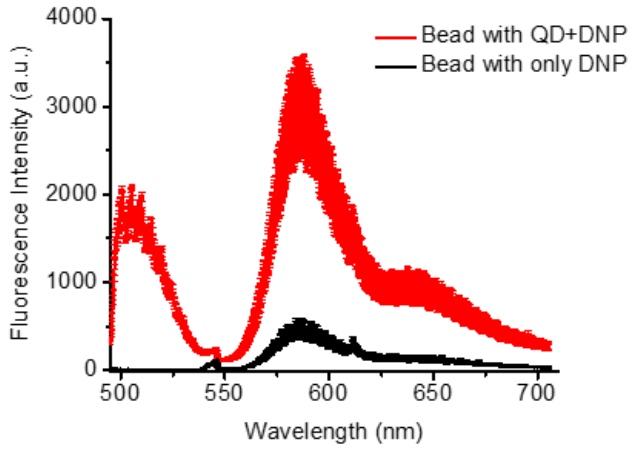

Figure 3.8: *Average fluorescence spectra of microspheres with and without QDs (QD 505) but with same amount of adsorbed dyeNPs.*

3.9.2 Experiment 2: Comparing the direct excitation and sensitized dyeNP emission in the absence or presence of QDs, at the single microsphere level, using fluorescence microscopy

Another experiment was performed to verify that the dyeNP emission mainly originate from energy transfer and not direct excitation. We prepared three different sets of microspheres, labeled only with QDs, only with dyeNPs, and with both QDs and dyeNPs. Figure 3.10 shows fluorescence microscopy images of these microspheres acquired with filter setting chosen to selectively excite and detect QDs (donor channel, left column), excite and detect dyeNPs (acceptor direct excitation channel, middle column), or excite QDs and detect emission from dyeNPs (energy transfer channel, right column). The wavelength ranges of these filters are the following:

Filter cubes	Excitation (nm)	Dichroic (nm)	Emission (nm)
QD direct: QD→QD	425-60	485	505-40
Dyedirect: dyeNP→dyeNP	560-55	595	645-75
Energy transfer: QD→dyeNP	435-40/25	565	LP590

Table 3.1: *List of filter sets with the wavelength cut offs.*

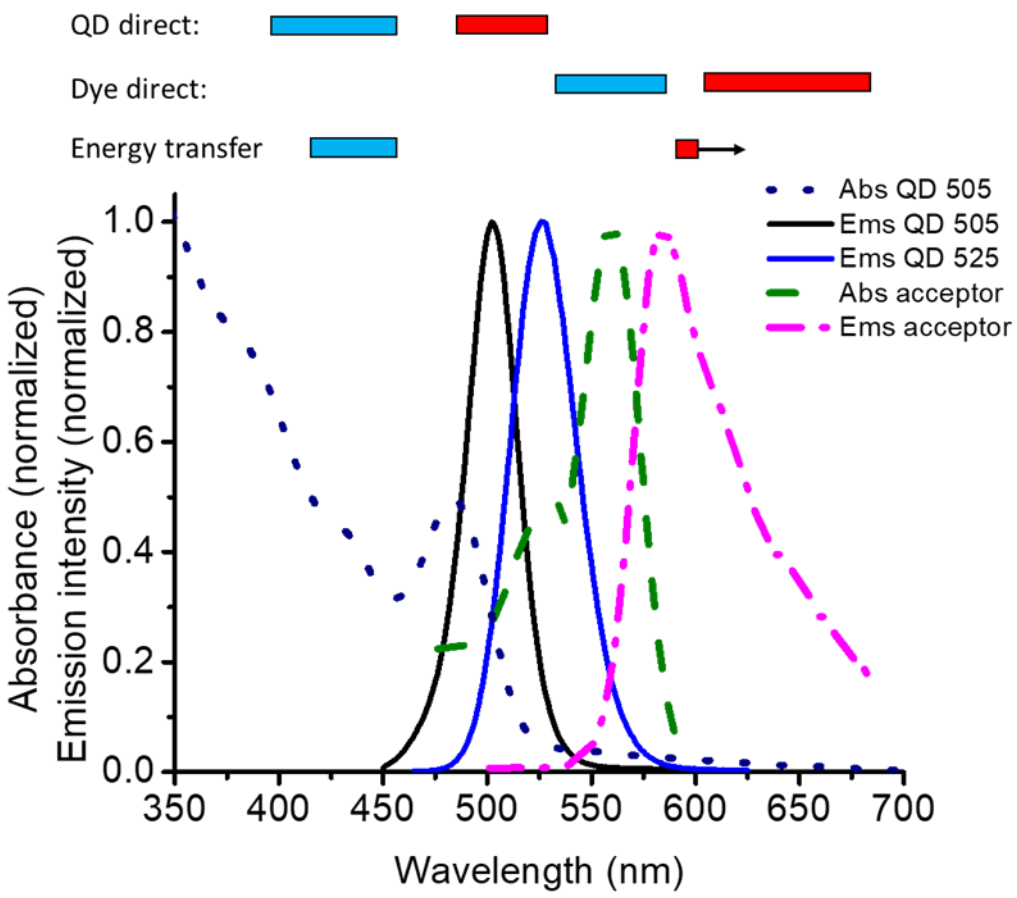

Figure 3.9: *In spectra (from left to right) absorption spectra of QD505, emission spectra of QD505, QD525, absorption and emission spectra of dyeNP. On top, filter channel ranges corresponding to QD direct, dye direct, and energy transfer (excitation in blue and emission filter in red)*

For the sake of easy visualization, the wavelength ranges of excitation and emission filters for all the filter sets are superimposed with the absorption and emission spectra of the QDs and the dyeNPs in the Figure 3.9.

The observation of microspheres labeled with only QDs or only dyeNPs (Figure 3.10, upper two rows) shows minimal contributions from emission cross-talks and dyeNPs direct excitation. Finally, acquisition of images from microspheres labeled with both QDs and dyeNPs (Figure 3.10, bottom row) shows a strong

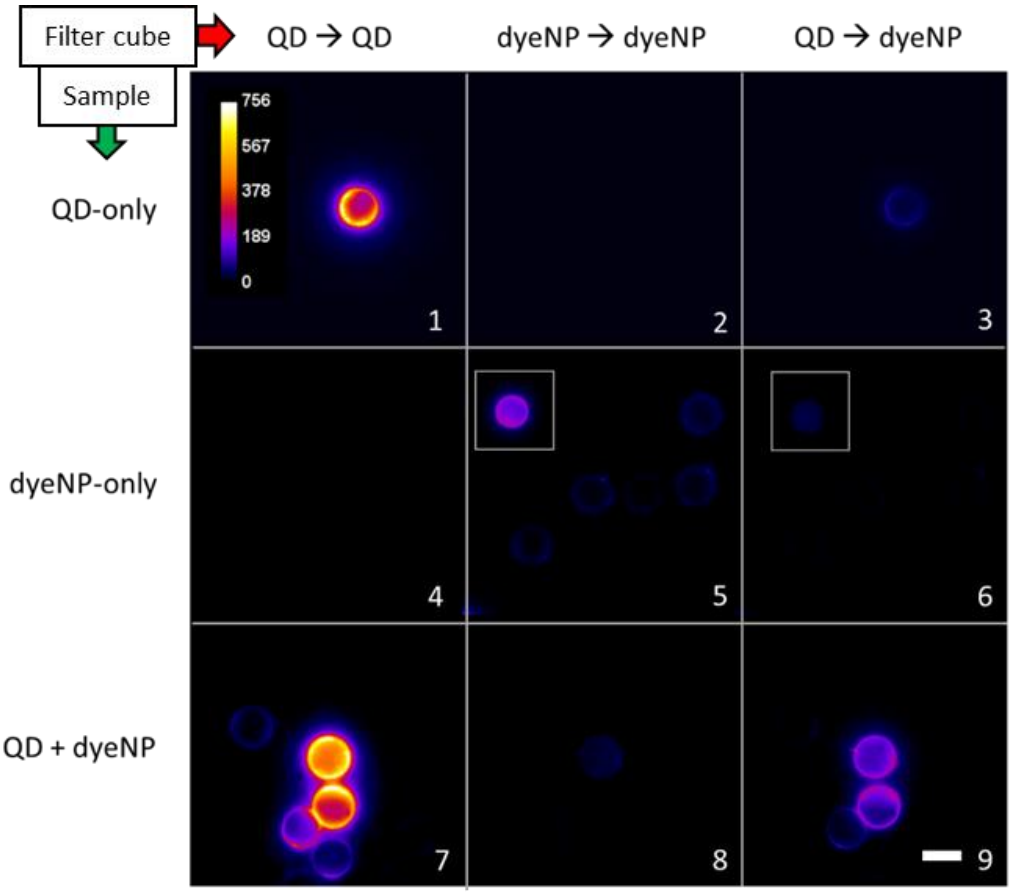

Figure 3.10: *Fluorescence microscopy images of microspheres loaded with QD only (top row), adsorbed dyeNP only (middle row) and both QD and dyeNP (bottom row). The images in the first column (1,4,7) were acquired by exciting and detecting the QD fluorescence, whereas images in the 2nd column (2,5,8) were acquired by exciting and detecting the dyeNP fluorescence and images in the 3rd column (3,6,9) were acquired by exciting the QD and detecting fluorescence from the dyeNP. (The insets in panels 5,6 shows a bead coated with 10 times more dyeNP for clarity.) Scale bar: 10 µm.*

emission in the energy transfer channel. Direct excitation of dyeNPs (panel 8) is minimal compared to the sensitized emission (panel 9). This confirms that the observed emission from dyeNPs in the QD+dyeNPs microspheres indeed originate from energy transfer from QDs, not from direct dye excitation.

3.9.3 Experiment 3: What happens if we change the refractive index of the cavity environment?

The energy transfer from the donor QDs to the acceptor dyeNPs can happen in a combination of two different pathways which are the following,

- Through the evanescent field of propagating WGMs.
- Via direct FRET from the QDs to the dyeNPs at the microcavity interface. As FRET only occurs in between fluorophores present within close range (< 10 nm), QDs that are located within a few nanometers from the surface may engage in direct FRET to the acceptors.

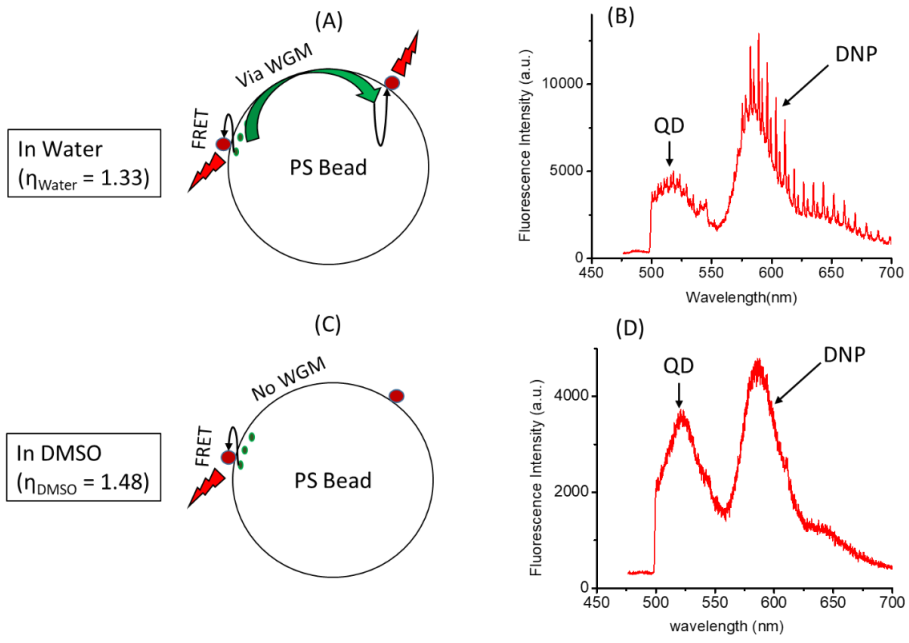

Figure 3.11: *(A, C) QDs to dyeNPs energy transfer mechanisms when the microspheres are in water and DMSO respectively, (B, D) Fluorescence emission spectra from the confocal volume on the equator of a QD microsphere + dyeNP system in water and DMSO respectively.*

An experimental attempt was made to separate the contribution of each process, WGET and direct FRET, in the total energy transfer rate. At first, the QD525-microspheres conjugated to dyeNPs was prepared in water using the same protocol of experiment 1.

Fluorescence emission spectra were recorded using a confocal microscope as described before. Then the solution of the microspheres was centrifuged at 2000g for 10 s so that the cavities sediment. The surrounding water medium ($\eta = 1.33$) of the QDs-microcavity + dyeNPs then was removed and replaced with the same volume of DMSO ($\eta = 1.48$). This will completely suppress the WGMs, so that the energy transfer can happen through only direct FRET (see Figure 3.11). This could help us to understand the influence of each process, but the experiment was inconclusive as even though the QD-microcavity system is chemically stable in DMSO, the polymeric shell of the dyeNPs would dissolve in the organic solvent, resulting in the leaching of dye molecules into the solution.

3.10 Origin of the WGM peaks: Comparison between the experiment and theory:

To verify that the WGM peaks in the spectral region of dyeNP emission have emerged due to the coupling of dye fluorescence to the modes of the same microcavity, we can compare the experimental peak positions to the ones obtained from the theory. As described in previous chapter, Lam et al. analytically expressed the wavelengths of WGMs of a microsphere of radius *R* asymptotically as a function of the angular mode number l, radial mode number n. (See section 2.7, chapter 2).

As the higher order modes are not distinguishable in the spectra (Figure 3.12 (A)), we only consider $n = 1$ modes. The best fit for the WGM peaks in the whole emission range can be obtained with a unique set of R and n_s parameters. For the spectrum shown in Figure 3.12 (A), the best fit (see Figure 3.12 (B)) can be achieved for the value of radius = 4.9 μm and refractive index = 1.593, for angular mode numbers in between 500 nm and 620 nm. It suggests that the WGMs in the dyeNP emission indeed originate from the same set of WGMs.

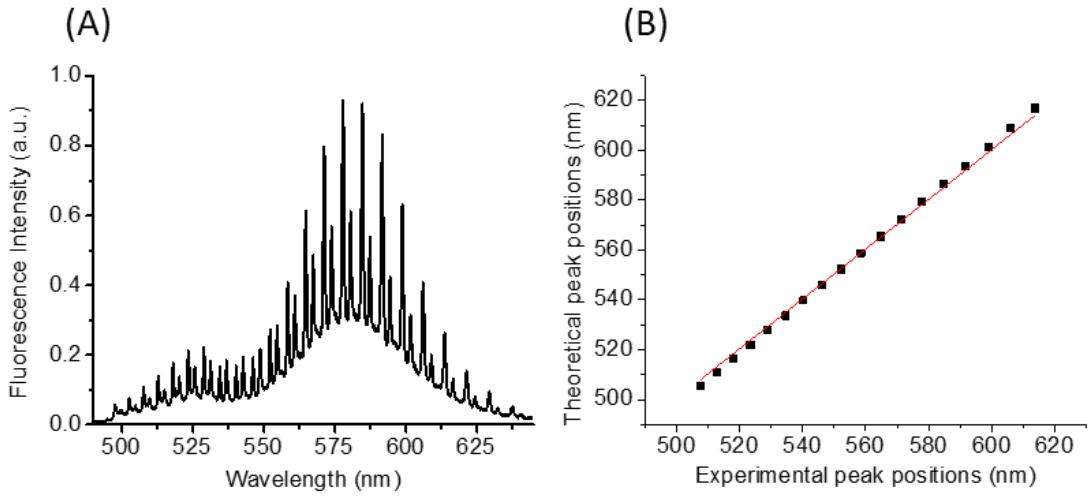

Figure 3.12: *Emission spectrum of a microsphere loaded with (A) QD525 and dye NPs, obtained from a point at the equator. The graph, (B) represents the comparison of theoretically predicted WGM peak positions vs. experimental peak positions corresponding to spectra (A). The best fit parameters for both dye NPs and QD 525 loaded microsphere are refractive index = 1.593 and radius = 4.9 µm.*

3.11 Characterization of WGET:

We have successfully demonstrated the energy transfer from the QD emission coupled to the WGMs of polystyrene microcavities to acceptor dyeNPs. In order to build a bio-sensing platform based on this, it is of great importance to first thoroughly understand and quantitatively characterize this energy transfer process.

We now set out to analyze in more detail the energy transfer rates and efficiencies. The rate of energy transfer, Γ_{ET}, depends on several factors of the donor-acceptor WGET system, such as the absorption cross section of the acceptor, the density of acceptors within the evanescent field, mode volume and the intensity of the mode at the acceptor position. Before getting into the details to calculate the energy transfer rate, some of the important parameters should be discussed.

3.11.1 Mode volume (V_{mode}):

The energy stored in a mode can be calculated as a product of mode volume (V_{mode}) and the maximum intensity of that particular mode. Thus, the mode volume is defined as the ratio of total energy stored inside the cavity for a particular mode and the maximum energy density of that mode. V_{mode} can be expressed as in Eq. 3.10.

$$V_{mode} = \frac{1}{M} \iiint_{\mathbb{R}^3} \left(\frac{\varepsilon(r)}{2} \left|\left|E(r)\right|\right|^2 + \frac{1}{2\mu(r)} \left|\left|B(r)\right|\right|^2 \right) dr \,, \qquad (Eq.\ 3.10)$$

where $\mathrm{E}(\mathrm{r})$ and $\mathrm{B}(\mathrm{r})$ are the electric and the magnetic field of the WGM at distanced r from the center of a spherical resonant cavity respectively, μ and ε are the magnetic permeability and electric permittivity respectively and $\left|\left| \quad \right|\right|$ denotes the Euclidian norm, in $\mathbb{C}^3$. The normalization factor (M) is the maximum energy density of the mode.

$$M = \max_{r \in \mathbb{R}^3} \left(\frac{\varepsilon(r)}{2} \left|\left|E(r)\right|\right|^2 + \frac{1}{2\mu(r)} \left|\left|B(r)\right|\right|^2 \right) . \qquad (Eq.\ 3.11)$$

For a non-magnetic dielectric sphere (where $\mu = \mu_0$), neglecting losses by diffraction and diffusion of the WGM, the energy conservation law implies that the contribution of the electric and the magnetic field to the energy density are equal (Eq. 3.12)

$$\iiint_{\mathbb{R}^3} \frac{\varepsilon(r)}{2} \left|\left|E(r)\right|\right|^2 dr = \iiint_{\mathbb{R}^3} \frac{1}{2\mu_0} \left|\left|B(r)\right|\right|^2 dr \,. \qquad (Eq.\ 3.12)$$

Consequently, the mode volume of a WGM can be expressed in terms of the electric field part only, and is often calculated as in Eq. 3.13, where $\mathrm{E}_{\max}$ indicates the maximum value of the Euclidean norm of the electric field.

$$V_{mode} = \frac{1}{\varepsilon_0 N^2 E_{max}^2} \iiint_{\mathbb{R}^3} \varepsilon(r) \left|\left|E(r)\right|\right|^2 dr \,. \qquad (Eq.\ 3.13)$$

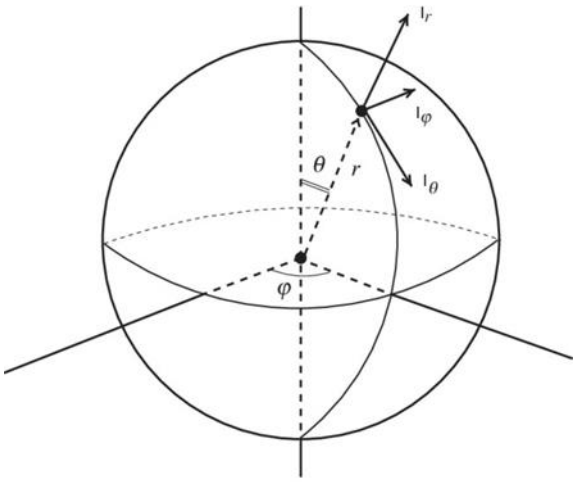

Figure 3.13: *A schematic of a microsphere showing the polar coordinates* (r,θ,*φ*) *of a point on the surface.*

In spherical coordinates, the mode volume for the WGMs can be calculated by integrating the intensity $I(r,\theta,\varphi)$ over the volume of the microsphere (See Figure 3.13).

$$V_{mode} = \frac{1}{M} \iiint I(r,\theta,\varphi)\, r^2 sin\theta \; d\theta \; d\varphi \; dr \; . \qquad (Eq.\ 3.14)$$

The normalization factor (M) related to the maximum energy density is a constant for a particular mode, thus can be taken as 1 for simplicity if I is normalized. As shown in chapter 2, the expression of the electromagnetic field as a function of r, θ, ϕ is separable in these variables, so that:

$$V_{mode} = \iiint I(r,\theta,\varphi)\, r^2 sin\theta \; d\theta \; d\varphi \; dr$$

$$= \int_0^{\infty} I(r)dr \int_0^{\pi} I(\theta) sin\theta \; d\theta \int_0^{2\pi} d\varphi$$

$$= I_{radial} \times I_{angular} \times 2\pi \; , \qquad (Eq.\ 3.15)$$

where, I_{radial} and $I_{angular}$ respectively stand for the integrals of radial and angular components of the mode intensity.

3.11.2 The Energy transfer rate:

A thin strip of surface area on the microsphere is chosen to represent the WGET rate from a WGM to the dyeNPs present in this strip. As shown in Figure 3.14, $\delta\theta$ is the angular width of the mode at the surface, thus the width of the strip is $R\delta\theta$, where R is the radius of the sphere and as the strip is present along the equator of the sphere, thus the length of it is $2\pi R$. So, the surface area of the strip is $2\pi R \times R\delta\theta$. Assuming that the acceptors are homogenously distributed on the surface of the microsphere with surface density ρ_s and at a distance z from the surface, then the numbers of dyeNPs present within this area is $\rho_s \times 2\pi R \times R\delta\theta$.

So, the rate of energy transfer, Γ_{ET}, from the WGM at wavelength λ to an acceptor located at a distance z from the surface of the microsphere can be estimated as:

$$\Gamma_{ET}(\lambda) = \sigma_A(\lambda) \times \frac{c}{n_s} \times \frac{\rho_S \times \delta\theta \times 2\pi R^2}{V_{mode}} \times \frac{I(z)}{I_{max}} \qquad (Eq.\ 3.16)$$

where $\sigma_A(\lambda)$ is the acceptor absorption cross section, c is the speed of light. The third factor of the right-side term in Eq. 3.16 therefore represents the effective concentration of acceptor species in interaction with the mode. $I(z)/I_{max}$ is the ratio of the WGM intensity at a distance z from the surface of the microsphere to the mode maximum. The factor, $I_{max} \times V_{mode}$ actually represents the total energy density of the WGM as per the definition.

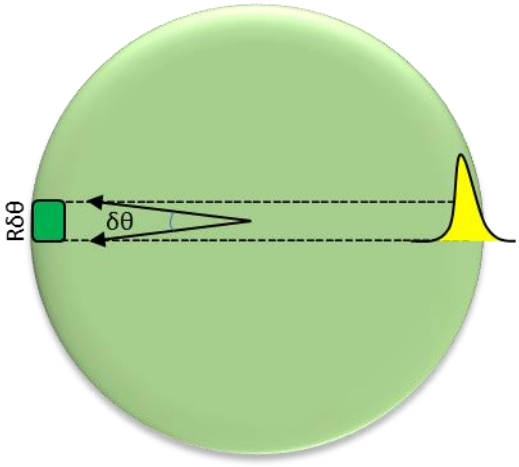

Figure 3.14: *The strip on the surface of the microsphere has the width of* $R\delta\theta$, *and the length of* $2\pi R$, *where the angular width is* θ. *The yellow shaded curve shows the approximate intensity profile of the WGM in radial direction (See section 3.3).*

Intuitively, the quality factor of a WGM relates to the time that a photon remains confined in this mode before exiting it by scattering or absorption. Thus, when the quality factor is high, a photon circulating in a WGM with a dyeNP adsorbed on its surface comes back many times in contact with this acceptor, increasing the probability of interaction.

Since the Purcell factor of the WGM cavity, and thus the efficiency of the coupling of the QD emission to the WGM, are proportional to the quality factor Q, the emission spectrum of a microsphere provides a wealth of information about energy transfer from WGMs to dyeNPs.

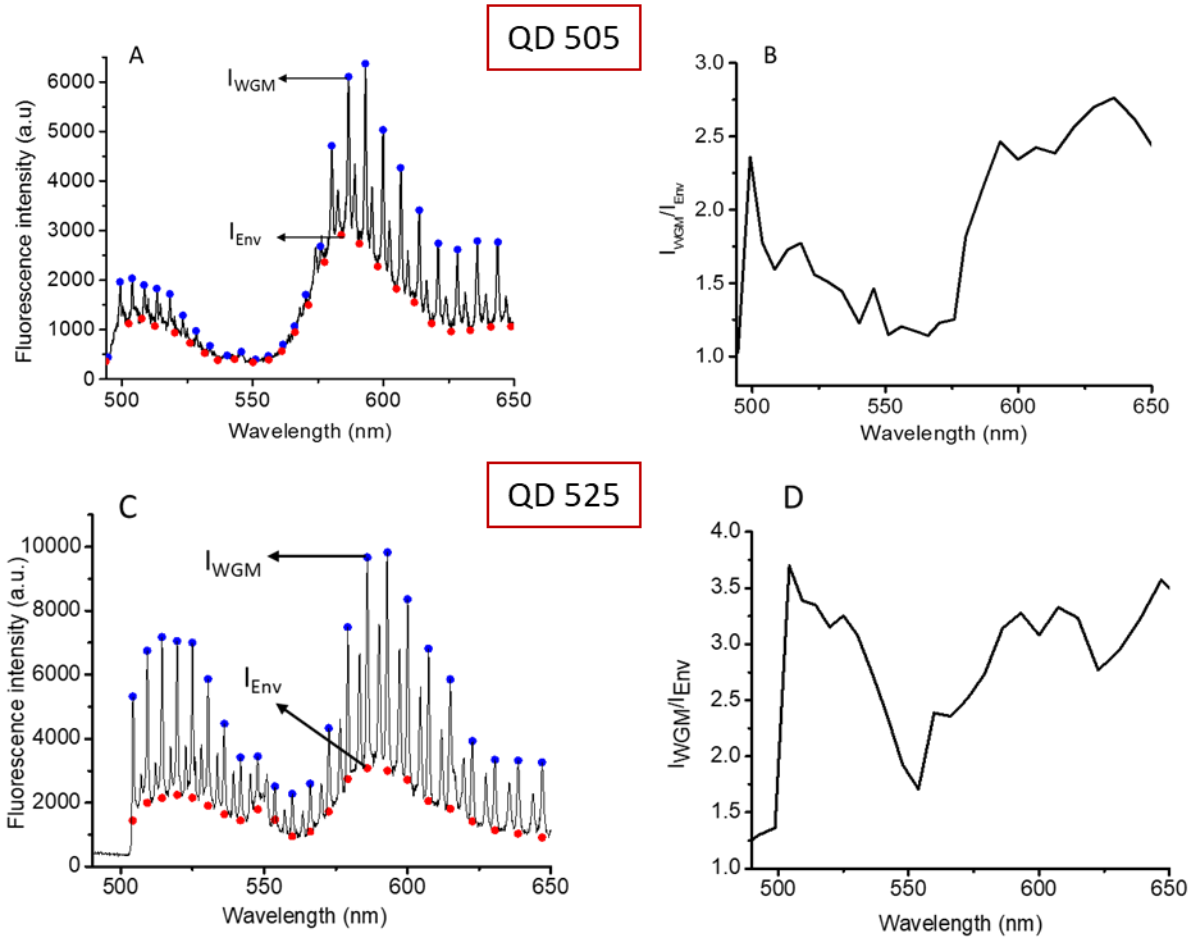

Figure 3.15: (A, C): *Typical confocal emission spectrum respectively collected from a QD 505, QD525 labeled microsphere with dye NPs assembled on its surface.* $I_{WGM}(\lambda)$ *and* $I_{Env}(\lambda)$ *respectively denote the intensities of the WGM peak and the envelope at a particular emission wavelength.* ***(B, D):*** *The ratio of peak to envelope intensities vs. the emission wavelength for the spectra shown in Figure 3.15 (A) and (C).*

Here, these two typical spectra, 3.15 (A) and (C) that have been obtained from microspheres loaded with respectively QD505 and QD525 and coated with dyeNPs following the protocol mentioned in control experiment 1 and 2 will be used to continue the discussion. Considering $I_{WGM}(\lambda)$ as the intensity of a WGM peak (blue points in Figure 3.15 (A) and (C)) at wavelength λ and $I_{Env}(\lambda)$ as the envelope intensity at the same wavelength, derived by interpolating the spectrum local minima (red points in Figure 3.15 (A) and (C)) we can estimate the variation of the quality factor at different wavelengths using Eq. 3.17.

$$Q(\lambda) \propto \frac{I_{WGM}}{I_{Env}} - 1 \qquad (Eq.\ 3.17)$$

Figure 3.15 (B) and (D) respectively show the evolution of the quality factor for the two spectra shown in Figure 3.15. Qualitatively, one can see that the quality factor reaches a minimum around 550-570 nm, where the absorption of the dyeNP is maximal, and is maximal in regions of minimal dyeNP absorption, as expected from Eq. 3.16. More quantitatively, the quality factor is inversely proportional to the rates of relaxation of the cavity mode, including contribution from scattering, re-absorption from QDs and absorption from dyeNPs. Considering that the quality factor Q(λ) of QD-only beads is mostly constant across the spectrum as seen in chapter 2, Figure 2.16, we assume that the rate of WGM relaxation due to all scattering and absorption processes other than energy transfer to dyeNP, Γ_0, is independent of wavelength within our limited spectral range. It can thus be inferred from values of Q observed outside of the dyeNP absorption range, at wavelengths longer than 600 nm. The variations of the energy transfer rate with the wavelength, $\Gamma_{ET}(\lambda)$ can thus be estimated from $Q(\lambda)$, as:

$$\Gamma_{ET}(\lambda) \propto \frac{1}{Q(\lambda)} - \frac{1}{Q(600\ nm)} \qquad (Eq.\ 3.18)$$

This dependence of the energy transfer rate on the emission wavelength was calculated for several microspheres, then averaged (over ~ 20 spectra from individual microspheres for each batch) and are shown in Figure 3.16 (A, B). As shown in these figures, the variations follow the same shape as the dyeNP absorption spectrum for both the populations of QDs, as expected from Eq. 3.16.

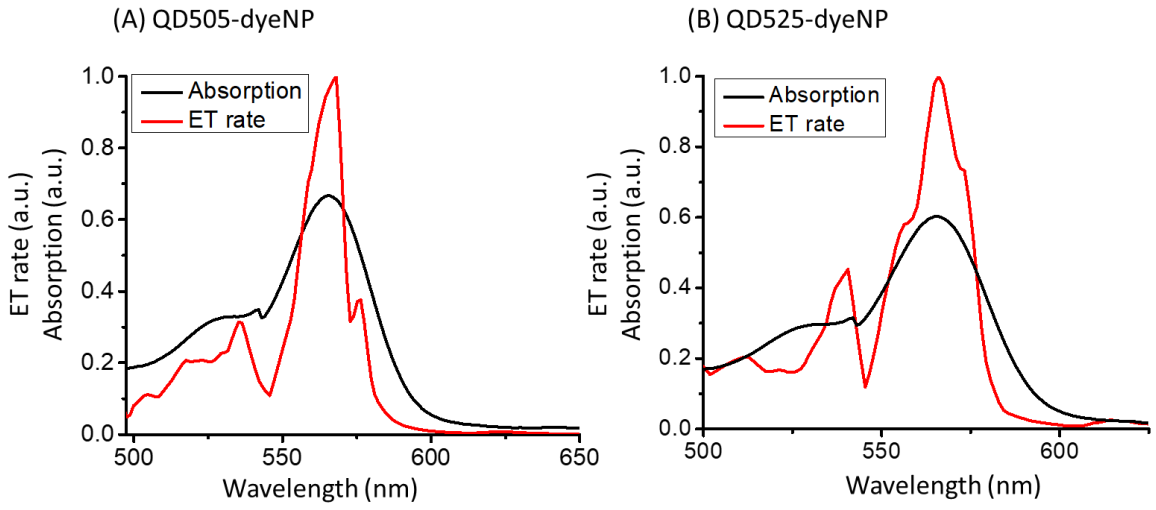

Figure 3.16 (A, B): *Absorption of the dye NPs (black) and energy transfer rate from WGM to dyeNPs in microspheres loaded with respectively (A) QD505 (red) and (B) QD525 (red).*

3.11.3 Energy transfer efficiency:

The energy transfer efficiency can be expressed as a function of Γ_{ET}, the energy transfer rate from Eq. 3.16 and Γ_0, the rate of WGM relaxation due to all other scattering or absorption processes:

$$E_{ET} = \frac{\Gamma_{ET}}{\Gamma_{ET}+\Gamma_0}. \qquad (Eq.\ 3.19)$$

Here, for easy understanding, the variations of the energy transfer efficiency with the wavelength, $E_{ET}(\lambda)$ can be estimated also from $Q(\lambda)$, since the quality factor is inversely proportional to the loss rates of the cavity:

$$E_{ET}(\lambda) = 1 - \frac{Q(\lambda)}{Q_0}, \qquad (Eq.\ 3.20)$$

where Q_0 is the quality factor of the microcavity without any acceptor. The efficiency of the energy transfer for both QD batches were calculated from the ET rate (Γ_{ET}) (previous section) using the Eq. 3.20. As expected, when compared to the absorption of the dyeNPs, the efficiency curves (Figure 3.17 (A, B)) also follow similar spectral features, as observed previously for Γ_{ET}.

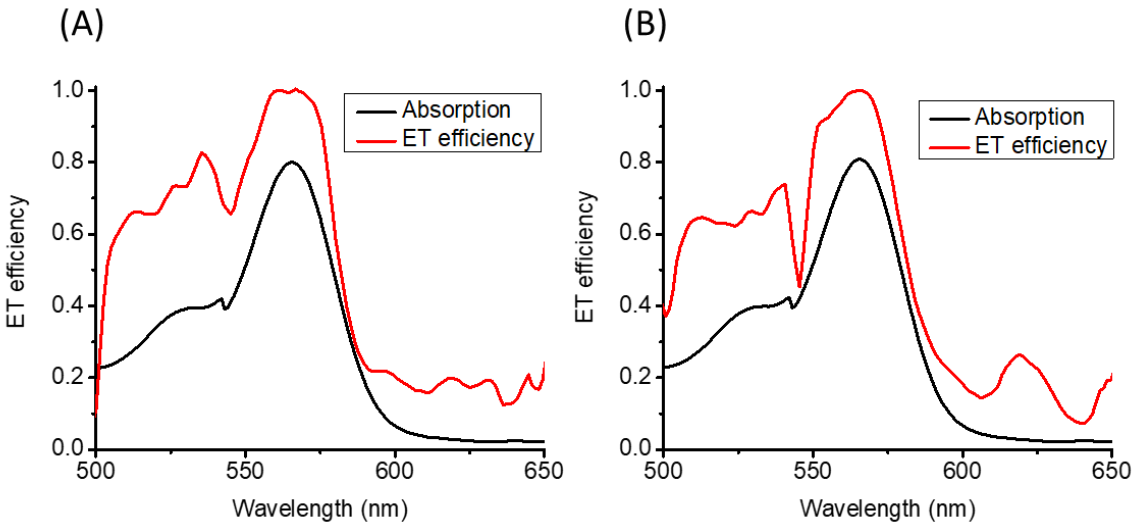

Figure 3.17 (A, B): *Absorption of the dye NPs (black) and efficiency of energy transfer from WGM to dyeNPs in microspheres loaded with respectively (A) QD505 (red) and (B) QD525 (red).*

3.11.4 Dependence of WGET on the acceptor density:

Another experiment was carried out to understand the effect of the acceptor concentration on this energy transfer process. To perform this experiment, the QD505-microspheres coated with different amount of dyeNPs were prepared using the protocol described before. Four different samples were prepared with the dyeNP concentrations in the final solution, respectively, 2.8 nM, 5.6 nM, 11.2 nM and 28 nM. The average energy transfer efficiencies for these samples were estimated from their emission spectra (18-20 for each sample) of individual microspheres using Eq. 3.18 and 3.20, as described previously.

Figure 3.18 (A) shows the evolution of the average energy transfer efficiencies for the four different samples. Similar to the ET rate curves in Figure 3.16, the transfer efficiency is maximal at the peak of dyeNP absorption.

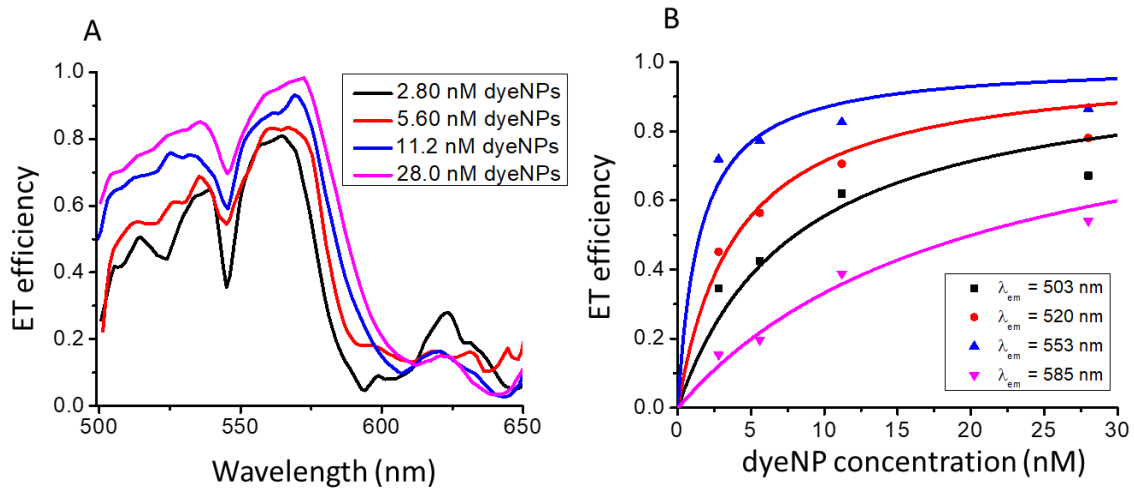

Figure 3.18 (A): *Energy transfer efficiencies as a function of WGM wavelength for different samples of microspheres that have same amount of QD 505 emitters but different amounts of dye NPs.* ***(B):*** *Energy transfer efficiency (QD505) from WGMs at different wavelengths as a function of the concentration of dyeNP acceptors.*

In addition, when the quantity of adsorbed dyeNP acceptor increases, the energy transfer efficiency increases. As shown in Figure 3.18 (B), at each wavelength, $E(\lambda)$ varies with the dyeNP acceptor concentration, ρ_S, as expected from Eq. 3.16 and 3.19, which can be rewritten as:

$$E(\lambda) = \frac{\rho_S}{\rho_S + \rho_0(\lambda)}, \qquad (Eq.\ 3.21)$$

where $\rho_0(\lambda)$ is a constant corresponding to the concentration of acceptors needed to reach $E(\lambda)$ = 50% at this specific wavelength.

ρ_0 can also be expressed as a function of the system characteristics;

$$\rho_0(\lambda) = \Gamma_0 \times \frac{1}{\sigma_A(\lambda)} \times \frac{n_s}{c} \times \frac{V_{mode}}{\delta\theta \times 2\pi R^2} \times \frac{I_{max}}{I(z)}, \qquad (Eq.\ 3.22)$$

where, for $\rho_S = \rho_0$, $\Gamma_{ET} = \Gamma_0$ (from Eq. 3.19 and 3.21), and

$$Q_0 = \frac{\omega}{\Gamma_0} = \frac{2\pi c}{\lambda \Gamma_0} \Longrightarrow \Gamma_0 = \frac{2\pi c}{\lambda Q_0} \qquad (Eq.\ 3.23)$$

Q_0 is the quality factor of the cavity without any acceptor.

3.11.5 Variation in absolute Q due to WGET:

In the previous sections, I have elaborately discussed how we can extract the dependence of Q qualitatively from the typical emission spectra, and then utilize this to understand the energy transfer process. We can also confirm this dependence by calculating the absolute Q of the microcavities as a function of emission wavelength.

Analyzing the spectra obtained with the high-resolution spectrophotometer, the variation of Q (either from TE or TM modes) with the wavelength is calculated from the width of each resonance peak using Eq. 2.12 (Chapter 2). A clear minimum is observed, corresponding to the absorption maximum of the dyeNPs (Figure 3.19). It confirms that the gallery modes at the range where the dyeNPs absorbs the highest are mostly affected due to the energy transfer.

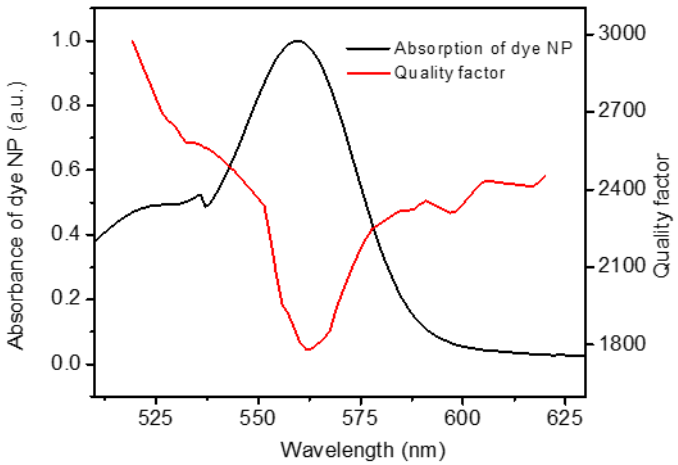

Figure 3.19: *Variations of the quality factor of WGMs (TE modes) as a function of wavelength (red) in a micro-sphere loaded with QD525 and coupled to dyeNPs. Absorbance spectrum of the dyeNP is represented in black for comparison.*

3.12 Comparison between FRET and WGET in regard of biosensing applications:

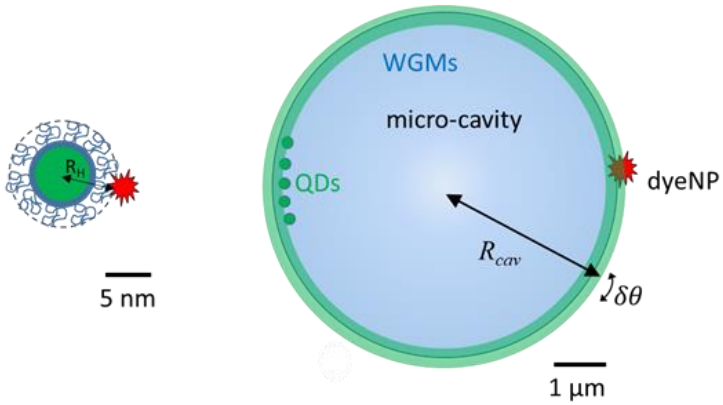

	FRET Single QD, 1 acceptor/QD	WGET Collective energy transfer
Donor surface	$4\pi \times R_H^2 \approx 400$ nm^2	$\delta\theta \times 2\pi R_{cav}^2 \approx 4\times10^7$ nm^2 $(Rc_{av} = 5\mu m;\ \delta\theta \sim 0.27)$
Acceptor density	1/400 nm^{-2}	1/400 nm^{-2}
#acceptors/donor	1	$\approx 10^5$

Figure 3.20/Scheme 1: *Comparison between FRET and WGET*

In this section, the specificities of energy transfer from WGM donors to dyeNP acceptors (WGET) that are expected to make them particularly efficient compared to FRET, will be thoroughly discussed. For this, the system is evaluated from a theoretical point of view to obtain an estimation of its possibilities: at first, it is to be noted that, in the case of WGET, the donor is a WGM mode, which is excited by many QDs, which provides a considerable brightness when compared with single donors.

As an illustration, I would like to compare energy transfer to dyeNPs from WGM donors (WGET) and from isolated QDs (FRET). In the context of biosensing, where for example capture antibodies would be used to bring dyeNP acceptors in close proximity of FRET or WGET donors, the energy transfer efficiencies are compared in conditions where the same amount of capture antibody is used. Assuming that in both cases, antibodies are linked to the different surfaces at similar surface densities, this is equivalent to comparing FRET and WGET at the same surface density of dyeNP acceptors (see Figure 3.20/Scheme 1).

3.12.1 WGET and FRET efficiency vs the density of acceptors:

As shown in Figure 3.20/Scheme 1, the representative WGET system is composed of a QD loaded microcavity of 10 µm size with acceptor dyeNP adsorbed on the surface. To theoretically calculate the *efficiency* of WGET, the rate of energy transfer should be computed first using Eq. 3.16.

To start, the intensity profile for the TE (or TM) mode can be calculated from the Eq. 2.4 and 2.5 in chapter 2 which can subsequently be approximated as a mono-exponential decay function $(\exp -d/r^*)$, where r^* is the characteristic decay length for the WGM. For the PS microsphere of radius = 5 µm, and for mode numbers, which are, $n=1$, $l=m=88$ and WGM wavelength = 516.6 nm, the characteristic length (r^*) is found to be 85.6 nm.

The energy transfer rate can be computed by plugging in the values of all the parameters in Eq. 3.16, such as σ_A (= 8.5×10^{7} m^2), ρ, V_{mode} and the intensity at the maximum of WGM is normalized to, I_{max} = 1. This calculation would stand accurate if the acceptor is assumed to be located at a single point, but in reality, the acceptor has a finite size, the range of which is significant compared to the characteristic decay length of the WGM. Thus, different parts of the dyeNP along the radial axis experience different exponential intensity tail of the WGM. Hence the correction of the energy transfer rate due to the acceptor's dimension is absolutely necessary. As seen in Figure 3.21 (A) for dyeNP directly adsorbed on the cavity surface, the dyeNP can be approximated to be consisted of a series of circular nano-discs with radius of $r_{dnp}\sin\theta$, where r_{dnp} is the radius of the dyeNP and each disc situated at the distance $r_{dnp}(1-\cos\theta)$ from the surface of the microsphere, where $\theta \in [0,\pi]$.

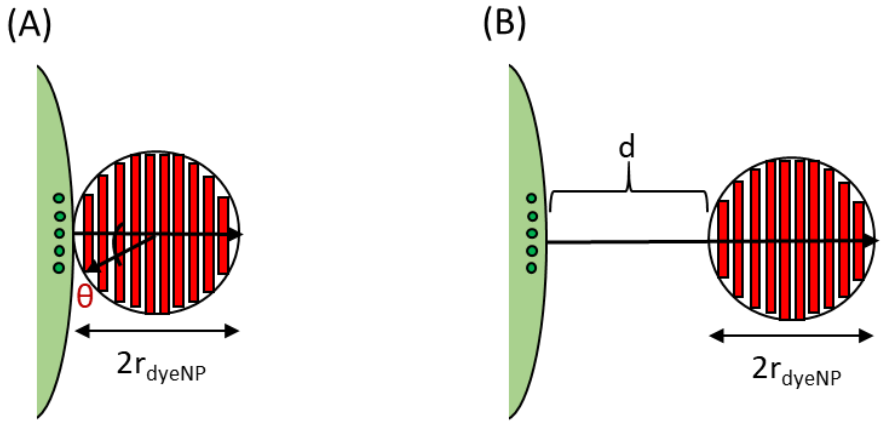

Figure 3.21: *The dyeNP has been approximated to be consisted of multiple circular discs to take its large size into account. (A) dyeNP adsorbed directly on the surface of the microcavity, (B) dyeNP present at a surface-to-surface distance d from the microsphere.*

The size correction factor (S_{WGET}) can be mathematically written as;

$$S_{WGET} = \int_0^{\pi} \left[\pi\left(r_{dnp}sin\theta\right)^2 \times r_{dnp}sin\theta\right] \times e^{-\frac{r_{dnp}(1-cos\theta)}{r^*}} \times \frac{1}{\frac{4}{3}\pi r_{dnp}^3} d\theta$$

$$= \int \text{Integral of all the discs over the whole volume of the dyeNP} \times$$

$$\text{the WGM field at various angular positions} \times$$

$$\text{Normalization factor considering the whole volume of the dyeNP.}$$

$$= \int_0^{\pi} \frac{3}{4}\sin^3\theta \times e^{-\frac{-r_{dnp}(cos\theta-1)}{r^*}} d\theta \qquad (Eq.\ 3.24)$$

So, the corrected energy transfer rate for a particular WGM mode (here, λ_{WGM} = 516.6 nm) will be,

$$\Gamma_{ET}(d=0)(Corrected) = S_{WGET} \times \Gamma_{ET}(d=0) \qquad (Eq.\ 3.25)$$

Where d is the surface-to-surface distance between the cavity and the dyeNP.

So finally, WGET efficiency (E_{ET}) can be expressed as Eq. 3.26;

$$E_{ET} = \frac{\rho_s}{\rho_s+\rho_0} \qquad (Eq.\ 3.26)$$

With ρ_0 being estimated from Eq. 3.16 and 3.22. In the case of FRET, dyeNPs present very large absorption cross-sections, and the most extreme case is considered where QDs undergo a FRET efficiency of 1 as soon as they are conjugated to at least one acceptor. Taking into account the surface chemistry of the QDs and a typical hydrodynamic radius R_H of 6 nm,[284] the total FRET efficiency can be expressed as a function of ρ_S, the acceptor surface density, as

$$E_{FRET}(\lambda) = \left(1 - e^{-\rho_S * 4\pi R_H^2}\right), \qquad (Eq.\ 3.27)$$

corresponding to the fraction of QDs conjugated to at least one acceptor, assuming a Poisson distribution of the acceptor:QD ratio.[96]

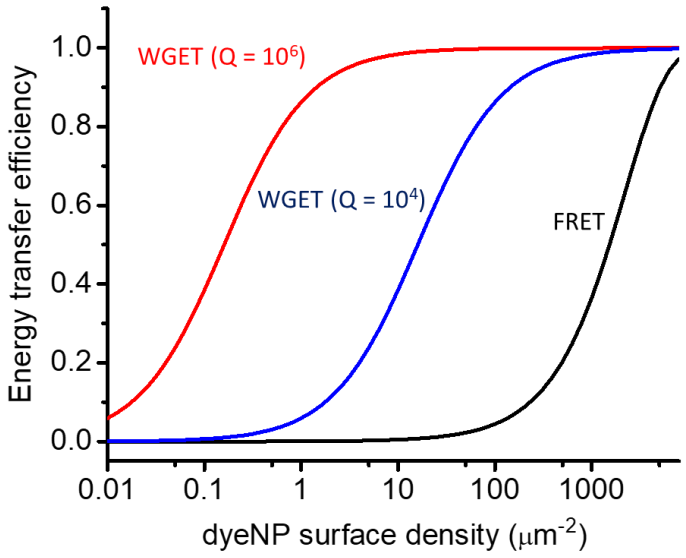

Figure 3.22: *Theoretical energy transfer efficiency as a function of dyeNP acceptor surface density for FRET, WGET (quality factors of 10^4 and 10^6), with the dyeNP placed directly at the surface.*

Figure 3.22 shows the predicted energy transfer efficiency for FRET and WGET as a function of the acceptor surface density, and for different quality factor, when dyeNP are directly adsorbed at the FRET or WGET donor surface. As a corollary of the Poisson distribution, for the ratio of QD:dyeNP = 1:1, the FRET efficiency that can be achieved is 0.67 which corresponds to acceptor surface density that is 100-1000 times more than what is required to achieve the same WGET efficiency.

The strikingly superior efficiency of WGET originates from the delocalized and collective nature of the WGM: instead of being confined to $4\pi R_H^2 \sim 400\ \mathrm{nm}^2$ as in the case of FRET, the WGM is delocalized over $\delta\theta \times 2\pi R^2 \sim 42\ \mu\mathrm{m}^2$, an effective surface that is 10^5 larger. In addition, the high-quality factor enables multiple interactions between the WGM field and each acceptor. This largely compensates for the lower electromagnetic intensity at the surface of the microsphere, compared to the higher near-field intensity in the case of FRET.

3.12.2 WGET and FRET rate vs the donor-acceptor distance:

I have already discussed before that the long evanescent tail of the WGM should provide a strong advantage over FRET in terms of achieving longer range for energy transfer. Now I will quantitatively compare how the *rate* of these two processes vary with the distance between the donor and the acceptor. When the dyeNP acceptor is located farther away from the surface, as would be expected in a biosensing scheme, the acceptor experiences a donor intensity that decays as a function of the separation between the donor surface and the acceptor surface, d. In the case of FRET, the donor intensity varies as d^{-6}. In contrast, in the case of WGET, the intensity decay is well approximated by a mono-exponential with a characteristic length of $r^* = 85$ nm as described before.

Using the help from the expression of S_{WGET}, the rate of WGET for a particular mode can be expressed as a function of the surface-to-surface distance (d) between the donor and the acceptor. As, $\Gamma_{ET}(d) \propto I(d)$ (from Eq. 3.16) where $I(d)$ is the WGM intensity at distance d, the rate of WGET after size correction of dyeNP can be written as:

$$\Gamma_{ET}(d)(corrected) = \Gamma_{ET}(d) \times \int_0^{\pi} \frac{3}{4}\sin^3\theta \times e^{-\frac{d-r_{dnp}(cos\theta-1)}{r^*}} d\theta \qquad (Eq.\ 3.28)$$

$$\propto I(d) \times \int_0^{\pi} \frac{3}{4}\sin^3\theta \times e^{-\frac{d-r_{dnp}(cos\theta-1)}{r^*}} d\theta$$

As mentioned before for WGET, the dyeNPs, due to their large size, cannot be approximated by a single dipole, thus FRET transfer rate also should be integrated over the volume of the dyeNP. Thus, the rate of FRET can also be represented as the donor-acceptor separation distance;

$$\Gamma_{FRET}(d) \propto \int_0^{\pi} sin\theta \times \frac{d\theta}{\{R_H+d-r_{dnp}(cos\theta-1)\}^6} \qquad (Eq.\ 3.29)$$

The rate of energy transfers through WGM and Förster process have been plotted (normalized) in Figure 3.23 which suggests that the FRET rate drops quickly to close to 0 when the D-A distance goes above 10 nm, but the WGET rate stays significant even at the distance that is more than 100 nm.

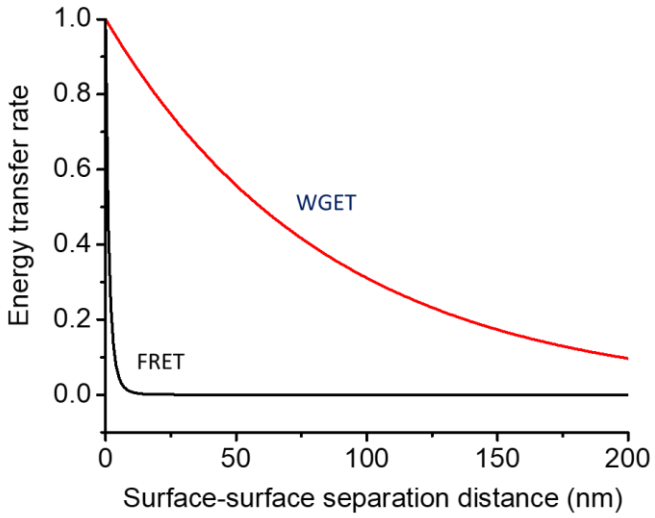

Figure 3.23: *Normalized energy transfer rate for FRET and WGET as a function of the surface-to-surface separation distance.*

3.12.3 WGET and FRET efficiency vs the donor-acceptor distance:

To compare how energy transfer *efficiency* varies with separation distance in FRET and WGET, I assume a surface density of 1 acceptor dyeNP for 400 nm^2 – in the case of FRET this corresponds to a 1:1 dyeNP:QD ratio. The WGET efficiency for microcavities with Q = 10^4 and 10^6 can be calculated as described before (section 3.12.1). For FRET, the efficiency can be calculated using the Eq. 1.6 and 1.7 (Chapter 1),

$$E = \frac{\Gamma_{FRET}(d)}{\Gamma_0+\Gamma_{FRET}(d)} \qquad (Eq.\ 3.30)$$

At a separation distance R_0, the efficiency of energy transfer = 50% and $\Gamma_0=\Gamma_{FRET}$. For our donor-acceptor system here, the R_0 has been found to be 23.2 nm.

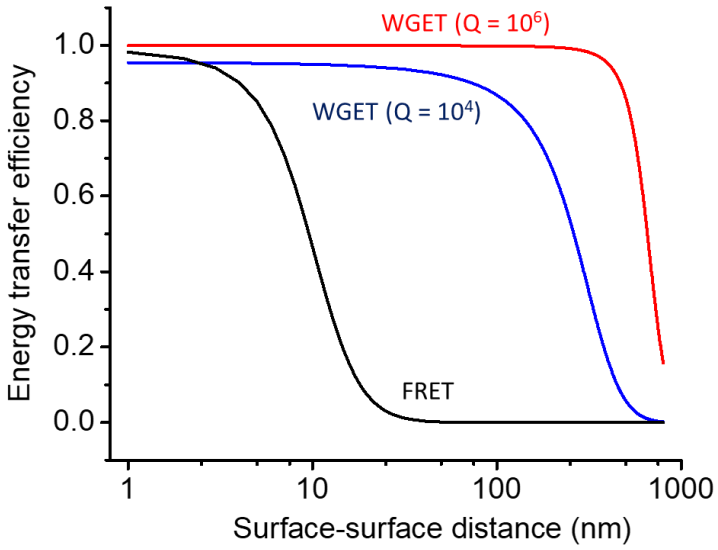

Figure 3.24: *Energy transfer efficiency as a function of the surface-to-surface separation distance for FRET and WGET (quality factors of 10^4 and 10^6), with a dyeNP density = 1/400 nm^2 (corresponding to 1 dyeNP/QD in the case of FRET).*

As shown in Figure 3.24 FRET efficiency reaches 50% at a QD surface-to-dyeNP surface of ~10 nm. In comparison, WGET is efficient over larger distances: when $Q=10^4$, the 50% distance is ~47 nm, while it reaches ~100 nm when $Q = 10^6$. This makes WGET advantageous to probe large biomolecular assemblies such as antibody-antigen sandwiches, large oligonucleotides, or even small viruses.

3.13 CONCLUSION:

In summary, we have explored the use of QD based PS microcavities to perform energy transfer from the resonance modes (WGM) to outside optical acceptors, in the context of optical sensing. In the previous chapter, we discussed the fabrication of polystyrene micro-cavities where bright and photostable colloidal quantum dots are placed inside to act as optical donors. Bright and highly absorbing dye NPs were assembled on the micro-cavities to act as optical acceptors. Analysis of the emission spectrum from the cavity enabled us to determine the nature of the energy transfer processes from WGM to these acceptors both qualitatively and quantitatively, as a function of the spectral overlap and the density of acceptors. Our experimental data and modeling show that energy transfer from WGM to acceptors placed in the vicinity of the cavity surface is greatly enhanced by the quality factor of the cavity. The energy transfer can be efficient over distances larger than 100 nm, compared to typically 10 nm for FRET. This would enable the use of WGET to design highly sensitive homogenous assays to detect large biomolecular entities from peptides, proteins or oligonucleotides to large antibody-antigen sandwiches or small viruses. Bio-specificity could be easily imparted on these microspheres by conjugating whole antibodies or other capture probes without the size constraints encountered in FRET assays. Further developments of WGET could thus enable faster, user friendly and more sensitive tools for bio-detection.

CHAPTER 4: DNA SENSING WITH MICROCAVITIES

CONTENTS

4.1 INTRODUCTION:

In the previous two chapters, I have introduced a QD loaded whispering gallery micro-resonator presenting interesting advantages in terms of ease of fabrication, stability and convenience of usage. Subsequently, a simple energy transfer conjugate was studied in detail where these microcavities were used as optical donors and dye loaded polymeric nanoparticles (dyeNPs) acted as optical acceptors. Due to the extension of evanescent field outside the surface of the resonators and high Q-factor of the resonance modes, the microcavity mediated energy transfer (WGET) have shown to be efficient over longer donor-acceptor distance ranges, when compared to non-radiative FRET. The significantly high brightness of the resonators arising from the trapping of fluorescence from many QDs, combined with the great energy transfer efficiency inspire us to fabricate a bio-sensing platform with enhanced sensitivity. One of the major challenges in building a good biosensor is to provide specificity to it so that biological entities can be detected selectively. Thanks to the vast variety of available chemical reaction techniques, physical absorption and adsorption of molecules that can be performed to modify the surface of the microcavities which would allow us to conjugate specific biomolecular capture probes covalently or non-covalently, moreover, to even reduce non-specific interactions. Here in this chapter, I will proceed towards building a microcavity based sandwich assay to detect a cancer biomarker DNA named survivin in aqueous buffer. DNA-based sensing is comparatively 'simpler' than the antibody-based detection schemes due to robustness and strong affinity of capture probes towards the complementary target strands. Thus, it is a good way to test the WGET-based sensing scheme with biomolecules without running into complex issues of antibodies, such as denaturation, structural changes in the binding site and high cost. I will also focus to translate this principle of detection to higher level of simplicity in terms of detection technique and instrumentation so that the work would be more appealing towards real life applications.

4.2 Prerequisites: The structure and properties of DNA:

Deoxyribonucleic acid or in short DNA, is a biological macromolecule essential for the existence of life and found in all prokaryotic and eukaryotic cells and in many viruses carrying genetic information regarding the development, functioning, growth and reproduction of all organisms and some viruses[285]. In 1953, James Watson and Francis Crick, aided by the work of biophysicists Rosalind Franklin and Maurice Wilkins, interpreted the 3D structure of DNA from an X-ray diffraction image of the molecule, which led them to win the Nobel Prize in 1962[286].

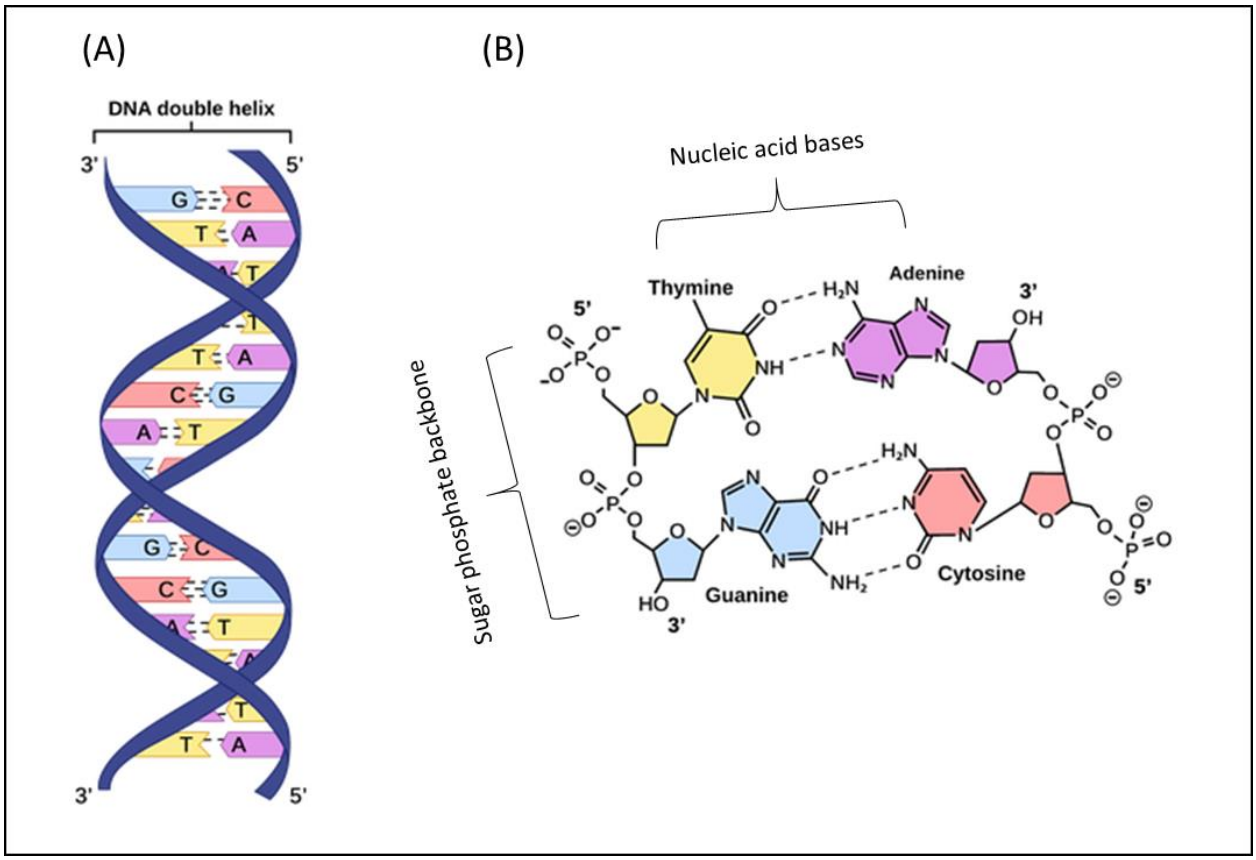

Figure 4.1: *(A) Structure of DNA double helix, (B) H-bonding interactions between the nucleotide bases of two single strands (A=T and G≡C). (Image source: theory.labster.com)*

4.2.1 Structure:

The DNA is composed of two polynucleotide chains that coil around a common axis forming a double helix[287], where the two chains are held together by H-bonding (see Figure 4.1 (A)). Individual strand of DNA is called polynucleotide because they are composed of simpler monomeric units called nucleotides[285]. Another polynucleotide macromolecule which plays crucial roles in the regulation and expression of genes is called RNA or ribonucleic acid. Like DNA, RNA also plays many necessary functions in the sustenance of cellular functions of organisms, one of which is to actively participate in the synthesis of proteins[288,289].

Each nucleotide unit is composed of one of the four nitrogen-rich nucleobases, deoxyribose sugar and a phosphate group. A chain of nucleotides is formed by phospho-diester covalent linkage between the sugar of a nucleotide and the phosphate group of the next one, resulting into an alternating sugar-phosphate backbone. In particular, this chain structure is derived as the phosphodiester bonds are formed between the third and fifth carbon atoms of two adjacent sugar rings in a polynucleotide chain. These two carbons on the sugar ring are quite significant as they are used to represent the directionality of a single strand. One end of a polynucleotide chain consists of a phosphate group attached to the 5' carbon of a sugar ring, this end is denoted as 5' (phosphoryl) end, whereas the other end of the same polynucleotide has a free hydroxyl group attached to the 3' carbon of the terminal sugar ring on this end of the chain, and this end is denoted as 3' (hydroxyl) end. The directionality of a DNA single strand is given either by 5'→3' or 3'→5'. In general, two single strands in a double helix have opposite directionality, hence antiparallel to each other[285] (See Figure 4.1). The four nitrogenous bases found in the structure of DNA are adenine (A), guanine (G), cytosine (C) and thymin (T). These bases from two different single helix form hydrogen bonds between them to construct a double helix. This base pairing occurs based on a certain exclusive rule where adenine forms two H-bonds with thymin, whereas guanine forms three H-bonds with cytosine (See Figure 4.1 (B))[285].

A process called transcription takes place in cells to create RNA strands using a DNA strand as template. The transcribed RNA strand has complementary nucleotides to the template DNA and the type of the sugar that forms the sugar-phosphate backbone is ribose instead of deoxyribose in DNA. Another important characteristic in RNA structure is that the thymin in the polynucleotide chain is replaced by uracil (U)[290]. DNA is predominantly found in the form of double helices in nature, whereas RNA is in general

single stranded but many of the RNA such as tRNA contains self-complementary segments in its structures that allow them to form intra-strand local double helices and form folded configurations[291].

4.2.2 DNA/RNA hybridization:

Even though most naturally occurring DNA are found in duplex form, two strands can be separated from each other by providing enough energy, for example in the form of heat or chemically breaking the H-bonding interactions between two strands. This process is called DNA denaturation or melting[292]. It is a key step for the generation of single stranded DNA that subsequently are used as probes for DNA hybridization based biological assays such as polymerase chain reactions (PCR)[293]. DNA hybridization or annealing is the process of pairing two complementary DNA strands by facilitating the H-bonding interactions between the base pairs of two strands. If appropriate conditions are achieved, then two RNA single strands or one RNA to one DNA strand can be hybridized together to form a duplex. The hybridization process is one of the most crucial ones for designing assays, such as, Southern Blot, Dot-Blot and sandwich hybridization assays[294].

Environmental factors such as temperature and pH of the solution play crucial role in the hybridization of two single strands. The negative charges arising from the phosphates in the backbone of the polynucleotides would cause repelling interactions with complementary strands. Using a particular salt (e.g., $MgCl_2$) concentration to screen the effect of the phosphates is necessary for the hybridization to proceed. As comparatively stronger (triple H-bonding) interaction takes place between guanine (G) and cytosine (C) than between the other two bases, the ratio G:C in the target strand plays an important role in the hybridization process[292,295].

DNA based probes are now widely used in many applications, such as, in the diagnosis of infectious diseases (e.g., human papilloma (HPV)[296,297], hepatitis-B[10,298] and HIV[299] viruses), in cytogenetic studies (for example, to study numerical and structural disorders in chromosomes)[300,301] and DNA fingerprinting[302,303]. In the recent time, techniques based on DNA or RNA sensing assays are being employed to detect certain genetic sequences as structural bio-markers in cells, offering many advantages over the current immunohistochemical methods for the identification of tumor cell types[304,305]. This chapter will be focused on detecting a cancer bio-marker called survivin, the identification of which has been a center of immense research in the field of clinical biology, especially for the diagnosis of cancers and targeted gene and Immunotherapy[306].

4.3 ENERGY TRANSFER DNA ASSAYS:

Non-radiative energy transfer (FRET) based bio-sensing schemes have been a topic of extensive research due to the simplicity of performance, high specificity and potentials to be executed in homogenous format[52]. Homogenous FRET assays, as they do not require any intermediate washing step, have made bio-sensing of specific analytes very simple for end-users.

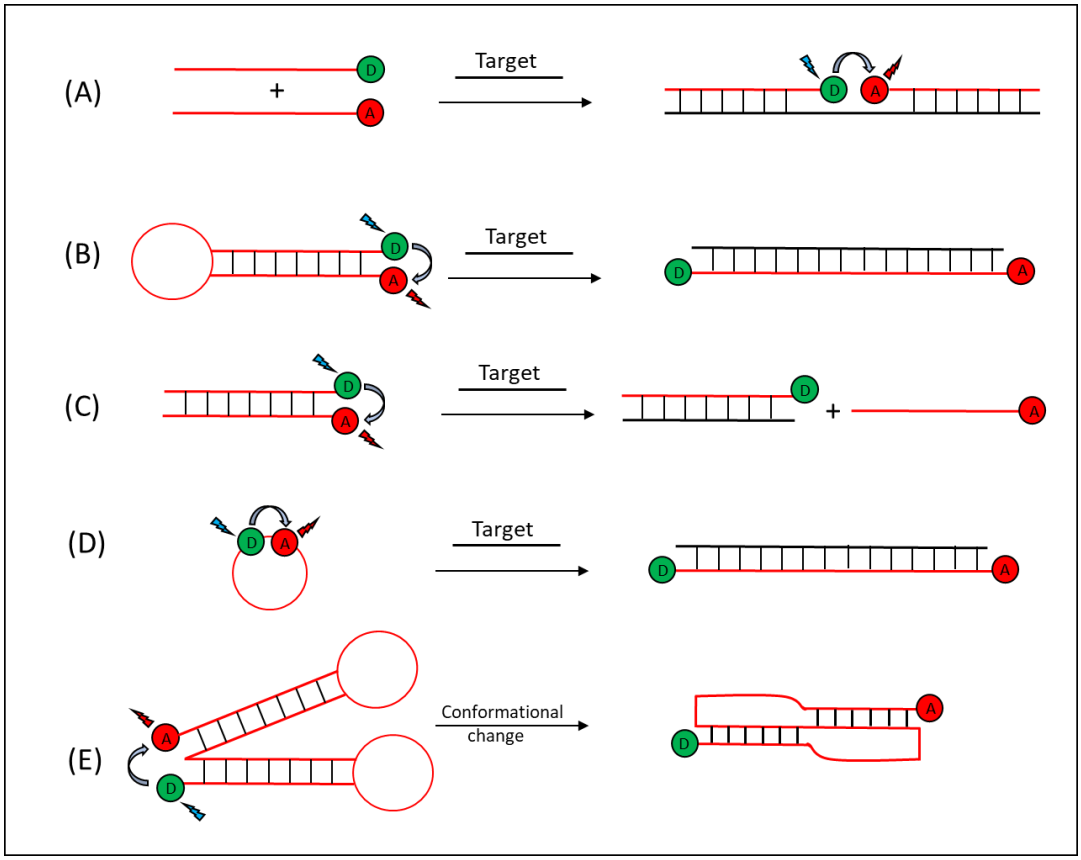

Figure 4.2: *Various DNA detection schemes; (A) Sandwich hybridization assay, (B) hairpin loop-based hybridization assay, (C) DNA strand substitution, (D) ssDNA-based hybridization assay, (E) Assay to detect DNA structural change.*

Since the beginning of the era of nano-sciences, many researchers have focused to design nanomaterial (NM) conjugated biomolecules for energy transfer assays, thanks to the interesting opto-electronic properties of low dimensional materials[65]. Numerous QD-bioconjugates have been designed to detect vast varieties of biological elements such as DNA[98], RNA[307], amino acids[308], proteins[309], and ions[310].

Depending on the type and properties of analytes, FRET assays can operate in both competitive and non-competitive mechanisms.

Myriad of studies have been performed to design and evaluate energy transfer assays based on nanomaterial bio-conjugates for detecting DNA[98,311] and RNA[307,312] strands, part of which is important to discuss in the context of this chapter. Some of the DNA detection schemes are shown in the Figure 4.2. The D (green sphere) and A (red sphere) respectively represent optical donor and acceptor.

Figure 4.2 (A) shows a typical sandwich FRET assay operating in a non-competitive format to detect DNA single strands. The capture and reporter probe oligonucleotides, and the fluorophore tags have to be carefully designed so that when hybridized, the donor and acceptor are in FRET range[307,313]. Figure 4.2 (C) represents an assay that works in competitive format where the target DNA replaces the acceptor attached strand, consequently preventing FRET[314]. Structures like hairpin loop[315] (Figure 4.2 (B)) and ssDNA strands[316] (Figure 4.2 (D)) are also often used for FRET DNA sensing assays. Hairpin loop based FRET assays widely known as molecular beacon probes are frequently used in SNP (single nucleotide polymorphisms) genotyping, RT-PCR (real time-polymerase chain reactions) and other diagnostic clinical assays[317]. Conformational changes in DNA structures can also be detected by specific FRET schemes (4.2 (E))[318]. TR-FRET (time resolved-FRET) techniques are also often used to study the dynamics of conformational changes[319,320]. In conclusion, all of the mentioned designs are generally based on the fact that FRET is inefficient for longer donor-acceptor distances which makes it possible to design distance sensitive assays but at the same time careful designs and modifications of strands are absolutely necessary.

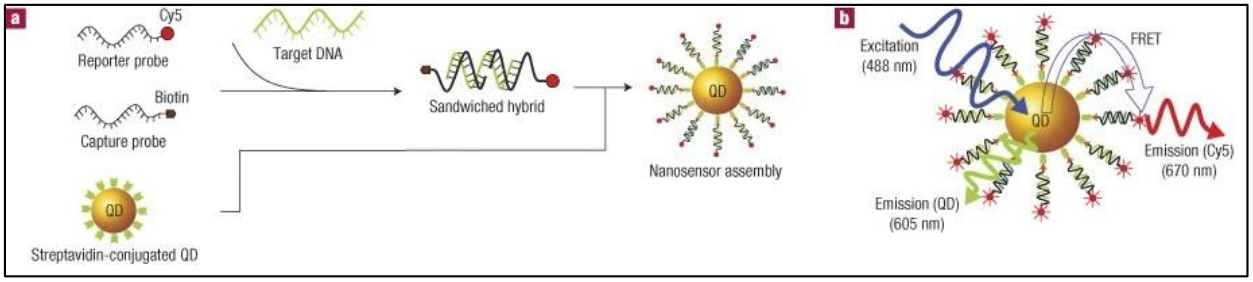

Figure 4.3: *QD-bioconjugate based FRET sandwich assay to detect target DNA single strand*[98].

As an example, Zhang et al. reported one of the early works to detect target DNA strands[98] using QD-bioconjugates in FRET sandwich assay. In this work, CdSe/ZnS core-shell QDs (emission = 605 nm) conjugated to streptavidin molecules were used as the donor bioconjugate, a Cy5 tagged oligonucleotide

was used as acceptor attached reporter probe, and a biotinylated strand was used to capture the target DNA (see Figure 4.3).

Regardless of vast usage and simplicity of FRET assays, they suffer from some major disadvantages which are inherited to the mechanism of FRET. Due to the sharp inverse dependence of FRET rate on the donor-acceptor distance, large biological assemblies with donor-acceptor distance more than 10 nm are complicated to detect[174]. In practical applications, for example, in case of designing sandwich biological assays for the detection of large proteins or virus DNA strands, FRET techniques might lead to inconclusive test results or false outcomes. This also restricts the flexibility of designing the assay.

4.4 SURVIVIN:

Survivin is a member of the inhibitor of apoptosis (IAP) protein family which is highly expressed in most malignancies. It inhibits the activation of caspase, a protease enzyme that plays essential roles in apoptosis, thus preventing programmed cell death. Survivin is one of the important genes involved in tumor aggressiveness and therapy resistance. A study reported by Salz et al. showed that transcriptional changes due to survivin expression in the tissue microenvironment further promotes tumorigenesis in the bladder tissue[321]. Another report by Khan et al. found that higher expression of survivin in head and neck squamous carcinoma can be related to radioresistance[322]. In humans, the protein is expressed by BIRC5 gene (baculoviral inhibitor of apoptosis repeat-containing 5). Tamm et al. examined 60 different cancer cell lines and observed that survivin was expressed in all of them. For many common malignancies such as cancers in lung, breast and pancreas, survivin protein is found to be overexpressed in even more than 80% of tumor cells which makes it one of the most abundant protein forms that is exclusively found in cancers[323]. Many clinical studies have suggested that the interruption in the induction pathways of survivin results in increasing apoptosis, decrease in tumor growth and suppression of tumor aggression[306]. Survivin protein is over expressed in cancers, but is completely absent in regular cells which makes it a potential target towards designing a highly specific cancer therapy[324]. In the recent time, survivin has been a great source of attention for cancer immunotherapy. Some studies have found that survivin can act as a strong T-cell activation antigen, which might help to develop some immunotherapeutic techniques[325]. For example, Xiang et al. showed that the inhibition of tumor growth and metastasis can be achieved by simultaneously attacking both the tumor and its vasculature by a cytotoxic T cell response against the survivin protein, which might lead to the activation of cellular apoptosis in cancer.

Thus, detection of survivin in the early stages of malignancies combined with these targeted therapies can provide alternative and efficient ways to treat cancers. This requires highly sensitive bio-sensing platform. At present, survivin is most often clinically identified by either using immunohistochemistry to detect the proteins or by detecting the mRNA with polymerase chain reaction (PCR) techniques[306]. To provide an order of magnitude of a clinically relevant sensitivity, we will consider the study by Morinaga et al, which studied the expression of surviving RNA in hepatocellular carcinoma (HCC) using calibrated RT-PCR[326]. They found a number of surviving copies in HCC tissues of about 10^6 copies / µg total RNA. Considering that one can extract about 70 µg RNA from a 10 mg tissue sample, our assay would need a limit of detection lower than 10^7 survivin RNA copies for a useful clinical test.

In the previous chapter, I have side-by-side compared the two energy transfer processes, FRET and WGET. On experimental basis, in addition to careful theoretical considerations, WGET could offer several advantages due to better efficiency and longer range of energy transfer, robustness and simplicity of the design, and higher sensitivity towards analytes. This motivates us to venture towards building a biological sensing (DNA sensing) platform based on surface functionalized WGET enabled microcavities. In this chapter, I will focus on designing a bio-sensing platform with the WGET enabled microcavities to detect the DNA analogue of survivin mRNA as DNA is more stable and easier to manipulate than RNA. After the development and optimization of the DNA assay, mRNA-based detection scheme can be targeted.

4.5 WGET MICROCAVITY DONOR:

In the last two chapters, the fabrication process and the energy transfer properties of QD-loaded microcavities have been thoroughly discussed. With the help of our understanding of the energy transfer processes through cavity resonance modes, here I will try to build a bio-sensing scheme based on these microcavities.

The first crucial step forward from our simple electrostatically assembled donor (microcavity) - acceptor (dyeNPs) conjugates is to provide biological specificity to the WGET pairs so that specific biological events or interactions can be detected. In order to achieve that, surfaces of both the microcavity and dyeNP have to be functionalized with biomolecules to enable specific interactions. Here, at first, I will discuss the surface modifications of the microspheres, later the surface nature of the acceptor dyeNPs and specific interactions between the donor-acceptor pair in the interest of bio-sensing will be discussed.

4.5.1 Strategy to functionalize the microspheres:

Many strategies are available to provide biological functionalities to the surfaces of micro-/nanostructures, most of which are decided depending on the electro-chemical properties of the surface as well as on the desired features.

4.5.1.1 Streptavidin-biotin interaction: A universal biotechnology technique

One of the frequently used techniques to introduce bio-functionality is to utilize streptavidin-biotin interactions[327,328]. Biotin (Vitamin B7 or H, see the structure in Figure 4.4) being a small molecule with a terminal carboxylic acid group that is accessible for bio-conjugation by reactions like amide, imine or ester mediated coupling provides opportunities for easy conjugation to proteins, antibodies, DNA and RNA without interfering with their structural and functional integrity.

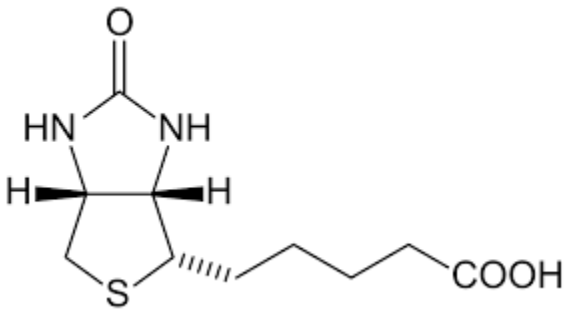

Figure 4.4: *Chemical structure of biotin (Source: Wikipedia)*

Streptavidin is a homo-tetrameric protein that has a very high affinity for biotin. This affinity is one of the strongest non-covalent interactions known in nature characterized by a dissociation constant of 10^{-14} mol/L[328]. Another important advantage of employing streptavidin-biotin interaction is the resistance of the complexes towards organic solvents, surfactants, extreme temperature and pH[329]. These extraordinary properties led the streptavidin-biotin complexes to be extensively used in many molecular biology and nano-biotechnology experiments. Many studies focusing towards understanding the origin of this extraordinarily high affinity between streptavidin and biotin have suggested that the shape of the binding pocket in streptavidin is highly complementary to the molecular shape of biotin. Moreover many direct and secondary H-bonding interactions in addition to van der Waals and hydrophobic interactions between biotin and the amino acid residues of streptavidin contribute to the high binding affinity[330]. The presence of four binding sites in the structure of streptavidin also facilitates the binding of biotin molecules. Furthermore, streptavidin being a protein of substantial size (66 kDa) has

abundance of amine and carboxylic acid groups that can also be directly or indirectly used for conjugation[331].

The polystyrene microspheres that were used for the WGET donor-acceptor electrostatic assembly in the previous chapter do not have any particular surface functionality that allows further modification of the surface, only the stability of the particles was ensured by the electrostatic repulsions between the sulfonate groups present on their surface. In this chapter, to impart biological functionality to the microcavities, I will start with microspheres that already have carboxylic acid groups on the surface which are accessible for further chemical modifications. These carboxylic acid groups can be reacted to the amine groups of streptavidin molecules via amide formation. Biotinylated biomolecules (biotinylated DNA strands for our purpose) can then be attached to the surface by exploiting the streptavidin-biotin interactions. As four binding sites are available in the streptavidin structure, even if one (or two) active sites are sterically or chemically inaccessible, there would still be remaining functioning pockets for the biotin binding.

4.5.2 Preparation of streptavidin functionalized QD loaded microcavities:

4.5.2.1 Loading QD525 into carboxylate microsphere:

An infusion process that is similar to the one used to load the non-carboxylated microspheres (Section 2.3, chapter 2) is also used here to load the carboxylated ones (average size = 10 µm) with QD525.

One drop (~ 40 µL) of 2.6% (w/v) aqueous suspension of carboxylated microspheres (~2×10^6) was taken in a 2 mL Eppendorf tube and 1 mL of ethanol was added to the solution and centrifuged at 2000g for 5 seconds. The liquid supernatant was discarded, and the solid precipitate of microspheres was dispersed in 1 mL infusion of butanol and chloroform (Butanol: Chloroform = 4:1) followed by mixing 10 µL of 12 µM QD525 solution (in $CHCl_3$) to the final concentration of 0.12 µM in the solution. The infusion was then mixed using a rotor at 50 rpm for 20 mins. The mentioned ratio of solvents (butanol and chloroform) resulted in homogenous and bright QD loaded microcavities.

In the next step, the QD loaded microspheres were separated from the free QDs by centrifuging the mixture at 2000g for 10 seconds, and after removing the liquid, 1 mL ethanol was added to the solution. This step was performed 5 more times to wash away most of the unloaded QDs from the sample. After

removing the ethanol from the solution in the final washing step, 40 µL of 50 mM pH 6.5 MES (4-morpholinoethanesulfonic acid) buffer was added to the microspheres.

4.5.2.2 Attaching Streptavidin to the surface of QD525 loaded carboxylated microsphere:

Most of the proteins such as streptavidin have free amine groups which can be reacted with carboxylic acid groups to form amide linkages by carbodiimide crosslinking chemistry[332].

Here, 1-Ethyl-3-(3-dimethylaminopropyl)carbodiimide.HCl (EDC.HCl) is used to first activate the carboxylic acid group to form an active o-acylisouera ester intermediate which can then be replaced by nucleophilic attack from primary amines forming an amide bond and an water-soluble isourea by-product (See Figure 4.5). The o-acylisourea intermediate that is unstable in aqueous media, hydrolyses to regenerate the carboxylic acid groups in absence of any amine to react with. EDC being water soluble allows the reaction to occur in aqueous medium whereas its alternative called dicyclohexylcarbodiimide (DCC) is used to perform the same in organic media[333].

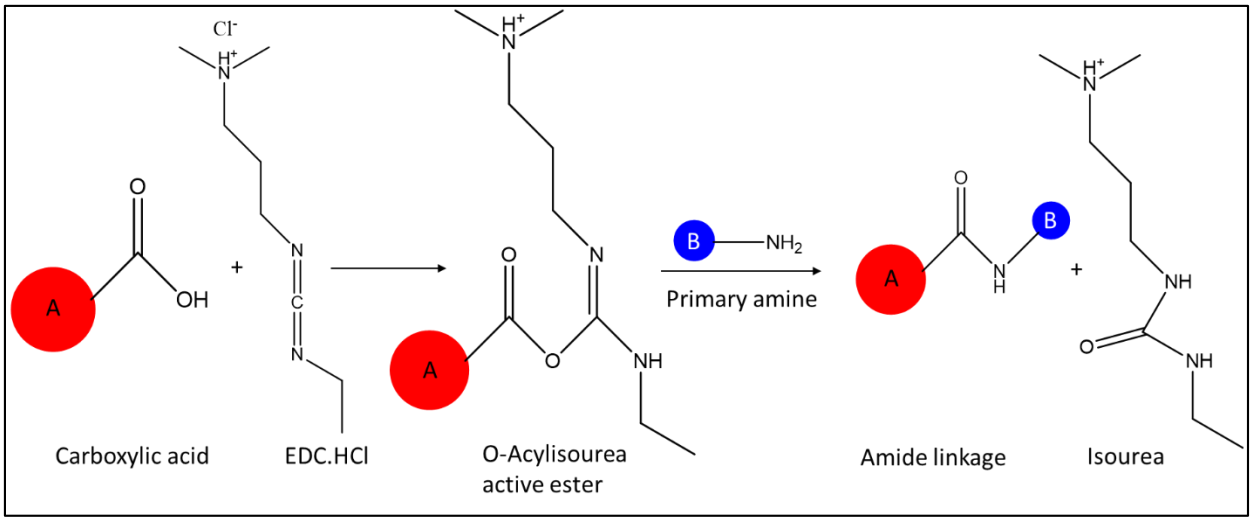

Figure 4.5: *Mechanism of EDC based carbodiimide coupling*

Coupling reactions with EDC works the best in slightly acidic pH conditions and in buffers such as MES (4-morpholinoethanesulfonic acid) buffers[334]. As in most of the cases, EDC comes with a molar equivalent of HCl which must be accounted for to maintain an optimum pH of the reaction medium.

For the purpose of EDC coupling with the carboxylated QD-loaded microspheres, first, a streptavidin solution at 5 g/L concentration was prepared in 50 mM pH 6.5 MES buffer; 45 µL of which was added to

the previously prepared (in previous section) 40 µL QD-loaded carboxylate microsphere solution (in 50 mM pH 6.5 MES buffer). The mixture was incubated at room temperature for 15 min. Then a solution of EDC.HCl was freshly prepared at a concentration of 5 g/L in 0.2 M pH 6.5 MES buffer, 72 µL of which was added to the incubating mixture. Then the reaction mixture (in an Eppendorf) was placed on a rotor at 50 rpm for 4 hours. Then some glycine was added with a final concentration of 100 mM to quench the reaction mixture.

The microspheres were then separated from the reaction mixture by centrifuging at 2000g for 20 seconds. The pellet of solid microspheres was then washed with 1X PBS buffer for 3 times and finally resuspended in 500 µL 1X PBS buffer containing 1% of bovine serum albumin (BSA), 1.5 mM $MgCl_2$ and 0.01 g/L Tween80 surfactant.

4.5.2.3 Detailed insights into the amide coupling: Comparing other ways of coupling

EDC mediated carbodiimide coupling being a very popular technique in biochemistry to work on proteins and enzymes, many variations of the technique are available in literature. Here, a few of the variations have been explored to determine which one leads to the best coupling result.

N-Hydroxysuccinimide (NHS) is an organic compound that is very commonly used in the carbodiimide coupling chemistry to increase the yield of the reaction[335]. NHS reacts with the o-acylisourea unstable intermediate to form a more stable ester that prevents vigorous hydrolysis of the intermediate and allows slower and more controlled reaction to the amine (see Figure 4.6 for the detailed mechanism)[334].

Here, I have compared three different strategies of the carbodiimide coupling with EDC and/or NHS on carboxylated microspheres (without QDs).

Strategy 1 would represent the reaction procedure mentioned in the last section (4.5.2.2). **Strategy 2** has everything same as strategy 1, except 1 mg of NHS (in solid form) is added to the incubating mixture of microspheres and streptavidin at the same time of adding the EDC.HCl (in MES). **Strategy 3** involves a more traditional approach where the carboxylic acid groups on the microspheres were first activated with EDC.HCl (in MES) and NHS (1mg) to form the stable NHS ester intermediate, followed by the addition of streptavidin for the nucleophilic substitution to occur. The amounts of all reactants, the reaction time, speed of rotation, temperature and all other conditions were maintained same for the simplicity of comparison. After the reactions have finished, the streptavidin functionalized microspheres were purified

using the same protocol as mentioned in 4.5.2.2 and the final pellet of microspheres were dispersed in 500 µL PBS (1X) with 1% BSA.

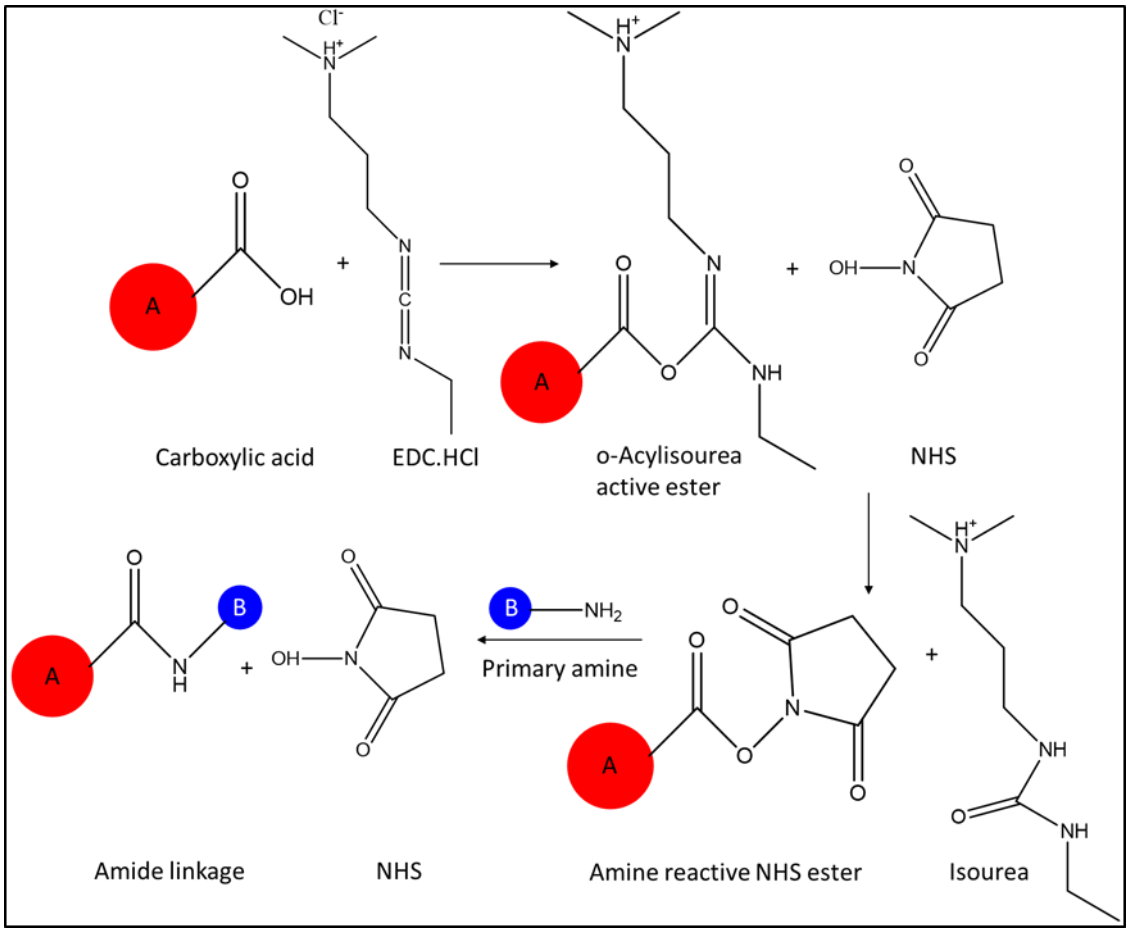

Figure 4.6: *Mechanism of carbodiimide coupling using EDC.HCl and NHS*

In the next step, the extent of coupling in each strategy is compared. Using protocol presented in the Annex, BSA molecules tagged with both biotin and cyanine 5 (Cy5) is prepared in PBS with the final concentration of 75 nM. Using EDC, NHS coupling chemistry, carboxylic acid functional groups on both Biotin and Cy5 can be activated to form NHS ester intermediates which can subsequently be reacted to the amines present in BSA protein molecules. Now 1 µL of Biotin and Cy5 tagged BSA (Bt-BSA-Cy5) solution is added to 10 µL of streptavidin functionalized microsphere suspension obtained from each of the three strategies and mixed well. The strong affinity of biotin molecules to streptavidin would help the Bt-BSA-Cy5 to adhere on the surface of the microspheres and the presence of Cy5 dyes should provide sufficient fluorescence signal to distinguish from the background. Additionally, a control mixture is prepared where

carboxylate microspheres with the same concentration and volume as the ones from the three strategies, but not conjugated to streptavidin, is mixed with 1 µL of Bt-BSA-Cy5 solution in order to be able to compare with the streptavidin functionalized microspheres.

Each of the microsphere sample was then studied under a wide-field microscope with a 100x NA 1.45 objective using a white lamp as excitation source. A filter set (exc: 620-60, dichroic: LP660, em: 700-75) was utilized to exclusively observe the fluorescence of Cy5. The images of the microspheres were projected, and their intensities were recorded with a CCD camera.

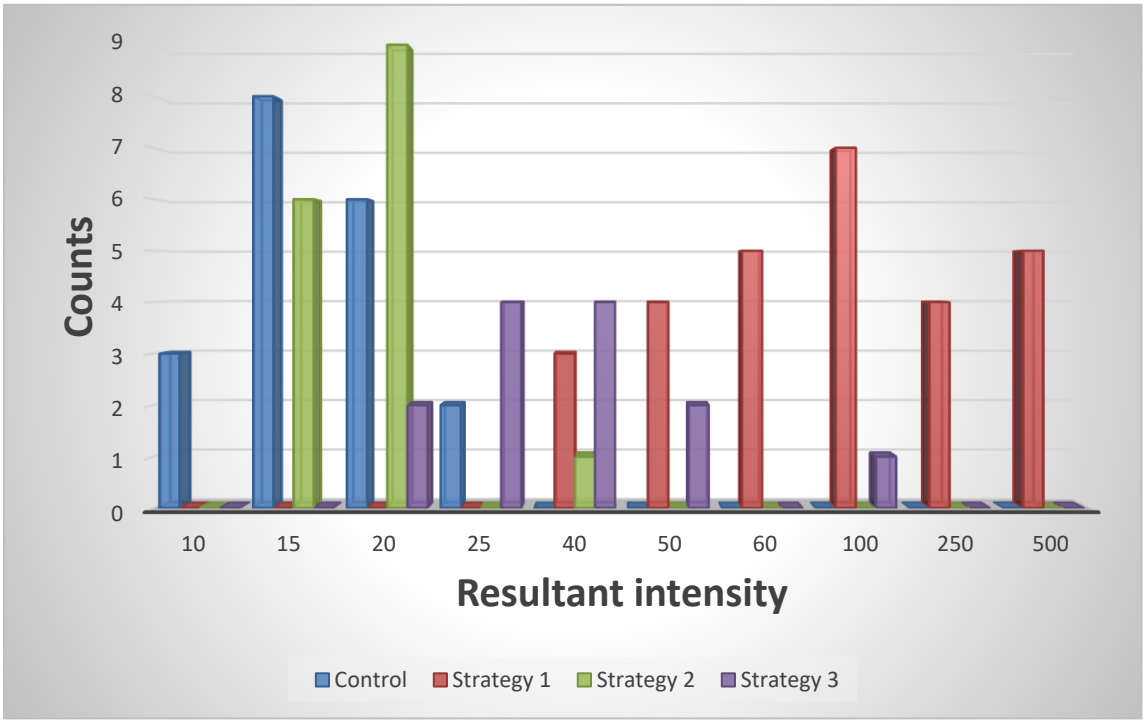

	#of microspheres	Mean intensity	Standard Deviation
Control	19	16.84	4.48
Strategy 1	28	172.14	169.21
Strategy 2	16	19.38	6.02
Strategy 3	13	38.46	21.35

Figure 4.7: *Cy5 fluorescence intensity distribution of microspheres obtained from different streptavidin coupling strategies.*

The Cy5 intensity distribution of several (13-28) microspheres for each sample (Figure 4.7) suggests that the reaction strategy 1 (EDC-only; procedure 4.5.2.2) yields in the best coupling results among all the strategies performed. As observed in Figure 4.7, the microspheres in the control experiment (with carboxylated microspheres) results in the lowest adsorption of Bt-BSA-Cy5 as expected intuitively. Use of NHS (in strategy 2 and 3) provided a functionalization that was significantly different from the control but did not improve the coupling with Bt-BSA-Cy5 compared to the first strategy (EDC only). The microspheres from the first strategy have more than four times Cy5 intensity than the microspheres obtained from NHS mediated coupling. It is difficult to pinpoint a particular reason for this significant difference.

This might have happened due to interactions between the streptavidin molecules and the microspheres during the first incubation step, and/or electrostatic interactions between the overall negatively charged proteins and the activated EDC esters, which are positively charged, in contrast to NHS esters which are neutral. The samples are quite inhomogeneous however, as can be observed from the important standard deviation. Further development should try to improve the reaction conditions (mixing rate, incubation time, protein:microsphere ratio) to yield more homogeneous microsphere functionality.

However, this experiment not only supports that the chosen coupling strategy (in 4.5.2.2 section) leads to a great extent of coupling compared to the other ones but also helps to verify the presence of functional biomolecules (streptavidin proteins) on the surface of microsphere which can engage in specific biological recognitions. In particular, streptavidin remains bound to the microspheres despite the presence of 1% w/v BSA in the solution. This suggests that streptavidin is covalently coupled and does not desorb from the microsphere surface, since it would have most likely been replaced with BSA otherwise. In the next sections, these microspheres will be utilized for bio-sensing purposes exploiting the advantages of the whispering gallery evanescent field as well as the specificity derived from the surface bio-functionalities.

4.6 WGET ACCEPTORS: DNA FUNCTIONALIZED DYENPS

After the fabrication of optical donor microcavities with biological functionalities, the next in line is the optical acceptors that can act as the complementary part in the WGET DNA bio-sensor system. In the previous chapter, polymeric dyeNPs that are bright and with high absorption cross-section were used as acceptors in the electrostatic assembly with the PEI coated microcavities. The preparation protocol of those dyeNPs can be slightly modified to introduce biological functionality, for example, to conjugate with polynucleotide single strands so that they can be used as acceptor probes in the DNA sensing assay with

bio-specificity towards target DNA, retaining all the other advantages. The nanoparticles that are utilized for the following experiments, have been provided to us by a group in LBP, university of Strasbourg (Dr. Nina Melnychuk, Dr. Andreas Reisch and Dr. Andrey Klymchenko).

In the first step, acceptor dyeNPs were prepared with azide functional groups on the surface that can later be used to graft DNA strands.[314] 100 µL of the poly (methyl methacrylate)-aspartic acid azide (PMMA-AspN_3) polymer solution in acetonitrile (2 mg mL^{-1} with 30 wt% R18/F5-TPB relative to the polymer) were added quickly using a micropipette to 900 µL of 20 mM phosphate buffer, pH 7.4 at 21 °C under shaking with Thermomixer (1,100 rpm). Then, the residues of acetonitrile were evaporated. This process is called nanoprecipitation and it yields in dye loaded polymeric nanoparticles with functional azide groups for further conjugation (see Figure 4.8).

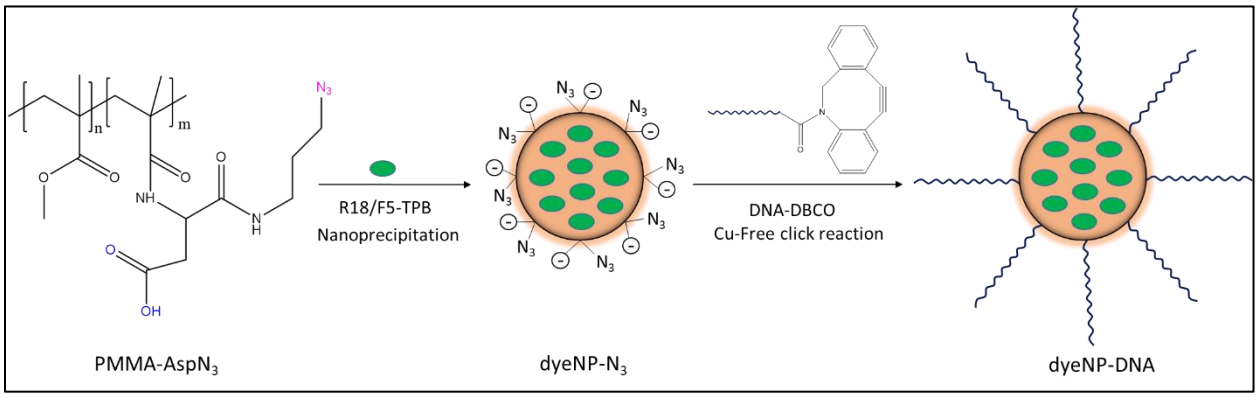

Figure 4.8: *Synthesis scheme of DNA functionalized acceptor dyeNPs*[314]

In the next step, DNA strands are reacted to the azide groups of the dyeNPs via DBCO mediated Cu-free click chemistry to prepare the dyeNP-DNA acceptor probes (see Figure 4.8). Three batches of dyeNPs, each functionalized with one kind of polynucleotide sequences (A20, T20 and surviving capture probe) were prepared to be used in the following DNA sensing assays. In the next sections, the structural and hybridization properties of these three DNA sequences will be elaborately discussed. Even though the sequences of DNA in each batch of dyeNPs are quite different but same reaction procedure was followed to attach them to the dyeNPs. Aliquots of DNA were added to 200 µL of nanoparticles with the final concentration of DNA in the solution to be 23 µM. The reaction was incubated overnight at 40 °C in Thermomixer without shaking and protected from light. Then the reaction mixture was cooled down to room temperature and diluted with 20 mM phosphate buffer and purified by centrifugation using centrifuge filters (Amicon, 0.5 mL, 100k) at 1000 g and 20 °C for 2 min. The procedure of centrifugation

was repeated 5 times to remove the unreacted oligonucleotides. Then the dyeNP-DNA acceptor probes were stored with the final volume of 1 mL in the dark at 4°C.

The particles are found to be 41 ± 12 nm in size (from TEM), and each particle is estimated to contain 3200 ± 400 dyes that makes them many times brighter than regular single dyes used in energy transfer experiments[314]. Moreover, the quantum yield of these particles was estimated to be ~46%, thus they are advantageous as fluorescent acceptors. There are 110-120 DNA strands per particle for each of the dyeNP batches.

4.7 A WGET BASED MODEL BIO-SENSING: SENSING DNA HYBRIDIZATION

After the successful functionalization of QD loaded microspheres with streptavidin molecules, now our main motivation will be focused on applying them for bio-sensing. Before going into complex applications, it is of great importance to first study the system in a simpler format for better understanding. Here in this section, I would focus on designing an assay to detect DNA hybridization between two simple single model strands. The QDs inside the microcavity would act as the optical donor whereas DNA functionalized probe dyeNPs would be used as optical acceptor. The emission from the QDs would be coupled to WGMs which would mediate the energy transfer (WGET) from the donor to the acceptor dyeNPs. This model DNA sensing is performed in two different schemes which are the following.

4.7.1 Scheme 1: Increasing the amount of DNA functionalized acceptor.

Figure 4.9 represents the scheme to detect the hybridization between two full complementary single strands respectively called A20 and T20. As their name suggests, A20 consists of 20 adenine nucleotides whereas T20 is composed of 20 thymins. As shown in the scheme, first, streptavidin functionalized QD loaded microspheres are mixed with biotinylated A20 DNA in PBS buffer (for each 10 µL of bio-functionalized microspheres from section 4.5.2.2, 6.7 µL biotin-A20 at 0.08 mM concentration was added). A few (seven for this experiment) different aliquots were prepared with the same ratio of microspheres and biotin A20 DNA solution. Then the aliquots were incubated for half an hour at room temperature to ensure the biotin-DNA adsorption on the surface of the microspheres. After that, progressively increasing volumes of dyeNPs at 1 nM concentration were added to the aliquots and incubated at room temperature for one hour for the hybridization to occur. The T20 DNA attached to the dyeNPs should hybridize to the

biotinylated A20 DNA, forming a complex (see Figure 4.9) that acts as a bridge between the donor microcavity and acceptor dyeNP and facilitates WGET mediated energy transfer.

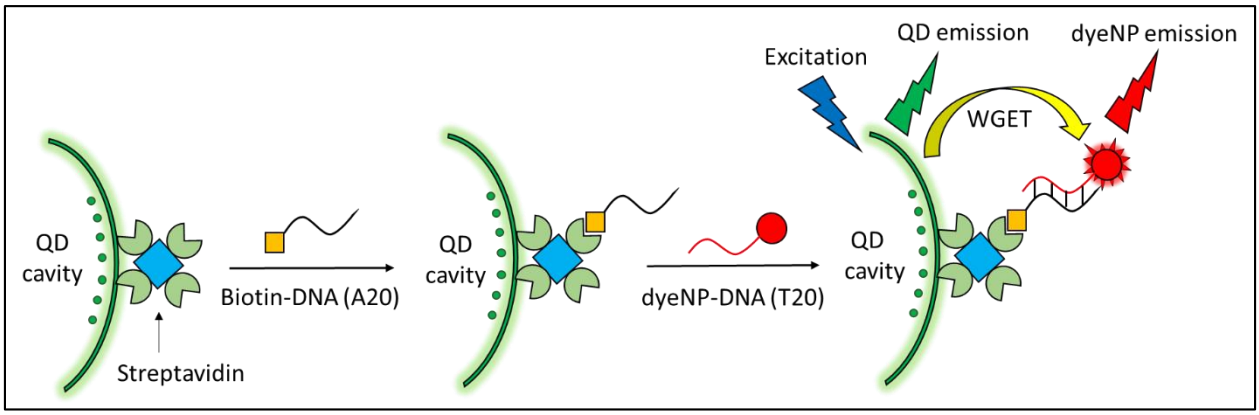

Figure 4.9: *The scheme 1 of the model DNA hybridization sensing using WGET cavity where the acceptor concentration is varied.*

4.7.1.1 Study on confocal microscope:

The microspheres were studied under a confocal microscope using the 405 nm laser as excitation source for the QDs. The confocal microscope was combined with a spectrophotometer that allowed to record the emission spectra of these microsphere samples from the confocal volume on the equator of these microspheres. The emission spectra have the same feature as the electrostatically conjugated QD-microcavity and dyeNP system; the spectrum consists of a broad envelope appearing from the free space emission and on top of it, there are regularly spaced sharp whispering gallery mode peaks. Moreover, the spectrum consists of two emission regions, arising from QDs and dyeNPs as expected.

Figure 4.10 (A) shows representative emission spectra from individual microspheres corresponding to increasing concentration of dyeNP-T20 that the QD emission is quenched, and acceptor fluorescence enhanced as dyeNP-T20 concentration is progressively increased. At higher dyeNP concentration, even the WGM peaks at QD emission range totally disappear suggesting their significant engagement in energy transfer. Figure 4.10 (B) shows the progressive increase in the dyeNP to QD emission intensity ratio (averaged over ~ 15 microspheres for each concentration) with the concentration of dyeNPs. A control experiment was performed where the dyeNP-T20 was substituted with dyeNP-A20 that being fully non-complementary to the biotin-A20 attached on the microsphere surface, should not hybridize together. The control experiment has really negligible dyeNP to QD emission intensity ratio (see Figure 4.10 (B))

that is in the same order as only QD loaded microspheres. This suggests low non-specific interactions between the microcavity-Biotin A20 and dyeNP-DNA system.

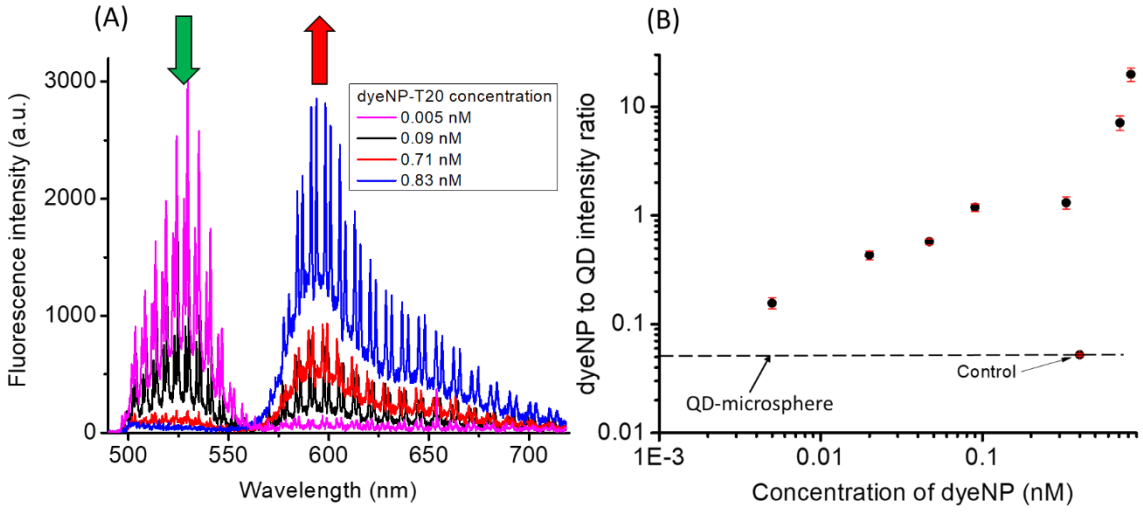

Figure 4.10: *(A) The emission spectra of microsphere samples with progressively higher amount of dyeNP-DNA in the confocal microscope, (B) corresponding dyeNP to QD emission intensity ratio vs the concentration of dyeNPs.*

4.7.1.2 Study on wide-field microscope:

As the experiments performed on the confocal setup resulted in very sharp and distinct changes in the signal due to the DNA hybridization process, a simpler experimental platform might also be able to detect these changes. Thus, the experimental setup is moved one step towards simplicity, to a wide-field microscope, to measure the same samples of streptavidin functionalized microspheres mixed with different amount of DNA-dyeNPs.

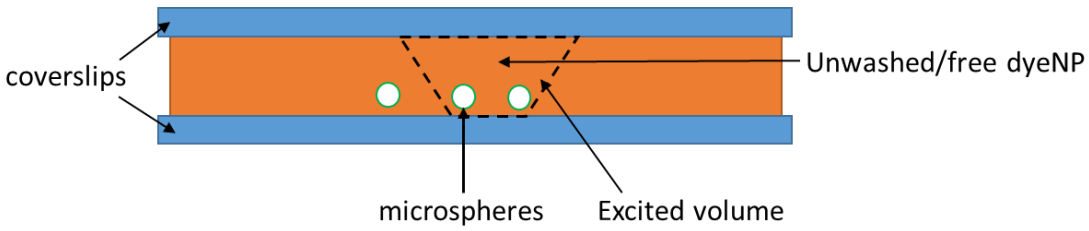

Figure 4.11: *Sample holding configuration (sandwiched between two glass coverslips) for the study with wide-field microscope.*

A droplet of the solution is placed in between two coverslips with a 170 µm spacer as seen in Figure 4.11. The volume of excitation that is approximately 10^{-3} µL lies within the cone. The fluorescence was acquired with a 40x NA 0.6 air objective and 450 nm excitation (using a white lamp) from the regions that contain

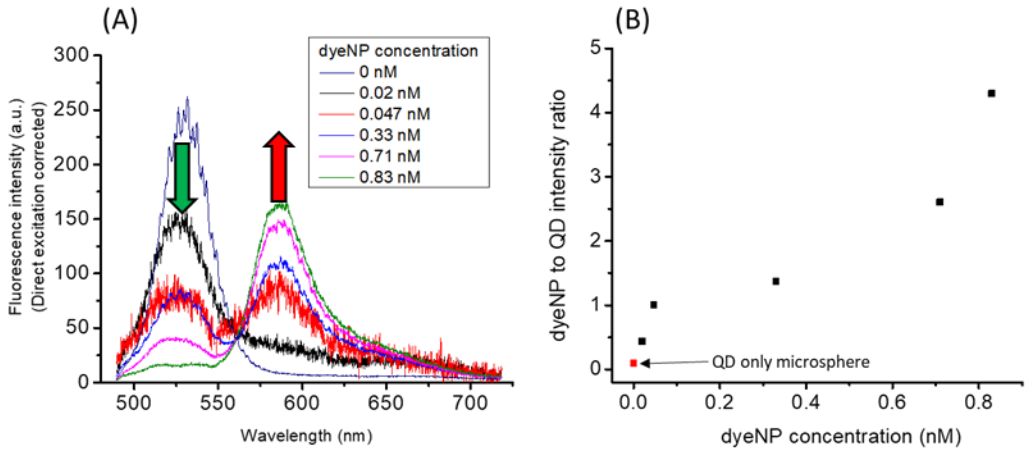

Figure 4.12: *(A) Area normalized emission spectra of microsphere samples with progressively higher amount of dyeNP-DNA in the wide-field microscopy setup, (B) corresponding dyeNP to QD emission intensity ratio vs the concentration of dyeNPs.*

1-3 microspheres and sent to a spectrophotometer via an optical fiber for the recording of the emission spectra (see Figure 4.12 (A)) that showed similar results as in the confocal microscope. The detected global intensity varies because of different number of microspheres in the field of view for each sample. To account for this, all the emission spectra represented in the Figure 4.12 (A) are area (under the curve) normalized. Due to specific hybridization interactions, the DNA-dyeNPs should effectively bind to the surface of the DNA functionalized microspheres, thus the acceptor signal should be well-distinguishable from the background signal of free dyeNPs in the solution. The emission spectra in Figure 4.12 are corrected for the direct excitation of dyeNPs in solution at the same concentrations. As evident from the graph Figure 4.12 (B), the dyeNP to QD intensity ratio increases with the dyeNP concentration, similar to the observations on confocal microscope. The progressive quenching of QD emission accompanied by the increase in the dyeNP emission suggests that the DNA hybridization can be easily detected even in solution using a simpler microscope setup.

4.7.1.3 Study on spectrofluorometer:

After the successful detection of DNA hybridization using the simple wide-field microscope setup, it is indeed intriguing to attempt to perform the experiment in even simpler fashion. In the next step, instead of measuring fluorescence from the confocal volume at the surface of a microsphere or from a collection of a few microspheres, the emission spectra from the whole solution are measured in order to see if the signature of DNA hybridization can be observed.

In order to do that, the microsphere samples mixed with different amount of DNA attached dyeNPs (as used in previous two parts) were put in a quartz cuvette (volume = 700 µL, optical path length = 10 mm) and some PBS buffer was added to maintain the total volume of each solution at ~ 200-225 µL. Then the cuvette was placed in a spectrofluorometer to record the fluorescence of the whole solution using a xenon lamp to excite at 420 nm.

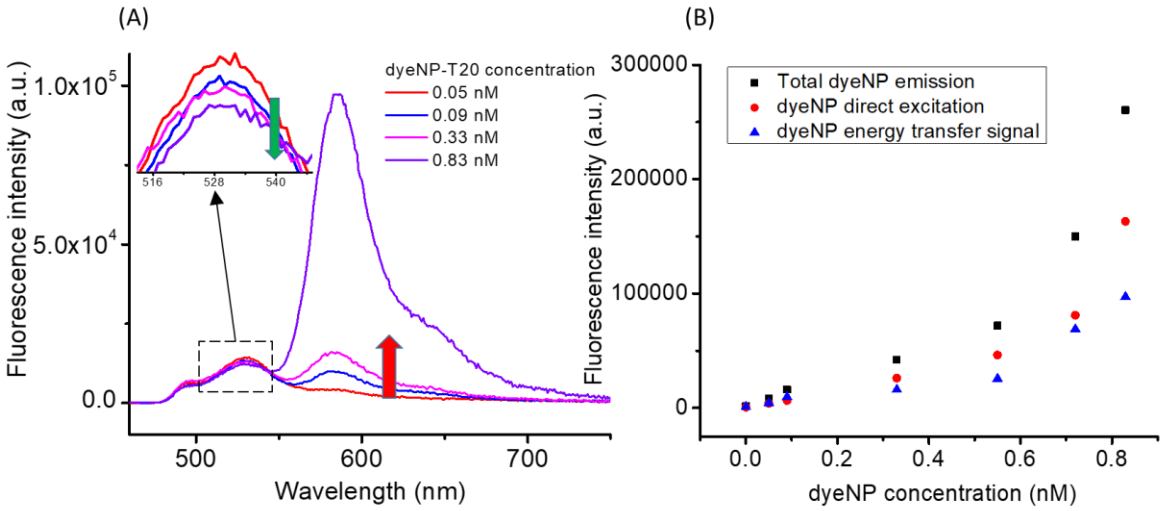

Figure 4.13: *(A) The emission spectra of microsphere samples with progressively higher amount of dyeNP-DNA in the spectrofluorometer, (B) comparison between the total acceptor signal and acceptor direct excitation for each sample, and the corresponding energy transfer intensity.*

A 485LP emission filter was used to exclude the scattering from the large microspheres. The representative fluorescence spectra of some of the samples with increasing concentration of dyeNP-T20 can be seen in Figure 4.13 (A). As most of the fluorescence coming out of the dyeNPs is due to direct excitation at high dyeNP concentrations, the change in dyeNP or QD emission due to energy transfer is difficult to distinguish from the spectra. But the inset on the left top corner of the Figure 4.13 (A) that is

focused on the QD emission region, shows the progressive quenching of the QDs. Moreover, as the concentration of dyeNP is increased, the significant emission tail of the dyeNP emission towards the QD side should contribute to the measured QD emission intensity. All the spectra were corrected to remove the remaining scattering from the microsphere. The process of spectral unmixing was used to perform this correction where emission spectra of empty microspheres (same concentration as the experiment samples), the QDs in hexane, and dyeNP in water were used altogether as the reference spectra of each component. Direct excitation signals from the dyeNPs for each sample were measured by keeping all the conditions same as their experimental counterpart only except by replacing the A20 biotin attached streptavidin (QD loaded) microcavities with the same amount of carboxylate microspheres without any QDs. How the total dyeNP emission intensities compare with the direct excitation signals can be found in Figure 4.13 (B). The sensitized intensity is calculated by subtracting the direct excitation from the total emission signal, is shown to increase as the acceptor concentration increases.

Overall, this set of experiments suggests that DNA-dyeNP hybridize to DNA-QD-microsphere in a specific manner, and that this induces changes in the fluorescence emission spectrum that are observable at the single microsphere and ensemble levels.

4.7.2 Scheme 2: Gradually increasing the amount of Biotin-DNA.

In order to better separate energy transfer-sensitized emission of the dyeNP from their direct excitation, the experiment to detect the hybridization of A20 and T20 DNA was also performed in a different format. Here, the concentration of biotinylated DNA was gradually increased, while keeping the amount of dyeNPs and streptavidin functionalized microspheres constant (See scheme 2). This way, we ensure that changes occurring during the experiment originate from the assembly of dyeNP onto the microspheres, and from the potential energy transfer.

For this experiment, several aliquots were prepared by mixing 10 µL of the streptavidin attached microsphere solution (~4000 microspheres) and 10 µL of 0.1 nM dyeNP-DNA (T20). Then different amount of biotin-A20 (in PBS) solutions were added to each of the aliquots and incubated for an hour for the DNA hybridization to occur such that the donor (QD-microcavity) and acceptor (dyeNP) systems are conjugated by the streptavidin-biotin attached DNA duplex. As more biotin-A20 molecules are added, there should be more of this complex formation, leading to higher rate of energy transfer. The number of biotinylated DNA per microsphere in the solution was varied from 0 to 10000. As a control experiment, dyeNPs

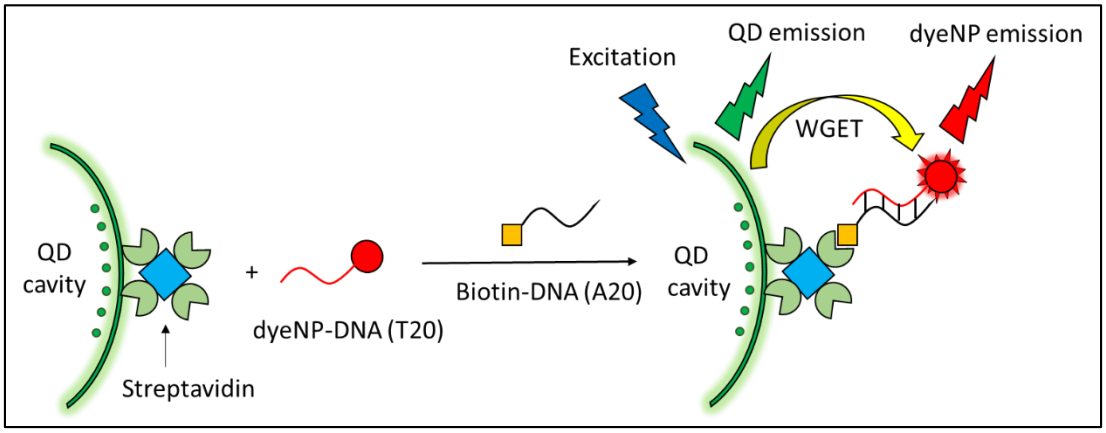

Figure 4.14: *The scheme 2 of the model DNA hybridization sensing using WGET cavity where the concentration of biotinylated DNA is varied.*

attached to A20 DNA were used in the solution which should not engage in the hybridization process with the A20-biotin molecules on the surface of microspheres. Rest of the aspects of the control experiment were kept same as the experiment.

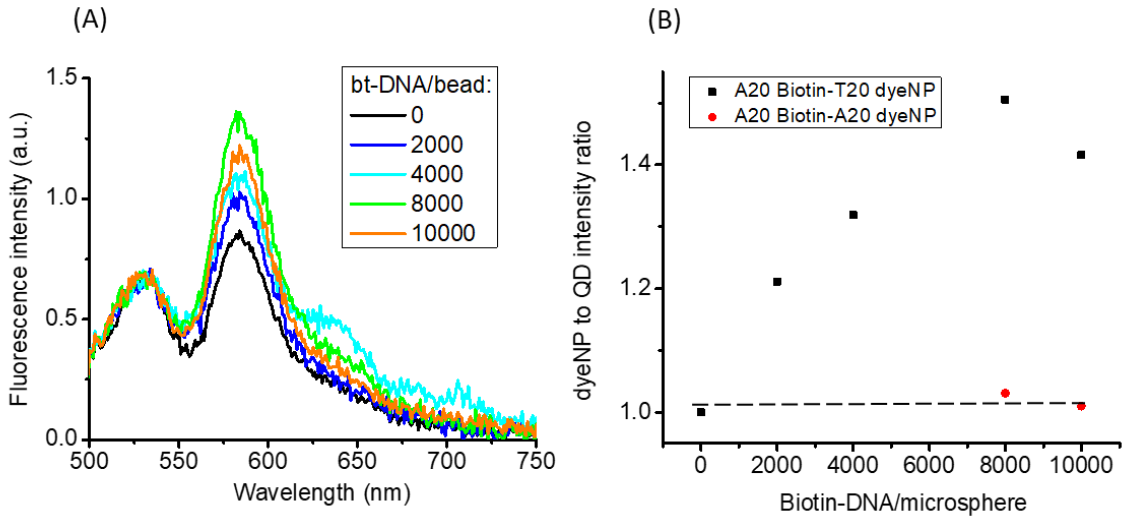

Figure 4.15: *(A) The emission spectra (normalized to the QD emission intensity) of scheme 2 samples varying the amount of biotin-A20 DNA, (B) dyeNP to QD emission intensity ratio (normalized at the first data point where the number of A20 biotin =0) for the experiment and the control (the dotted line emphasizes the negligible change in the intensity ratio for the control experiment).*

The emission spectra for the experiment are normalized to the QD emission maxima to eliminate the fluctuations in the global intensity profiles (see Figure 4.15 (A)). It can be seen from the spectra (Figure 4.15 (A, B)) that as the number of the biotin-A20 DNA is increased in the solution, the dyeNP to QD emission intensity ratio also increases, implying higher extent of DNA hybridization. In case of the control experiment, the change in the intensity ratio of dyeNP to QD is negligible (see Figure 4.15 (B)). This suggests that the detection scheme can specifically detect the hybridization between two complementary DNA strands.

4.8 Assay to detect survivin target DNA strand

After the successful demonstration of the model bio-detection scheme of DNA hybridization between A20 and T20 DNA strands, the next goal is to develop a microcavity based biosensor for detecting survivin DNA target strand. It has also been performed in two different schemes.

4.8.1 Scheme 1: Increasing the amount of DNA functionalized acceptor.

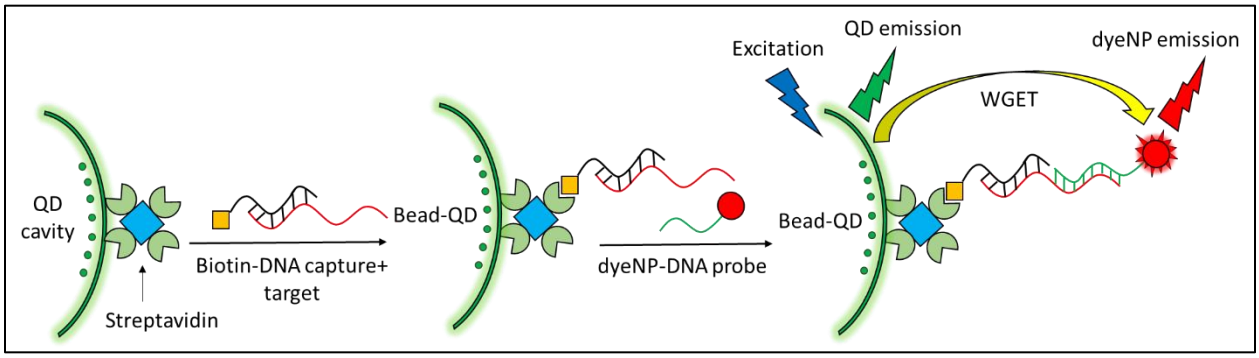

Figure 4.16: *The scheme 1 to detect survivin target DNA using WGET cavity where the dyeNP-DNA probe concentration is varied.*

The first detection scheme is a crucial step that would help us to verify the hybridization of the target DNA to both capture probes, and also find an optimum microsphere to dyeNP ratio for the next detection schemes/experiments. The detection scheme has been elaborated in the Figure 4.16, where in the first step, the biotinylated DNA capture probe (2 µL at 10 µM) and target DNA (20 µL at 1 µM) are mixed for 1 hour in 1:1 equivalent to prepare the pre-hybridized DNA duplex, which then added to the solution of

streptavidin functionalized QD530 loaded microspheres (100 µL volume or 4×10^5 microspheres). After the incubation of the mixture, the microspheres are washed with 1X PBS buffer (containing 1.5 mM $MgCl_2$ and Tween80 0.01 g/L) for 3 times with a centrifuge at 2000g for 30 seconds and finally redispersed into 100 µL PBS buffer (with 1.5 mM $MgCl_2$ and Tween80 0.01 g/L). In the next step, few aliquots are prepared with 10 µL of the (above prepared) microsphere solution and increasing volumes of 1 nM dyeNP-survivin probe DNA such that the probe strand on the dyeNPs can hybridize with the remaining single strand terminal of the target and form a sandwich complex. As a control experiment to differentiate between specific and non-specific interactions, a set of aliquots were prepared where everything was used exactly the same as the experiment, except microspheres with A20 biotin were used instead of the prehybridized biotin capture-target DNA attached microspheres. As biotinylated A20 DNA is not complementary to the probe DNA on the dyeNPs, they should not hybridize together and form sandwich complex.

The sequences of the target (bottom strand), biotinylated capture (top left) and the dyeNP attached probe (top right) are given here in the Figure 4.17. The red box indicates the complementary parts between the biotinylated capture and the target, and the green one shows the complementary sequential part between the dyeNP and the target DNA.

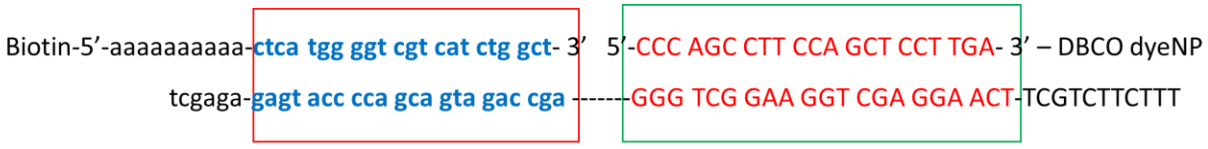

Figure 4.17: *The sequence of survivin target (bottom row), and the capture and probe DNA attached to respectively biotin and dyeNPs (top row).*

The spectra for the experiment and the control both shows the quenching of the QD intensity, but the extent of quenching is higher in case of the experiment (see Figure 4.18 (A, C and D)). The significant quenching of QD emission in case of the control experiment can be attributed to the non-specific binding of dyeNP-probe DNA onto the microspheres. The dyeNP to QD intensity ratio vs. volume of added dyeNP (at 1 nM concentration) graph shows a drastic difference between the experiment and the control which suggests that specific hybridization significantly increase the number of dyeNP in close proximity to the microsphere surface. The slight slope in the control line suggests some contributions from non-specific binding and the direct excitation of the dyeNPs.

From the observation of this experiment, I will select 1 µL as the volume of dyeNP stock solution to add to 10 µL of microsphere solution, where the change of QD emission quenching and dye to QD intensity ratio is not saturated and significantly different from the control conditions.

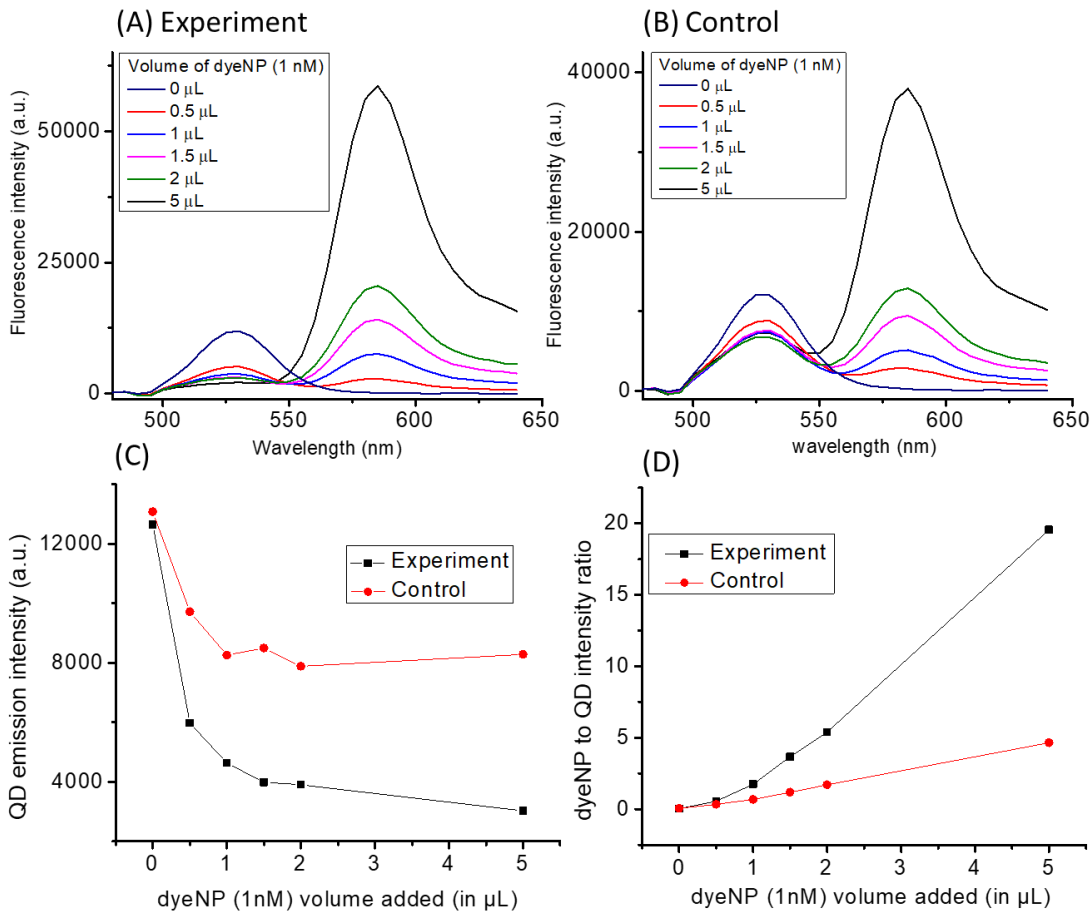

Figure 4.18: *The emission spectra of (A) the experiment, and (B) the control for survivin target detection scheme 1 where the concentration of dyeNP-DNA is varied. The comparison between the experiment and control in terms of how (C) QD emission intensity, and (D) dyeNP to QD intensity ratio vary with amount of dyeNPs-DNA in the sample.*

4.8.2 Scheme 2: Varying the target concentration in the solution.

The detection of survivin DNA strand was then performed in another scheme that is much closer to the real detection scenarios. In this scheme, at first, the streptavidin functionalized microspheres were conjugated to biotinylated capture probes, then dyeNP-probe DNA strands are added to it. When target strands are added to the solution, they should hybridize to the capture and probe DNA forming a sandwich complex between the donor cavities and the acceptor dyeNPs. As more target strands are added, the extent of hybridization would increase, enhancing the energy transfer from the QDs to the acceptor as seen in the Figure 4.19.

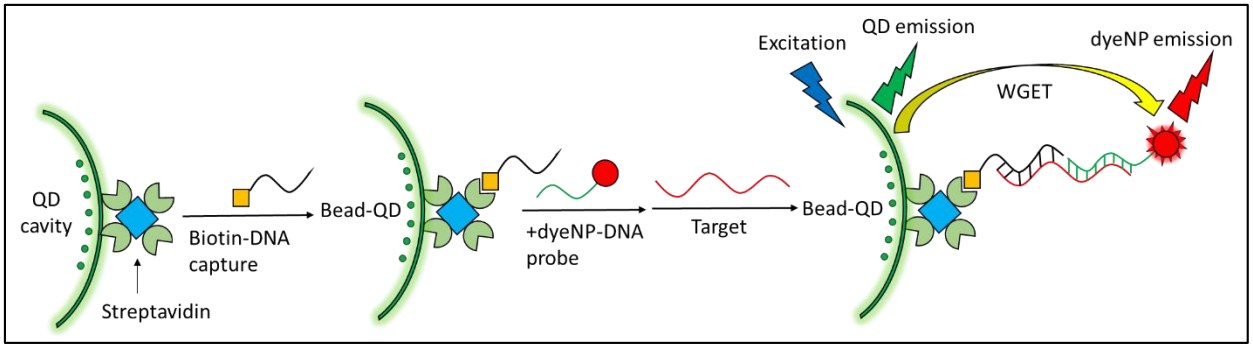

Figure 4.19: *The scheme 2 to detect survivin target DNA using WGET cavity where the target concentration is varied.*

For the experiment, first 200 µL (8×10^5 microspheres) streptavidin functionalized microsphere (loaded with QD530) solution was incubated with the solution of biotinylated survivin capture probe (4 µL at 10 µM concentration) for 15 mins. The medium of the incubation is 1X PBS (1.5 mM $MgCl_2$, 0.01 g/L Tween80). After the incubation, the microspheres were separated from the unbound biotinylated DNA and washed twice with 1X PBS (1.5 mM $MgCl_2$, 0.01 g/L Tween80) and redispersed in 200 µL of the PBS buffer. Then, 10 µL of that microsphere solution is taken in a cuvette and 1 µL dyeNP-survivin probe at 1 nM (in PBS) concentration was added to it. 190 µL PBS (1X, 1.5 mM $MgCl_2$, 0.01 g/L Tween80) was also added to the solution to maintain the measurable volume (at more than 200 µL). Then solution of target DNA strands (in PBS 1X containing 1.5 mM $MgCl_2$, 0.01 g/L Tween80) was gradually added to the cuvette and the mixture was incubated for 1 hour after each addition and the fluorescence from the whole solution is measured in a spectrofluorometer.

The fluorescence emission spectra obtained from the solution gradually increasing the number of the targets is shown in the Figure 4.20 (A). As the target concentration increases, the emission intensity of the QDs is quenched but the expected re-emission from the dyeNPs is not observed.

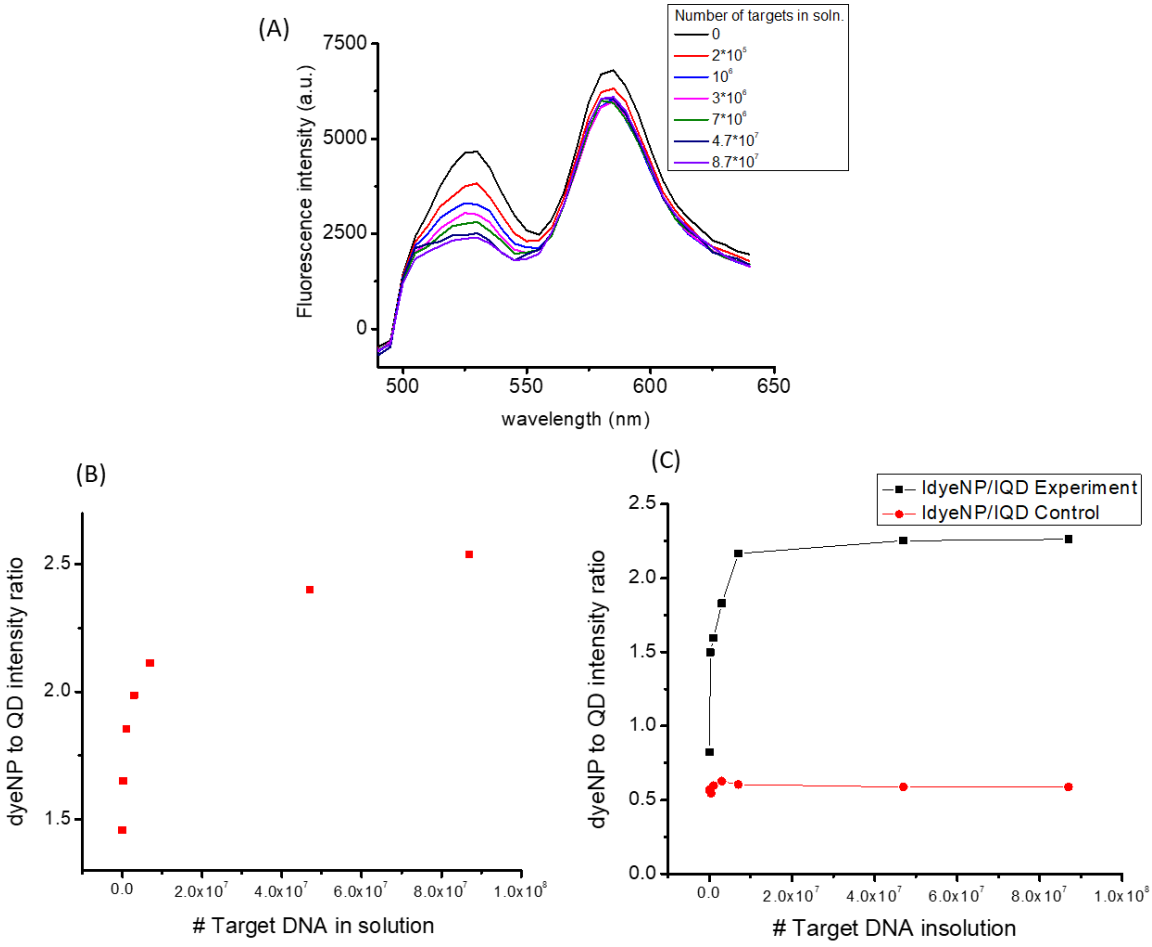

Figure 4.20: *(A) Emission spectra of scheme 2 (survivin detection) samples where concentration of target strands in varied, (B) How dyeNP to QD intensity ratio varies with the number of target strands in a typical experiment, (C) The comparison of dyeNP to QD intensity ratio vs. the number of targets in case of experiment and control.*

The ratio of dyeNP to QD intensities first increases linearly as more target DNA copies are added to the solution, suggesting the formation of the energy transfer sandwich complexes. After reaching a certain threshold, the intensity ratio saturates which suggests that the maximum possible quenching through the energy transfer from QDs to the dyeNPs has been reached (See Figure 4.20 (B)). A control experiment was

performed to verify that the quenching of QDs that is observed here is due to specific interaction (formation of sandwich complexes) rather than non-specific binding activity and/or other sources. For the control experiment, the mixture of microspheres and dyeNP-probe DNA were prepared that is exactly same as used for the experiment, but the only difference is that no target DNA is added to the mixture. If non-specific interaction is the cause of the QD emission quenching, then the dyeNPs would in the course of time interact or adsorb on the microspheres, leading to the similar quenching of QDs. Thus, just to make the procedure for the control similar to the experiment, the solution was incubated for 1 hour and mixed with a pipette before recording each emission spectra. Each of these emission intensities would represent the control values on the curve (to compare with the values on the experiment curve). The control curve shows negligible changes (see Figure 4.20 (C)) in comparison to the curve obtained from the addition of targets (the experiment curve) to the solution which suggests that the change in dyeNP to QD intensity in case of the experiment has arisen from specific DNA sandwich formation between the probe, capture and the target.

4.8.3 Limit of Detection:

After the successful demonstration of WGET mediated survivin target DNA sensing, the next goal is to find out how sensitive this detection scheme is! The sensitivity of the system can be quantitatively represented with the limit of detection (LOD), which in general shows the minimum amount of target that can be detected using this technique with negligible error. Thus, measuring LOD requires us to perform the experiment few times in similar conditions so that the statistical error value of each measurement can be obtained, and repeatability can be estimated.

Several experiments were performed to observe the change in dyeNP to QD emission intensity ratio with the number of targets in the solution. Even though the shapes of these curves are similar (with the same value of target DNA copies where the curves saturate), the amplitude of response to the addition of targets vary in the linear part of the curve as can be seen in Figure 4.21 (A). This is probably due to the variation in the initial dye/QD ratio originally from dilution/pipetting errors at these very low concentrations. In order to ensure more reproducible evolution of the curve, the volumes of microsphere solution and dyeNP was adjusted to start with a fixed initial ratio of dyeNP to QD intensity for all the experiments.

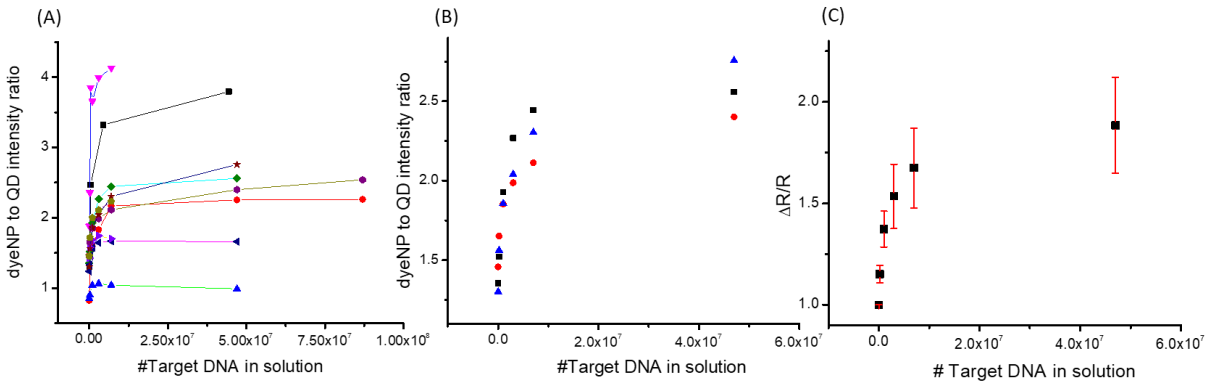

Figure 4.21: *(A) dyeNP to QD intensity ratio vs. the number of target strands obtained from several experiments without controlling the starting intensity ratio. (B) dyeNP to QD intensity ratio vs. the number of target strands obtained from three experiments with similar starting intensity ratio, (C) The average dyeNP (from the data in 4.21 (B)) to QD intensity ratio vs. the number of targets.*

Then, the experiment was performed 3 times to calculate the limit of detection (LOD) of the target in the solution (see Figure 4.21 (B)). Later the curves were averaged together (see Figure 4.21 (C)) to find the error values (standard deviation or σ). The limit of detection can be calculated as,

$$LOD = \frac{3\sigma}{Slope\ of\ the\ curve}$$

The LOD of targets was calculated by considering the slope and standard deviation from the first two points of the curve and it was found to be 1.68 × 10^5 targets in the whole solution = 42 targets/microspheres (A direct count under wide field set up suggests that 4000 microspheres are present in the solution). Moreover, the dyeNP to QD intensity curve starts to show saturation when there are 100-200 target copies/microsphere is present in the solution.

4.8.4 Discussion:

In the previous section, I have demonstrated a WGET based sensing platform to detect survivin target DNA strands using QD loaded microcavities as optical donors and DNA functionalized dye loaded nanoparticles as optical acceptors. The sensing procedure is as simple and user-friendly as homogenous one step FRET assays. Additionally, the strategy possesses very high sensitivity and specificity towards the target DNA strands with LOD reaching clinically relevant value, on the order of 10^5 target DNA strands,

compared to 10^7 target survivin strands that can be extracted from a tumor tissue sample. In comparison, the most recent developments in mRNA QD-based FRET sensor yield a LOD of about 250 amol, or about 10^8 copies based on a lanthanide-to-QD FRET assay[336]. Our greater sensitivity is achieved thanks to the highly delocalized nature of our WGM donors. Indeed, several million QDs participate in exciting one WGM donor, providing extremely bright donors. Therefore, a very small number of donors (4000 microspheres) is enough to provide a bright detectable signal. Also, the large absorption coefficient of the acceptors makes energy transfer very efficient: only 100-200 dyeNPs per microsphere are enough to saturate the energy transfer.

Still, there are a few observations that should be discussed to provide us a more comprehensible understanding regarding the sensing mechanism.

4.8.4.1 Insights into the quenching of donor QDs.

From the DNA (A20 T20 hybridization and detection of survivin target) sensing experiments performed in spectrofluorometer where emission from the whole solution were recorded showed that the QD intensity quenches by about a third of the initial intensity for each of the assays. However, if WGMs are only responsible for the energy transfer, then just a few percent of QD intensity is expected to drop, as only a fraction of QD fluorescence efficiently couples to the modes (as observed in the emission spectra from the confocal microscope).

This phenomenon can be explained by looking at the radiation pattern of dipoles inside the microcavity. The physical and analytical representation of radiation pattern of a dipole near the interface of two materials with different refractive indices have been elaborately explained by Professor Walter Lukosz during 1970s[337,338,339,340].

In the Figure 4.22, $\vec{A}$ is a dipole with an arbitrary orientation near an interface of two materials with refractive indices respectively η_1 and η_2, where $\eta_2 > \eta_1$ and the dipole is embedded into the medium with

η_2 refractive index. It makes an angle α with the axis perpendicular to the interface (z-axis) and an angle φ with the xz plane.

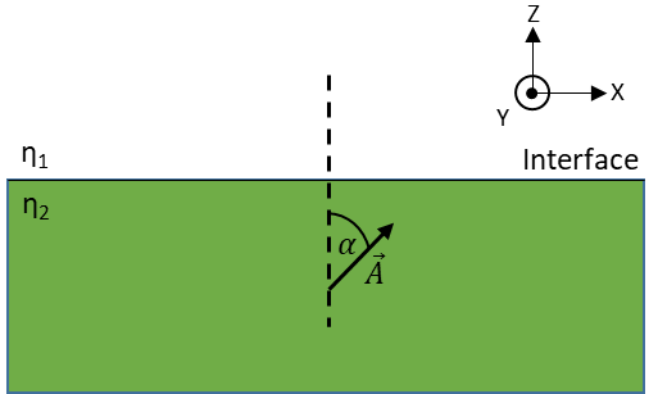

Figure 4.22: *A dipole ($\vec{A}$) with an arbitrary orientation near the interface of two materials with different refractive indices.*

In the first step, the components of the dipole moment respectively along z-axis ($\mu_{\parallel}$) and transverse to z-axis ($\mu_{\perp}$) have to be calculated. In the next step, reflection coefficient can be calculated for both the polarizations (s and p) of light using the Fresnel equations. The power emitted at different directions, with different θ angles with respect to the normal to the interface, is recalculated and summed up for both the polarizations at along and perpendicular to z-axis. In the step after, the power has to be integrated over all φ angles. The average power (P_{avg}) over all possible orientation can be calculated by considering twice the contribution from parallel dipole orientation, and one from the perpendicular orientation.

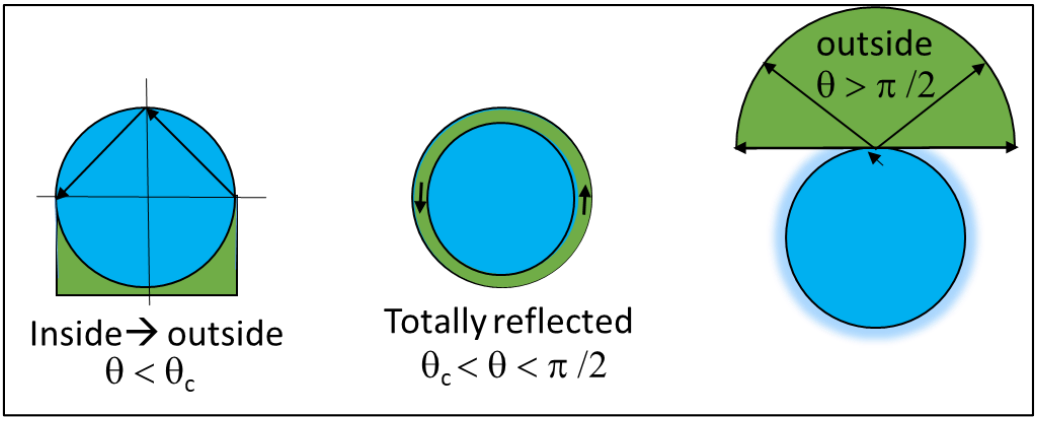

Figure 4.23: *The pattern of radiation at different range of incident θ angles; (from left to right) P_{Inside}, P_{TIR} and $P_{Outside}$. θ_C = critical angle*

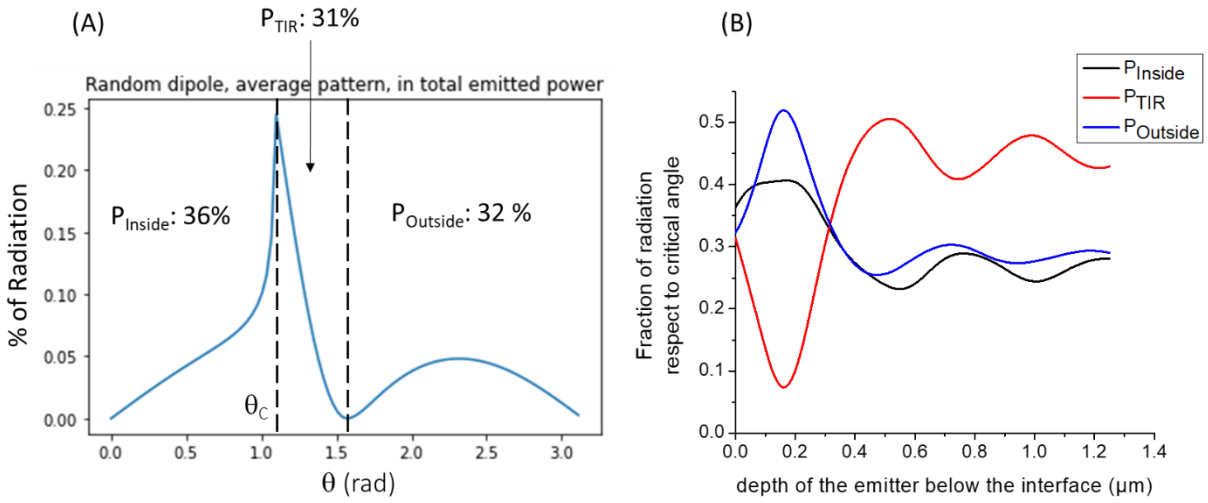

Figure 4.24: *(A) Radiation pattern (in percentage) of a microcavity as a function of incident angle of light (θ) at the PS/water interface, (B) Radiation pattern (normalized) of a microcavity as a function of the depth of the emitter below the interface.*

The power at different range of θ can be integrated to find out proportions of light that is trapped inside the cavity via total internal reflections and would contribute to energy transfer or the fraction of light that is not trapped inside and do not contribute to the WGMs.

$P = \int P(\theta) d\theta$ = P_{Inside}, when $0 < \theta < \theta_C$ = Total radiation reflected towards inside of the sphere

= P_{TIR}, when $\theta_C < \theta < \pi/2$ = Radiation total internally reflected

= $P_{Outside}$, when $\pi/2 < \theta < \pi$ = Total radiation transmitted towards outside of the sphere

How the light inside the dielectric microcavity behaves depending on the incident θ angle is given the Figure 4.23. When $\theta < \theta_C$, the light is emitted towards inside of the cavity but then goes out, whereas for light with $\pi/2 < \theta < \pi$, the radiation directly goes out at the interface towards the external medium without any reflection. Only for light that fulfills the condition $\theta_C < \theta < \pi/2$, the radiation is trapped inside via total internal reflections where light reaches the next dielectric interface with the same θ angle and keeps on reflecting at the interface inside the microsphere.

When calculated for dipoles with random orientations exactly at the interface, the total radiation reflected towards inside (P_{Inside}) is ~ 36%, outside ($P_{Outside}$) is ~ 32% and total internally reflected (P_{TIR}) ~ 31%. The radiation intensity pattern of a dipole of arbitrary orientation at the microcavity interface as a function of

angle θ (in radians) can be seen in Figure 4.24 (A). How the radiation pattern varies with the location of the emitter inside the microsphere can be found in the Figure 4.24 (B). The fraction of total internally reflected radiation that is around a third of the total radiation, is responsible for to participate in the energy transfer. Indeed, this light also remains trapped within the microsphere, with the same quality factor as the WGM, and thus contributes to the overall evanescent field, even though it is not necessarily at the wavelengths corresponding to the resonances. This may explain the general observation of why the emission intensity of donor QDs quench by much more than a few percent (generally about a third) due to energy transfer to acceptors.

4.8.4.2 Why are the QDs quenched but the dyeNPs don't re-emit?

In a regular energy transfer experiment, as more fluorescent acceptors are conjugated to the donors, the emission of the donor moiety is quenched and the fluorescence from the acceptor is enhanced as a rule of thumb, unless the acceptor is a nonfluorescent quencher. In our experiment (Section 4.8.2, changing the survivin target amount), as the target concentration increases the donor QDs are quenched but the emission of the acceptor dyeNP did not increase as expected. In this section, an investigation is attempted with a goal to understand this behavior of the acceptor.

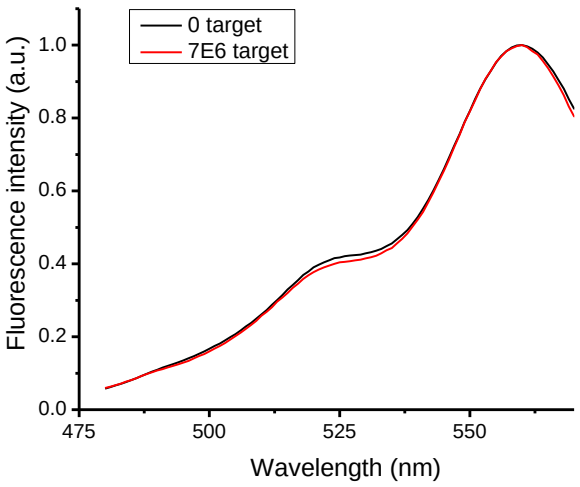

Figure 4.25: *Excitation spectra of sandwich WGET assay with and without target DNA strands (normalized at 560 nm).*

Excitation spectra were recorded of target (7×10^6 copies) added sandwich system (QD-microcavity-streptavidin-biotin Capture-target-probe DNA-dyeNP) and without any target sandwich system (QD-microcavity-streptavidin-biotin Capture + dyeNP – probe DNA) at the monitoring emission wavelength of

585 nm. Both the excitation spectra (normalized at 560 nm) showed similar shape and features (Figure 4.25), suggesting that the emission of the dyeNPs is almost entirely caused by direct excitation and not from the energy transfer from the QDs. This is consistent with the steady state emission spectra of the system where we see no increase in dye emission upon assembly.

To investigate the reason of why there is no energy transfer mediated enhanced emission from the dyeNPs, I looked into a few hypotheses which are the following,

1. The target DNA strands are causing the quenching of the QD emission, not the dyeNPs.
2. The hybridization of target DNAs to the dyeNPs make them non-fluorescent by some complex interactions. As only a small fraction of dyeNPs is actually hybridized with the target DNAs, the direct excitation (the major contributor to the dye emission) originates from the free dyeNPs,
3. A complex interaction happening between the dyeNPs and the microspheres which causes the bound dyeNPs to be quenched.

To check if the first hypotheses is true, an experiment was performed where QD loaded microspheres with streptavidin-biotin capture DNA on the surface (10 µL of the solution from section 4.5.2.2) were mixed with target DNA strands (4.8×10^7 copies or 8 µL at 10 pM concentration) and incubated for the hybridization to occur. The solution was transferred into a quartz cuvette and mixed with 190 µL of 1x PBS (1.5 mM $MgCl_2$ and Tween80 0.01 g/L) to maintain a measurable volume for spectrofluorometer. Emission spectra were recorded from the solution for 1 hour in 10 minutes intervals but no quenching of the QD intensity was observed which suggests that the hybridization of target DNAs do not cause the quenching of QDs (see Figure 4.26 (A, B))).

The second hypothesis was also tested using a similar experiment. The dyeNPs (10 µL at 0.1 nM) were hybridized with the target DNA (6×10^8 copies or 1 µL at 1 nM concentration) in absence of biotinylated capture probe attached microspheres. The ratio of target to dyeNP ratio was kept at 1 (much higher than in the previous experiments) to ensure hybridization to significant fraction of the dyeNPs present in the sample. The mixture was transferred to a quartz cuvette and 190 µL of 1x PBS (1.5 mM $MgCl_2$ and Tween80 0.01 g/L) to maintain a measurable volume for spectrofluorometer. Emission spectra of the sample were recorded for 1 hour in 10 minutes intervals. The spectra suggest that there is no quenching of the dyeNPs due to the hybridization process (see Figure 4.26 (C, D)).

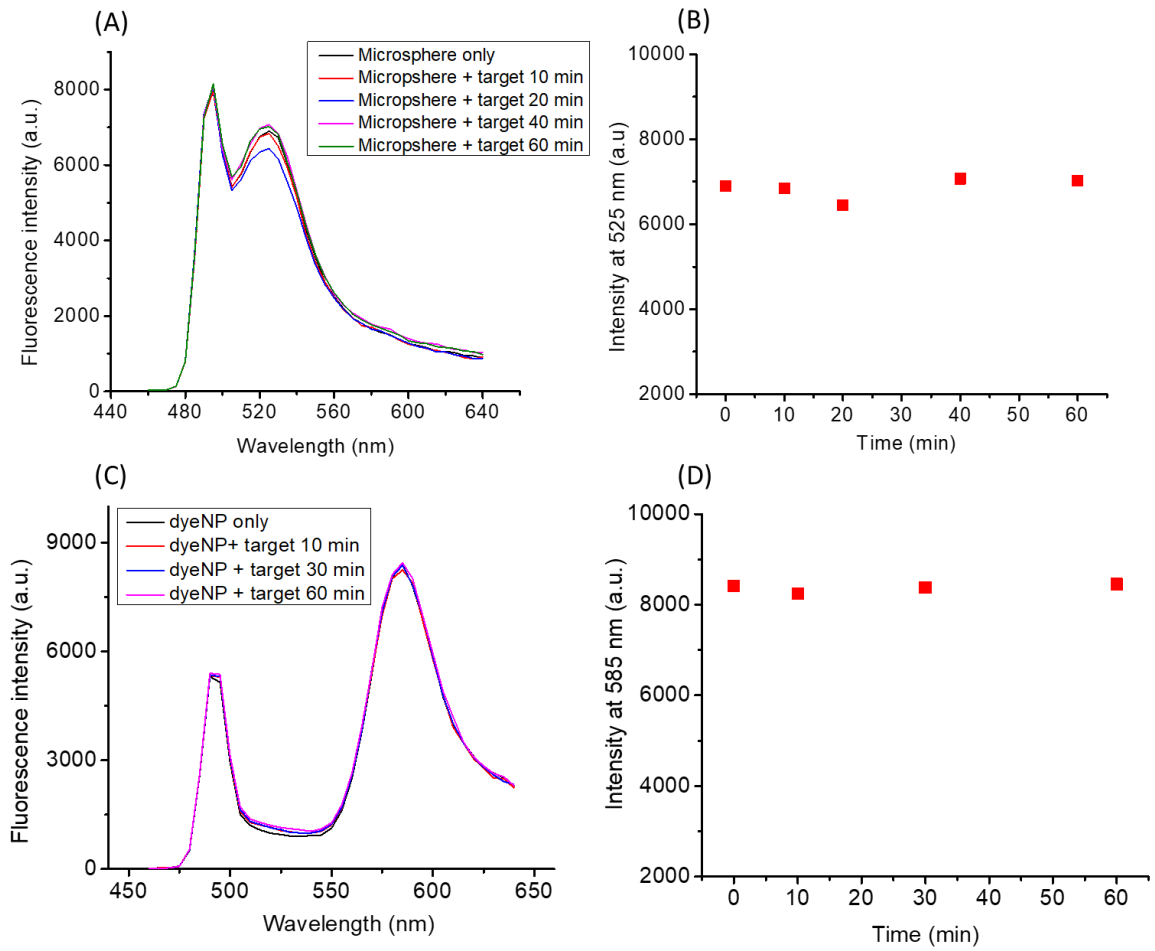

Figure 4.26: *(A) Emission spectra and (B) peak intensities of QD-microsphere-streptavidin-biotin Survivin capture + survivin target in different time intervals (experiment to check the hypothesis 1). (C) Emission spectra and (B) intensities dyeNP-Probe DNA + survivin target in different time intervals (experiment to check the hypothesis 2).*

These experiments suggest that the first two hypotheses do not explain the lack of re-emission from the dyeNPs. The third possibility is that there might be some complex interactions between the hydrophobic surface of the microspheres and the dyeNPs when they are in close proximity which might cause the quenching of dyeNPs that are attached to the microsphere surface. Moreover, as only a fraction of dyeNPs participate in the hybridization process, the direct excitation from the free dyeNPs still can be observed almost entirely. But yet the actual reason for the suppression of the fluorescence of dyeNPs is not totally understood and should be further investigated.

4.9 CONCLUSION:

In the beginning of the thesis, I have discussed about the fundamentals of optical microcavities and their potential to be used in highly sensitive biological assays. In this chapter, a bio-sensing strategy to detect survivin target strands in a solution has been explored. Many sensing schemes based on Forster resonance energy transfer have been explored in the last fifty years, but the sensitivity of those systems is limited by the inherited disadvantages of FRET such as small range of donor-acceptor distance. These disadvantages often lead to poor signal to noise ratio and false test outcomes and complicated designs of assays. In the other hand, optical microcavities can confine the emission from the optical donors via total internal reflection and form high quality resonances that can engage in energy transfer to optical acceptors located as far as 100s of nm which allows designing energy transfer assays for large biological complexes. Furthermore, large surface area of the microcavities allow conjugation to many targets in contrast to just a few for regular FRET assays. Additionally, assays based on microcavities have high sensitivity as the propagating photon inside a resonator travels many turns before going out, potentially increasing the probability of interaction with the acceptor fluorophore.

In this chapter, a further step is taken from the proof of concept towards demonstrating a DNA (survivin) sensing assay based on whispering gallery microcavities. At first, functionalization of carboxylate microcavities with biologically active molecules (e.g., streptavidin) have been performed and later this strategy enabled us to further attach other biomolecules such as DNA capture probes to the microcavities to construct the DNA detection platform. The assay showed high sensitivity with a limit of detection as low as just 42 targets per microsphere or ~2 fM concentration. Biotin being a simple molecule that can be easily conjugated to variety of biological molecules such as DNA, RNA, amino acids, proteins, and antibodies, makes biotin-streptavidin interaction a versatile option for facile bio-conjugation. The distance from the donor cavity to the acceptor dyeNP (surface to surface) for this scheme can be even more than 40 nm which is much greater than the regular FRET range whereas sensitive detection of these large DNA sandwich complexes is easily possible with WGET enabled microcavity based bio-detection schemes. Thus, this strategy opens up interesting possibilities to design bio-detection assays based on WGM mediated energy transfer with improved sensitivity and high specificity.

CONCLUSION & PERSPECTIVES

CONCLUSION:

To conclude, aiming towards the main motivation of this thesis, I have designed a bio-sensing platform by interfacing two very different sensing techniques to retain the advantages from both the schemes for sensitive and specific bio-detection. The first technique utilizes Förster resonance energy transfer (FRET); assays based on it are one of the commonly used bio-sensing techniques which possess many advantages such as high specificity, and availability in homogenous format but they often suffer from a few major issues such as lack of sensitivity and inability to detect very large biomolecules. The other technique, however, is a recent development in the field of bio-sensing and still a subject of extensive research. This technique exploits the reactive shift of whispering gallery resonances in optical microcavities to detect binding activities of specific bio-analytes. Even though this technique comes with improved sensitivity, it still suffers from high background noises due to thermal fluctuations in the media and non-specific interactions, also often require expensive tunable lasers, and tedious and precise alignment of the setup. However, a great advantage that optical microcavities provide, comes from their ability to participate in long-range energy transfer through the evanescent field of the cavity modes (WGMs). These observations motivated us to combine these two techniques into a single platform where the long evanescent tail of microcavity resonances can be engaged to perform energy transfer (WGET) to acceptor moieties located as far as tens to hundreds of nanometers away from the cavity surface, thus enabling us to detect large biological assemblies, the sensing of which is not often possible with FRET based assays.

A brief introduction regarding the main motivation of the project and topics related to different aspects of the experiments are discussed in **Chapter-1**.

In **Chapter-2** of the thesis, I have discussed the fabrication process and important optoelectronic properties of the dielectric microcavities that are loaded with fluorescent semiconductor quantum dots (QDs). As the first step of fabrication, a few batches of QDs were prepared using colloidal synthesis methods and characterized using the traditional structural and optical characterization techniques. Then in the second step, these QDs were successfully incorporated

into polymer microspheres that resulted in bright optical microcavities where the fluorescence from the QDs is strongly coupled to the WGMs of the resonator. Photo-physical characterization using spectroscopic and imaging techniques were performed on these optical microcavities that revealed the high-quality factor, and great photo-chemical stability of these resonators.

In Chapter-3, I have investigated the energy transfer process through WGMs from the donor QDs to acceptor dyeNPs located in the vicinity of the microsphere. A simple electrostatically conjugated donor-acceptor system was prepared by adsorbing negatively charged dyeNPs onto the positively charged surface of the microspheres. Spectroscopic characterizations suggested WGM mediated enhanced energy transfer from the QDs to the acceptors aided by the high-quality factor of the microcavities. A quantitative analysis was also performed to determine the rate and the efficiency of the energy transfer. We constructed a theoretical model to compare FRET and WGET processes side-by-side in two equivalent systems. This comparison revealed that the WGET mediated scheme possesses higher distance range for energy transfer, and improved sensitivity owing to the high Q-factor of the WGMs, which overall resulted into a greater sensitivity compared to FRET schemes.

The Chapter-4 is focused on translating our WGET donor-acceptor system towards a real bio-sensing platform. As the first step towards our goal, biological specificity was imparted onto the microspheres by surface functionalization techniques. Streptavidin molecules were covalently linked to the surface of the cavities, then strong binding affinity of streptavidin-biotin interaction was exploited to attach biotinylated capture probes onto the microspheres. Then, in the next step, a model bio-sensing experiment was performed to detect hybridization between two simple DNA strands. The WGET sensor successfully transduced the hybridization process. As this experiment resulted into great sensitivity, we moved from the sophisticated confocal setup (measurement in single microcavity level) to a much simpler setup (spectrofluorometer) that measures the fluorescence from the whole solution, which also showed the signature of the hybridization process. As the final step of our bio-sensing demonstration, a sandwich WGET assay was configured to detect a cancer biomarker DNA called survivin. This scheme could successfully detect the presence of the biomarker in a buffer solution, with a very high sensitivity (limit of detection ~ 2fM).

FUTURE PERSPECTIVES OF WGET SENSING:

The successful demonstration of the DNA cancer bio-marker detection with our WGET sensing scheme potentially opens up numerous possibilities for designing highly sensitive and specific biosensors. Having several advantages in terms of sensitivity, cost-effectivity, ease of fabrication and usage, WGET based sensors clearly hold a high ground in terms of commercial and practical applications compared to traditional assays, such as FRET and ELISA.

The WGET sensing of the survivin biomarker has been performed in PBS buffer which is the simplest for the preliminary testing of the detection scheme. To get closer towards the practical application of this scheme, one future goal should be to perform this assay in blood plasma or cell lysate medium to examine the interference from the non-specific interactions of other biomolecules that might increase the background noise, thus decreasing the sensitivity of the system in real life measurements.

Instead of an antibody-antigen pair, a DNA based scheme was chosen to perform the preliminary demonstration of our WGET based biosensing assay owing to the robustness and strong hybridization affinity between complementary DNA strands. However, antibody-based detection on the other hand is more complex due to the denaturation and structural changes in the binding sites. Now after the successful demonstration of DNA sensing, a vast horizon of antibody conjugated WGET sensors can be explored for the sensitive detection of antigenic analytes.

In this thesis, I have focused on solution phase WGM microcavities because of their easy bulk preparations and purification schemes. However, on chip WGM cavities (arrays of micro pillars, micro discs) that are fabricated by lithographic techniques, would allow more precise and long-term measurement on fixed individual microcavities. It would be of great interest for building portable and compact biosensors. Moreover, this would also provide the flexibility to perform parallel/switchable measurements in both ensemble as well as single microcavity level.

PUBLICATIONS & COMMUNICATIONS

PUBLICATION:

- **Microcavity-enhanced fluorescence energy transfer from quantum dot excited whispering gallery modes to acceptor dye nanoparticles.**

  Subha Jana, XIangzhen Xu, Andrey Klymchenko, Andreas Reisch, Thomas Pons.

  ***ACS Nano* 2021**, 15, 1, 1445–1453

CONFERENCE PROCEEDING:

- **Biodetection with whispering quantum dots.**

  Subha Jana, XIangzhen Xu, Andrey Klymchenko, Andreas Reisch, Thomas Pons.

  SPIE Digital proceedings, **Optical sensors** 2021, 1177204

COMMUNICATIONS:

- **SPIE Optics + Optoelectronics** digital forum, April 2021
  Title: Biodetection with whispering quantum dots

- Internet **NanoGe** conference on nanocrystals, 2021
  Title: Microcavity-enhanced fluorescence energy transfer from quantum dot-excited whispering gallery modes to acceptor dye nanoparticles.

- Journées de l'école doctorale 397 (ED397), 2020

PRIZE:

- Best poster presentation in **SFNano-C'Nano** joint meeting 2019 (Category: Nanophotonics & nano-optics)

Annex

Chapter 2: QD synthesis.

QD525: 170 mg cadmium myristate were resuspended in 9 mL octadecene (ODE) and degassed under vacuum for 15 min at 50°C. Under argon, the temperature was raised to 250°C and a mixture of 9.5 mg selenium powder and 3.9 mg sulfur powder in 1.2 mL ODE was injected. After 10 minutes, the reaction solution was cooled to room temperature and 1 mL oleic acid was added. The QDs were precipitated using ethanol and resuspended in 10 mL hexane. 2.3 mL of this solution was added to 2 mL decane and 8 mL oleylamine. The solution was degassed at room temperature under vacuum. The solution was then placed under argon. A shell of ca. 6 monolayers of $Cd_{0.65}Zn_{0.35}S$ was then synthesized using cadmium and zinc diethyldithiocarbamate precursors. The calculated quantity of precursors for each monolayer was prepared at 0.1M in decane:oleylamine 3:1 v/v and injected at 60°C, then the temperature was raised at 160°C for 20 minutes for growth, and cooled down to 60°C before the injection of the precursors for the next monolayer. The final core/shell QD solution was precipitated using ethanol and resuspended in hexane.

QD505: CdSe cores were synthesized using 0.6 g of cadmium tetradecylphosphonate in 5 mL ODE. The solution was degassed at 60°C under vacuum for 20 minutes. Under argon, the temperature was raised to 300°C and 4 mL of selenium dissolved at 1 M in trioctylphosphine were injected. The solution was cooled to room temperature as soon as it turned bright orange. The QDs were precipitated in ethanol and resuspended in hexane. For the shell growth, these CdSe cores were mixed with 2 mL oleylamine and 5 mL octadecene. The solution was degassed under vacuum at 60°C and raised to 200°C under argon. A mixture of 2.5 mL trioctylphosphine, 22 mg zinc diethyldithiocarbamate, 400 mg zinc stearate and 1 mL trioctylamine was injected dropwise over 30 minutes. The core/shell QDs were precipitated in ethanol and resuspended in hexane.

Chapter 4: Synthesis protocol of Cy5-BSA-biotin:

Biotinylated-NHS was first prepared by reaction of biotin with equivalent molar quantities of EDC and NHS in DMSO. One equivalent of BSA was then mixed with 3 equivalent biotin-NHS and 3 equivalent Cy5-NHS in HEPES buffer (100 mM, pH 7.4, 150 mM NaCl) and reacted for 2 hours. Then the solution was purified

by three rounds of ultrafiltration (vivaspin, 10kDa) to remove the free unreacted dye and biotin. The correct functionalization of the BSA with both dye and biotin was checked by incubation with commercial agarose beads functionalized with biotin or streptavidin After washing and centrifugation, the pellet with streptavidin-modified agarose beads is blue from the color of Cy5, showing the correct co functionalization of BSA with biotin and Cy5, while the pellet with biotin-modified agarose beads remains white, confirming that the interactions indeed come from biotin.

REFERENCES

(1) International Union of Pure and Applied Chemistry (1992) IUPAC Compendium of Chemical Terminology, 2nd Edn (1997). International Union of Pure and Applied Chemistry, Research Triangle Park, NC.

(2) *Biosensors and Biodetection: Methods and Protocols Volume 1: Optical-Based Detectors*; Rasooly, A., Prickril, B., Eds.; Methods in Molecular Biology; Springer New York: New York, NY, 2017; Vol. 1571. https://doi.org/10.1007/978-1-4939-6848-0.

(3) van Wijck, K.; van Eijk, H. M. H.; Buurman, W. A.; Dejong, C. H. C.; Lenaerts, K. Novel Analytical Approach to a Multi-Sugar Whole Gut Permeability Assay. *J. Chromatogr. B* **2011**, *879* (26), 2794–2801. https://doi.org/10.1016/j.jchromb.2011.08.002.

(4) Denisov, I.; Lukyanenko, K.; Yakimov, A.; Kukhtevich, I.; Esimbekova, E.; Belobrov, P. Disposable Luciferase-Based Microfluidic Chip for Rapid Assay of Water Pollution. *Luminescence* **2018**, *33* (6), 1054–1061. https://doi.org/10.1002/bio.3508.

(5) Vijitvarasan, P.; Oaew, S.; Surareungchai, W. Paper-Based Scanometric Assay for Lead Ion Detection Using DNAzyme. *Anal. Chim. Acta* **2015**, *896*, 152–159. https://doi.org/10.1016/j.aca.2015.09.011.

(6) Gu, Z.; Zhao, M.; Sheng, Y.; Bentolila, L. A.; Tang, Y. Detection of Mercury Ion by Infrared Fluorescent Protein and Its Hydrogel-Based Paper Assay. *Anal. Chem.* **2011**, *83* (6), 2324–2329. https://doi.org/10.1021/ac103236g.

(7) Kalluri, J. R.; Arbneshi, T.; Afrin Khan, S.; Neely, A.; Candice, P.; Varisli, B.; Washington, M.; McAfee, S.; Robinson, B.; Banerjee, S.; Singh, A. K.; Senapati, D.; Ray, P. C. Use of Gold Nanoparticles in a Simple Colorimetric and Ultrasensitive Dynamic Light Scattering Assay: Selective Detection of Arsenic in Groundwater. *Angew. Chem.* **2009**, *121* (51), 9848–9851. https://doi.org/10.1002/ange.200903958.

(8) Geißler, D.; Hildebrandt, N. Recent Developments in Förster Resonance Energy Transfer (FRET) Diagnostics Using Quantum Dots. *Anal. Bioanal. Chem.* **2016**, *408* (17), 4475–4483. https://doi.org/10.1007/s00216-016-9434-y.

(9) Arola, H. O.; Tullila, A.; Kiljunen, H.; Campbell, K.; Siitari, H.; Nevanen, T. K. Specific Noncompetitive Immunoassay for HT-2 Mycotoxin Detection. *Anal. Chem.* **2016**, *88* (4), 2446–2452. https://doi.org/10.1021/acs.analchem.5b04591.

(10) Aliyu, S. H.; Aliyu, M. H.; Salihu, H. M.; Parmar, S.; Jalal, H.; Curran, M. D. Rapid Detection and Quantitation of Hepatitis B Virus DNA by Real-Time PCR Using a New Fluorescent (FRET) Detection System. *J. Clin. Virol.* **2004**, *30* (2), 191–195. https://doi.org/10.1016/j.jcv.2003.11.005.

(11) Wang, X.; Lou, X.; Wang, Y.; Guo, Q.; Fang, Z.; Zhong, X.; Mao, H.; Jin, Q.; Wu, L.; Zhao, H.; Zhao, J. QDs-DNA Nanosensor for the Detection of Hepatitis B Virus DNA and the Single-Base Mutants. *Biosens. Bioelectron.* **2010**, *25* (8), 1934–1940. https://doi.org/10.1016/j.bios.2010.01.007.

(12) Hjertner, B.; Meehan, B.; McKillen, J.; McNeilly, F.; Belák, S. Adaptation of an Invader® Assay for the Detection of African Swine Fever Virus DNA. *J. Virol. Methods* **2005**, *124* (1), 1–10. https://doi.org/10.1016/j.jviromet.2004.10.009.

(13) Jothikumar, N.; Cromeans, T. L.; Hill, V. R.; Lu, X.; Sobsey, M. D.; Erdman, D. D. Quantitative Real-Time PCR Assays for Detection of Human Adenoviruses and Identification of Serotypes 40 and 41. *Appl. Environ. Microbiol.* **2005**, *71* (6), 3131–3136. https://doi.org/10.1128/AEM.71.6.3131-3136.2005.

(14) White, J. W. The Role of HMF and Diastase Assays in Honey Quality Evaluation. *Bee World* **1994**, *75* (3), 104–117. https://doi.org/10.1080/0005772X.1994.11099213.

(15) Singh, J.; Sharma, S.; Nara, S. Evaluation of Gold Nanoparticle Based Lateral Flow Assays for Diagnosis of Enterobacteriaceae Members in Food and Water. *Food Chem.* **2015**, *170*, 470–483. https://doi.org/10.1016/j.foodchem.2014.08.092.

(16) Stewart Anderson, J.; Lall, S. P.; Anderson, D. M.; McNiven, M. A. Evaluation of Protein Quality in Fish Meals by Chemical and Biological Assays. *Aquaculture* **1993**, *115* (3), 305–325. https://doi.org/10.1016/0044-8486(93)90145-O.

(17) Trintinaglia, L.; Bianchi, E.; Silva, L. B.; Nascimento, C. A.; Spilki, F. R.; Ziulkoski, A. L. Cytotoxicity Assays as Tools to Assess Water Quality in the Sinos River Basin. *Braz. J. Biol.* **2015**, *75*, 75–80. https://doi.org/10.1590/1519-6984.0113.

(18) Palácio, S. M.; Espinoza-Quiñones, F. R.; de Pauli, A. R.; Piana, P. A.; Queiroz, C. B.; Fabris, S. C.; Fagundes-Klen, M. R.; Veit, M. T. Assessment of Anthropogenic Impacts on the Water Quality of Marreco River, Brazil, Based on Principal Component Analysis and Toxicological Assays. *Water. Air. Soil Pollut.* **2016**, *227* (9), 307. https://doi.org/10.1007/s11270-016-3025-6.

(19) Slabbert, J. L. Microbial Toxicity Assays Used for Water Quality Evaluation in South Africa. *Toxic. Assess.* **1988**, *3* (2), 101–115. https://doi.org/10.1002/tox.2540030202.

(20) Lequin, R. M. Enzyme Immunoassay (EIA)/Enzyme-Linked Immunosorbent Assay (ELISA). *Clin. Chem.* **2005**, *51* (12), 2415–2418. https://doi.org/10.1373/clinchem.2005.051532.

(21) Mere, L.; Bennett, T.; Coassin, P.; England, P.; Hamman, B.; Rink, T.; Zimmerman, S.; Negulescu, P. Miniaturized FRET Assays and Microfluidics: Key Components for Ultra-High-Throughput Screening. *Drug Discov. Today* **1999**, *4* (8), 363–369. https://doi.org/10.1016/S1359-6446(99)01377-X.

(22) Liao, J.; Song, Y.; Liu, Y. A New Trend to Determine Biochemical Parameters by Quantitative FRET Assays. *Acta Pharmacol. Sin.* **2015**, *36* (12), 1408–1415. https://doi.org/10.1038/aps.2015.82.

(23) Takkinen, K.; Žvirblienė, A. Recent Advances in Homogenous Immunoassays Based on Resonance Energy Transfer. *Curr. Opin. Biotechnol.* **2019**, *55*, 16–22. https://doi.org/10.1016/j.copbio.2018.07.003.

(24) Mitchell, J. Small Molecule Immunosensing Using Surface Plasmon Resonance. *Sensors* **2010**, *10* (8), 7323–7346. https://doi.org/10.3390/s100807323.

(25) Haes, A. J.; Hall, W. P.; Chang, L.; Klein, W. L.; Van Duyne, R. P. A Localized Surface Plasmon Resonance Biosensor: First Steps toward an Assay for Alzheimer's Disease. *Nano Lett.* **2004**, *4* (6), 1029–1034. https://doi.org/10.1021/nl049670j.

(26) Giannetti, A. M.; Koch, B. D.; Browner, M. F. Surface Plasmon Resonance Based Assay for the Detection and Characterization of Promiscuous Inhibitors. *J. Med. Chem.* **2008**, *51* (3), 574–580. https://doi.org/10.1021/jm700952v.

(27) Vollmer, F.; Arnold, S. Whispering-Gallery-Mode Biosensing: Label-Free Detection down to Single Molecules. *Nat. Methods* **2008**, *5* (7), 591–596. https://doi.org/10.1038/nmeth.1221.

(28) Chakravarty, S.; Lai, W.-C.; Zou, Y.; Drabkin, H. A.; Gemmill, R. M.; Simon, G. R.; Chin, S. H.; Chen, R. T. Multiplexed Specific Label-Free Detection of NCI-H358 Lung Cancer Cell Line Lysates with Silicon Based Photonic Crystal Microcavity Biosensors. *Biosens. Bioelectron.* **2013**, *43*, 50–55. https://doi.org/10.1016/j.bios.2012.11.012.

(29) Santiago-Cordoba, M. A.; Boriskina, S. V.; Vollmer, F.; Demirel, M. C. Nanoparticle-Based Protein Detection by Optical Shift of a Resonant Microcavity. *Appl. Phys. Lett.* **2011**, *99* (7), 073701. https://doi.org/10.1063/1.3599706.
(30) *Rall JE. Solomon A. Berson. In "Biographical Memoirs". National Academy of Sciences 1990;59:54-71. ISBN 0-309-04198-8.*
(31) Wide, L. RADIOIMMUNOASSAYS EMPLOYING IMMUNOSORBENTS. *Eur. J. Endocrinol.* **1969**, *62* (1_Suppl), S207–S221. https://doi.org/10.1530/acta.0.062S207.
(32) Proximity hybridization-regulated chemiluminescence resonance energy transfer for homogeneous immunoassay - ScienceDirect https://www.sciencedirect.com/science/article/abs/pii/S0039914016300583 (accessed 2020 -04 -21).
(33) Bacart, J.; Corbel, C.; Jockers, R.; Bach, S.; Couturier, C. The BRET Technology and Its Application to Screening Assays. *Biotechnol. J.* **2008**, *3* (3), 311–324. https://doi.org/10.1002/biot.200700222.
(34) *R., Crowther, J. (1995). ELISA : Theory and Practice. Totowa, N.J.: Humana Press. ISBN 978-0896032798*.
(35) Lin, A. V. Direct ELISA. In *ELISA: Methods and Protocols*; Hnasko, R., Ed.; Methods in Molecular Biology; Springer: New York, NY, 2015; pp 61–67. https://doi.org/10.1007/978-1-4939-2742-5_6.
(36) Lin, A. V. Indirect ELISA. In *ELISA: Methods and Protocols*; Hnasko, R., Ed.; Methods in Molecular Biology; Springer: New York, NY, 2015; pp 51–59. https://doi.org/10.1007/978-1-4939-2742-5_5.
(37) Wei, Q.; Lee, M.; Yu, X.; Lee, E. K.; Seong, G. H.; Choo, J.; Cho, Y. W. Development of an Open Sandwich Fluoroimmunoassay Based on Fluorescence Resonance Energy Transfer. *Anal. Biochem.* **2006**, *358* (1), 31–37. https://doi.org/10.1016/j.ab.2006.08.019.
(38) He, X.; Li, Z.; Jia, X.; Wang, K.; Yin, J. A Highly Selective Sandwich-Type FRET Assay for ATP Detection Based on Silica Coated Photon Upconverting Nanoparticles and Split Aptamer. *Talanta* **2013**, *111*, 105–110. https://doi.org/10.1016/j.talanta.2013.02.050.
(39) Sun, Y.; Lu, J. Chemiluminescence-Based Aptasensors for Various Target Analytes. *Luminescence* **2018**, *33* (8), 1298–1305. https://doi.org/10.1002/bio.3557.
(40) Arai, R.; Nakagawa, H.; Tsumoto, K.; Mahoney, W.; Kumagai, I.; Ueda, H.; Nagamune, T. Demonstration of a Homogeneous Noncompetitive Immunoassay Based on Bioluminescence Resonance Energy Transfer. *Anal. Biochem.* **2001**, *289* (1), 77–81. https://doi.org/10.1006/abio.2000.4924.
(41) Hurley, I. P.; Coleman, R. C.; Ireland, H. E.; Williams, J. H. H. Measurement of Bovine IgG by Indirect Competitive ELISA as a Means of Detecting Milk Adulteration. *J. Dairy Sci.* **2004**, *87* (3), 543–549. https://doi.org/10.3168/jds.S0022-0302(04)73195-1.
(42) Pulli, T.; Höyhtyä, M.; Söderlund, H.; Takkinen, K. One-Step Homogeneous Immunoassay for Small Analytes. *Anal. Chem.* **2005**, *77* (8), 2637–2642. https://doi.org/10.1021/ac048379l.
(43) Dinis-Oliveira, R. J. Heterogeneous and Homogeneous Immunoassays for Drug Analysis. *Bioanalysis* **2014**, *6* (21), 2877–2896. https://doi.org/10.4155/bio.14.208.
(44) Algar, W. R.; Hildebrandt, N.; Vogel, S. S.; Medintz, I. L. FRET as a Biomolecular Research Tool — Understanding Its Potential While Avoiding Pitfalls. *Nat. Methods* **2019**, *16* (9), 815–829. https://doi.org/10.1038/s41592-019-0530-8.
(45) Soler, M.; McCusker, J. K. Distinguishing between Dexter and Rapid Sequential Electron Transfer in Covalently Linked Donor−Acceptor Assemblies. *J. Am. Chem. Soc.* **2008**, *130* (14), 4708–4724. https://doi.org/10.1021/ja077096i.

(46) Tamura, M.; Berg, P. A.; Harrington, J. E.; Luque, J.; Jeffries, J. B.; Smith, G. P.; Crosley, D. R. Collisional Quenching of CH(A), OH(A), and NO(A) in Low Pressure Hydrocarbon Flames. *Combust. Flame* **1998**, *114* (3), 502–514. https://doi.org/10.1016/S0010-2180(97)00324-6.
(47) Dhami, S.; Mello, A. J. D.; Rumbles, G.; Bishop, S. M.; Phillips, D.; Beeby, A. Phthalocyanine Fluorescence at High Concentration: Dimers or Reabsorption Effect? *Photochem. Photobiol.* **1995**, *61* (4), 341–346. https://doi.org/10.1111/j.1751-1097.1995.tb08619.x.
(48) Andrews, D. L. A Unified Theory of Radiative and Radiationless Molecular Energy Transfer. *Chem. Phys.* **1989**, *135* (2), 195–201. https://doi.org/10.1016/0301-0104(89)87019-3.
(49) Deal, J.; Pleshinger, D. J.; Johnson, S. C.; Leavesley, S. J.; Rich, T. C. Milestones in the Development and Implementation of FRET-Based Sensors of Intracellular Signals: A Biological Perspective of the History of FRET. *Cell. Signal.* **2020**, *75*, 109769. https://doi.org/10.1016/j.cellsig.2020.109769.
(50) Clegg, R. M. The History of Fret. In *Reviews in Fluorescence 2006*; Geddes, C. D., Lakowicz, J. R., Eds.; Reviews in Fluorescence; Springer US: Boston, MA, 2006; pp 1–45. https://doi.org/10.1007/0-387-33016-X_1.
(51) Energy Transfer. In *Principles of Fluorescence Spectroscopy*; Lakowicz, J. R., Ed.; Springer US: Boston, MA, 2006; pp 443–475. https://doi.org/10.1007/978-0-387-46312-4_13.
(52) Sahoo, H. Förster Resonance Energy Transfer – A Spectroscopic Nanoruler: Principle and Applications. *J. Photochem. Photobiol. C Photochem. Rev.* **2011**, *12* (1), 20–30. https://doi.org/10.1016/j.jphotochemrev.2011.05.001.
(53) Uhm, H.; Kang, W.; Ha, K. S.; Kang, C.; Hohng, S. Single-Molecule FRET Studies on the Cotranscriptional Folding of a Thiamine Pyrophosphate Riboswitch. *Proc. Natl. Acad. Sci.* **2018**, *115* (2), 331–336. https://doi.org/10.1073/pnas.1712983115.
(54) Woźniak, A. K.; Schröder, G. F.; Grubmüller, H.; Seidel, C. A. M.; Oesterhelt, F. Single-Molecule FRET Measures Bends and Kinks in DNA. *Proc. Natl. Acad. Sci.* **2008**, *105* (47), 18337–18342. https://doi.org/10.1073/pnas.0800977105.
(55) Dragan, A. I.; Privalov, P. L. Chapter 9 Use of Fluorescence Resonance Energy Transfer (FRET) in Studying Protein-induced DNA Bending. In *Methods in Enzymology*; Fluorescence Spectroscopy; Academic Press, 2008; Vol. 450, pp 185–199. https://doi.org/10.1016/S0076-6879(08)03409-5.
(56) Yuan, C.; Chen, H.; Lou, X. W.; Archer, L. A. DNA Bending Stiffness on Small Length Scales. *Phys. Rev. Lett.* **2008**, *100* (1), 018102. https://doi.org/10.1103/PhysRevLett.100.018102.
(57) Blouin, S.; Craggs, T. D.; Lafontaine, D. A.; Penedo, J. C. Functional Studies of DNA-Protein Interactions Using FRET Techniques. In *DNA-Protein Interactions: Principles and Protocols, Third Edition*; Leblanc, B., Moss, T., Eds.; Methods in Molecular Biology™; Humana Press: Totowa, NJ, 2009; pp 475–502. https://doi.org/10.1007/978-1-60327-015-1_28.
(58) Rehman, S.; Gladman, J. T.; Periasamy, A.; Sun, Y.; Mahadevan, M. S. Development of an AP-FRET Based Analysis for Characterizing RNA-Protein Interactions in Myotonic Dystrophy (DM1). *PLOS ONE* **2014**, *9* (4), e95957. https://doi.org/10.1371/journal.pone.0095957.
(59) Maurel, D.; Comps-Agrar, L.; Brock, C.; Rives, M.-L.; Bourrier, E.; Ayoub, M. A.; Bazin, H.; Tinel, N.; Durroux, T.; Prézeau, L.; Trinquet, E.; Pin, J.-P. Cell-Surface Protein-Protein Interaction Analysis with Time-Resolved FRET and Snap-Tag Technologies: Application to GPCR Oligomerization. *Nat. Methods* **2008**, *5* (6), 561–567. https://doi.org/10.1038/nmeth.1213.
(60) Time-Resolved Energy Transfer and Conformational Distributions of Biopolymers. In *Principles of Fluorescence Spectroscopy*; Lakowicz, J. R., Ed.; Springer US: Boston, MA, 2006; pp 477–506. https://doi.org/10.1007/978-0-387-46312-4_14.
(61) Stryer, L.; Haugland, R. P. Energy Transfer: A Spectroscopic Ruler. *Proc. Natl. Acad. Sci. U. S. A.* **1967**, *58* (2), 719–726.

(62) Gemma, E.; Meyer, O.; Uhrín, D.; Hulme, A. N. Enabling Methodology for the End Functionalisation of Glycosaminoglycan Oligosaccharides. *Mol. Biosyst.* **2008**, *4* (6), 481–495. https://doi.org/10.1039/B801666F.

(63) Kashida, H.; Takatsu, T.; Sekiguchi, K.; Asanuma, H. An Efficient Fluorescence Resonance Energy Transfer (FRET) between Pyrene and Perylene Assembled in a DNA Duplex and Its Potential for Discriminating Single-Base Changes. *Chem. – Eur. J.* **2010**, *16* (8), 2479–2486. https://doi.org/10.1002/chem.200902078.

(64) Sahoo, H.; Roccatano, D.; Zacharias, M.; Nau, W. M. Distance Distributions of Short Polypeptides Recovered by Fluorescence Resonance Energy Transfer in the 10 Å Domain. *J. Am. Chem. Soc.* **2006**, *128* (25), 8118–8119. https://doi.org/10.1021/ja062293n.

(65) Hildebrandt, N.; Spillmann, C. M.; Algar, W. R.; Pons, T.; Stewart, M. H.; Oh, E.; Susumu, K.; Díaz, S. A.; Delehanty, J. B.; Medintz, I. L. Energy Transfer with Semiconductor Quantum Dot Bioconjugates: A Versatile Platform for Biosensing, Energy Harvesting, and Other Developing Applications. *Chem. Rev.* **2017**, *117* (2), 536–711. https://doi.org/10.1021/acs.chemrev.6b00030.

(66) Chen, H.; Ding, F.; Zhou, Z.; He, X.; Shen, J. FRET-Based Sensor for Visualizing PH Variation with Colorimetric/Ratiometric Strategy and Application for Bioimaging in Living Cells, Bacteria and Zebrafish. *Analyst* **2020**, *145* (12), 4283–4294. https://doi.org/10.1039/D0AN00841A.

(67) Chereddy, N. R.; Thennarasu, S.; Mandal, A. B. A Highly Selective and Efficient Single Molecular FRET Based Sensor for Ratiometric Detection of Fe3+ Ions. *Analyst* **2013**, *138* (5), 1334–1337. https://doi.org/10.1039/C3AN36577H.

(68) Peroza, E. A.; Boumezbeur, A.-H.; Zamboni, N. Rapid, Randomized Development of Genetically Encoded FRET Sensors for Small Molecules. *Analyst* **2015**, *140* (13), 4540–4548. https://doi.org/10.1039/C5AN00707K.

(69) Dennis, A. M.; Rhee, W. J.; Sotto, D.; Dublin, S. N.; Bao, G. Quantum Dot–Fluorescent Protein FRET Probes for Sensing Intracellular PH. *ACS Nano* **2012**, *6* (4), 2917–2924. https://doi.org/10.1021/nn2038077.

(70) Zhang, X.-F.; Zhang, T.; Shen, S.-L.; Miao, J.-Y.; Zhao, B.-X. A Ratiometric Lysosomal PH Probe Based on the Naphthalimide–Rhodamine System. *J. Mater. Chem. B* **2015**, *3* (16), 3260–3266. https://doi.org/10.1039/C4TB02082K.

(71) Dong, B.; Song, X.; Wang, C.; Kong, X.; Tang, Y.; Lin, W. Dual Site-Controlled and Lysosome-Targeted Intramolecular Charge Transfer–Photoinduced Electron Transfer–Fluorescence Resonance Energy Transfer Fluorescent Probe for Monitoring PH Changes in Living Cells. *Anal. Chem.* **2016**, *88* (7), 4085–4091. https://doi.org/10.1021/acs.analchem.6b00422.

(72) Feng, L.; Sha, J.; He, Y.; Chen, S.; Liu, B.; Zhang, H.; Lü, C. Conjugated Polymer and Spirolactam Rhodamine-B Derivative Co-Functionalized Mesoporous Silica Nanoparticles as the Scaffold for the FRET-Based Ratiometric Sensing of Mercury (II) Ions. *Microporous Mesoporous Mater.* **2015**, *208*, 113–119. https://doi.org/10.1016/j.micromeso.2015.01.039.

(73) Cardoso Dos Santos, M.; Algar, W. R.; Medintz, I. L.; Hildebrandt, N. Quantum Dots for Förster Resonance Energy Transfer (FRET). *TrAC Trends Anal. Chem.* **2020**, *125*, 115819. https://doi.org/10.1016/j.trac.2020.115819.

(74) S. Varghese, S.; Zhu, Y.; J. Davis, T.; C. Trowell, S. FRET for Lab-on-a-Chip Devices — Current Trends and Future Prospects. *Lab. Chip* **2010**, *10* (11), 1355–1364. https://doi.org/10.1039/B924271F.

(75) Niemi, M. H.; Turunen, L.; Pulli, T.; Nevanen, T. K.; Höyhtyä, M.; Söderlund, H.; Rouvinen, J.; Takkinen, K. A Structural Insight into the Molecular Recognition of a (-)-Delta9-Tetrahydrocannabinol and the Development of a Sensitive, One-Step, Homogeneous

Immunocomplex-Based Assay for Its Detection. *J. Mol. Biol.* **2010**, *400* (4), 803–814. https://doi.org/10.1016/j.jmb.2010.05.048.
(76) Tan, Y. H.; Liu, M.; Nolting, B.; Go, J. G.; Gervay-Hague, J.; Liu, G. A Nanoengineering Approach for Investigation and Regulation of Protein Immobilization. *ACS Nano* **2008**, *2* (11), 2374–2384. https://doi.org/10.1021/nn800508f.
(77) Achermann, M.; Petruska, M. A.; Crooker, S. A.; Klimov, V. I. Picosecond Energy Transfer in Quantum Dot Langmuir−Blodgett Nanoassemblies. *J. Phys. Chem. B* **2003**, *107* (50), 13782–13787. https://doi.org/10.1021/jp036497r.
(78) Cao, Y.; Xie, T.; Qian, R.-C.; Long, Y.-T. Plasmon Resonance Energy Transfer: Coupling between Chromophore Molecules and Metallic Nanoparticles. *Small* **2017**, *13* (2), 1601955. https://doi.org/10.1002/smll.201601955.
(79) Naghdi, M.; Taheran, M.; Brar, S. K.; Verma, M.; Surampalli, R. Y.; Valero, J. R. Green and Energy-Efficient Methods for the Production of Metallic Nanoparticles. *Beilstein J. Nanotechnol.* **2015**, *6* (1), 2354–2376. https://doi.org/10.3762/bjnano.6.243.
(80) Hohenester, U.; Trugler, A. Interaction of Single Molecules With Metallic Nanoparticles. *IEEE J. Sel. Top. Quantum Electron.* **2008**, *14* (6), 1430–1440. https://doi.org/10.1109/JSTQE.2008.2007918.
(81) Algar, W. R.; Kim, H.; Medintz, I. L.; Hildebrandt, N. Emerging Non-Traditional Förster Resonance Energy Transfer Configurations with Semiconductor Quantum Dots: Investigations and Applications. *Coord. Chem. Rev.* **2014**, *263–264*, 65–85. https://doi.org/10.1016/j.ccr.2013.07.015.
(82) Geißler, D.; Linden, S.; Liermann, K.; Wegner, K. D.; Charbonnière, L. J.; Hildebrandt, N. Lanthanides and Quantum Dots as Förster Resonance Energy Transfer Agents for Diagnostics and Cellular Imaging. *Inorg. Chem.* **2014**, *53* (4), 1824–1838. https://doi.org/10.1021/ic4017883.
(83) Díaz, S. A.; Lasarte-Aragones, G.; Lowery, R. G.; Aniket; Vranish, J. N.; Klein, W. P.; Susumu, K.; Medintz, I. L. Quantum Dots as Förster Resonance Energy Transfer Acceptors of Lanthanides in Time-Resolved Bioassays. *ACS Appl. Nano Mater.* **2018**, *1* (6), 3006–3014. https://doi.org/10.1021/acsanm.8b00613.
(84) Efros, A. L.; Brus, L. E. Nanocrystal Quantum Dots: From Discovery to Modern Development. *ACS Nano* **2021**, *15* (4), 6192–6210. https://doi.org/10.1021/acsnano.1c01399.
(85) Nanocrystals in Their Prime. *Nat. Nanotechnol.* **2014**, *9* (5), 325–325. https://doi.org/10.1038/nnano.2014.101.
(86) Kagan, C. R.; Murray, C. B.; Nirmal, M.; Bawendi, M. G. Electronic Energy Transfer in CdSe Quantum Dot Solids. *Phys. Rev. Lett.* **1996**, *76* (9), 1517–1520. https://doi.org/10.1103/PhysRevLett.76.1517.
(87) Kagan, C. R.; Murray, C. B.; Bawendi, M. G. Long-Range Resonance Transfer of Electronic Excitations in Close-Packed CdSe Quantum-Dot Solids. *Phys. Rev. B* **1996**, *54* (12), 8633–8643. https://doi.org/10.1103/PhysRevB.54.8633.
(88) Chan, W. C. W.; Nie, S. Quantum Dot Bioconjugates for Ultrasensitive Nonisotopic Detection. *Science* **1998**, *281* (5385), 2016–2018. https://doi.org/10.1126/science.281.5385.2016.
(89) Bruchez, M.; Moronne, M.; Gin, P.; Weiss, S.; Alivisatos, A. P. Semiconductor Nanocrystals as Fluorescent Biological Labels. *Science* **1998**, *281* (5385), 2013–2016. https://doi.org/10.1126/science.281.5385.2013.
(90) Willard, D. M.; Carillo, L. L.; Jung, J.; Van Orden, A. CdSe−ZnS Quantum Dots as Resonance Energy Transfer Donors in a Model Protein−Protein Binding Assay. *Nano Lett.* **2001**, *1* (9), 469–474. https://doi.org/10.1021/nl015565n.

(91) Wang, S.; Mamedova, N.; Kotov, N. A.; Chen, W.; Studer, J. Antigen/Antibody Immunocomplex from CdTe Nanoparticle Bioconjugates. *Nano Lett.* **2002**, *2* (8), 817–822. https://doi.org/10.1021/nl0255193.

(92) Tran, P. t.; Anderson, G. p.; Mauro, J. m.; Mattoussi, H. Use of Luminescent CdSe–ZnS Nanocrystal Bioconjugates in Quantum Dot-Based Nanosensors. *Phys. Status Solidi B* **2002**, *229* (1), 427–432. https://doi.org/10.1002/1521-3951(200201)229:1<427::AID-PSSB427>3.0.CO;2-K.

(93) Cassette, E.; Helle, M.; Bezdetnaya, L.; Marchal, F.; Dubertret, B.; Pons, T. Design of New Quantum Dot Materials for Deep Tissue Infrared Imaging. *Adv. Drug Deliv. Rev.* **2013**, *65* (5), 719–731. https://doi.org/10.1016/j.addr.2012.08.016.

(94) Carion, O.; Mahler, B.; Pons, T.; Dubertret, B. Synthesis, Encapsulation, Purification and Coupling of Single Quantum Dots in Phospholipid Micelles for Their Use in Cellular and in Vivo Imaging. *Nat. Protoc.* **2007**, *2* (10), 2383–2390. https://doi.org/10.1038/nprot.2007.351.

(95) Medintz, I. L.; Berti, L.; Pons, T.; Grimes, A. F.; English, D. S.; Alessandrini, A.; Facci, P.; Mattoussi, H. A Reactive Peptidic Linker for Self-Assembling Hybrid Quantum Dot−DNA Bioconjugates. *Nano Lett.* **2007**, *7* (6), 1741–1748. https://doi.org/10.1021/nl070782v.

(96) Pons, T.; Medintz, I. L.; Wang, X.; English, D. S.; Mattoussi, H. Solution-Phase Single Quantum Dot Fluorescence Resonance Energy Transfer. *J. Am. Chem. Soc.* **2006**, *128* (47), 15324–15331. https://doi.org/10.1021/ja0657253.

(97) Muro, E.; Pons, T.; Lequeux, N.; Fragola, A.; Sanson, N.; Lenkei, Z.; Dubertret, B. Small and Stable Sulfobetaine Zwitterionic Quantum Dots for Functional Live-Cell Imaging. *J. Am. Chem. Soc.* **2010**, *132* (13), 4556–4557. https://doi.org/10.1021/ja1005493.

(98) Zhang, C.-Y.; Yeh, H.-C.; Kuroki, M. T.; Wang, T.-H. Single-Quantum-Dot-Based DNA Nanosensor. *Nat. Mater.* **2005**, *4* (11), 826–831. https://doi.org/10.1038/nmat1508.

(99) Zhang, C.; Hu, J. Single Quantum Dot-Based Nanosensor for Multiple DNA Detection. *Anal. Chem.* **2010**, *82* (5), 1921–1927. https://doi.org/10.1021/ac9026675.

(100) Dutta Chowdhury, A.; Takemura, K.; Memdi Khorish, I.; Nasrin, F.; Tun, M. M. N.; Morita, K.; Y. Park, E. The Detection and Identification of Dengue Virus Serotypes with Quantum Dot and AuNP Regulated Localized Surface Plasmon Resonance. *Nanoscale Adv.* **2020**, *2* (2), 699–709. https://doi.org/10.1039/C9NA00763F.

(101) Ma, Y.; Mao, G.; Huang, W.; Wu, G.; Yin, W.; Ji, X.; Deng, Z.; Cai, Z.; Zhang, X.-E.; He, Z.; Cui, Z. Quantum Dot Nanobeacons for Single RNA Labeling and Imaging. *J. Am. Chem. Soc.* **2019**, *141* (34), 13454–13458. https://doi.org/10.1021/jacs.9b04659.

(102) Choi, J. H.; Chen, K. H.; Strano, M. S. Aptamer-Capped Nanocrystal Quantum Dots: A New Method for Label-Free Protein Detection. *J. Am. Chem. Soc.* **2006**, *128* (49), 15584–15585. https://doi.org/10.1021/ja066506k.

(103) Xing, Y.; So, M.; Koh, A. L.; Sinclair, R.; Rao, J. Improved QD-BRET Conjugates for Detection and Imaging. *Biochem. Biophys. Res. Commun.* **2008**, *372* (3), 388–394. https://doi.org/10.1016/j.bbrc.2008.04.159.

(104) Sapsford, K. E.; Pons, T.; Medintz, I. L.; Higashiya, S.; Brunel, F. M.; Dawson, P. E.; Mattoussi, H. Kinetics of Metal-Affinity Driven Self-Assembly between Proteins or Peptides and CdSe−ZnS Quantum Dots. *J. Phys. Chem. C* **2007**, *111* (31), 11528–11538. https://doi.org/10.1021/jp073550t.

(105) Hoshino, A.; Fujioka, K.; Manabe, N.; Yamaya, S.; Goto, Y.; Yasuhara, M.; Yamamoto, K. Simultaneous Multicolor Detection System of the Single-Molecular Microbial Antigen with Total Internal Reflection Fluorescence Microscopy. *Microbiol. Immunol.* **2005**, *49* (5), 461–470. https://doi.org/10.1111/j.1348-0421.2005.tb03750.x.

(106) Cui, D.; Pan, B.; Zhang, H.; Gao, F.; Wu, R.; Wang, J.; He, R.; Asahi, T. Self-Assembly of Quantum Dots and Carbon Nanotubes for Ultrasensitive DNA and Antigen Detection. *Anal. Chem.* **2008**, *80* (21), 7996–8001. https://doi.org/10.1021/ac800992m.
(107) Zhou, L.; Zhu, A.; Lou, X.; Song, D.; Yang, R.; Shi, H.; Long, F. Universal Quantum Dot-Based Sandwich-like Immunoassay Strategy for Rapid and Ultrasensitive Detection of Small Molecules Using Portable and Reusable Optofluidic Nano-Biosensing Platform. *Anal. Chim. Acta* **2016**, *905*, 140–148. https://doi.org/10.1016/j.aca.2015.12.003.
(108) Rabouw, F. T.; de Mello Donega, C. Excited-State Dynamics in Colloidal Semiconductor Nanocrystals. *Top. Curr. Chem.* **2016**, *374* (5), 58. https://doi.org/10.1007/s41061-016-0060-0.
(109) Mastria, R.; Rizzo, A. Mastering Heterostructured Colloidal Nanocrystal Properties for Light-Emitting Diodes and Solar Cells. *J. Mater. Chem. C* **2016**, *4* (27), 6430–6446. https://doi.org/10.1039/C6TC01334A.
(110) Ramalingam, G.; Kathirgamanathan, P.; Ravi, G.; Elangovan, T.; Arjun kumar, B.; Manivannan, N.; Kasinathan, K. Quantum Confinement Effect of 2D Nanomaterials. In *Quantum Dots - Fundamental and Applications*; Divsar, F., Ed.; IntechOpen, 2020. https://doi.org/10.5772/intechopen.90140.
(111) Pietka, B. Excitonic Complexes in Natural Quantum Dots Formed in Type II GaAs/AlAs Structures. 174.
(112) Klimov, V. I. *Nanocrystal Quantum Dots*; CRC Press, 2017.
(113) Deutsch, Z.; Avidan, A.; Pinkas, I.; Oron, D. Energetics and Dynamics of Exciton–Exciton Interactions in Compound Colloidal Semiconductor Quantum Dots. *Phys. Chem. Chem. Phys.* **2011**, *13* (8), 3210–3219. https://doi.org/10.1039/C0CP02253E.
(114) Shen, H.; Lin, Q.; Cao, W.; Yang, C.; Shewmon, N. T.; Wang, H.; Niu, J.; Li, L. S.; Xue, J. Efficient and Long-Lifetime Full-Color Light-Emitting Diodes Using High Luminescence Quantum Yield Thick-Shell Quantum Dots. *Nanoscale* **2017**, *9* (36), 13583–13591. https://doi.org/10.1039/C7NR04953F.
(115) Ratnesh, R. K.; Mehata, M. S. Synthesis and Optical Properties of Core-Multi-Shell CdSe/CdS/ZnS Quantum Dots: Surface Modifications. *Opt. Mater.* **2017**, *64*, 250–256. https://doi.org/10.1016/j.optmat.2016.11.043.
(116) Pu, Y.; Cai, F.; Wang, D.; Wang, J.-X.; Chen, J.-F. Colloidal Synthesis of Semiconductor Quantum Dots toward Large-Scale Production: A Review. *Ind. Eng. Chem. Res.* **2018**, *57* (6), 1790–1802. https://doi.org/10.1021/acs.iecr.7b04836.
(117) LaMer, V. K.; Dinegar, R. H. Theory, Production and Mechanism of Formation of Monodispersed Hydrosols. *J. Am. Chem. Soc.* **1950**, *72* (11), 4847–4854. https://doi.org/10.1021/ja01167a001.
(118) Dunne, P. W.; Munn, A. S.; Starkey, C. L.; Huddle, T. A.; Lester, E. H. Continuous-Flow Hydrothermal Synthesis for the Production of Inorganic Nanomaterials. *Philos. Trans. R. Soc. Math. Phys. Eng. Sci.* **2015**, *373* (2057), 20150015. https://doi.org/10.1098/rsta.2015.0015.
(119) Sugimoto, T. Preparation of Monodispersed Colloidal Particles. *Adv. Colloid Interface Sci.* **1987**, *28*, 65–108. https://doi.org/10.1016/0001-8686(87)80009-X.
(120) Battaglia, D.; Peng, X. Formation of High Quality InP and InAs Nanocrystals in a Noncoordinating Solvent. *Nano Lett.* **2002**, *2* (9), 1027–1030. https://doi.org/10.1021/nl025687v.
(121) Smith, A. M.; Nie, S. Semiconductor Nanocrystals: Structure, Properties, and Band Gap Engineering. *Acc. Chem. Res.* **2010**, *43* (2), 190–200. https://doi.org/10.1021/ar9001069.
(122) Petryayeva, E.; Algar, W. R.; Medintz, I. L. Quantum Dots in Bioanalysis: A Review of Applications Across Various Platforms for Fluorescence Spectroscopy and Imaging. *Appl. Spectrosc.* **2013**, *67* (3), 215–252.

(123) Algar, W. R.; Tavares, A. J.; Krull, U. J. Beyond Labels: A Review of the Application of Quantum Dots as Integrated Components of Assays, Bioprobes, and Biosensors Utilizing Optical Transduction. *Anal. Chim. Acta* **2010**, *673* (1), 1–25. https://doi.org/10.1016/j.aca.2010.05.026.
(124) Leatherdale, C. A.; Woo, W.-K.; Mikulec, F. V.; Bawendi, M. G. On the Absorption Cross Section of CdSe Nanocrystal Quantum Dots. *J. Phys. Chem. B* **2002**, *106* (31), 7619–7622. https://doi.org/10.1021/jp025698c.
(125) Linkov, P.; Krivenkov, V.; Nabiev, I.; Samokhvalov, P. High Quantum Yield CdSe/ZnS/CdS/ZnS Multishell Quantum Dots for Biosensing and Optoelectronic Applications. *Mater. Today Proc.* **2016**, *3* (2), 104–108. https://doi.org/10.1016/j.matpr.2016.01.033.
(126) Greytak, A. B.; Allen, P. M.; Liu, W.; Zhao, J.; Young, E. R.; Popović, Z.; Walker, B. J.; Nocera, D. G.; Bawendi, M. G. Alternating Layer Addition Approach to CdSe/CdS Core/Shell Quantum Dots with near-Unity Quantum Yield and High on-Time Fractions. *Chem. Sci.* **2012**, *3* (6), 2028–2034. https://doi.org/10.1039/C2SC00561A.
(127) Peng, X.; Schlamp, M. C.; Kadavanich, A. V.; Alivisatos, A. P. Epitaxial Growth of Highly Luminescent CdSe/CdS Core/Shell Nanocrystals with Photostability and Electronic Accessibility. *J. Am. Chem. Soc.* **1997**, *119* (30), 7019–7029. https://doi.org/10.1021/ja970754m.
(128) Choi, S.-H.; Song, H.; Park, I. K.; Yum, J.-H.; Kim, S.-S.; Lee, S.; Sung, Y.-E. Synthesis of Size-Controlled CdSe Quantum Dots and Characterization of CdSe–Conjugated Polymer Blends for Hybrid Solar Cells. *J. Photochem. Photobiol. Chem.* **2006**, *179* (1), 135–141. https://doi.org/10.1016/j.jphotochem.2005.08.004.
(129) Baker, D. R.; Kamat, P. V. Tuning the Emission of CdSe Quantum Dots by Controlled Trap Enhancement. *Langmuir* **2010**, *26* (13), 11272–11276. https://doi.org/10.1021/la100580g.
(130) Lim, S. J.; Zahid, M. U.; Le, P.; Ma, L.; Entenberg, D.; Harney, A. S.; Condeelis, J.; Smith, A. M. Brightness-Equalized Quantum Dots. *Nat. Commun.* **2015**, *6* (1), 8210. https://doi.org/10.1038/ncomms9210.
(131) Ostapenko, I. A.; Hönig, G.; Kindel, C.; Rodt, S.; Strittmatter, A.; Hoffmann, A.; Bimberg, D. Large Internal Dipole Moment in InGaN/GaN Quantum Dots. *Appl. Phys. Lett.* **2010**, *97* (6), 063103. https://doi.org/10.1063/1.3477952.
(132) Kilina, S. V.; Tamukong, P. K.; Kilin, D. S. Surface Chemistry of Semiconducting Quantum Dots: Theoretical Perspectives. *Acc. Chem. Res.* **2016**, *49* (10), 2127–2135. https://doi.org/10.1021/acs.accounts.6b00196.
(133) Goldman, E. R.; Medintz, I. L.; Whitley, J. L.; Hayhurst, A.; Clapp, A. R.; Uyeda, H. T.; Deschamps, J. R.; Lassman, M. E.; Mattoussi, H. A Hybrid Quantum Dot−Antibody Fragment Fluorescence Resonance Energy Transfer-Based TNT Sensor. *J. Am. Chem. Soc.* **2005**, *127* (18), 6744–6751. https://doi.org/10.1021/ja043677l.
(134) Wegner, K. D.; Lindén, S.; Jin, Z.; Jennings, T. L.; Khoulati, R. el; van Bergen en Henegouwen, P. M. P.; Hildebrandt, N. Nanobodies and Nanocrystals: Highly Sensitive Quantum Dot-Based Homogeneous FRET Immunoassay for Serum-Based EGFR Detection. *Small* **2014**, *10* (4), 734–740. https://doi.org/10.1002/smll.201302383.
(135) Chiasera, A.; Dumeige, Y.; Féron, P.; Ferrari, M.; Jestin, Y.; Conti, G. N.; Pelli, S.; Soria, S.; Righini, G. C. Spherical Whispering-Gallery-Mode Microresonators. *Laser Photonics Rev.* **2010**, *4* (3), 457–482. https://doi.org/10.1002/lpor.200910016.
(136) Lee, B.-Y.; Kim, J.; Kim, H.; Kim, C.; Lee, S.-D. Low-Cost Flexible Pressure Sensor Based on Dielectric Elastomer Film with Micro-Pores. *Sens. Actuators Phys.* **2016**, *240*, 103–109. https://doi.org/10.1016/j.sna.2016.01.037.

(137) Sarychev, A. K.; Ivanov, A.; Lagarkov, A.; Barbillon, G. Light Concentration by Metal-Dielectric Micro-Resonators for SERS Sensing. *Materials* **2019**, *12* (1), 103. https://doi.org/10.3390/ma12010103.
(138) Foreman, M. R.; Swaim, J. D.; Vollmer, F. Whispering Gallery Mode Sensors. *Adv. Opt. Photonics* **2015**, *7* (2), 168–240. https://doi.org/10.1364/AOP.7.000168.
(139) Righini, G. C.; Dumeige, Y.; Féron, P.; Ferrari, M.; Nunzi Conti, G.; Ristic, D.; Soria, S. Whispering Gallery Mode Microresonators: Fundamentals and Applications. *Riv. Nuovo Cimento* **2011**, *34* (7), 435–488. https://doi.org/10.1393/ncr/i2011-10067-2.
(140) Chattopadhyay, B. A. C.V. Raman and image building through media--India Science Wire http://vigyanprasar.gov.in/isw/CVRaman-and-image-building-through-media.html (accessed 2021 -10 -13).
(141) Jiang, X.-F.; Xiao, Y.-F.; Yang, Q.-F.; Shao, L.; Clements, W. R.; Gong, Q. Free-Space Coupled, Ultralow-Threshold Raman Lasing from a Silica Microcavity. *Appl. Phys. Lett.* **2013**, *103* (10), 101102. https://doi.org/10.1063/1.4820133.
(142) Lee, H.; Chen, T.; Li, J.; Yang, K. Y.; Jeon, S.; Painter, O.; Vahala, K. J. Chemically Etched Ultrahigh-Q Wedge-Resonator on a Silicon Chip. *Nat. Photonics* **2012**, *6* (6), 369–373. https://doi.org/10.1038/nphoton.2012.109.
(143) Nowicki-Bringuier, Y.-R.; Claudon, J.; Böckler, C.; Reitzenstein, S.; Kamp, M.; Morand, A.; Forchel, A.; Gérard, J. M. High Q Whispering Gallery Modes in GaAs/AlAs Pillar Microcavities. *Opt. Express* **2007**, *15* (25), 17291–17304. https://doi.org/10.1364/OE.15.017291.
(144) Spillane, S. M.; Kippenberg, T. J.; Vahala, K. J. Ultralow-Threshold Raman Laser Using a Spherical Dielectric Microcavity. *Nature* **2002**, *415* (6872), 621–623. https://doi.org/10.1038/415621a.
(145) Pöllinger, M.; O'Shea, D.; Warken, F.; Rauschenbeutel, A. Ultrahigh-Q Tunable Whispering-Gallery-Mode Microresonator. *Phys. Rev. Lett.* **2009**, *103* (5), 053901. https://doi.org/10.1103/PhysRevLett.103.053901.
(146) Henze, R.; Seifert, T.; Ward, J.; Benson, O. Tuning Whispering Gallery Modes Using Internal Aerostatic Pressure. *Opt. Lett.* **2011**, *36* (23), 4536–4538. https://doi.org/10.1364/OL.36.004536.
(147) Xu, Q.; Schmidt, B.; Pradhan, S.; Lipson, M. Micrometre-Scale Silicon Electro-Optic Modulator. *Nature* **2005**, *435* (7040), 325–327. https://doi.org/10.1038/nature03569.
(148) Zamora, V.; Díez, A.; Andrés, M. V.; Gimeno, B. Cylindrical Optical Microcavities: Basic Properties and Sensor Applications. *Photonics Nanostructures - Fundam. Appl.* **2011**, *9* (2), 149–158. https://doi.org/10.1016/j.photonics.2010.09.007.
(149) Médard, F.; Lagarde, D.; Zúñiga-Pérez, J.; Disseix, P.; Leymarie, J.; Mihailovic, M.; Solnyshkov, D. D.; Malpuech, G.; Frayssinet, E.; Sergent, S.; Semond, F.; Leroux, M.; Bouchoule, S. Toward Polariton Lasing in a Zinc Oxide Microcavity: Design and Preliminary Results. *J. Phys.: Conf. Ser.* **2010**, *210*, 012026. https://doi.org/10.1088/1742-6596/210/1/012026.
(150) Vollmer, F.; Yang, L. Review Label-Free Detection with High-Q Microcavities: A Review of Biosensing Mechanisms for Integrated Devices. *Nanophotonics* **2012**, *1* (3–4), 267–291. https://doi.org/10.1515/nanoph-2012-0021.
(151) Antonello, A.; Guglielmi, M.; Bello, V.; Mattei, G.; Chiasera, A.; Ferrari, M.; Martucci, A. Titanate Nanosheets as High Refractive Layer in Vertical Microcavity Incorporating Semiconductor Quantum Dots. *J. Phys. Chem. C* **2010**, *114* (43), 18423–18428. https://doi.org/10.1021/jp106951y.
(152) Chen, D.; Xu, J.; Qian, B.; Chen, S.; Mei, J.; Li, W.; Xu, L.; Chen, K. Luminescence Behavior from Amorphous Silicon-Carbide Film-Based Optical Microcavities. *Mater. Chem. Phys.* **2008**, *111* (2), 279–282. https://doi.org/10.1016/j.matchemphys.2008.04.008.

(153) Levy, J. S.; Foster, M. A.; Gaeta, A. L.; Lipson, M. Harmonic Generation in Silicon Nitride Ring Resonators. *Opt. Express* **2011**, *19* (12), 11415–11421. https://doi.org/10.1364/OE.19.011415.
(154) Tavernier, H.; Salzenstein, P.; Volyanskiy, K.; Chembo, Y. K.; Larger, L. Magnesium Fluoride Whispering Gallery Mode Disk-Resonators for Microwave Photonics Applications. *IEEE Photonics Technol. Lett.* **2010**, *22* (22), 1629–1631. https://doi.org/10.1109/LPT.2010.2075923.
(155) Cao, J. R.; Kuang, W.; Wei, Z.-J.; Choi, S.-J.; Yu, H.; Bagheri, M.; O'Brien, J. D.; Dapkus, P. D. Sapphire-Bonded Photonic Crystal Microcavity Lasers and Their Far-Field Radiation Patterns. *IEEE Photonics Technol. Lett.* **2005**, *17* (1), 4–6. https://doi.org/10.1109/LPT.2004.837245.
(156) Zhu, G.; Li, J.; Li, P.; Tian, Z.; Dai, J.; Wang, Y.; Shi, Z.; Xu, C. Different Wavelength Ranges' WGM Lasing from a ZnO Microrod/R6G:PMMA Microcavity. *EPL* **2015**, *110* (6), 67007. https://doi.org/10.1209/0295-5075/110/67007.
(157) Hu, X.; Jiang, P.; Ding, C.; Yang, H.; Gong, Q. Picosecond and Low-Power All-Optical Switching Based on an Organic Photonic-Bandgap Microcavity. *Nat. Photonics* **2008**, *2* (3), 185–189. https://doi.org/10.1038/nphoton.2007.299.
(158) Li, B.-B.; Xiao, Y.-F.; Yan, M.-Y.; Clements, W. R.; Gong, Q. Low-Threshold Raman Laser from an on-Chip, High-Q, Polymer-Coated Microcavity. *Opt. Lett.* **2013**, *38* (11), 1802–1804. https://doi.org/10.1364/OL.38.001802.
(159) Bigourdan, F.; Marquier, F.; Hugonin, J.-P.; Greffet, J.-J. Design of Highly Efficient Metallo-Dielectric Patch Antennas for Single-Photon Emission. *Opt. Express* **2014**, *22* (3), 2337–2347. https://doi.org/10.1364/OE.22.002337.
(160) Kakarantzas, G.; Dimmick, T. E.; Birks, T. A.; Roux, R. L.; Russell, P. S. J. Miniature All-Fiber Devices Based on CO_2 Laser Microstructuring of Tapered Fibers. *Opt. Lett.* **2001**, *26* (15), 1137–1139. https://doi.org/10.1364/OL.26.001137.
(161) Honari, S.; Haque, S.; Lu, T. Ultra-High Q Silica Microcavity Fabrication Using Conventional Photolithography Combined with Chemo-Mechanical Polishing. In *Conference on Lasers and Electro-Optics (2021), paper JTu3A.85*; Optical Society of America, 2021; p JTu3A.85. https://doi.org/10.1364/CLEO_AT.2021.JTu3A.85.
(162) Fang, Z.; Chormaic, S. N.; Wang, S.; Wang, X.; Yu, J.; Jiang, Y.; Qiu, J.; Wang, P. Bismuth-Doped Glass Microsphere Lasers. *Photonics Res.* **2017**, *5* (6), 740–744. https://doi.org/10.1364/PRJ.5.000740.
(163) Dong, B.; Hao, J.; Zhang, T.; Lim, J. L. High Sensitive Fiber-Optic Liquid Refractive Index Tip Sensor Based on a Simple Inline Hollow Glass Micro-Sphere. *Sens. Actuators B Chem.* **2012**, *171–172*, 405–408. https://doi.org/10.1016/j.snb.2012.05.001.
(164) Fang, J.; Xuan, Y.; Li, Q. Preparation of Polystyrene Spheres in Different Particle Sizes and Assembly of the PS Colloidal Crystals. *Sci. China Technol. Sci.* **2010**, *53* (11), 3088–3093. https://doi.org/10.1007/s11431-010-4110-5.
(165) Piaopiao, W.; Zihui, M. Progress in Polystyrene Microspheres. *IOP Conf. Ser.: Mater. Sci. Eng.* **2019**, *563*, 022001. https://doi.org/10.1088/1757-899X/563/2/022001.
(166) Hai, N. H.; Luong, N. H.; Chau, N.; Tai, N. Q. Preparation of Magnetic Nanoparticles Embedded in Polystyrene Microspheres. *J. Phys.: Conf. Ser.* **2009**, *187*, 012009. https://doi.org/10.1088/1742-6596/187/1/012009.
(167) Poostforooshan, J.; Belbekhouche, S.; Shaban, M.; Alphonse, V.; Habert, D.; Bousserrhine, N.; Courty, J.; Weber, A. P. Aerosol-Assisted Synthesis of Tailor-Made Hollow Mesoporous Silica Microspheres for Controlled Release of Antibacterial and Anticancer Agents. *ACS Appl. Mater. Interfaces* **2020**, *12* (6), 6885–6898. https://doi.org/10.1021/acsami.9b20510.
(168) Rubino, E.; Ioppolo, T. Electrostrictive Optical Resonators for Non-Contact Displacement Measurement. *Appl. Opt.* **2017**, *56* (2), 229–233. https://doi.org/10.1364/AO.56.000229.

(169) Radin, S.; Chen, T.; Ducheyne, P. The Controlled Release of Drugs from Emulsified, Sol Gel Processed Silica Microspheres. *Biomaterials* **2009**, *30* (5), 850–858. https://doi.org/10.1016/j.biomaterials.2008.09.066.
(170) De, G.; Karmakar, B.; Ganguli, D. Hydrolysis–Condensation Reactions of TEOS in the Presence of Acetic Acid Leading to the Generation of Glass-like Silica Microspheres in Solution at Room Temperature. *J. Mater. Chem.* **2000**, *10* (10), 2289–2293. https://doi.org/10.1039/B003221M.
(171) Karmakar, B.; De, G.; Ganguli, D. Dense Silica Microspheres from Organic and Inorganic Acid Hydrolysis of TEOS. *J. Non-Cryst. Solids* **2000**, *272* (2), 119–126. https://doi.org/10.1016/S0022-3093(00)00231-3.
(172) Braginsky, V. B.; Gorodetsky, M. L.; Ilchenko, V. S. Quality-Factor and Nonlinear Properties of Optical Whispering-Gallery Modes. *Phys. Lett. A* **1989**, *137* (7), 393–397. https://doi.org/10.1016/0375-9601(89)90912-2.
(173) Gorodetsky, M. L.; Ilchenko, V. S. Optical Microsphere Resonators: Optimal Coupling to High-Q Whispering-Gallery Modes. *JOSA B* **1999**, *16* (1), 147–154. https://doi.org/10.1364/JOSAB.16.000147.
(174) Jana, S.; Xu, X.; Klymchenko, A.; Reisch, A.; Pons, T. Microcavity-Enhanced Fluorescence Energy Transfer from Quantum Dot Excited Whispering Gallery Modes to Acceptor Dye Nanoparticles. *ACS Nano* **2020**. https://doi.org/10.1021/acsnano.0c08772.
(175) Jana, S.; Klymchenko, A.; Pons, T.; Reisch, A. Biodetection with Whispering Quantum Dots. In *Optical Sensors 2021*; International Society for Optics and Photonics, 2021; Vol. 11772, p 1177204. https://doi.org/10.1117/12.2585563.
(176) Barnes, W. L. Fluorescence near Interfaces: The Role of Photonic Mode Density. *J. Mod. Opt.* **1998**, *45* (4), 661–699. https://doi.org/10.1080/09500349808230614.
(177) Andrew, P.; Barnes, W. L. Förster Energy Transfer in an Optical Microcavity. *Science* **2000**, *290* (5492), 785–788. https://doi.org/10.1126/science.290.5492.785.
(178) Purcell, E. M.; Torrey, H. C.; Pound, R. V. Resonance Absorption by Nuclear Magnetic Moments in a Solid. *Phys. Rev.* **1946**, *69* (1–2), 37–38. https://doi.org/10.1103/PhysRev.69.37.
(179) Charlebois, M.; Paquet, A.; Verret, L. S.; Boissinot, K.; Boissinot, M.; Bergeron, M. G.; Allen, C. N. Toward Automatic Label-Free Whispering Gallery Modes Biodetection with a Quantum Dot-Coated Microsphere Population. *Nanoscale Res. Lett.* **2010**, *5* (3), 524–532. https://doi.org/10.1007/s11671-010-9541-1.
(180) Ilchenko, V. S.; Savchenkov, A. A.; Matsko, A. B.; Maleki, L. Nonlinear Optics and Crystalline Whispering Gallery Mode Cavities. *Phys. Rev. Lett.* **2004**, *92* (4), 043903. https://doi.org/10.1103/PhysRevLett.92.043903.
(181) Matsko, A. B.; Savchenkov, A. A.; Strekalov, D.; Ilchenko, V. S.; Maleki, L. Review of Applications of Whispering-Gallery Mode Resonators in Photonics and Nonlinear Optics. *Interplanet. Netw. Prog. Rep.* **2005**, *42–162*, 1–51.
(182) Baaske, M. D.; Foreman, M. R.; Vollmer, F. Single-Molecule Nucleic Acid Interactions Monitored on a Label-Free Microcavity Biosensor Platform. *Nat. Nanotechnol.* **2014**, *9* (11), 933–939. https://doi.org/10.1038/nnano.2014.180.
(183) Toropov, N.; Cabello, G.; Serrano, M. P.; Gutha, R. R.; Rafti, M.; Vollmer, F. Review of Biosensing with Whispering-Gallery Mode Lasers. *Light Sci. Appl.* **2021**, *10* (1), 42. https://doi.org/10.1038/s41377-021-00471-3.
(184) Urquhart, P. Compound Optical-Fiber-Based Resonators. *JOSA A* **1988**, *5* (6), 803–812. https://doi.org/10.1364/JOSAA.5.000803.
(185) Rabiei, P.; Steier, W. H. Tunable Polymer Double Micro-Ring Filters. *IEEE Photonics Technol. Lett.* **2003**, *15* (9), 1255–1257. https://doi.org/10.1109/LPT.2003.816111.

(186) Darmawan, S. Microring Resonator Based Photonic Devices Using High-Contrast Waveguides. Thesis, 2009. https://doi.org/10.32657/10356/15715.
(187) Huang, S.; Maleki, L.; Le, T. A 10 GHz Optoelectronic Oscillator with Continuous Frequency Tunability and Low Phase Noise. In *Proceedings of the 2001 IEEE International Frequncy Control Symposium and PDA Exhibition (Cat. No.01CH37218)*; 2001; pp 720–727. https://doi.org/10.1109/FREQ.2001.956370.
(188) Yuan, Z.; Wang, Z.; Guan, P.; Wu, X.; Chen, Y.-C. Lasing-Encoded Microsensor Driven by Interfacial Cavity Resonance Energy Transfer. *Adv. Opt. Mater.* **2020**, *8* (7), 1901596. https://doi.org/10.1002/adom.201901596.
(189) Chen, Y.-C.; Chen, Q.; Fan, X. Lasing in Blood. *Optica* **2016**, *3* (8), 809–815. https://doi.org/10.1364/OPTICA.3.000809.
(190) Orucevic, F.; Hare, J.; Lefèvre-Seguin, V. Neodymium Photoluminescence in Whispering Gallery Modes of Toroidal Microcavities. In *Optics East*; Piprek, Wang, J., Jim, J., Eds.; Proceedings of SPIE; SPIE: Boston, United States, 2006; Vol. 6368, p 63680Q.
(191) Chen, Z.; Tu, X.; Zhao, J.; Fu, H. Y. An Erbium-Doped Fiber Whispering-Gallery-Mode Microcavity Laser. *IEEE Photonics Technol. Lett.* **2019**, *31* (20), 1650–1653. https://doi.org/10.1109/LPT.2019.2942046.
(192) AlSalhi, M. S.; Prasad, S.; Aljaafreh, M. J.; Othman, A. H. S. Broadband Frequency-Tunable Whispering-Gallery-Mode Superradiant Light from Quantum Dots in Colloidal Solution. *J. Nanomater.* **2018**, *2018*, e3754307. https://doi.org/10.1155/2018/3754307.
(193) Flatae, A.; Grossmann, T.; Beck, T.; Wiegele, S.; Kalt, H. Strongly Confining Bare Core CdTe Quantum Dots in Polymeric Microdisk Resonators. *APL Mater.* **2014**, *2* (1). https://doi.org/10.1063/1.4862695.
(194) Steiner, S.; Hare, J.; Lefèvre-Seguin, V.; Gérard, J.-M. Room Temperature Lasing of InAs/GaAs Quantum Dots in the Whispering Gallery Modes of a Silica Microsphere. *Opt. Express* **2007**, *15* (16), 10052. https://doi.org/10.1364/OE.15.010052.
(195) Fan, H.; Zhou, D.; Fan, L.; Wu, Y.; Tao, H.; Gong, J. Excitation of Multi-Beam Interference and Whispering-Gallery Mode in Silica Taper-Assisted Polymer Microspheres for Refractometric Sensing. *Photonics* **2021**, *8* (4), 117. https://doi.org/10.3390/photonics8040117.
(196) Sun, Y.; Shopova, S. I.; Frye-Mason, G.; Fan, X. Rapid Chemical-Vapor Sensing Using Optofluidic Ring Resonators. *Opt. Lett.* **2008**, *33* (8), 788–790. https://doi.org/10.1364/OL.33.000788.
(197) Liang, L.; Li, M.; Liu, N.; Sun, H.; Rong, Q.; Hu, M. A High-Sensitivity Optical Fiber Relative Humidity Sensor Based on Microsphere WGM Resonator. *Opt. Fiber Technol.* **2018**, *45*, 415–418. https://doi.org/10.1016/j.yofte.2018.07.023.
(198) Yebo, N. A.; Lommens, P.; Hens, Z.; Baets, R. An Integrated Optic Ethanol Vapor Sensor Based on a Silicon-on-Insulator Microring Resonator Coated with a Porous ZnO Film. *Opt. Express* **2010**, *18* (11), 11859–11866. https://doi.org/10.1364/OE.18.011859.
(199) Ioppolo, T.; Kozhevnikov, M.; Stepaniuk, V.; Ötügen, M. V.; Sheverev, V. Micro-Optical Force Sensor Concept Based on Whispering Gallery Mode Resonators. *Appl. Opt.* **2008**, *47* (16), 3009–3014. https://doi.org/10.1364/AO.47.003009.
(200) Soler-Carracedo, K.; Estévez-Alonso, P.; Martin, I. R.; Rios, S. Improving the Sensitivity of WGM Pressure Sensors with Oxyfluoride Glass Microspheres. *J. Lumin.* **2021**, *238*, 118249. https://doi.org/10.1016/j.jlumin.2021.118249.
(201) Matsko, A. B.; Savchenkov, A. A.; Ilchenko, V. S.; Maleki, L. Erratum to “Optical Gyroscope with Whispering Gallery Mode Optical Cavities” [Opt. Commun. 233 (2004) 107–112]. *Opt. Commun.* **2006**, *259* (1), 393–394. https://doi.org/10.1016/j.optcom.2005.08.017.

(202) Vollmer, F.; Braun, D.; Libchaber, A.; Khoshsima, M.; Teraoka, I.; Arnold, S. Protein Detection by Optical Shift of a Resonant Microcavity. *Appl. Phys. Lett.* **2002**, *80* (21), 4057–4059. https://doi.org/10.1063/1.1482797.

(203) Arnold, S.; Khoshsima, M.; Teraoka, I.; Holler, S.; Vollmer, F. Shift of Whispering-Gallery Modes in Microspheres by Protein Adsorption. *Opt. Lett.* **2003**, *28* (4), 272–274. https://doi.org/10.1364/OL.28.000272.

(204) Teraoka, I.; Arnold, S.; Vollmer, F. Perturbation Approach to Resonance Shifts of Whispering-Gallery Modes in a Dielectric Microsphere as a Probe of a Surrounding Medium. *JOSA B* **2003**, *20* (9), 1937–1946. https://doi.org/10.1364/JOSAB.20.001937.

(205) Arnold, S.; Keng, D.; Shopova, S. I.; Holler, S.; Zurawsky, W.; Vollmer, F. Whispering Gallery Mode Carousel – a Photonic Mechanism for Enhanced Nanoparticle Detection in Biosensing. *Opt. Express* **2009**, *17* (8), 6230–6238. https://doi.org/10.1364/OE.17.006230.

(206) N. Passaro, V. M.; Troia, B.; La Notte, M.; De Leonardis, F. Photonic Resonant Microcavities for Chemical and Biochemical Sensing. *RSC Adv.* **2013**, *3* (1), 25–44. https://doi.org/10.1039/C2RA21984K.

(207) Wang, Z.; Jin, G. Feasibility of Protein A for the Oriented Immobilization of Immunoglobulin on Silicon Surface for a Biosensor with Imaging Ellipsometry. *J. Biochem. Biophys. Methods* **2003**, *57* (3), 203–211. https://doi.org/10.1016/S0165-022X(03)00109-X.

(208) De Stefano, L.; Oliviero, G.; Amato, J.; Borbone, N.; Piccialli, G.; Mayol, L.; Rendina, I.; Terracciano, M.; Rea, I. Aminosilane Functionalizations of Mesoporous Oxidized Silicon for Oligonucleotide Synthesis and Detection. *J. R. Soc. Interface* **2013**, *10* (83), 20130160. https://doi.org/10.1098/rsif.2013.0160.

(209) Marcello, A.; Sblattero, D.; Cioarec, C.; Maiuri, P.; Melpignano, P. A Deep-Blue OLED-Based Biochip for Protein Microarray Fluorescence Detection. *Biosens. Bioelectron.* **2013**, *46*, 44–47. https://doi.org/10.1016/j.bios.2013.02.017.

(210) Ramakrishan, S. K.; Martin Fernandez, M.; Cloitre, T.; Agarwal, V.; Cuisinier, F. J. G.; Gergely, C. Porous Silicon Microcavities Redefine Colorimetric ELISA Sensitivity for Ultrasensitive Detection of Autoimmune Antibodies. *Sens. Actuators B Chem.* **2018**, *272*, 211–218. https://doi.org/10.1016/j.snb.2018.05.154.

(211) Vollmer, F.; Arnold, S.; Braun, D.; Teraoka, I.; Libchaber, A. Multiplexed DNA Quantification by Spectroscopic Shift of Two Microsphere Cavities. *Biophys. J.* **2003**, *85* (3), 1974–1979. https://doi.org/10.1016/S0006-3495(03)74625-6.

(212) Ren, H.-C.; Vollmer, F.; Arnold, S.; Libchaber, A. High-Q Microsphere Biosensor - Analysis for Adsorption of Rodlike Bacteria. *Opt. Express* **2007**, *15* (25), 17410–17423. https://doi.org/10.1364/OE.15.017410.

(213) Arnold, S.; Ramjit, R.; Keng, D.; Kolchenko, V.; Teraoka, I. MicroParticle Photophysics Illuminates Viral Bio-Sensing. *Faraday Discuss.* **2008**, *137* (0), 65–83. https://doi.org/10.1039/B702920A.

(214) Sun, Y.; Shopova, S. I.; Wu, C.-S.; Arnold, S.; Fan, X. Bioinspired Optofluidic FRET Lasers via DNA Scaffolds. *Proc. Natl. Acad. Sci. U. S. A.* **2010**, *107* (37), 16039–16042. https://doi.org/10.1073/pnas.1003581107.

(215) Lee, W.; Chen, Q.; Fan, X.; Yoon, D. K. Digital DNA Detection Based on a Compact Optofluidic Laser with Ultra-Low Sample Consumption. *Lab. Chip* **2016**, *16* (24), 4770–4776. https://doi.org/10.1039/C6LC01258B.

(216) Duan, R.; Hao, X.; Li, Y.; Li, H. Detection of Acetylcholinesterase and Its Inhibitors by Liquid Crystal Biosensor Based on Whispering Gallery Mode. *Sens. Actuators B Chem.* **2020**, *308*, 127672. https://doi.org/10.1016/j.snb.2020.127672.

(217) Ouyang, X.; Liu, T.; Zhang, Y.; He, J.; He, Z.; Zhang, A. P.; Tam, H.-Y. Ultrasensitive Optofluidic Enzyme-Linked Immunosorbent Assay by on-Chip Integrated Polymer Whispering-Gallery-Mode Microlaser Sensors. *Lab. Chip* **2020**, *20* (14), 2438–2446. https://doi.org/10.1039/D0LC00240B.
(218) Wu, X.; Oo, M. K. K.; Reddy, K.; Chen, Q.; Sun, Y.; Fan, X. Optofluidic Laser for Dual-Mode Sensitive Biomolecular Detection with a Large Dynamic Range. *Nat. Commun.* **2014**, *5* (1), 3779. https://doi.org/10.1038/ncomms4779.
(219) Beier, H. T.; Coté, G. L.; Meissner, K. E. Whispering Gallery Mode Biosensors Consisting of Quantum Dot-Embedded Microspheres. *Ann. Biomed. Eng.* **2009**, *37* (10), 1974–1983. https://doi.org/10.1007/s10439-009-9713-2.
(220) Shambat, G.; Kothapalli, S.-R.; Provine, J.; Sarmiento, T.; Harris, J.; Gambhir, S. S.; Vučković, J. Single-Cell Photonic Nanocavity Probes. *Nano Lett.* **2013**, *13* (11), 4999–5005. https://doi.org/10.1021/nl304602d.
(221) Himmelhaus, M.; Francois, A. In-Vitro Sensing of Biomechanical Forces in Live Cells by a Whispering Gallery Mode Biosensor. *Biosens. Bioelectron.* **2009**, *25* (2), 418–427. https://doi.org/10.1016/j.bios.2009.07.021.
(222) Schubert, M.; Steude, A.; Liehm, P.; Kronenberg, N. M.; Karl, M.; Campbell, E. C.; Powis, S. J.; Gather, M. C. Lasing within Live Cells Containing Intracellular Optical Microresonators for Barcode-Type Cell Tagging and Tracking. *Nano Lett.* **2015**, *15* (8), 5647–5652. https://doi.org/10.1021/acs.nanolett.5b02491.
(223) Chen, Y.-C.; Fan, X. Biological Lasers for Biomedical Applications. *Adv. Opt. Mater.* **2019**, *7* (17), 1900377. https://doi.org/10.1002/adom.201900377.
(224) Martino, N.; Kwok, S. J. J.; Liapis, A. C.; Forward, S.; Jang, H.; Kim, H.-M.; Wu, S. J.; Wu, J.; Dannenberg, P. H.; Jang, S.-J.; Lee, Y.-H.; Yun, S.-H. Wavelength-Encoded Laser Particles for Massively Multiplexed Cell Tagging. *Nat. Photonics* **2019**, *13* (10), 720–727. https://doi.org/10.1038/s41566-019-0489-0.
(225) Lv, Z.; Man, Z.; Xu, Z.; Feng, C.; Yang, Y.; Liao, Q.; Wang, X.; Zheng, L.; Fu, H. Intracellular Near-Infrared Microlaser Probes Based on Organic Microsphere–SiO2 Core–Shell Structures for Cell Tagging and Tracking. *ACS Appl. Mater. Interfaces* **2018**, *10* (39), 32981–32987. https://doi.org/10.1021/acsami.8b09380.
(226) Schubert, M.; Woolfson, L.; Barnard, I. R. M.; Dorward, A. M.; Casement, B.; Morton, A.; Robertson, G. B.; Appleton, P. L.; Miles, G. B.; Tucker, C. S.; Pitt, S. J.; Gather, M. C. Monitoring Contractility in Cardiac Tissue with Cellular Resolution Using Biointegrated Microlasers. *Nat. Photonics* **2020**, *14* (7), 452–458. https://doi.org/10.1038/s41566-020-0631-z.
(227) Zlatanovic, S.; Mirkarimi, L. W.; Sigalas, M. M.; Bynum, M. A.; Chow, E.; Robotti, K. M.; Burr, G. W.; Esener, S.; Grot, A. Photonic Crystal Microcavity Sensor for Ultracompact Monitoring of Reaction Kinetics and Protein Concentration. *Sens. Actuators B Chem.* **2009**, *141* (1), 13–19. https://doi.org/10.1016/j.snb.2009.06.007.
(228) Robbiano, V.; Paternò, G. M.; La Mattina, A. A.; Motti, S. G.; Lanzani, G.; Scotognella, F.; Barillaro, G. Room-Temperature Low-Threshold Lasing from Monolithically Integrated Nanostructured Porous Silicon Hybrid Microcavities. *ACS Nano* **2018**, *12* (5), 4536–4544. https://doi.org/10.1021/acsnano.8b00875.
(229) Pezeshki, H.; Darvish, G. Design of Photonic Crystal Microcavity Based Optical Switches Using Fano Resonance Effect. *Optik* **2015**, *126* (23), 4202–4205. https://doi.org/10.1016/j.ijleo.2015.08.033.
(230) Caruge, J. M.; Halpert, J. E.; Wood, V.; Bulović, V.; Bawendi, M. G. Colloidal Quantum-Dot Light-Emitting Diodes with Metal-Oxide Charge Transport Layers. *Nat. Photonics* **2008**, *2* (4), 247–250. https://doi.org/10.1038/nphoton.2008.34.

(231) Han, H.-V.; Lin, H.-Y.; Lin, C.-C.; Chong, W.-C.; Li, J.-R.; Chen, K.-J.; Yu, P.; Chen, T.-M.; Chen, H.-M.; Lau, K.-M.; Kuo, H.-C. Resonant-Enhanced Full-Color Emission of Quantum-Dot-Based Micro LED Display Technology. *Opt. Express* **2015**, *23* (25), 32504–32515. https://doi.org/10.1364/OE.23.032504.

(232) Medintz, I. L.; Uyeda, H. T.; Goldman, E. R.; Mattoussi, H. Quantum Dot Bioconjugates for Imaging, Labelling and Sensing. *Nat. Mater.* **2005**, *4* (6), 435–446. https://doi.org/10.1038/nmat1390.

(233) Jaiswal, J. K.; Goldman, E. R.; Mattoussi, H.; Simon, S. M. Use of Quantum Dots for Live Cell Imaging. *Nat. Methods* **2004**, *1* (1), 73–78. https://doi.org/10.1038/nmeth1004-73.

(234) Reithmaier, J. P.; Sęk, G.; Löffler, A.; Hofmann, C.; Kuhn, S.; Reitzenstein, S.; Keldysh, L. V.; Kulakovskii, V. D.; Reinecke, T. L.; Forchel, A. Strong Coupling in a Single Quantum Dot–Semiconductor Microcavity System. *Nature* **2004**, *432* (7014), 197–200. https://doi.org/10.1038/nature02969.

(235) Alivisatos, A. P. Semiconductor Clusters, Nanocrystals, and Quantum Dots. *Science* **1996**, *271* (5251), 933–937. https://doi.org/10.1126/science.271.5251.933.

(236) Murray, C. B.; Norris, D. J.; Bawendi, M. G. Synthesis and Characterization of Nearly Monodisperse CdE (E = Sulfur, Selenium, Tellurium) Semiconductor Nanocrystallites. *J. Am. Chem. Soc.* **1993**, *115* (19), 8706–8715. https://doi.org/10.1021/ja00072a025.

(237) Hu, M. Z.; Zhu, T. Semiconductor Nanocrystal Quantum Dot Synthesis Approaches Towards Large-Scale Industrial Production for Energy Applications. *Nanoscale Res. Lett.* **2015**, *10* (1), 469. https://doi.org/10.1186/s11671-015-1166-y.

(238) José-Yacamán, M.; Marín-Almazo, M.; Ascencio, J. A. High Resolution TEM Studies on Palladium Nanoparticles. *J. Mol. Catal. Chem.* **2001**, *173* (1), 61–74. https://doi.org/10.1016/S1381-1169(01)00145-5.

(239) Liu, J. Scanning Transmission Electron Microscopy and Its Application to the Study of Nanoparticles and Nanoparticle Systems. *J. Electron Microsc. (Tokyo)* **2005**, *54* (3), 251–278. https://doi.org/10.1093/jmicro/dfi034.

(240) Siverns, P. D.; Malik, S.; McPherson, G.; Childs, D.; Roberts, C.; Murray, R.; Joyce, B. A.; Davock, H. Scanning Transmission-Electron Microscopy Study of InAs/GaAs Quantum Dots. *Phys. Rev. B* **1998**, *58* (16), R10127–R10130. https://doi.org/10.1103/PhysRevB.58.R10127.

(241) Kirmse, H.; Schneider, R.; Rabe, M.; Neumann, W.; Henneberger, F. Transmission Electron Microscopy Investigation of Structural Properties of Self-Assembled CdSe/ZnSe Quantum Dots. *Appl. Phys. Lett.* **1998**, *72* (11), 1329–1331. https://doi.org/10.1063/1.120984.

(242) Buhr, E.; Senftleben, N.; Klein, T.; Bergmann, D.; Gnieser, D.; Frase, C. G.; Bosse, H. Characterization of Nanoparticles by Scanning Electron Microscopy in Transmission Mode. *Meas. Sci. Technol.* **2009**, *20* (8), 084025. https://doi.org/10.1088/0957-0233/20/8/084025.

(243) Sokolova, V.; Ludwig, A.-K.; Hornung, S.; Rotan, O.; Horn, P. A.; Epple, M.; Giebel, B. Characterisation of Exosomes Derived from Human Cells by Nanoparticle Tracking Analysis and Scanning Electron Microscopy. *Colloids Surf. B Biointerfaces* **2011**, *87* (1), 146–150. https://doi.org/10.1016/j.colsurfb.2011.05.013.

(244) Mohan, A. C.; Renjanadevi, B. Preparation of Zinc Oxide Nanoparticles and Its Characterization Using Scanning Electron Microscopy (SEM) and X-Ray Diffraction(XRD). *Procedia Technol.* **2016**, *24*, 761–766. https://doi.org/10.1016/j.protcy.2016.05.078.

(245) Dubes, A.; Parrot-Lopez, H.; Abdelwahed, W.; Degobert, G.; Fessi, H.; Shahgaldian, P.; Coleman, A. W. Scanning Electron Microscopy and Atomic Force Microscopy Imaging of Solid Lipid Nanoparticles Derived from Amphiphilic Cyclodextrins. *Eur. J. Pharm. Biopharm.* **2003**, *55* (3), 279–282. https://doi.org/10.1016/S0939-6411(03)00020-1.

(246) Rao, A.; Schoenenberger, M.; Gnecco, E.; Glatzel, T.; Meyer, E.; Brändlin, D.; Scandella, L. Characterization of Nanoparticles Using Atomic Force Microscopy. *J. Phys. Conf. Ser.* **2007**, *61* (1), 192. https://doi.org/10.1088/1742-6596/61/1/192.

(247) Mühlen, A. zur; Mühlen, E. zur; Niehus, H.; Mehnert, W. Atomic Force Microscopy Studies of Solid Lipid Nanoparticles. *Pharm. Res.* **1996**, *13* (9), 1411–1416. https://doi.org/10.1023/A:1016042504830.

(248) Hoo, C. M.; Starostin, N.; West, P.; Mecartney, M. L. A Comparison of Atomic Force Microscopy (AFM) and Dynamic Light Scattering (DLS) Methods to Characterize Nanoparticle Size Distributions. *J. Nanoparticle Res.* **2008**, *10* (1), 89–96. https://doi.org/10.1007/s11051-008-9435-7.

(249) Ong, Q. K.; Reguera, J.; Silva, P. J.; Moglianetti, M.; Harkness, K.; Longobardi, M.; Mali, K. S.; Renner, C.; De Feyter, S.; Stellacci, F. High-Resolution Scanning Tunneling Microscopy Characterization of Mixed Monolayer Protected Gold Nanoparticles. *ACS Nano* **2013**, *7* (10), 8529–8539. https://doi.org/10.1021/nn402414b.

(250) Centrone, A.; Hu, Y.; Jackson, A. M.; Zerbi, G.; Stellacci, F. Phase Separation on Mixed-Monolayer-Protected Metal Nanoparticles: A Study by Infrared Spectroscopy and Scanning Tunneling Microscopy. *Small* **2007**, *3* (5), 814–817. https://doi.org/10.1002/smll.200600736.

(251) Jackson, A. M.; Hu, Y.; Silva, P. J.; Stellacci, F. From Homoligand- to Mixed-Ligand- Monolayer-Protected Metal Nanoparticles: A Scanning Tunneling Microscopy Investigation. *J. Am. Chem. Soc.* **2006**, *128* (34), 11135–11149. https://doi.org/10.1021/ja061545h.

(252) Walton, A. S.; Lauritsen, J. V.; Topsøe, H.; Besenbacher, F. MoS2 Nanoparticle Morphologies in Hydrodesulfurization Catalysis Studied by Scanning Tunneling Microscopy. *J. Catal.* **2013**, *308*, 306–318. https://doi.org/10.1016/j.jcat.2013.08.017.

(253) *Advanced Transmission Electron Microscopy: Applications to Nanomaterials*, 1st ed. 2015.; Deepak, F. L., Mayoral, A., Arenal, R., Eds.; Springer International Publishing : Imprint: Springer: Cham, 2015. https://doi.org/10.1007/978-3-319-15177-9.

(254) Nellist, P. D.; McCallum, B. C.; Rodenburg, J. M. Resolution beyond the "information Limit" in Transmission Electron Microscopy. *Nature* **1995**, *374* (6523), 630–632. https://doi.org/10.1038/374630a0.

(255) Sugimoto, H.; Yamamura, M.; Sakiyama, M.; Fujii, M. Visualizing a Core–Shell Structure of Heavily Doped Silicon Quantum Dots by Electron Microscopy Using an Atomically Thin Support Film. *Nanoscale* **2018**, *10* (16), 7357–7362. https://doi.org/10.1039/C7NR09474D.

(256) Stratton, J. A.; Hebenstreit, J. *Théorie de l'électromagnétisme: ["Electromagnetic theory"], par Julius Adams Stratton ... Traduit par J. [Jacques] Hebenstreit ...*; Dunod (Orléans, Impr. nouvelle): Paris, 1960.

(257) John David Jackson. Classical Electrodynamics, 3rd Edition | Wiley https://www.wiley.com/en-us/Classical+Electrodynamics%2C+3rd+Edition-p-9780471309321 (accessed 2021 -10 -06).

(258) Whispering Gallery Mode Microresonators: Fundamentals and Applications. *Riv. Nuovo Cimento* **2011**, *34* (7), 435–488. https://doi.org/10.1393/ncr/i2011-10067-2.

(259) Lam, C. C.; Leung, P. T.; Young, K. Explicit Asymptotic Formulas for the Positions, Widths, and Strengths of Resonances in Mie Scattering. *JOSA B* **1992**, *9* (9), 1585–1592. https://doi.org/10.1364/JOSAB.9.001585.

(260) Srinivasan, K.; Barclay, P. E.; Painter, O.; Chen, J.; Cho, A. Y.; Gmachl, C. Experimental Demonstration of a High Quality Factor Photonic Crystal Microcavity. *Appl. Phys. Lett.* **2003**, *83* (10), 1915–1917. https://doi.org/10.1063/1.1606866.

(261) Tien, P. K. Light Waves in Thin Films and Integrated Optics. *Appl. Opt.* **1971**, *10* (11), 2395–2413. https://doi.org/10.1364/AO.10.002395.

(262) Gorodetsky, M. L.; Savchenkov, A. A.; Ilchenko, V. S. Ultimate Q of Optical Microsphere Resonators. *Opt. Lett.* **1996**, *21* (7), 453–455. https://doi.org/10.1364/OL.21.000453.
(263) Lin, H.-B.; Eversole, J. D.; Campillo, A. J. Spectral Properties of Lasing Microdroplets. *JOSA B* **1992**, *9* (1), 43–50. https://doi.org/10.1364/JOSAB.9.000043.
(264) Lutti, J.; Langbein, W.; Borri, P. High Q Optical Resonances of Polystyrene Microspheres in Water Controlled by Optical Tweezers. *Appl. Phys. Lett.* **2007**, *91* (14), 141116. https://doi.org/10.1063/1.2795332.
(265) Riesen, N.; Reynolds, T.; François, A.; Henderson, M. R.; Monro, T. M. Q-Factor Limits for Far-Field Detection of Whispering Gallery Modes in Active Microspheres. *Opt. Express* **2015**, *23* (22), 28896–28904. https://doi.org/10.1364/OE.23.028896.
(266) Zhang, H.; Jia, Z.; Lv, X.; Zhou, J.; Chen, L.; Liu, R.; Ma, J. Porous Silicon Optical Microcavity Biosensor on Silicon-on-Insulator Wafer for Sensitive DNA Detection. *Biosens. Bioelectron.* **2013**, *44*, 89–94. https://doi.org/10.1016/j.bios.2013.01.012.
(267) Poddubny, A. N.; Belov, P. A.; Kivshar, Y. S. Purcell Effect in Wire Metamaterials. *Phys. Rev. B* **2013**, *87* (3), 035136. https://doi.org/10.1103/PhysRevB.87.035136.
(268) Sultanova, N.; Kasarova, S.; Nikolov, I. Dispersion Properties of Optical Polymers. *Acta Phys. Pol. A* **2009**, *116* (4), 585–587. https://doi.org/10.12693/APhysPolA.116.585.
(269) Yu, W. W.; Peng, X. Formation of High-Quality CdS and Other II–VI Semiconductor Nanocrystals in Noncoordinating Solvents: Tunable Reactivity of Monomers. *Angew. Chem. Int. Ed.* **2002**, *41* (13), 2368–2371. https://doi.org/10.1002/1521-3773(20020703)41:13<2368::AID-ANIE2368>3.0.CO;2-G.
(270) Li, J. J.; Wang, Y. A.; Guo, W.; Keay, J. C.; Mishima, T. D.; Johnson, M. B.; Peng, X. Large-Scale Synthesis of Nearly Monodisperse CdSe/CdS Core/Shell Nanocrystals Using Air-Stable Reagents via Successive Ion Layer Adsorption and Reaction. *J. Am. Chem. Soc.* **2003**, *125* (41), 12567–12575. https://doi.org/10.1021/ja0363563.
(271) Tsotsis, P.; Eldridge, P. S.; Gao, T.; Tsintzos, S. I.; Hatzopoulos, Z.; Savvidis, P. G. Lasing Threshold Doubling at the Crossover from Strong to Weak Coupling Regime in GaAs Microcavity. *New J. Phys.* **2012**, *14* (2), 023060. https://doi.org/10.1088/1367-2630/14/2/023060.
(272) Hernández-Romano, I.; Cruz-Garcia, M. A.; Moreno-Hernández, C.; Monzón-Hernández, D.; López-Figueroa, E. O.; Paredes-Gallardo, O. E.; Torres-Cisneros, M.; Villatoro, J. Optical Fiber Temperature Sensor Based on a Microcavity with Polymer Overlay. *Opt. Express* **2016**, *24* (5), 5654–5661. https://doi.org/10.1364/OE.24.005654.
(273) Qi, X.; Wang, S.; Jiang, J.; Liu, K.; Wang, X.; Yang, Y.; Liu, T. Fiber Optic Fabry-Perot Pressure Sensor With Embedded MEMS Micro-Cavity for Ultra-High Pressure Detection. *J. Light. Technol.* **2019**, *37* (11), 2719–2725. https://doi.org/10.1109/JLT.2018.2876717.
(274) Le Dantec, R.; Benyattou, T.; Guillot, G.; Spisser, A.; Seassal, C.; Leclercq, J. L.; Viktorovitch, P.; Rondi, D.; Blondeau, R. Tunable Microcavity Based on InP-Air Bragg Mirrors. *IEEE J. Sel. Top. Quantum Electron.* **1999**, *5* (1), 111–114. https://doi.org/10.1109/2944.748113.
(275) Folan, L. M.; Arnold, S.; Druger, S. D. Enhanced Energy Transfer within a Microparticle. *Chem. Phys. Lett.* **1985**, *118* (3), 322–327. https://doi.org/10.1016/0009-2614(85)85324-0.
(276) Cortes, C. L.; Jacob, Z. Fundamental Figures of Merit for Engineering FöRster Resonance Energy Transfer. *Opt. Express* **2018**, *26* (15), 19371–19387. https://doi.org/10.1364/OE.26.019371.
(277) Rustomji, K.; Dubois, M.; Kuhlmey, B.; de Sterke, C. M.; Enoch, S.; Abdeddaim, R.; Wenger, J. Direct Imaging of the Energy-Transfer Enhancement between Two Dipoles in a Photonic Cavity. *Phys. Rev. X* **2019**, *9* (1), 011041. https://doi.org/10.1103/PhysRevX.9.011041.

(278) Enderlein, J. Modification of Förster Resonance Energy Transfer Efficiencyat Interfaces. *Int. J. Mol. Sci.* **2012**, *13* (11), 15227–15240. https://doi.org/10.3390/ijms131115227.
(279) Kushida, S.; Braam, D.; Dao, T. D.; Saito, H.; Shibasaki, K.; Ishii, S.; Nagao, T.; Saeki, A.; Kuwabara, J.; Kanbara, T.; Kijima, M.; Lorke, A.; Yamamoto, Y. Conjugated Polymer Blend Microspheres for Efficient, Long-Range Light Energy Transfer. *ACS Nano* **2016**, *10* (5), 5543–5549. https://doi.org/10.1021/acsnano.6b02100.
(280) Microcavity-Enhanced Light-Trapping for Highly Efficient Organic Parallel Tandem Solar Cells - Zuo - 2014 - Advanced Materials - Wiley Online Library https://onlinelibrary.wiley.com/doi/full/10.1002/adma.201402782 (accessed 2021 -08 -26).
(281) Reisch, A.; Trofymchuk, K.; Runser, A.; Fleith, G.; Rawiso, M.; Klymchenko, A. S. Tailoring Fluorescence Brightness and Switching of Nanoparticles through Dye Organization in the Polymer Matrix. *ACS Appl. Mater. Interfaces* **2017**, *9* (49), 43030–43042. https://doi.org/10.1021/acsami.7b12292.
(282) Reisch, A.; Didier, P.; Richert, L.; Oncul, S.; Arntz, Y.; Mély, Y.; Klymchenko, A. S. Collective Fluorescence Switching of Counterion-Assembled Dyes in Polymer Nanoparticles. *Nat. Commun.* **2014**, *5* (1), 4089. https://doi.org/10.1038/ncomms5089.
(283) Andreiuk, B.; Reisch, A.; Bernhardt, E.; Klymchenko, A. S. Fighting Aggregation-Caused Quenching and Leakage of Dyes in Fluorescent Polymer Nanoparticles: Universal Role of Counterion. *Chem. – Asian J.* **2019**, *14* (6), 836–846. https://doi.org/10.1002/asia.201801592.
(284) Debayle, M.; Balloul, E.; Dembele, F.; Xu, X.; Hanafi, M.; Ribot, F.; Monzel, C.; Coppey, M.; Fragola, A.; Dahan, M.; Pons, T.; Lequeux, N. Zwitterionic Polymer Ligands: An Ideal Surface Coating to Totally Suppress Protein-Nanoparticle Corona Formation? *Biomaterials* **2019**, *219*, 119357. https://doi.org/10.1016/j.biomaterials.2019.119357.
(285) Understanding DNA - 3rd Edition https://www.elsevier.com/books/understanding-dna/calladine/978-0-12-155089-9 (accessed 2021 -09 -22).
(286) Watson, J. D.; Berry, A. *DNA : The Secret of Life*; New York : Alfred A. Knopf, 2003.
(287) Ferry, G. The Structure of DNA. *Nature* **2019**, *575* (7781), 35–36. https://doi.org/10.1038/d41586-019-02554-z.
(288) Higgs, P. G. RNA Secondary Structure: Physical and Computational Aspects. *Q. Rev. Biophys.* **2000**, *33* (3), 199–253. https://doi.org/10.1017/S0033583500003620.
(289) Nissen, P.; Hansen, J.; Ban, N.; Moore, P. B.; Steitz, T. A. The Structural Basis of Ribosome Activity in Peptide Bond Synthesis. *Science* **2000**, *289* (5481), 920–930. https://doi.org/10.1126/science.289.5481.920.
(290) Lee, J. C.; Gutell, R. R. Diversity of Base-Pair Conformations and Their Occurrence in RRNA Structure and RNA Structural Motifs. *J. Mol. Biol.* **2004**, *344* (5), 1225–1249. https://doi.org/10.1016/j.jmb.2004.09.072.
(291) Tinoco, I.; Bustamante, C. How RNA Folds. *J. Mol. Biol.* **1999**, *293* (2), 271–281. https://doi.org/10.1006/jmbi.1999.3001.
(292) Fixman, M.; Freire, J. J. Theory of DNA Melting Curves. *Biopolymers* **1977**, *16* (12), 2693–2704. https://doi.org/10.1002/bip.1977.360161209.
(293) DNA Hybridization - an overview | ScienceDirect Topics https://www.sciencedirect.com/topics/biochemistry-genetics-and-molecular-biology/dna-hybridization (accessed 2021 -09 -22).
(294) Khandelwal, G.; Bhyravabhotla, J. A Phenomenological Model for Predicting Melting Temperatures of DNA Sequences. *PLoS ONE* **2010**, *5* (8), e12433. https://doi.org/10.1371/journal.pone.0012433.

(295) Wittwer, C. T. High-Resolution DNA Melting Analysis: Advancements and Limitations. *Hum. Mutat.* **2009**, *30* (6), 857–859. https://doi.org/10.1002/humu.20951.
(296) Human Papillomavirus (HPV) Test https://labtestsonline.org/tests/human-papillomavirus-hpv-test (accessed 2021 -09 -22).
(297) Benevolo, M.; Vocaturo, A.; Caraceni, D.; French, D.; Rosini, S.; Zappacosta, R.; Terrenato, I.; Ciccocioppo, L.; Frega, A.; Rossi, P. G. Sensitivity, Specificity, and Clinical Value of Human Papillomavirus (HPV) E6/E7 MRNA Assay as a Triage Test for Cervical Cytology and HPV DNA Test. *J. Clin. Microbiol.* **2011**, *49* (7), 2643–2650. https://doi.org/10.1128/JCM.02570-10.
(298) Loeb, K. R.; Jerome, K. R.; Goddard, J.; Huang, M.; Cent, A.; Corey, L. High-Throughput Quantitative Analysis of Hepatitis B Virus DNA in Serum Using the TaqMan Fluorogenic Detection System. *Hepatology* **2000**, *32* (3), 626–629. https://doi.org/10.1053/jhep.2000.9878.
(299) A. Rohrman, B.; R. Richards-Kortum, R. A Paper and Plastic Device for Performing Recombinase Polymerase Amplification of HIV DNA. *Lab. Chip* **2012**, *12* (17), 3082–3088. https://doi.org/10.1039/C2LC40423K.
(300) Natesan, S. A.; Handyside, A. H.; Thornhill, A. R.; Ottolini, C. S.; Sage, K.; Summers, M. C.; Konstantinidis, M.; Wells, D.; Griffin, D. K. Live Birth after PGD with Confirmation by a Comprehensive Approach (Karyomapping) for Simultaneous Detection of Monogenic and Chromosomal Disorders. *Reprod. Biomed. Online* **2014**, *29* (5), 600–605. https://doi.org/10.1016/j.rbmo.2014.07.007.
(301) Wilkie, A. O. M.; Byren, J. C.; Hurst, J. A.; Jayamohan, J.; Johnson, D.; Knight, S. J. L.; Lester, T.; Richards, P. G.; Twigg, S. R. F.; Wall, S. A. Prevalence and Complications of Single-Gene and Chromosomal Disorders in Craniosynostosis. *Pediatrics* **2010**, *126* (2), e391–e400. https://doi.org/10.1542/peds.2009-3491.
(302) Burke, T.; Bruford, M. W. DNA Fingerprinting in Birds. *Nature* **1987**, *327* (6118), 149–152. https://doi.org/10.1038/327149a0.
(303) Webb, M. B.; Debenham, P. G. Cell Line Characterisation by DNA Fingerprinting; a Review. *Dev. Biol. Stand.* **1992**, *76*, 39–42.
(304) Thakur, B. K.; Zhang, H.; Becker, A.; Matei, I.; Huang, Y.; Costa-Silva, B.; Zheng, Y.; Hoshino, A.; Brazier, H.; Xiang, J.; Williams, C.; Rodriguez-Barrueco, R.; Silva, J. M.; Zhang, W.; Hearn, S.; Elemento, O.; Paknejad, N.; Manova-Todorova, K.; Welte, K.; Bromberg, J.; Peinado, H.; Lyden, D. Double-Stranded DNA in Exosomes: A Novel Biomarker in Cancer Detection. *Cell Res.* **2014**, *24* (6), 766–769. https://doi.org/10.1038/cr.2014.44.
(305) Liu, M. C.; Oxnard, G. R.; Klein, E. A.; Swanton, C.; Seiden, M. V.; Liu, M. C.; Oxnard, G. R.; Klein, E. A.; Smith, D.; Richards, D.; Yeatman, T. J.; Cohn, A. L.; Lapham, R.; Clement, J.; Parker, A. S.; Tummala, M. K.; McIntyre, K.; Sekeres, M. A.; Bryce, A. H.; Siegel, R.; Wang, X.; Cosgrove, D. P.; Abu-Rustum, N. R.; Trent, J.; Thiel, D. D.; Becerra, C.; Agrawal, M.; Garbo, L. E.; Giguere, J. K.; Michels, R. M.; Harris, R. P.; Richey, S. L.; McCarthy, T. A.; Waterhouse, D. M.; Couch, F. J.; Wilks, S. T.; Krie, A. K.; Balaraman, R.; Restrepo, A.; Meshad, M. W.; Rieger-Christ, K.; Sullivan, T.; Lee, C. M.; Greenwald, D. R.; Oh, W.; Tsao, C.-K.; Fleshner, N.; Kennecke, H. F.; Khalil, M. F.; Spigel, D. R.; Manhas, A. P.; Ulrich, B. K.; Kovoor, P. A.; Stokoe, C.; Courtright, J. G.; Yimer, H. A.; Larson, T. G.; Swanton, C.; Seiden, M. V.; Cummings, S. R.; Absalan, F.; Alexander, G.; Allen, B.; Amini, H.; Aravanis, A. M.; Bagaria, S.; Bazargan, L.; Beausang, J. F.; Berman, J.; Betts, C.; Blocker, A.; Bredno, J.; Calef, R.; Cann, G.; Carter, J.; Chang, C.; Chawla, H.; Chen, X.; Chien, T. C.; Civello, D.; Davydov, K.; Demas, V.; Desai, M.; Dong, Z.; Fayzullina, S.; Fields, A. P.; Filippova, D.; Freese, P.; Fung, E. T.; Gnerre, S.; Gross, S.; Halks-Miller, M.; Hall, M. P.; Hartman, A.-R.; Hou, C.; Hubbell, E.; Hunkapiller, N.; Jagadeesh, K.; Jamshidi, A.; Jiang, R.; Jung, B.; Kim, T.; Klausner, R. D.; Kurtzman, K. N.; Lee, M.; Lin, W.; Lipson, J.; Liu, H.; Liu, Q.; Lopatin, M.; Maddala, T.; Maher, M.

C.; Melton, C.; Mich, A.; Nautiyal, S.; Newman, J.; Newman, J.; Nicula, V.; Nicolaou, C.; Nikolic, O.; Pan, W.; Patel, S.; Prins, S. A.; Rava, R.; Ronaghi, N.; Sakarya, O.; Satya, R. V.; Schellenberger, J.; Scott, E.; Sehnert, A. J.; Shaknovich, R.; Shanmugam, A.; Shashidhar, K. C.; Shen, L.; Shenoy, A.; Shojaee, S.; Singh, P.; Steffen, K. K.; Tang, S.; Toung, J. M.; Valouev, A.; Venn, O.; Williams, R. T.; Wu, T.; Xu, H. H.; Yakym, C.; Yang, X.; Yecies, J.; Yip, A. S.; Youngren, J.; Yue, J.; Zhang, J.; Zhang, L.; Zhang, L. (Quan); Zhang, N.; Curtis, C.; Berry, D. A. Sensitive and Specific Multi-Cancer Detection and Localization Using Methylation Signatures in Cell-Free DNA. *Ann. Oncol.* **2020**, *31* (6), 745–759. https://doi.org/10.1016/j.annonc.2020.02.011.

(306) Jaiswal, P. K.; Goel, A.; Mittal, R. D. Survivin: A Molecular Biomarker in Cancer. *Indian J. Med. Res.* **2015**, *141* (4), 389–397. https://doi.org/10.4103/0971-5916.159250.

(307) Zhang, C.; Johnson, L. W. Quantum-Dot-Based Nanosensor for RRE IIB RNA−Rev Peptide Interaction Assay. *J. Am. Chem. Soc.* **2006**, *128* (16), 5324–5325. https://doi.org/10.1021/ja060537y.

(308) Gao, Y.; Gao, F.; Zhang, G.; Chen, L.; Wu, Q.; Liu, X. Sensor Array Based on Single Carbon Quantum Dot for Fluorometric Differentiation of All Natural Amino Acids. *Microchim. Acta* **2019**, *186* (12), 858. https://doi.org/10.1007/s00604-019-3864-0.

(309) Boeneman, K.; Mei, B. C.; Dennis, A. M.; Bao, G.; Deschamps, J. R.; Mattoussi, H.; Medintz, I. L. Sensing Caspase 3 Activity with Quantum Dot−Fluorescent Protein Assemblies. *J. Am. Chem. Soc.* **2009**, *131* (11), 3828–3829. https://doi.org/10.1021/ja809721j.

(310) Jaiswal, A.; Ghsoh, S. S.; Chattopadhyay, A. Quantum Dot Impregnated-Chitosan Film for Heavy Metal Ion Sensing and Removal. *Langmuir* **2012**, *28* (44), 15687–15696. https://doi.org/10.1021/la3027573.

(311) Zhang, H.; Feng, G.; Guo, Y.; Zhou, D. Robust and Specific Ratiometric Biosensing Using a Copper-Free Clicked Quantum Dot–DNA Aptamer Sensor. *Nanoscale* **2013**, *5* (21), 10307–10315. https://doi.org/10.1039/C3NR02897F.

(312) Hu, T.; Zhang, L.; Wen, W.; Zhang, X.; Wang, S. Enzyme Catalytic Amplification of MiRNA-155 Detection with Graphene Quantum Dot-Based Electrochemical Biosensor. *Biosens. Bioelectron.* **2016**, *77*, 451–456. https://doi.org/10.1016/j.bios.2015.09.068.

(313) LightCycler / FRET Probes https://eurofinsgenomics.eu/en/dna-rna-oligonucleotides/optimised-application-oligos/qpcr-probes/lightcycler-probes/ (accessed 2021 -09 -22).

(314) Melnychuk, N.; Klymchenko, A. S. DNA-Functionalized Dye-Loaded Polymeric Nanoparticles: Ultrabright FRET Platform for Amplified Detection of Nucleic Acids. *J. Am. Chem. Soc.* **2018**, *140* (34), 10856–10865. https://doi.org/10.1021/jacs.8b05840.

(315) Huang, J.; Wu, J.; Li, Z. Biosensing Using Hairpin DNA Probes. *Rev. Anal. Chem.* **2015**, *34* (1–2), 1–27. https://doi.org/10.1515/revac-2015-0010.

(316) Phelps, C.; Israels, B.; Jose, D.; Marsh, M. C.; von Hippel, P. H.; Marcus, A. H. Using Microsecond Single-Molecule FRET to Determine the Assembly Pathways of T4 SsDNA Binding Protein onto Model DNA Replication Forks. *Proc. Natl. Acad. Sci. U. S. A.* **2017**, *114* (18), E3612–E3621. https://doi.org/10.1073/pnas.1619819114.

(317) Tyagi, S.; Kramer, F. R. Molecular Beacons: Probes That Fluoresce upon Hybridization. *Nat. Biotechnol.* **1996**, *14* (3), 303–308. https://doi.org/10.1038/nbt0396-303.

(318) Jepsen, M. D. E.; Sparvath, S. M.; Nielsen, T. B.; Langvad, A. H.; Grossi, G.; Gothelf, K. V.; Andersen, E. S. Development of a Genetically Encodable FRET System Using Fluorescent RNA Aptamers. *Nat. Commun.* **2018**, *9* (1), 18. https://doi.org/10.1038/s41467-017-02435-x.

(319) Cui, X.; Liang, Q.; Liang, Y.; Lu, M.; Ding, Y.; Lu, B. TR-FRET Assays of Huntingtin Protein Fragments Reveal Temperature and PolyQ Length-Dependent Conformational Changes. *Sci. Rep.* **2014**, *4*, 5601. https://doi.org/10.1038/srep05601.

(320) Lin, Y.; Fan, H.; Frederiksen, M.; Zhao, K.; Jiang, L.; Wang, Z.; Zhou, S.; Guo, W.; Gao, J.; Li, S.; Harrington, E.; Meier, P.; Scheufler, C.; Xu, Y.-C.; Atadja, P.; Lu, C.; Li, E.; Justin Gu, X. Detecting S-Adenosyl-l-Methionine-Induced Conformational Change of a Histone Methyltransferase Using a Homogeneous Time-Resolved Fluorescence-Based Binding Assay. *Anal. Biochem.* **2012**, *423* (1), 171–177. https://doi.org/10.1016/j.ab.2012.01.019.

(321) Salz, W.; Eisenberg, D.; Plescia, J.; Garlick, D. S.; Weiss, R. M.; Wu, X.-R.; Sun, T.-T.; Altieri, D. C. A Survivin Gene Signature Predicts Aggressive Tumor Behavior. *Cancer Res.* **2005**, *65* (9), 3531–3534. https://doi.org/10.1158/0008-5472.CAN-04-4284.

(322) Khan, Z.; Khan, N.; Tiwari, R. P.; Patro, I. K.; Prasad, G. B. K. S.; Bisen, P. S. Down-Regulation of Survivin by Oxaliplatin Diminishes Radioresistance of Head and Neck Squamous Carcinoma Cells. *Radiother. Oncol.* **2010**, *96* (2), 267–273. https://doi.org/10.1016/j.radonc.2010.06.005.

(323) Tamm, I.; Wang, Y.; Sausville, E.; Scudiero, D. A.; Vigna, N.; Oltersdorf, T.; Reed, J. C. IAP-Family Protein Survivin Inhibits Caspase Activity and Apoptosis Induced by Fas (CD95), Bax, Caspases, and Anticancer Drugs. *Cancer Res.* **1998**, *58* (23), 5315–5320.

(324) Ambrosini, G.; Adida, C.; Altieri, D. C. A Novel Anti-Apoptosis Gene, Survivin, Expressed in Cancer and Lymphoma. *Nat. Med.* **1997**, *3* (8), 917–921. https://doi.org/10.1038/nm0897-917.

(325) Friedrichs, B.; Siegel, S.; Hald Andersen, M.; Schmitz, N.; Zeis, M. Survivin-Derived Peptide Epitopes and Their Role for Induction of Antitumor Immunity in Hematological Malignancies. *Leuk. Lymphoma* **2006**, *47* (6), 978–985. https://doi.org/10.1080/10428190500464062.

(326) Morinaga, S.; Nakamura, Y.; Ishiwa, N.; Yoshikawa, T.; Noguchi, Y.; Yamamoto, Y.; Rino, Y.; Imada, T.; Takanashi, Y.; Akaike, M.; Sugimasa, Y.; Takemiya, S. Expression of Survivin MRNA Associates with Apoptosis, Proliferation and Histologically Aggressive Features in Hepatocellular Carcinoma. *Oncol. Rep.* **2004**, *12* (6), 1189–1194. https://doi.org/10.3892/or.12.6.1189.

(327) Guesdon, J. L.; Ternynck, T.; Avrameas, S. The Use of Avidin-Biotin Interaction in Immunoenzymatic Techniques. *J. Histochem. Cytochem.* **1979**, *27* (8), 1131–1139. https://doi.org/10.1177/27.8.90074.

(328) Dundas, C. M.; Demonte, D.; Park, S. Streptavidin–Biotin Technology: Improvements and Innovations in Chemical and Biological Applications. *Appl. Microbiol. Biotechnol.* **2013**, *97* (21), 9343–9353. https://doi.org/10.1007/s00253-013-5232-z.

(329) Grunwald, C. A Brief Introduction to the Streptavidin-Biotin System and Its Usage in Modern Surface Based Assays. *Z. Für Phys. Chem.* **2008**, *222* (5–6), 789–821. https://doi.org/10.1524/zpch.2008.6009.

(330) DeChancie, J.; Houk, K. N. The Origins of Femtomolar Protein–Ligand Binding: Hydrogen Bond Cooperativity and Desolvation Energetics in the Biotin–(Strept)Avidin Binding Site. *J. Am. Chem. Soc.* **2007**, *129* (17), 5419–5429. https://doi.org/10.1021/ja066950n.

(331) Green, N. M. Avidin. In *Advances in Protein Chemistry*; Anfinsen, C. B., Edsall, J. T., Richards, F. M., Eds.; Academic Press, 1975; Vol. 29, pp 85–133. https://doi.org/10.1016/S0065-3233(08)60411-8.

(332) Williams, A.; Ibrahim, I. T. Carbodiimide Chemistry: Recent Advances. *Chem. Rev.* **1981**, *81* (6), 589–636. https://doi.org/10.1021/cr00046a004.

(333) Hu, Y.; Liu, L.; Dan, W.; Dan, N.; Gu, Z.; Yu, X. Synergistic Effect of Carbodiimide and Dehydrothermal Crosslinking on Acellular Dermal Matrix. *Int. J. Biol. Macromol.* **2013**, *55*, 221–230. https://doi.org/10.1016/j.ijbiomac.2013.01.009.

(334) Carbodiimide Crosslinker Chemistry - FR //www.thermofisher.com/fr/fr/home/life-science/protein-biology/protein-biology-learning-center/protein-biology-resource-library/pierce-protein-methods/carbodiimide-crosslinker-chemistry.html (accessed 2021 -09 -22).

(335) Fischer, M. J. E. Amine Coupling Through EDC/NHS: A Practical Approach. In *Surface Plasmon Resonance: Methods and Protocols*; Mol, N. J., Fischer, M. J. E., Eds.; Methods in Molecular Biology; Humana Press: Totowa, NJ, 2010; pp 55–73. https://doi.org/10.1007/978-1-60761-670-2_3.
(336) Xu, J.; Guo, J.; Golob-Schwarzl, N.; Haybaeck, J.; Qiu, X.; Hildebrandt, N. Single-Measurement Multiplexed Quantification of MicroRNAs from Human Tissue Using Catalytic Hairpin Assembly and Förster Resonance Energy Transfer. *ACS Sens.* **2020**, *5* (6), 1768–1776. https://doi.org/10.1021/acssensors.0c00432.
(337) Lukosz, W. Light Emission by Magnetic and Electric Dipoles Close to a Plane Dielectric Interface. III. Radiation Patterns of Dipoles with Arbitrary Orientation. *JOSA* **1979**, *69* (11), 1495–1503. https://doi.org/10.1364/JOSA.69.001495.
(338) Lukosz, W.; Kunz, R. E. Errata: Light Emission by Magnetic and Electric Dipoles Close to a Plane Dielectric Interface. II. Radiation Pattern of Perpendicular Oriented Dipoles. *JOSA* **1978**, *68* (8), 1155_2-1155. https://doi.org/10.1364/JOSA.68.1155_2.
(339) Lukosz, W.; Kunz, R. E. Light Emission by Magnetic and Electric Dipoles Close to a Plane Interface. I. Total Radiated Power. *JOSA* **1977**, *67* (12), 1607–1615. https://doi.org/10.1364/JOSA.67.001607.
(340) Lukosz, W.; Kunz, R. E. Light Emission by Magnetic and Electric Dipoles Close to a Plane Dielectric Interface. II. Radiation Patterns of Perpendicular Oriented Dipoles. *JOSA* **1977**, *67* (12), 1615–1619. https://doi.org/10.1364/JOSA.67.001615.

RÉSUMÉ

La quantification de biomarqueurs spécifiques est un outil de diagnostic important. Les tests immunologiques standards tels que ELISA nécessitent de nombreuses étapes de lavage et une amplification du signal, en particulier à faible concentration. D'autre part, le transfert d'énergie résonant de type Förster (FRET) a été utilisé pour concevoir des tests biologiques homogènes en une seule étape qui ne nécessitent aucune étape de lavage, où le biomarqueur permet la formation d'un complexe "sandwich" impliquant des anticorps marqués par le donneur et d'autres marqués par l'accepteur. Le FRET du donneur vers l'accepteur fournit alors une signature optique de la formation du complexe, et donc du biomarqueur d'intérêt. Cependant, le FRET, qui est très sensible à la distance donneur-accepteur, ne se produit à un taux significatif que lorsque la distance donneur-accepteur est inférieure à 10 nm; la grande taille de nombreux complexes biologiques limite l'efficacité du transfert d'énergie, empêchant une détection sensible. Je propose ici une nouvelle modalité de transfert d'énergie qui utilise des microcavités optiques en solution. Ensuite, je décris un schéma de biodétection pour détecter un oligonucléotide biomarqueur de cancer en solution.

À cette fin, j'ai conçu des structures de microcavité dans lesquelles des nanocristaux fluorescents sont placées à l'intérieur de microsphères diélectriques pour permettre un couplage fort de leur émission de fluorescence avec les modes de résonance de la cavité, appelés modes de galerie (WGM). J'ai étudié les propriétés structurelles et optiques de ces microcavités optiques. J'ai également caractérisé le transfert d'énergie entre ces modes et des nanoparticules acceptrices chargées de colorants présentes dans le champ évanescent, à quelques dizaines de nm au-dessus de la surface des microsphères. J'ai développé un modèle analytique pour caractériser les mécanismes de transfert d'énergie médié par les WGM (WGET). De plus, une comparaison entre WGET et FRET a révélé la supériorité du WGET dans le contexte de la construction de capteurs en termes de sensibilité et de portée de détection. Dans la dernière partie de la thèse, j'ai développé une stratégie pour fonctionnaliser ces microcavités optiques et leur permettre d'interagir avec des analytes cibles tels que l'ADN, l'ARN et les protéines avec une bonne spécificité. Cette stratégie a ensuite été adaptée pour fixer des sondes de capture d'ADN sur les microcavités activées par WGM. En utilisant les microsphères fixées à l'ADN comme donneur optique en combinaison avec des nanoparticules de colorants fonctionnalisées par un ADN complémentaire comme accepteurs optiques, un test de biodétection a été démontré avec succès pour détecter en solution un biomarqueur de cancer appelé survivine. Ce test a démontré une bonne sensibilité envers la cible, et s'est également avéré très spécifique. Le schéma de détection a été démontré dans un microscope confocal, au niveau de microsphères individuelles, puis transposé avec succès dans un instrument beaucoup plus simple tel qu'un spectrofluoromètre qui mesure la fluorescence de l'ensemble de la solution; la signature de la formation d'un complexe sandwich a été détectée efficacement.

En conclusion, j'ai démontré que le transfert d'énergie assisté par microcavité présente plusieurs avantages par rapport aux tests FRET ordinaires. Un véritable test de biodétection basé sur le principe du WGET a également été conçu avec succès pour détecter des biomarqueurs du cancer avec une sensibilité et une spécificité élevées. Cette étude ouvre donc de nombreuses possibilités pour concevoir des tests plus performants et plus précis pour détecter diverses entités biologiques

MOTS CLÉS

Quantum dots (QDs), nanoparticules polymèriques chargées de colorants, transfert d'énergie résonant de Förster (FRET), modes de galerie (WGM), transfert d'énergie par WGM (WGET), détection de l'ADN, tests sandwich.

ABSTRACT

Quantification of specific biomarkers is an important diagnostic tool. Standard immunoassays such as ELISA require extensive washing steps and signal amplification, in particular when the biomarker of interest is only present at very low concentrations. On the other hand, non-radiative Förster resonance energy transfer (FRET) has been used to design one-step homogenous bioassays which do not require any washing steps, where the biomarker enables the formation of a sandwich complex involving donor-labeled and acceptor-labeled antibodies. FRET from the donor to the acceptor then provides an optical signature of the complex formation, hence of the biomarker of interest. However, FRET which is highly sensitive to the donor-acceptor distance, only occurs in a significant rate when the distance between the donor and acceptor is less than 10 nanometers; thus the large size of many biological complexes limits the efficiency of energy transfer, preventing sensitive detection. Here I propose a novel energy transfer modality that uses solution-phase optical microcavities to enhance energy transfer. Following that, I describe a bio-sensing scheme designed to detect a cancer biomarker DNA in solution.

To this aim, I have designed microcavity structures in which fluorescent colloidal quantum dots are located inside dielectric polymer microspheres to enable strong coupling of their fluorescence emission with the cavity resonance modes or whispering gallery modes (WGMs) of the microspheres. A detailed study was carried out to comprehend the structural and optical properties of these optical microcavities. I also characterized the energy transfer between these modes and acceptor dye-loaded nanoparticles present in the evanescent field, within a few tens of nanometers above the microsphere surface. An analytical model was constructed to provide insights into the WGM mediated energy transfer (WGET) mechanisms. Moreover, a comparison between WGET and FRET revealed the superiority of WGET in the context of building sensors with improved sensitivity and longer range of detection. In the last part of the thesis, a strategy is discussed in detail to provide biological functionalities to these optical microcavities which would enable them to interact with target analytes such as DNA, RNA, and proteins with high specificity, and moreover to reduce non-specific interactions. This strategy then was adapted to attach DNA capture probes onto the WGM enabled microcavities. Using the DNA attached microspheres as optical donor in combination with probe-DNA functionalized dye nanoparticles as optical acceptors, a biosensing assay has been successfully demonstrated to detect a cancer biomarker DNA called survivin in the solution phase. This assay did not only show good sensitivity towards the target, but also it has proven to be highly specific. The detection scheme has been demonstrated in a sophisticated confocal microscope at the single microsphere level, then successfully translated to a much simpler spectrofluorometer that measures fluorescence from the whole sample solution; the signature of the sandwich complex formation was also effectively detected. In conclusion, I demonstrated that microcavity-assisted energy transfer has several advantages over regular FRET assays. A real bio-sensing assay based on the WGET principle has also been successfully designed to detect cancer biomarkers with high sensitivity and specificity. This study thus opens up many possibilities to design high-performing and more accurate assays to detect varieties of biological entities.

KEYWORDS

Quantum dots (QDs), dye-loaded polymeric nanoparticles, Förster resonance energy transfer (FRET), whispering gallery modes (WGMs), WGM mediated energy transfer (WGET), DNA sensing, sandwich assays.